Alexander Shtukenberg
Yurii Punin

Edited by Bart Kahr

Optically Anomalous Crystals

Springer

OPTICALLY ANOMALOUS CRYSTALS

Optically Anomalous Crystals

by

ALEXANDER SHTUKENBERG
St. Petersburg State University, St. Petersburg, Russia

YURII O. PUNIN
St. Petersburg State University, St. Petersburg, Russia

Edited with foreword by

BART KAHR
University of Washington, Seattle, Washington, USA

Springer

A C.I.P. Catalogue record for this book is available from the Library of Congress.

ISBN-10 1-4020-5287-1 (HB)
ISBN-13 978-1-4020-5287-3 (HB)
ISBN-10 1-4020-5353-3 (e-book)
ISBN-13 978-1-4020-5353-5 (e-book)

Published by Springer,
P.O. Box 17, 3300 AA Dordrecht, The Netherlands.

www.springer.com

Printed on acid-free paper

TABLE OF CONTENTS

FOREWORD

WHAT ARE OPTICAL ANOMALIES?

Charles Darwin (Darwin, 1859), quoting one Professor Owen in the *Origin of Species*, said "There is no greater anomaly in nature than a bird that does not fly; yet there are several." If we were to construct a parallel, though more restricted statement about the objects of our interest, crystals, it would be something like this: "There is no greater anomaly in solid state science than a crystal without a unique symmetry; yet there are many." The present volume, *Optically Anomalous Crystals* by Alexander Shtukenberg and Yurii Punin, is devoted to the analysis of crystals with ill-defined symmetries whose pathologies are signaled by the unexpected effects that they impart to transmitted light. Such crystals have long puzzled scientists.

The problem posed by optically anomalous crystals was brilliantly summed up by Jaeger in his famous *Lectures on the Principle of Symmetry and Its Applications in All Natural Sciences* (Jaeger, 1917).

> With respect to their internal structure, crystals are objects whose behaviour is chiefly governed by the laws of symmetrical configuration. In general it may appear that no essential discordances exist between the external forms of each crystalline individual and its molecular structure; and the world of crystals appeared from this to be rigorously ruled by stubborn laws which do not allow any exception in the behavior of the individuals which have a part in it.
>
> However, on closer examination, this appears to be by no means the case under all circumstances. In this well-governed society too, with its clear lines of demarcation and its strictly defined distinctions of classes and systems, there are a number of individuals which behave certainly not as they should do. Numbers of eccentricities are to be noted, and the somewhat revolutionary manifestations of many individuals take place here in a similar degree, as in our much more insufficiently ruled human society.

It is nearly impossible to read Jaeger without the suspicion that he was reflecting on the events of Russia's contemporaneous, revolutionary year. This feeling becomes a certainty when examining the 1920 edition of *Lectures on the Principle of Symmetry*. The flush of the historic events faded, and with it, so did the revolutionary language. We cannot help but wonder what Jaeger would have made of the fact that our understanding of optically anomalous crystals would take its great leap forward with the publication of a book by scientists from the former Petrograd, only after languishing for the better part of a century. (Saint Petersburg State University, the one-time home of our authors, is just a stone throw across the Neva River from the Winter Palace, the home of the Romanovs.) Their inquiry derives importance from, and takes solace in, the longevity

of optically anomalous crystals. As scientists, we can crow over the endurance of our enterprise, having quietly outlived the Soviet empire, and well on the way to outliving the American empire, however insufficiently ruled.

What is an *optically anomalous crystal*? Before answering this question we must distinguish between the term's literal interpretations and its typical usage. "Optically anomalous" has commonly been used to describe crystals that display *linear birefringence* under circumstances where we would not expect it. For example, if a cubic, optically isotropic crystal should become slightly deformed or desymmetrized by some mechanism—these will be discussed at length throughout—the crystal may become linearly birefringent and transmit light between crossed polarizers. Such a crystal would be quintessentially *optically anomalous*. If a centrosymmetric, triclinic crystal should lose its center of symmetry by the same mechanism, symmetry arguments tell us that such a crystal should be *circularly birefringent* and rotate the azimuth of applied, linearly polarized light. The second crystal would surely be optically anomalous in the literal sense. It would be optically rotatory despite the fact that the habit and x-ray structure may not show detectable deviations from centrosymmetry. However, the near impossibility of measuring small optical rotations reliably in triclinic systems (Kaminsky, 2000), obviates such examples. Given the overwhelming predominance of observations of anomalous linear birefringence as opposed to anomalous circular birefringence, or other effects such as linear or circular dichroism (although these phenomena are touched on herein), *optical anomaly*, has become synonymous with *anomalous linear birefringence* and we will use it as such unless otherwise specified.

BRIEF HISTORY OF OPTICAL ANOMALIES

The most striking features of crystals are their symmetric, polyhedral forms. Federov said that crystals "flash-forth their symmetry" (Shubnikov and Kopstik, 1974), a strong allusion to the sharp, highly reflecting surfaces of well-formed crystals prized by enthusiasts. We learned from Häuy that the shapes of crystals reflect the arrangements of the particles from which they are constructed. Today, these arrangements are routinely deduced from x-ray diffraction patterns. In the 19th Century, prior to the discovery of x-rays, the perturbations to the state of visible light traversing a crystal were used to assay symmetry.

Ideally, the symmetry of a crystal that an investigator would deduce from shape, from the transmission of visible light, from the scattering of x-rays, or from any other method, should be the same. However, as early as 1818, David Brewster in Edinburgh first noticed that some crystals appeared to have lower optical symmetries than morphological symmetries (Brewster, 1818b).

> Philosophers will no doubt be surprised to learn, that *muriate of soda, fluate of lime, the Diamond, Alum* have actually the property of Double Refraction, but under circumstances of such a singular kind, as to entitle them to be regarded as a new class of doubly refracting crystals.

Shown in Figure 1 are typical examples of anomalous birefringence in diamond cut perpendicular to the three-fold axis (Figure 1a) and the four-fold axis (Figure 1b). The false color scale is related to the birefringence in these images (Glazer *et al*., 1996). While the birefringence is heterogeneous is both cases, in (*a*) it forms a well-defined pattern while in (*b*) the property is scattered throughout in a helter-skelter arrangement. The images in Figure 1 were made with a contemporary birefringence imaging device. However, Brewster recorded comparable patterns hand-drawn from his observations through a microscope crudely fitted with polarizers (Brewster, 1835).

In his attempt to understand these strange specimens of otherwise cubic crystals, Brewster enlisted the assistance of the greatest contemporary mineralogist/chemist, Jöns Jakob Berzelius, who concluded, after extensive chemical analyses, that optically anomalous and optically normal crystals of the same ostensible species were composed of the same constituents. On this basis, Berzelius minimized the importance of the optical differences. Brewster's retort, in its essence, contained the argument that the elemental analyses of an ostrich and an eagle might be indistinguishable, but that doesn't mean both will fly (Brewster, 1822).

Theories offered to explain away inconsistencies in optical and morphological symmetry emerged in France. Biot (1842) and then Mallard (1886) speculated that symmetrical forms might arise from dissymmetric individuals via the twinning of lamellae. In Germany, Klocke and Klein favored explanations that resulted from strain induced in high-symmetry minerals through tectonic forces or during rapid crystallization. Arguments in the literature were spirited, and became mean-spirited during and after the Franco-Prussian war (Kahr and McBride, 1992).

The debate concerning the etiology of anomalous birefringence had become so confused that a scientific society in Leipzig sponsored a prize competition aimed at settling this contentious issue. The prize was awarded to Marburg privatdozent Reinhard Brauns, whose comprehensive 380 page book *Die optischen Anomalien der Krystalle* was published in 1891 (Brauns, 1891). Brauns presented discussions of some six dozen anomalously birefringent substances (Figure 2). The book presented research on optically anomalous crystals as a closed subject by parsing the list of optically anomalous substances among categories that represented the various proposed etiologies.

Gustav Tammann (1917), speculated that although internal stress from impurities should play a role, the ordering of components alone would suffice to cause birefringence. He indicated that such arrangements resulted from kinetic, not thermodynamic, control of crystal growth, whereby sites that would otherwise be related by symmetry have not had time to reach equilibrium.

When the discovery of x-ray diffraction transformed crystallography in 1912, several investigators tried to find a substantial difference in the atomic structures of optically anomalous and optical normal crystals of the same species. Given the qualitative methods of intensity analysis available in the two decades following the Braggs' first x-ray crystal structures, these searches were doomed to fail. In this

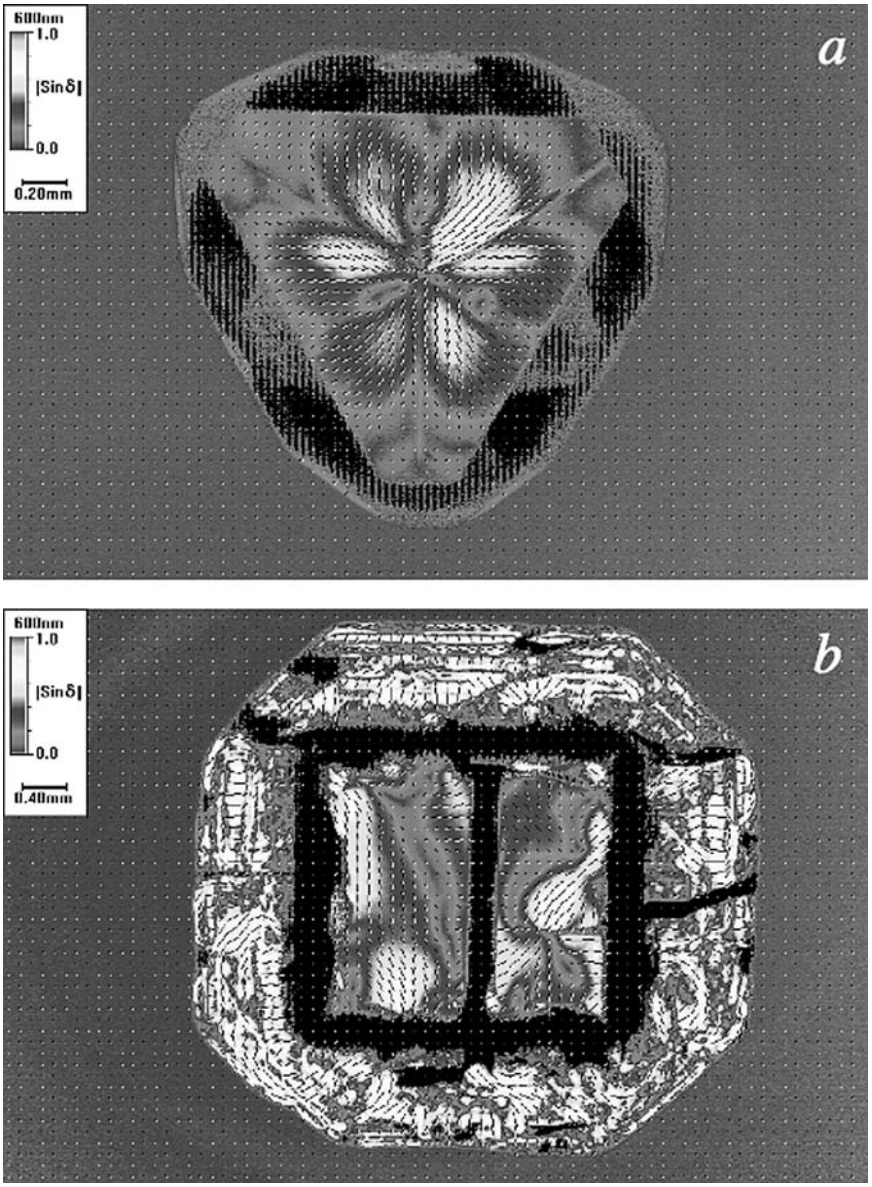

Figure 1. Anomalous birefringence images of sections of diamond cut (*a*) perpendicular to the threefold axis, and (*b*) perpendicular to the fourfold axis. The false color scale plotted as $|\sin\delta|$ where $\delta = 2\pi\Delta nL/\lambda$, $\Delta n = n_{\perp} - n_{\parallel}$, L is the sample thickness, and λ is the wavelength of light. Hash marks indicate the extinction directions, the orientation of the most refracting directions
Source: Figure courtesy of Dr. M. Geday (see Color Section following page 254)

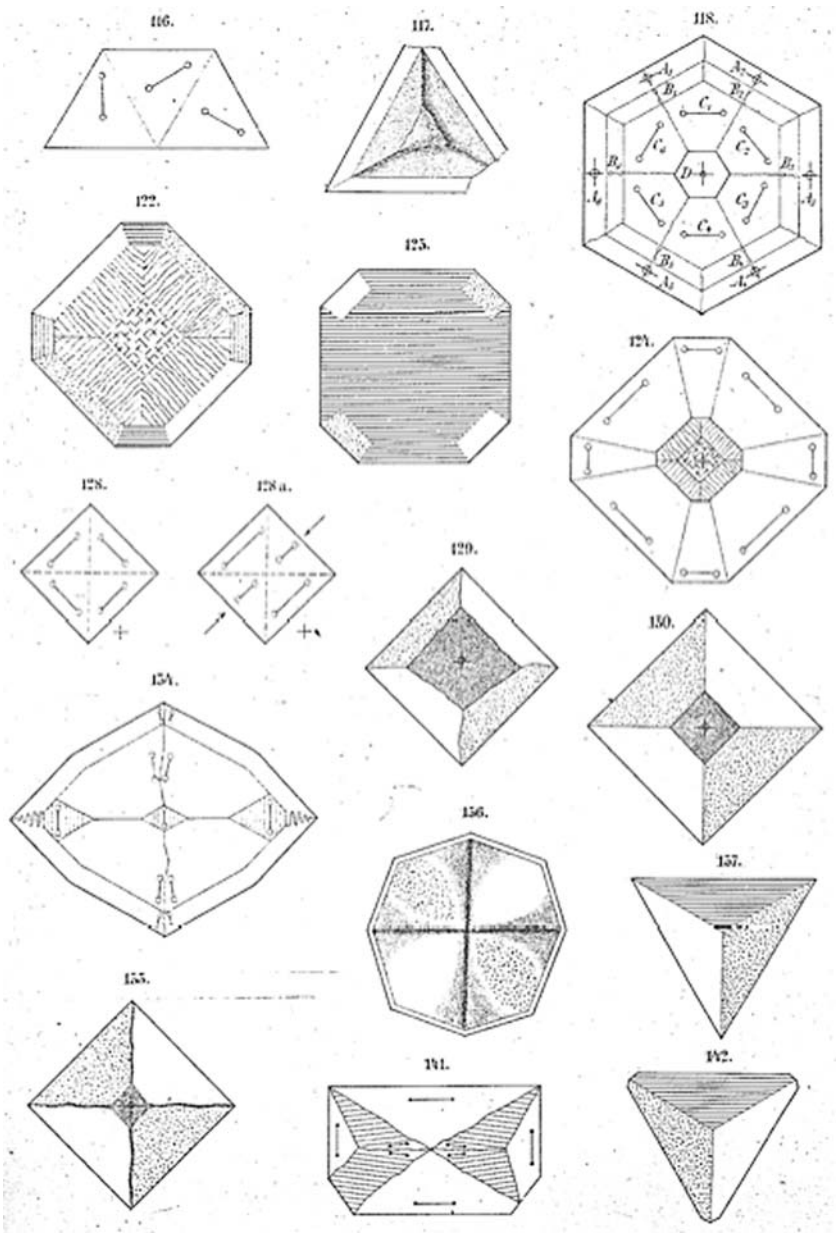

Figure 2. Typical array of optically anomalous crystals from Brauns' *Die optischen Anomalien der Krystalle* (1891)
Source: From Brauns, R. *Die Optischen Anomalien der Krystalle*; S. Hirzel: Leipzig, 1891.

new climate, the insights of Tammann fell largely on deaf ears. The community of crystallographers was focused on fixing the positions of atoms.

NEUMANN-CURIE PRINCIPLE

Optically anomalous crystals appear to violate Pierre Curie's Symmetry Principle, one of the most general and powerful organizing concepts in the physical sciences. The Curie Symmetry Principle, when applied to problems in crystal physics, is usually referred to as the Neumann-Curie Principle after one of its progenitors, Franz Neumann. It states that the properties of a system are invariant to its symmetry operations. Curie asserted the impossibility of bringing about certain effects under circumstances lacking essential dissymmetries that are characteristic of the effects.

A contemporary articulation of the Symmetry Principle would embody the following statements:

1. The symmetry elements of a cause must reappear in the effects it produces.
2. Dissymmetric effects must be evident in the cause from which they arise.
3. The converse of the previous statements must hold: Effects can be more symmetrical than their associated causes.

The Neumann-Curie Principle has its origins in the classification of crystals according to their effects on transmitted light. Réné Just Haüy recognized in 1792 that only crystals with the forms of the cube, octahedron, or rhombic dodecahedron were isotropic with respect to light refraction (Burke, 1966). Haüy did not make distinctions within the class of optically anisotropic crystals. This was accomplished simultaneously by Brewster (1818a) and Biot (1818), following the discovery of light polarization by reflection. They were now equipped to exploit the observation of interference in some crystals as sensitive signatures of anisotropy, and thus began the real work of classifying crystals optically. Brewster and Biot succeeded in partitioning anisotropic crystals into the uniaxial (trigonal, tetragonal, and hexagonal) and biaxial (less than threefold symmetry) classes, indicating the numbers of directions characterized by polarization independent refraction. The wavelength dependence of the refractive index, dispersion, ultimately enabled a distinction among biaxial crystals with zero, one, or three directions fixed by symmetry for all wavelengths. This brought the total number of optical classes to five.

An account of the conceptual development of the Neumann–Curie Principle is continued by Shubnikov and Kopstik (1974). To Vivell (1830) they attribute the following statement: "the optical symmetry of crystals corresponds to their geometric symmetry." Neumann generalized the principle of Vivell by claiming that "in all its physical properties, a material exhibits the same kind of symmetry as its crystallographic shape" (Neumann, 1841). This message was carried forward by his pupil Minnigerode, who abandoned shape as a point of reference: "the symmetry group of a crystal is a subgroup of the symmetry groups of all the physical phenomena which may possibly occur in that crystal." Pierre Curie went one step further by replacing "crystal" with "medium" (Curie, 1894). Ultimately,

Woldemar Voigt, another Neumann student, systematized the Symmetry Principle in crystal physics by introducing tensor notation (Voigt, 1910).

What is remarkable to this observer in hindsight is that just as Brewster and Biot were developing their optical classification of crystals on the basis of symmetry, they were focusing also on the exceptions, the so-called optically anomalous crystals. Despite the fact that there were many crystals that seemed to have inconsistent optical and morphological symmetries, faith in the developing Symmetry Principle—whether fully articulated or just intuitive—gave researchers the confidence to push on with the symmetry-based classification of crystals certain that explanations for the anomalies would arrive in due course. This has not necessarily been the case.

DIE OPTISCHEN ANOMALIEN DER KRISTALLE

The high water mark in the study of optical anomalies, prior to the publication of the present volume, was Brauns' book from 1891 (Brauns, 1891). Here, we have the opportunity to make a unique comparison between *Die optischen Anomalien der Kristalle* by Brauns, and *Optically Anomalous Crystals* by Shtukenberg and Punin, the only two monographs on a subject between which sits the entire 20th Century.

Brauns created six classes of optical anomalies.

1. Optical anomalies due to differently crossed lamellae.
2. Optical anomalies due to dimorphism (the coexistence of more than one phase).
3. Optical anomalies due to mechanical pressure, rapid cooling, etc. (by the etc. Brauns was invoking any harsh treatment during the life of the crystal).
4. Optical anomalies due to isomorphous admixtures (and the strain induced by the mismatch of components).
5. Optical anomalies as a result of efflorescence.
6. Optical anomalies whose cause is not known or which do not fit into any of the above categories.

Brauns encapsulated all the experimental and theoretical observations on optical anomalies within a single volume and in doing so he may have given his work more authority than it merited. Subsequent writers frequently cited *Die optischen Anomalien* as the definitive source on the subject. Many of Brauns' assignments therefore went unchallenged.

How does Brauns's presentation and classification square with the revelations of the present reanalysis? After a brief introduction to classical crystal optics and the interaction of light and matter, in Chapter 1, Shtukenberg and Punin discuss in depth photoelastic and/or piezo-optic sources of optical anomalies in Chapter 2. This overlaps with observations in Brauns' classes #2 and #3. In Chapter 3, the kinetic ordering of constituents during growth is modeled, leading to impressive predictions of the optical distortions to be expected as a function of growth rates and temperatures; optical properties are connected to activation parameters. Kinetic order often requires admixture and here the overlap is largely with class #4. Anomalies due

to heterogeneities in lamellar crystals and other complex accretions is taken up in Chapter 4. Comparisons can be made to materials in class #1. While there is surely no one-to-one correspondence of themes, we see the vindication of the main ideas of Brauns and his progenitors in one way or another, in one substance or another. Like the final category of *Die optischen Anomalien*, Chapter 5 tackles the vexing confluence and interplay of the variety of sources of optical anomalies.

Optically Anomalous Crystals departs from the format of Brauns, in that it does not attempt to digest all that is known for each known optically anomalous crystal. Given the exponential growth of the scientific literature over the past century and the discovery of many new optically anomalous substances, Brauns's 380-page treatise could easily fill 3,800 comparable, contemporary pages. Rather, the strength of Shtukenberg and Punin's book is the development of quantitative models based on in-depth analyses of a smaller number of substances. One family of minerals, the garnets, and one family of water-soluble salts, the alums, are treated exhaustively, and many other systems are treated in lesser detail. The presentation is largely based on research that comes from the authors' laboratories. However, the generality of the models developed enable their application to almost any substance.

What naturally distinguishes Shtukenberg and Punin from Brauns is an extra century experience and sophistication. The concepts that the present authors can draw upon that were unknown in 1891 include the following: the tensorial description of physical properties, the enumerations of the space groups, x-ray diffraction, the spiral crystal growth mechanism, transition state theory, the theory and direct observations of dislocations.

The mission of Shtukenberg and Punin can be likened to that of physicians. The crystal sections in Figure 1 both show optical anomalies but their strikingly different character is evidence of distinct origins. It is the job of the optical crystallographer to properly characterize the symptoms (the anomalous birefringence), propose a disease (strain, kinetic ordering, etc.), and then find evidence for it (dislocations, selective atoms occupancies, etc.). Sometimes, it is obvious that a patient is gravely ill, but the origin of the malady can be extraordinary subtle. Perhaps, one amino acid of one enzyme is not what it should be. As with optically anomalous crystals, it is often obvious that something is "wrong", but the challenge, which can captivate, is diagnosing the illness. The full sweep of developments in solid state science in the twentieth century were requisite for the accounting of optically anomalous crystals contained herein. Brauns, like a nineteenth century physician, similarly without x-rays, was by and large shooting in the dark.

Optically Anomalous Crystals was first published in Russian by Nauka in 2004 (Shtukenberg and Punin, 2004). Conspicuously absent from that work are molecular/organic crystals, not a part of the mineralogy. Likewise, Brauns barely touches molecular crystals.He discussed only one organic crystal, strychnine sulfate hexahydrate. Moreover, he isolates strychnine—perhaps he was afraid of it—in a class by itself. Strychnine sulfate ($C_{21}H_{24}O_6N_2S \cdot 6H_2O$) hexahydrate was optical anomalies class #5, the singular substance that became anomalous due to the loss of solvent. However, as *Die optischen Anomalien* went to press, Martin (1891)

completed a thesis on optically anomalous organics. Many others have been found, and we have added, a discussion of several organic examples to the present volume where most appropriate.

Large, polyfunctional organic molecules may at first blush seem to complicate many of the ideas and models put forward throughout. However, the size of organic molecules amplifies surface topography and simplifies arguments based upon shape. Moreover, intuitive judgments about intermolecular interactions are supported in polyfunctional organic molecules that are much more difficult to formulate with monatomic, or simple, symmetrical polyatomic ions.

OPTICAL ANOMALIES EXCLUDED

As with any finite investigation in the natural sciences, authors must establish boundaries and the more fully explained are the choices of boundaries, the less arbitrary they may seem. The following discussion is restricted to the 32 classical crystal point groups of the Nineteenth Century, those involving rotational symmetries of 2π, π, $2\pi/3$, $\pi/2$, and $\pi/3$. The International Union of Crystallography has subsequently broadened the definition of a crystal so as to include aperiodic materials (Report of the Ad Interim Commission on Aperiodic Crystals, 1992) with impossible rotational symmetries of order 5, 7, 8, 10, 12…the beautiful subject quasicrystals (Steuer, 2004). Presently, there is little information on the refractivity of quasicrystals save for a prediction of a negative index of refraction in 12-fold symmetric quasicrystals (Feng *et al.*, 2005). Despite the fact that negative indices of refraction, previously considered to be an impossibility but now rather firmly established, are perhaps the ultimate optical anomalies, negative refraction in 12-fold symmetric quasicrystals takes us immeasurably far afield of the subject of our interest, unexpected linear birefringence of visible light in crystals of common experience.

Likewise, omitted from this book is a discussion of the magnetic crystal point groups, or more generally the Shubnikov two color groups. These groups are necessary in order to fully describe the birefringence of magnetic boracites containing Co and Ni (Mao *et al.*, 1999) Boracite, most commonly $Mg_7Cl_2B_{16}O_{30}$, is ostensibly cubic but its birefringence was reported in 1821 by Brewster (Anonymous, 1821) just a few years after launching the study of anomalous birefringence. Given the dizzying interplay of ferromagnetism, ferroelectricity, and ferroelasticity in these crystals, each of which is manifested directly and/or indirectly on the optical indicatrix of individual domains, the optics are expected to be extraordinarily complex, however they do not necessarily fall under the banner of *anomalous*.

Jones (1948) recognized certain symmetries in the formal expression of crystal optics that argue for a second pair of extinction or absorption axes bisecting the usual ones. Graham and Raab (1983) predicted circumstances and magnitudes of so-called “Jones birefringence” and “Jones dichroism”. Lorentz predicted that some cubic crystals could be weakly birefringent because of the non-uniformity of the electric field of a plane wave across a unit cell

(Lorentz, 1936; Agranovich and Ginzburg, 1984). We can say that Jones birefringence and the Lorentz effect are surely *unusual* examples of birefringence, but they would not qualify as optical anomalies.

The inquiry of Shtukenberg and Punin is restricted to linear optical anomalies. Even though precisely the same processes of desymmetrization that may give rise to linear birefringence in an otherwise isotropic crystal may give rise to second harmonic generation in an otherwise centrosymmetric crystal (Weissbuch *et al*., 1989), *Optically Anomalous Crystals* is restricted to phenomena made manifest in modest electric fields from incandescent light sources, as the subject is rooted in classical, linear crystal optics.

Google will find innumerable uses of *optical anomaly* in the scientific literature. For example, Overhauser and Butler (1976) wrote about the optical anomaly in the reflection spectrum of potassium metal that is induced by a surface layer of KOH causing a distortion of the optical indicatrix of the metal. Why is this not a fitting subject of *Optically Anomalous Crystals*? It might be. Its grounds for disqualification are soft at best. The study of optical anomalies is closely related to mineralogy and the use of the polarized light microscope to study birefringence in transmission. Potassium metal does not occur naturally, it is studied in reflection, indicatrix distortion is detected by absorption, and the problem is disconnected from the rich tradition of optical anomalies.

OPTICALLY ANOMALOUS CRYSTALS *FROM RUSSIA*

The study of optically anomalous crystals began in Scotland, moved to France, reached its zenith in Germany, and then expired. The themes of optical anomalies, particular those due to kinetic ordering, reemerged among scientists from Israel, Japan, and the United States among other places, in the 1980's and 1990's. Unfortunately, this mini-renaissance passed over a number of seminal contributions, elaborated herein, first published in Russian in the 1960s and 1970s. A history of optically anomalous crystals that attempted to be comprehensive (Kahr and McBride, 1992) missed some essential Russian papers. This is an unfortunate consequence of the increasingly Anglo-centric scientific enterprise that time and again overlooks more than half of the world that does not use the Roman alphabet.

Shubnikov, a serious student of Pierre Curie (Shubnikov, 1988) first articulated the idea that growth pyramids, those sub-volumes of a crystal whose bases represent the growing faces and whose coincident apices mark the site of nucleation, must have a reduced symmetry (Shubnikov, 1961). Such faces cannot have cubic symmetry; that would require symmetry axes not normal to the faces. They can not be centrosymmetric; inside is the crystal, while outside is the growth medium. In fact, such faces can only admit ten point groups: 1, 2, 3, 4, 6, *m*, 2*mm*, 3*m*, 4*mm*, 6*mm*. Shubnikov recognized that crystals with geometrically polar growth sectors could, in principle, display polar properties even when the idealized structure of the medium was centric. He further realized that cubic crystals with dissymmetric pyramids could lead to double refraction or

double absorption, or any number of other properties. He did not discuss in detail the mechanisms of desymmetrization, but he did, on the basis of symmetry, presuppose the process of kinetic growth desymmetrization discussed in detail in Chapter 3. A rigorous group theoretical analysis of the symmetry reduction inherent in mixed crystal growth is also provided in Chapter 3.

Immediately thereafter, Tsinober and coworkers began a series of investigations into the anomalous pleochroism of smoky quartz and amethyst (Tsinober, 1962). On the basis of single crystal ESR intensity measurements it was established that these crystals trap Al^{3+} and Fe^{3+} in three crystallographically equivalent silicon positions that are not translationally related on the growth face. When adsorbed to the $\{01\bar{1}1\}$ and $\{\bar{1}\bar{1}20\}$ sectors of surface symmetry 1 and 2, respectively, the corresponding pyramids were biaxial with anomalous pleochroism, whereas the $\{0001\}$ sectors of symmetry 3 were uniaxial showing ordinary dichroism (Tsinober *et al*., 1967a). A slightly different explanation was offered more recently (Partlow and Cohen, 1986). The local symmetry of growth active faces was used to interpret optically anomalous cordierite $Al_3Mg_2(Si_5AlO_{18})$ (Tsinober *et al*., 1977). Similar analyses were applied to quartz, (Tsinober and Samoilovich, 1975), zinc selenate (Nizamutdinov *et al*., 1977) and sodium kröhnkite $Na_2Cu(SO_4)_2 \cdot 2H_2O$ (Vinokurov *et al*., 1977).

THE ABOLITION OF OPTICAL ANOMALIES?

As we will see in Chapter 1, properties of crystals can be evaluated classically or even quantum mechanically, using first principles applied to crystal structures. Given this rather complete understanding of crystal physics, optical anomalies should not exist. However, crystals often display distortions of structure that cannot be revealed by standard methods of analysis or are often overlooked/ignored by researchers. Because subtle structural distortions can profoundly influence optical manifestations of crystals, the study of optically anomalous crystals has endured for almost two centuries.

Are optical anomalies in the eyes of the beholder? One investigator's anomaly may be an expectation for another more knowledgeable or more sophisticated scientist. An über-investigator with the wherewithal to characterize a crystalline substance by any means necessary to the greatest conceivable effect would witness the melting away of anomalies. They would be replaced by a more nuanced understanding of the structure and physical properties. Anomalies are supported by a measure of ignorance. This is why the study of optically anomalous crystals flourished at the end of the nineteenth century prior to the discovery of x-ray diffraction, when the analysis of crystal structure and properties was circumscribed by light microscopy. In the absence of complementary methods of structure determination, investigators were free to inject their well-earned prejudices into the debate. To the extent that Shtukenberg and Punin have succeeded in their purpose, this book, or at least large parts of it, could be called *Formerly Optically Anomalous Crystals*. For example, we now know from x-ray analysis that chlorate and bromate ions in

mixed sodium salts are not statistically distributed among lattice sites otherwise related by symmetry in the cubic space group $P2_13$. Thus, the observation of birefringent cubes is no longer vexing (Gopalan *et al.*, 1993; Shtukenberg *et al.*, 2004). However, birefringence in mixed sodium halates has long been considered anomalous. It is discussed at length by Brauns (1891), and classified in the "not sure" class #6. As such, the mixed halates are likewise considered herein.

On the other hand, investigators run the danger of seeing etiologies of anomalous birefringence in data from methods of analysis that complement the light microscope when the evidence may not really be substantial. Akizuki, a pioneer in the study of optically anomalous silicates, and his coworkers (Tanaka *et al*., 2002b) observed a monoclinic optical indicatrix in the {011} growth sectors of yugawaralite ($CaAl_2Si_6O_{16} \cdot 4H_2O$). The {120} sectors were optically triclinic. x-ray data from single growth sectors supported this difference. However, when the data was re-analyzed by Baur and Fischer (2002), lattice constants and interatomic distances were not found to be significantly different, while systematic absences were maintained in the triclinic dataset. The optical analysis tells us that the sectors are monoclinic and triclinic but that doesn't mean that the nature of the deviations from symmetry can be precisely defined. The light microscope, old as it may be, is astonishingly sensitive to small deviations in symmetry. It is for this reason that optically anomalous crystals will continue to test the ingenuity of crystallographers for another century at least.

CHAPTER 1

CRYSTAL OPTICS

1.1. INTRODUCTION TO CRYSTAL OPTICS IN TRANSMITTED LIGHT

The science of crystal optics describes the interactions of electromagnetic radiation with crystalline solids. The vast majority of research in this field is focused on the changes in the state of visible light transmitted by dielectrics, the class of non-conducting materials to which most non-opaque minerals belong. The optical properties of crystals can also be studied by reflection, or in more or less energetic regions of the electromagnetic spectrum, but because the common petrographic or polarizing microscope (Hartshorne and Stuart, 1970) is suited to visible light, we will focus on crystals in transmitted, visible light, detectable with the human eye. Before discussing what might be *anomalous* about the optical properties of some crystals, we must first review the optics of well-behaved crystals. For analyses of the theoretical foundations of crystal optics and reviews of techniques we refer reader to classic texts (Shubnikov, 1960; Bloss, 1961; Tatarsky, 1965; Hartshorne and Stuart, 1970; Stoiber and Morse, 1994; Shuvalov, 2005). What follows is a cursory review of basic principles.

1.1.1. Light in Isotropic Media

Amorphous solids such as glasses are said to be isotropic; their physical properties are the same in each Cartesian direction. Crystals that belong to the cubic system in which the lattice constant $a = b = c$, and the angle between basis vectors, $\alpha = \beta = \gamma = 90\,°$, share this characteristic of isotropy. The interaction of light with isotropic substances has been reviewed (Batsanov, 1966; Kittel, 1996; Shuvalov, 2005).

Charges in a dielectric placed within an electric field of strength (E) will be displaced resulting in a polarization (P) that is linearly proportional to the applied field:

$$P = \psi E. \tag{1.1}$$

The proportionality constant (ψ) is the dielectric susceptibility of the medium. Since polarization creates an electric field that opposes the applied field, the total electric field, in cgs units, is equal to:

$$E = E_0 - 4\pi P = E_0 - 4\pi\psi E. \tag{1.2}$$

Rearrangement gives:

$$E = \frac{E_0}{1+4\pi\psi} = \frac{E_0}{\kappa} = \eta E_0, \tag{1.3}$$

where κ is the dielectric constant or relative permittivity of the medium. It is often replaced with the inverse η, the impermittivity. Interaction between an electric field and an isotropic medium is characterized not only by a polarization vector **P**, the dipole moment per unit volume, but also by the electric displacement vector **D**, the total charge displaced through a unit area. **D** is co-linear with the electric field vector **E** and numerically exceeds it κ times

$$D = \kappa E = E + 4\pi P = E_0. \tag{1.4}$$

Electromagnetic waves force electrons to oscillate with a certain frequency. Consequently, periodic changes of dipole moments induce secondary electromagnetic waves that are superimposed on the driving fields, resulting in a new wave with an associated amplitude and phase. This interaction reduces the velocity (ν) of light in a medium with respect to the velocity of light in a vacuum c. According to Maxwell's theory, ν is equal to

$$\nu = \frac{c}{\sqrt{\kappa\mu}} \approx \frac{c}{\sqrt{\kappa}} = c\sqrt{\eta}, \tag{1.5}$$

where μ is the magnetic constant or permeability of the medium, approximately equal to unity in weakly magnetic dielectrics. The refractive index of the medium n is by definition the ratio of light velocity in vacuum to that in the medium:

$$n = \frac{c}{\nu} = \frac{1}{\sqrt{\eta}} = \sqrt{\kappa}. \tag{1.6}$$

Thus, the relation between electric field (E) and electric displacement (D) defines the refractive index of an isotropic medium in accordance with Equations (1.4) and (1.6). In isotropic media, the electric field vector is always parallel to electric displacement. The refractive index depends also on the optical frequency. This phenomenon is called dispersion.

1.1.2. Light in Anisotropic Medium: Linear Birefringence

In isotropic insulators, the induced dipoles generated through dielectric polarization are parallel to the applied electric field. Consequently, P and E are related by a scalar, a single value. This is not so in anisotropic media, substances whose properties depend on direction. Due to the anisotropy of forces acting on each charge in a non-cubic crystal structure, the displacement of electrons and the consequent polarization may depend on the orientation of the crystal with respect to the applied electric field. As a result, polarization can be characterized by three principal values of dielectric permittivity (or impermittivity), oriented along Cartesian directions. Displacement of charges and the displacement vector **D** no longer must be co-linear with the electric field vector **E**. These vectors in anisotropic media are linked one to another by dielectric permittivity κ_{ij} or dielectric impermittivity η_{ij} having the form of second rank tensors (Equations (1.7) and (1.8) respectively), not by scalars as in isotropic media:

$$E_i = \kappa_{ij} D_j \qquad i, j = 1, 2, 3$$

$$D_i = \eta_{ij} E_j \qquad i, j = 1, 2, 3 \tag{1.7}$$

In vector form,

$$\mathbf{E} = \kappa \mathbf{D}$$

$$\mathbf{D} = \eta \mathbf{E}. \tag{1.8}$$

Tensors describe the physical properties of crystals as they relate to the so-called crystal physical basis, a Cartesian coordinate system that has a specific orientation with respect to the usual crystallographic basis.

Solution of Maxwell's Equations leads to the conclusion that in a general direction in an anisotropic medium, two plane-polarized waves propagate with mutually perpendicular displacement vectors. This result is seemingly counterintuitive, but a derivation can be found in Nye (1985). Each of these waves or eigenmodes is characterized by a refractive index. This is the situation that characterizes double refraction or linear birefringence, the difference in the refractive indices of the eigenmodes, $\Delta n = n_1 - n_2$.

Directing the principal values of the dielectric permittivity tensor along the coordinate axes $(x_i, i = 1, 2, 3)$ one can get the following Equation:

$$\frac{x_1^2}{n_1^2} + \frac{x_2^2}{n_2^2} + \frac{x_3^2}{n_3^2} = 1. \tag{1.9}$$

This is the Equation for the ellipsoid known as the *optical indicatrix*. The principal values of refractive indices n_1, n_2 and n_3 in crystal optics are usually denoted as n_α

or α for the smallest value, n_β or β or the intermediate value, and n_γ or γ for the largest value (see Bloss, 1961, for other systems of notations). Since eigenvalues of refractive indices are equal to $n_i = \sqrt{\kappa_i} = 1/\sqrt{\eta_i}$, (1.9) is equivalent to:

$$\frac{x_1^2}{\kappa_1} + \frac{x_2^2}{\kappa_2} + \frac{x_3^2}{\kappa_3} = 1 \text{ and} \tag{1.10}$$

$$x_1^2\eta_1 + x_2^2\eta_2 + x_3^2\eta_3 = 1. \tag{1.11}$$

For an indicatrix in a general orientation with respect to a Cartesian system, (1.11) is expressed as

$$\eta_{11}x_1^2 + \eta_{22}x_2^2 + \eta_{33}x_3^2 + 2\eta_{12}x_1x_2 + 2\eta_{23}x_2x_3 + 2\eta_{31}x_3x_1 = 1.$$

1.1.3. Symmetry of the Optical Indicatrix

According to the Neumann-Curie principle (Curie, 1894) the symmetry of each physical property of a crystal is a super-group of the point group of the crystal. As the physical properties of crystals are controlled by structure, the symmetry of the optical indicatrix must not be lower than the symmetry of the crystal structure (Figure 1.1, Table 1.1).

In isotropic, *cubic* crystals, the optical indicatrix is a sphere (symmetry ∞/∞) and the refractive index has a constant value independent of orientation.

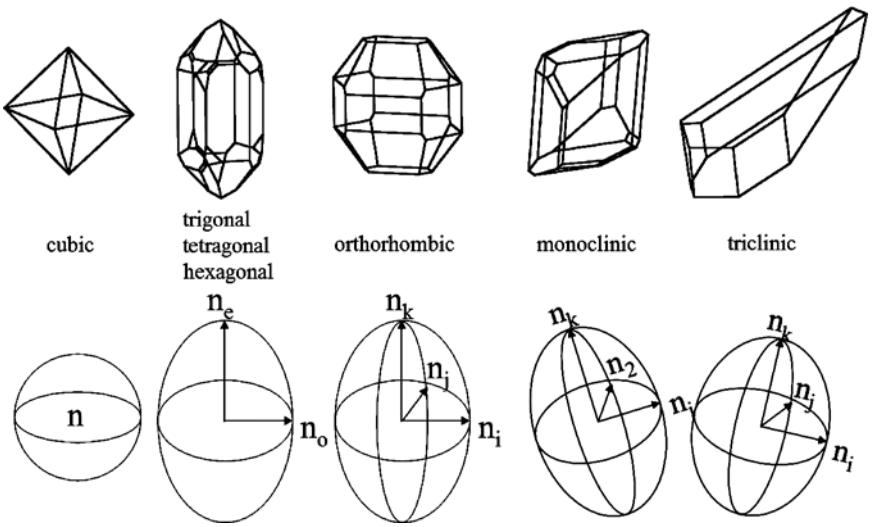

Figure 1.1. Typical crystal habits representing the five distinct optical classes based on indicatrix symmetries and indicatrix dispersion shown schematically below
Source: Figure courtesy of Professor Werner Kaminsky, Department of Chemistry, University of Washington.

Table 1.1. Crystals belong to one of five optical symmetry groups, depending upon the shape of the indicatrix and the character of its dispersion (Shubnikov, 1960)

Indicatrix Symmetry	Biaxial			Uniaxial	Isotropic
	$\bar{1}$	$2/m$	mmm	∞/mmm	∞/∞
Morphological symmetries	1, $\bar{1}$	2, m, $2/m$	$2mm$, 222, mmm	3, 4, 6, $\bar{3}$, $\bar{4}$, $\bar{6}$, $3m$, $4mm$, $6mm$, 32, 422, 622, $4/m$, $6/m$, $4/mmm$, $6/mmm$, $\bar{3}m$, $\bar{4}2m$, $\bar{6}m2$	23, 432, $\bar{4}3m$, $m\bar{3}$, $m\bar{3}m$

In *hexagonal, trigonal*, and *tetragonal* crystals, the optical indicatrix is an ellipsoid of revolution (symmetry ∞/mmm). Crystals with such indicatrices belong to the *uniaxial* optical class. The infinite order axis of the indicatrix of symmetry ∞/mmm coincides with the three-fold, four-fold or six-fold axis of the crystal. This direction is called the optic axis. The refractive indices in transparent crystals are the same for vibrations anywhere in the plane perpendicular to the optic axis. Polarized light passing along the optic axis will retain its state of polarization (excepting gyrotropy, see next section). Such a ray obeys Snell's Law of refraction and is called the *ordinary ray*. The orthogonal ray does not obey Snell's Law. It is designated as the *extraordinary ray*. If the refractive index of the ordinary ray is smaller than that of the extraordinary ray, the crystal is *optically positive*. If the refractive index of the ordinary ray is larger the crystal is *optically negative*.

Orthorhombic, monoclinic, and *triclinic* belong to the biaxial optical class. The optical indicatrix is a general ellipsoid with three different principal refractive indices. In orthorhombic crystals the principal indicatrix axes coincide with two-fold axes. The symmetry of the indicatrix is *mmm*. In monoclinic crystals, one axis of the indicatrix is coincident with the one two-fold axis. Two other axes lie in the perpendicular plane, but are otherwise unconstrained. Since the orientation of the subordinate axes are not restricted by the crystal symmetry, monoclinic optical indicatrices are dispersive; their shapes and orientations depend on wavelength. For monoclinic crystals, indicatrices corresponding to different wavelengths of light have different orientations with respective to rotation about the two-fold symmetry axis. Although any one indicatrix has symmetry *mmm*, the set of indicatrices for a range of wavelengths has symmetry $2/m$. In triclinic crystals, all three principal indicatrix axes are dispersive. While any one indicatrix has symmetry *mmm*, a set of indictrices representing a range of wavelengths has symmetry $\bar{1}$.

The general ellipsoid that describes biaxial crystals is often characterized in part by specifying the special plane that contains the two optic axes, called the axial plane. The angle between the optic axes, the axial angle ($2V$), is a convenient, quick measure of the biaxial indicatrix. The axial plane is used to orient the indicatrix in conoscopic interference figures (see section 1.2). The optic axes are bisected on the near and far sides by the *acute bisectrix* and the *obtuse bisectrix*, respectively (Figure 1.2).

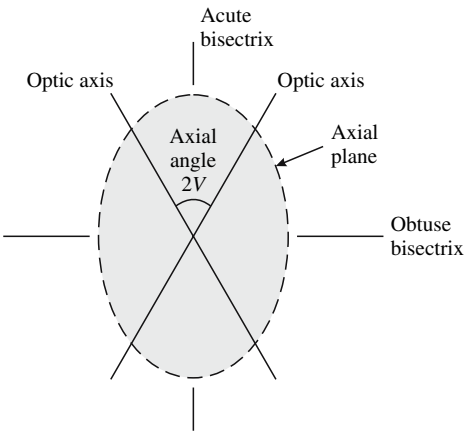

Figure 1.2. The axial plane, a special cross section of a biaxial indicatrix

1.1.4. Other Linear Optical Phenomena

1.1.4.1. Linear dichroism

Most generally, the refractive index is a complex quantity: $n = n' + ik''$ where k is the absorption coefficient describing that part of the intensity (I) of a light wave attenuated by an absorbing medium of thickness (L):

$$I/I_0 = e^{-kL} \tag{1.12}$$

The real component represents the dispersive refractive index. The imaginary component represents the dissipative absorption. *Linear dichroism* (often *pleochroism* in the mineralogy literature) is the change in the intensity or hue of a light absorbing material depending on the direction of the dielectric displacement vector. A fuller statement of linear birefringence, accounting for absorption, is

$$\Delta n_{\text{linear}} = (n_1 - n_2) + i(k_1 - k_2), \tag{1.13}$$

where the subscripts refer to the orthogonal eigenmode directions.

The absorption of light is constrained by the properties of the *absorption ellipsoid* in the same way as the ordinary refraction is constrained by the optical indicatrix. Due to symmetry restrictions, linear dichroism can not be observed in cubic crystals. In uniaxial crystals there are two principal absorption axes parallel and perpendicular to the optic axis. Such crystals are said to be dichroic. In biaxial crystals, the absorption ellipsoid has three unique axes corresponding to vibrations along the principal axes of the indicatrix. In orthorhombic crystals, all three principal axes of the absorption ellipsoid are constrained by symmetry. In monoclinic crystals, only one principal axis of the absorption ellipsoid is constrained by symmetry, the two-fold axis. Two other principal absorption axes in monoclinic crystals

and all three absorption axes in triclinic crystals are in general not parallel to the principal vibration directions. Usually, however, deviations are slight and for practical purposes the principal axes of the absorption ellipsoid and optical indicatrix are taken as parallel.

Anomalous pleochroism has been observed. For example, Tsinober *et al*. (1967a) reported optical anisotropy in the basal-plane section of smoky quartz where there should be none. The origin of this phenomenon is closely linked to the origin of anomalous birefringence and will be discussed further in sections 3.4.4, 3.4.6. Crystals containing oriented organic dyes can show large deviations between the axes of the absorption ellipsoids and vibration directions of the optical indicatrices (Claborn *et al*., 2005). These will be discussed further in section 3.4.4.

1.1.4.2. Gyrotropy: circular birefringence and circular dichroism

If the orthogonal rays propagating through a crystal become out of phase by $\pi/2$ the emergent wave will be *circularly polarized*. The electric vector will rotate uniformly about the ray such that the end point traces a helix with time. The sense of rotation can be clockwise (right-handed) or counter-clockwise (left-handed) when looking at the light source (although conventions vary). *Circular birefringence* is a consequence of the difference in the refractive index for left and right-handed circularly polarized light. *Circular dichroism* is the difference in the absorption of left and right-handed circularly polarized light. Circular birefringence and circular dichroism are manifestations of *gyrotropy*. They can be expressed by analogy with linear birefringence and linear dichroism

$$\Delta n_{\text{circular}} = (n_{\text{R}} - n_{\text{L}}) + \text{i}(k_{\text{R}} - k_{\text{L}}). \tag{1.14}$$

Circular birefringence will cause a rotation of the plane of linearly polarized light, the vector sum of two counter-progagating circularly polarized rays of equal amplitude. Circular birefringence is synonymous with *optical rotation*, measured in degrees of azimuthal rotation per unit length. Similarly, any medium that will cause the differential absorption of circularly polarized light—circular dichroism—will render the linearly polarized input elliptically polarized, a state intermediate between ideal linear and circular polarizations.

Equation 1.1 assumes that **E** is everywhere constant in the crystal unit cell. Its variation underlies circular birefringence and circular dichroism and requires modification of the expression for the dielectric displacement. Details can be found in the text by Agranovich and Ginzburg (1984).

In keeping with the Neumann-Curie principle, chiroptical effects require certain dissymmetries. The necessary condition for circular birefringence and circular dichroism in crystals (O'Loane, 1980) is not so easily stated, requiring the absence of a center of symmetry, the absence of a symmetry axis of order ≥ 3 lying in a symmetry plane, or any other group (e.g. $\bar{4}3m$) in which each optical rotation tensor elements must be zero. The relationships between the symmetries of surfaces representing circular birefringence and circular dichroism and the morphological symmetries of crystals manifesting these surfaces can be found in Shubnikov (1960).

Gyrotropy is typically 10^3–10^4 times smaller than linear anisotropies and therefore very difficult to measure (Kaminsky, 2000). As such, many fewer examples exist of anomalous circular birefringence than anomalous linear birefringence, or anomalous circular dichroism than anomalous linear dichroism. Nevertheless, gyrotropy, an essential part of the science of crystal optics, can not be altogether ignored, coexisting as it does in many crystals that are classically optical anomalous.

1.1.5. Composition, Structure, and Optics

1.1.5.1. Lorentz-Lorenz formula

Under an applied external electric field, a dipole moment is induced in each of the crystal's constituent atoms. Assuming these dipole moments are of equal magnitude p, the total polarization or dipole moment per unit volume P is given as

$$P = N_V p = \frac{\rho N_A}{M} p, \tag{1.15}$$

where ρ is the density, M is the molecular mass, N_V is the number of molecules per unit volume and N_A is Avogadro's number. Each point (x, y, z) inside the crystal feels a *local* electric field E_l, a sum of the average macroscopic electric field inside the medium, E, and the electric field created by the induced dipoles in the immediate surroundings of the point at which E_l is evaluated. It can be shown that this field is $\sim \frac{4\pi}{3} P$. Thus,

$$E_l = E + \frac{4\pi}{3} P. \tag{1.16}$$

This local field induces a dipole moment at some point of:

$$p = \alpha E_l, \tag{1.17}$$

where α is average polarizability of the substance. Combining Equations (1.15)–(1.17) we obtain

$$P = \left(\frac{N_V \alpha}{1 - \frac{4\pi}{3} N_V \alpha} \right) E. \tag{1.18}$$

Substituting (1.18) into (1.4) yields the relationship between polarizability (α) and dielectric permittivity (κ). Then, substituting the square of the refractive index for the dielectric constant (1.6) gives the celebrated Lorentz-Lorenz formula that expresses refractivity in terms of electronic polarizability:

$$\alpha = \frac{3M}{4\pi\rho N_A} \frac{\kappa - 1}{\kappa + 2} = \frac{3M}{4\pi\rho N_A} \frac{n^2 - 1}{n^2 + 2}. \tag{1.19}$$

The average molecular refractivity $R_m = \frac{4\pi}{3} N_A \alpha \approx 2.5 \cdot 10^{24} \alpha$ can be used in place of polarizability in the Lorentz-Lorenz formula thereby simplifying (1.19):

$$R_m = \frac{M}{\rho} \frac{n^2 - 1}{n^2 + 2}. \quad (1.20)$$

Thus, we see the utility in relating the refractive index to the molar refractivity. Both R_m and α have dimensions of volume [m^3]. The inverse relationship follows:

$$n = \sqrt{\frac{M + 2R_m\rho}{M - R_m\rho}} = \sqrt{\frac{V_{\text{cell}} N_A + 2R_m z}{V_{\text{cell}} N_A - R_m z}} = \sqrt{\frac{3V_{\text{cell}} + 8\pi z\alpha}{3V_{\text{cell}} - 4\pi z\alpha}}, \quad (1.21)$$

where V_{cell} denotes the volume of unit cell containing z species.

1.1.5.2. Effect of composition

In optically anisotropic crystals, the average refractive index $\overline{n} = (n_\alpha n_\beta n_\gamma)^{1/3}$, where n_α, n_β and n_γ denote the principal refractive indices. The average refraction can be found from the refractivity of the constituent atoms.

The refractivity of gas and liquid mixtures obey additivity rules

$$\overline{R_m} = \sum_i \omega_i (R_m)_i, \quad (1.22)$$

or

$$\overline{R_m} = \sum_i N_i (R_m)_i, \quad (1.23)$$

where ω_i corresponds to the molar fraction of the ith component in a mixture and N_i is the number of type-i atoms, ions, or molecules. Knowledge of atomic refractivity of chemical elements and the additivity rules (Equations (1.22), (1.23)) can be used to estimate the refractivity of any compound and any mixture of compounds. However, for molecules and crystals deviations from atom additivity can be significant as a result of interatomic and intermolecular interactions (Jaffe, 1988; Winchell and Winchell, 1951; Tröger *et al.*, 1979). Batsanov (1966, 2000) has constructed various *refraction systems*—tabulations of refractivity increments for atoms, ions, and bonding electrons. Unfortunately, no workable system can presuppose all possible combinations of atoms and associated contributions; a universal refraction system cannot be constructed.

A hierarchy of chemical effects on refraction can summarized in several rules:

1. Polarizability and refractivity increase with the number of electrons from top to bottom in the periodic table of the elements for a series of atoms or ions in the same oxidation state. The variance within a row depends on the balance of the effective number of valence electrons with the nuclear charge.
2. Strong covalent bonding decreases polarizability and refractivity compared to comparable weakly bonded or non-bonded atoms.

3. In ionic compounds:
   a. Cations have a deficit of electrons, tightly bound, with smaller polarizabilities than corresponding neutral atoms.
   b. The opposite situation pertains to anions—they have a surfeit of highly polarizable electrons.
   c. Ionic bonding decreases refractivity of anions through the influence of cations. Conversely, ionic bonding increases refraction of cations. The first effect is usually stronger resulting in a decrease in overall refraction.
   d. Increasing coordination number typically decreases refractivity. High cation valence decreases the deformability of anions. The converse effect is small and can be neglected.
4. Hydrogen bonding increases refractivity. Interactions between protons and lone electron pair donors in effect contribute to populating anti-bonding orbitals which are then highly polarizable.

1.1.5.3. Spatial distribution of atoms in a crystal

In crystals and other organized media, polarizability is anisotropic and depends on the geometric arrangements of atoms. The shape of the optical indicatrix reflects the anisotropy of the polarizability. Consider a hypothetical crystal consisting of chains of atoms separated from one another by a distance larger than the distance between the atoms in the chain r. The electric vector $\mathbf{E}$ may have different orientations with respect to the chain direction. Polarization of atoms occurs along the electric vector and induced atomic dipoles (assume $\mathbf{E}$ parallel to $\mathbf{D}$). Let $r_{\mathbf{E}}$ be the projection of $\mathbf{r}$ on $\mathbf{E}$. If vector $\mathbf{E}$ is parallel to the chain ($r_{\mathbf{E}} = r$) the induced dipole moment increases due to the inductive effect of neighboring dipoles (Figure 1.3). Hence, polarizability of atoms in the chain, and consequently the refractive index, increases for this electric vector. If vector $\mathbf{E}$ is perpendicular to the chain ($r_{\mathbf{E}} = 0$) the induced dipole moment decreases due to neighboring charges of like sign (Figure 1.3). Therefore, the polarizability and refractive index perpendicular to a chain decreases.

The polarizability of atoms in a chain can be found from the following expression (Hartshorne and Stuart, 1970):

$$\alpha_c = \frac{\alpha}{1 - \alpha \dfrac{3r_{\mathrm{E}}^2 - r^2}{r^5}}. \tag{1.24}$$

If the difference between atoms in a chain exceeds $r > 5$Å, the denominator in Equation (1.24) tends to unity and interactions within a chain becomes negligible ($\alpha_c = \alpha$). From this observation follow several conclusions:

1. Polarizability and refractive index are larger for electric vibrations parallel to chains and smaller for vibrations perpendicular to chains. The optical sign of such a crystal should be positive.
2. In lamellar crystals such as graphite the opposite situation pertains; the refractive index in the direction normal to the layers will be smaller and the optical sign will be negative. A crystal such as gibbsite $Al(OH)_3$ with strong hydrogen bonded layers are optically positive exceptions.

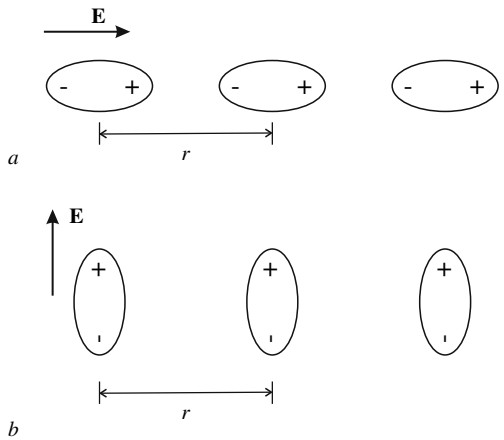

Figure 1.3. Chain of atoms (*a*) parallel and (*b*) perpendicular to the electric vector **E**. Induced atomic dipoles and the resultant polarization depends on the mutual dipole orientations

3. Crystals containing only monatomic ions or ions with cubic symmetry such as alkali sulfates are typically weakly birefringent irrespective of the crystal structure.

1.1.5.4. Modeling the indicatrix

In previous sections, we found quantitative relationships between the refractive index, density, and crystal composition in isotropic substances. On the other hand, we discussed only qualitatively features that affect the shape of the optical indicatrix in anisotropic crystals. Here, we consider the more rigorous point-dipole model that allows us to calculate the characteristics of the optical indicatrix based on the crystal structure and polarizabilities of structural units. This model will be used in section 3.4.3 for the analysis of optical anomalies related to growth ordering of atoms.

Bragg (1924) first attempted to calculate the principle refractive indices of crystals from the positions of atoms. He invoked point-dipole interactions to explain the double refraction of calcium carbonate polymorphs, calcite and aragonite. The model was not put into wide practice until the advent of digital computers (Zakharchenko, 1976; Pohl, 1978; Lager *et al*., 1987; Abbott, 1993; Glazer, 2002).

The point-dipole model considers each atom as an independent dipole that gives its own contribution to the local electric field at any point in a crystal. The local electric field at any site k in the crystal $\mathbf{E}_l(k)$ is defined as the sum of all dipoles located in a crystal lattice k' and a macroscopic field **E**:

$$\mathbf{E}_l(k) = \mathbf{E} + \sum_{k'} \widehat{\mathbf{L}}(k, k') \frac{\mathbf{p}(k')}{V_{\text{cell}}}. \tag{1.25}$$

Here, $\mathbf{L}(k, k')$ is the Lorentz tensor that depends on the geometry of the structure and $\mathbf{p}(k')$ is thedipole moment of an atom at site k'. The Lorentz tensor can be calculated in several ways (De Wette and Schacher, 1965; Dunmur, 1972; Cummins *et al*., 1976). Since the dipole moment of any atom is proportional to the local electric field acting at that point $\mathbf{p}(k') = \alpha(k')\mathbf{E}_l(k')$, Equation (1.25) can be transformed to

$$\mathbf{E}_l(k) = \mathbf{E} + \frac{1}{V_{\text{cell}}} \sum_{k'} \widehat{\mathbf{L}}(k, k')\, \alpha(k')\, \mathbf{E}_l(k') \,. \tag{1.26}$$

If the crystal structure and therefore the Lorentz tensor, as well as the polarizabilities of atoms are known, the resulting system of linear Equations can be solved for any given macroscopic field. The induced polarization, the electric dipole per unit volume, represents the sum of all dipoles and can be evaluated as

$$\mathbf{P} = \frac{1}{V_{\text{cell}}} \sum_{k'} \mathbf{p}(k') = \frac{1}{V_{\text{cell}}} \sum_{k'} \alpha(k') \mathbf{E}_l(k') \,, \tag{1.27}$$

and provides the connection between macroscopic and microscopic views. Polarization can be related to the dielectric susceptibility tensor, $\widehat{\psi}$, according to (1.1) written in a tensor form. The optical indicatrix, described by the dielectric permittivity tensor $\widehat{\kappa}$, can then be calculated with (1.26) and (1.27) as can the relationship between dielectric susceptibility and permittivity $\widehat{\kappa} = 4\pi\widehat{\psi} + \widehat{\mathbf{I}}$ ($\widehat{\mathbf{I}}$ is the unit second rank tensor). This method was first applied by Zakharchenko (1976).

The components of the dielectric pemittivity tensor are functions of polarizabilities. The polarizabilities can often be determined on the basis of crystal structure and measured optical properties so long as the number of the independent atomic polarizabilities does not exceed the number of independent components of the dielectric permittivity tensor (1 component for cubic crystals, 2 for hexagonal, trigonal, or tetragonal crystals, 3 for orthorhombic crystals, 4 for the monoclinic crystals, and 6 for triclinic).

Today, the birefringence of crystals can be approached quantum mechanically with density functional theory coupled to linear response theory (Katz and Rikukawa, 2005). However, such methods have as yet to be applied to optical anomalies. Methods suited to molecular crystals, combining the results of molecular orbital calculations for molecular polarizabilities with classical interactions between molecules summed over the lattice, are described in section 3.4.3.

1.2. CHARACTERIZING THE OPTICAL INDICATRIX

We expect that the typical reader of this book will have some experience with crystal optics and the polarizing microscope. We anticipate that this book will also be of value to crystallographers who usually pass over the optical properties of the objects of their study. We hope that scientists in other fields may also find something of value herein. With this diverse audience in mind, we offer a very

brief overview of crystal optics in order to define some jargon that will recur. In the absence of an introductory explanation the meaning of *axial angle, axial plane, isogyre*, and *melatope* may only be a distraction to some. On the other hand, it is of no use to rehash the information that can be found in the many excellent books on crystal optics such as those by Shubnikov (1960) and Hartshorne and Stuart (1970), among others.

Characterizing the optical indicatrix is tantamount to measuring the refractive index for different directions of incident light. Any two such measurements for light incident in a given direction but with orthogonal polarizations is a measurement of birefringence. For a given wavevector incident upon an optical indicatrix, the birefringence is the difference in the largest and smallest refractive indices for electrical vibrations in an elliptical cross section of the indicatrix perpendicular to the wavevector. The major and minor ellipse axes define the refractive indices.

As the principal optical anomaly described in this book is anomalous linear birefringence, some discussion of how birefringence is measured is appropriate. In actual fact, the quantity that is invariably determined in a birefringence measurement is the *retardance* or phase difference (δ) between the two orthogonal rays or eigenmodes propagating through the anisotropic medium where $\delta = (2\pi\Delta nL)/\lambda$. The birefringence ($\Delta n$) can be easily calculated from a knowledge of the wavelength (λ) of observation and the sample thickness (L).

When the two orthogonal modes passing through an anisotropic crystal at different rates are recombined in the analyzer of a polarized light microscope they will interfere with one another and give characteristic interference colors. The relationship between interference color and path difference was worked out by Isaac Newton (1952). The interrelationships among interference spectra, birefringence, phase difference, and sample thickness, have been codified in the Michel-Lévy chart, an essential aid to optical crystallographers.

Considerably more accurate methods for measuring phase differences rely on compensation. If we have a crystal of unknown birefringence upon which we superimpose a compensating crystal of known and variable birefringence so that the *fast axis* (the direction with the smaller refractive index) of the sample and compensator are orthogonal, then the compensator crystal can be adjusted so as to null the birefringence of the sample. At this point, no light will be transmitted between crossed polarizers. The simplest such device is a wedge of quartz cut at a shallow angle of about 0.5° along a direction parallel to the optic axis with gradually varying retardance. The position of the wedge inserted into the sample by the amount required to achieve compensation establishes the unknown phase difference. Ingenious and more accurate compensators were developed in the Nineteenth Century by Babinet, Berek, Ehringhaus, Senarmont and others whose names are remembered by their inventions. These eponymous compensators and their methods of operation have been described in great detail, particularly in older texts on mineralogy and petrology (Tatarsky, 1965; Johanssen, 1918).

The most accurate methods for measuring linear birefringence rely on careful electrophotometric intensity measurements. If a crystal is placed so that its

eigenmodes or vibration directions bisect the crossed polarizers of a microscope, the fraction of the intensity transmitted (I/I_0) is given by

$$\frac{I}{I_0} = \frac{1}{2}\sin^2\left(\delta/2\right) \tag{1.28}$$

which can be measured with a photomultiplier tube. If one then adds as variables the position of the polarizer relative to the analyzer (χ) as well as the position of the vibration directions of the sample (ϕ) it can be shown that the transmitted intensity is equal to

$$\frac{I}{I_0} = \frac{1}{2}\left[1 + \sin 2(\chi - \phi)\sin\delta\right]. \tag{1.29}$$

Glazer *et al*. (1996) fashioned a polarized light microscope with a rotating polarizer and a CCD camera in order to image birefringence in heterogeneous samples. Their device produces false color maps of δ and ϕ, usually convolved in a polarized light micrograph. The diamond images in Figure 1 were produced by the rotating polarizer technique.

Crystallography is the science of determining the properties of certain bodies in three dimensions. However, our primary evidence of optical anomalies comes from microscopy in orthoscopic or parallel ray illumination, which usually establishes a projection of a 3D object in 2D. On the other hand, conoscopy, the observation in convergent light, enables the investigator to extract 3D information of the optical properties of a crystal from a single orientation of the sample by passing a cone of light through the sample in the widest range of directions possible. A substage condenser and the insertion of a Bertrand lens are required to convert a microscope from the orthoscopic to the conoscopic configuration. Because the conoscopic image is made in the back focal plane of the objective, the additional lens is required to bring the image to the eyepiece.

Conoscopy is typically introduced through the analysis of a uniaxial interference figure made from a section cut normal to the optic axis of a trigonal, tetragonal, or hexagonal crystal. The rays, having travelled right through the sample, are collected in the center. Those having taken the most oblique paths are focused around the edge. Superimposed on the image is a dark cross corresponding to those electric vibrations that are parallel either to the polarizer or analyzer, and are thus extinguished. Such dark bands are more generally called *isogyres*. If the phase difference (δ) is very high, the isogyre centered on the optic axis will by ringed with concentric bands indicating the progress of interference colors through *orders* of 2π. Conoscopic interference figures offer a projection of the indicatrix onto a plane and can be instructive in the characterization of the indicatrix and of optical anomalies.

In a biaxial crystal viewed not along but between the optic axes, particularly for the view along the acute bisectrix, the pair of optic axes are seen as eyes or *melatopes* around the extreme of the image (Figure 1.2). The separation between the melatopes is an indication of the axial angle $(2V)$ one of the most important

parameters characterizing the indicatrix. Conoscopic interference figures can be made with the rotating polarizer method. Shown in Figure 1.4*b* is an acute bisectrix figure in which the false colors specify the direction of the vibration corresponding to the *slow direction* with the larger refractive index.

Approximate measurement of the axial angle follows Mallard's method (Bloss, 1961; Tatarsky, 1965) if melatopes appear within the field of view and with the Kamb or Michel-Lévy methods if both melatopes lie outside the field of view (Johannsen, 1918; Kamb, 1958; Stoiber and Morse, 1994).

Mallard, the pioneering researcher of optical anomalies described in the foreword, showed that half the separation (D) between melatopes in a biaxial interference figure of the kind shown in Figure 1.4*b*, is proportional to the sine of the apparent angle between the optic axis and the bisectrix (E), and a constant (K) that depends on the lens system and which can be defined for a particular configuration using a standard material. Mallard's formula is thus

$$D = K \sin E. \tag{1.30}$$

The actual axial angle ($2V$) can be found from the apparent angle ($2E$) by

$$\sin E = n_\beta \sin V. \tag{1.31}$$

For details of other methods of determining the axial angle, the reader is referred to the texts above.

Some difficulties arise with very small values of birefringence or with very acute axial angles. The small angles with $2V < 5°$ can be measured with specially designed optical systems, as in the study of anomalous biaxiality of potassium dihydrogen phosphate and beryl (Belyustin *et al*., 1970; Belyustin and Stepanova, 1981;

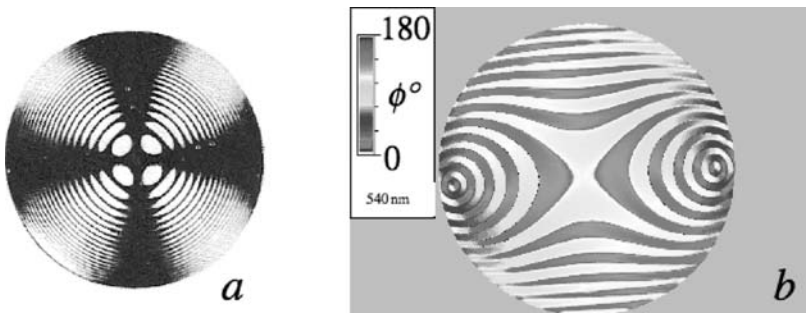

Figure 1.4. (*a*) Typical uniaxial interference figure in monochromatic light from Shubnikov (1960). (*b*) Conoscopic interference of a biaxial crystal along the acute bisectrix made with rotating polarizer method (Glazer *et al*., 1996). Image plotted as the direction of the most refractive vibration measured in degrees counterclockwise from the horizontal axis
Source (a): Taken from Shubnikov, A.V. *Principals of Optical Crystallography* 1960, reproduced with permission from 'Consultants Bureau, New York'
Source (b): Figure courtesy of Professor Werner Kaminsky, Department of Chemistry, University of Washington (see Color Section following page 254)

Shtukenberg *et al*., 1994b). Shubnikov's method (Melankholin and Grum-Grzhimailo, 1954) is also very useful whereby one or several glass hemispheres are placed onto the crystal section, which is located between the crossed polarizers. By moving the hemispheres along the crystal surface it is easy to gain some insight into the orientation of optic axial plane and values of axial angle.

1.3. DEFINITION OF OPTICAL ANOMALIES IN TERMS OF THE INDICATRIX

Let us ask again, what are optically anomalous crystals? Which optical manifestations are to be considered anomalous and which not so? What is the class of crystals that falls under the banner that is the title of this monograph? As discussed in the Foreword, these questions are not so easy to answer. While the class of optically anomalous crystalline objects is necessarily fuzzy both historically and operationally most crystals that have been and should be considered as optically anomalous display linear birefringence under circumstances where we might not otherwise expect it

According to the US Bureau of Mines (US Bureau of Mines, 1997), which dares to give a straight-up definition, *optical anomalies* are: "Optical properties apparently at variance with optical rules, such as: anisotropy in isotropic minerals, such as birefringent diamond; biaxiality in uniaxial minerals, such as quartz. . ."

This definition is poor. It is conditioned on our understanding of *optical rules*. Moreover, it is here terminated by the ellipses because it loses whatever coherence it does have. This definition, however arbitrary and incomplete, does emphasize that most but not all of the objects that we consider herein are those in which optical symmetry is inconsistent with symmetry presumed or determined by other methods of analysis. As such, we can characterize and classify most optically anomalous crystals in terms of the peculiarities of their optical indicatrices or lack thereof.

1. Optical properties are not consistent with a single optical indicatrix. In such cases, crystals cannot be extinguished in orthoscopic illumination. In conoscopic examination, interference figures are distorted.
2. The optical indicatrix describes optical properties locally, but the crystal does not everywhere possess a common optical indicatrix.
3. Eigenvectors (directions of the principal refractive indices) are common throughout a crystal but the eigenvalues (magnitudes of the principal refractive indices) are variable.
4. The shape and/or orientation of the optical indicatrix is not consistent with the idealized crystal structure.

1.4. ANOMALIES OF OBVIOUS ETIOLOGY

Before beginning our analysis of optically anomalous crystals, we can focus our inquiry by identifying imperfect crystals not considered anomalous. This will condition the reader both to what we will be discussing herein and what we will

not be discussing. Below are some examples of crystals in which optical contrast is a consequence of either gross compositional variation (section 1.4.1) or mechanical deformation (section 1.4.2).

1.4.1. Gross Compositional Inhomogeneity

Refractivity depends on composition. Naturally, gross compositional inhomogeneities cause variations in the optical properties evidenced by refractive index (Becke) constrast, differences in birefringence, or differences in color. The most frequent inhomogeneities manifest themselves as concentric zones or growth sectors containing different amounts of trace impurities. The plagioclase $(Na, Ca)(Si, Al)_4O_8$ in (Figure 1.5) well illustrates concentric zoning of albite ($NaAlSi_3O_8$) and anorthite ($CaAl_2Si_2O_8$). Growth zoning and sector zoning is evident in the birefringence differences in epidote, $Ca_2(Al, Fe)_3O(SiO_4)(Si_2O_7)OH$ (Figure 1.6). Eudialyte $Na_4(Ca, Ce, Fe, Mn)_2ZrSi_6O_{17}(OH, Cl)_2$ shows a complex optical pattern some of which is a consequence of growth sectors zoning, some of which is a consequence of concentric zoning, and some of which is a consequence of other etiologies still (Figure 1.7)

Becke contrast is well illustrated in garnets of the grossular-andradite series (Figure 2.28) (Shtukenberg *et al*., 2001a) - see Appendix 1 for garnet nomenclature.

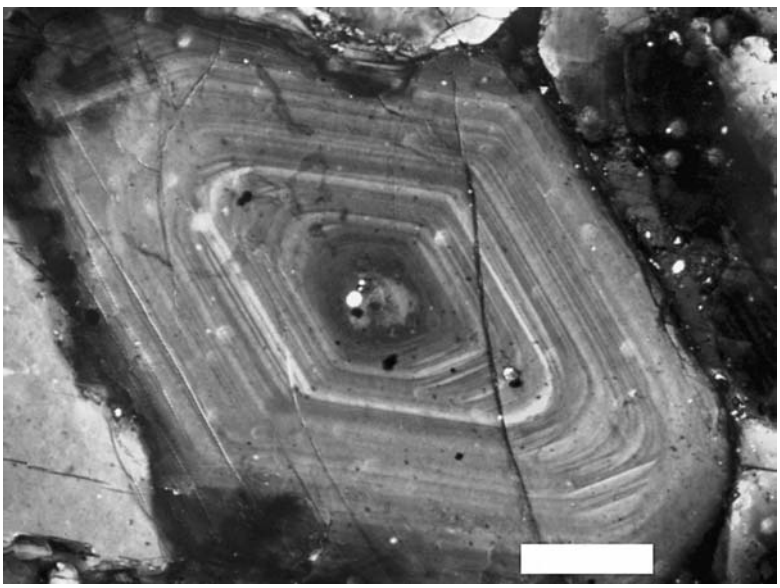

Figure 1.5. Concentric, compositional zoning of plagioclase ($(Na, Ca)(Al, Si)_4O_8$) from crystal-lapilli (volcano B. Tolbacheck, Kamchatka, Russia). Variation in albite ($NaAlSi_3O_8$) to anorthite ($CaAl_2Si_2O_8$) ratio manifests itself in variations of birefringence and extinction position. Scale bar = 0.22 mm (see Color Section following page 254)

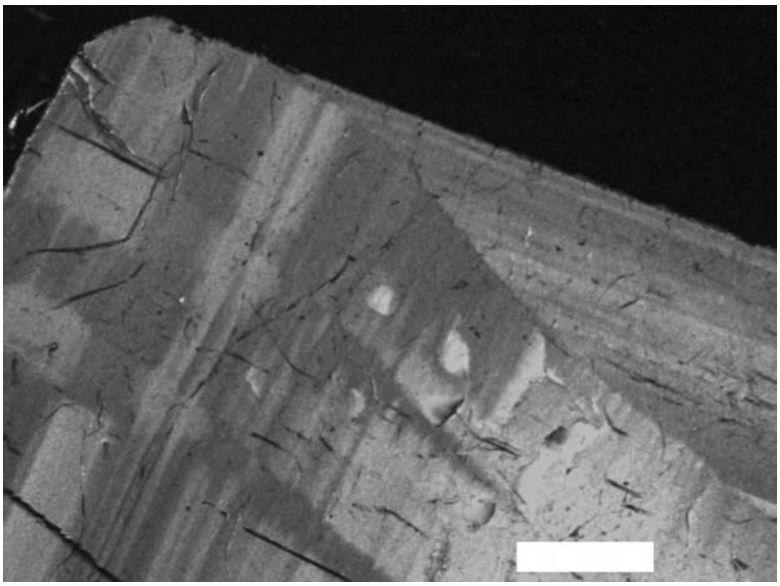

Figure 1.6. Concentric zoning and growth sector zoning of birefringence in epidote [$Ca_2(Al, Fe)_3O(SiO_4)(Si_2O_7)OH$] related to variations of chemical composition. The sample was kindly provided by P.B. Sokolov. Scale bar = 0.88 mm (see Color Section following page 254)

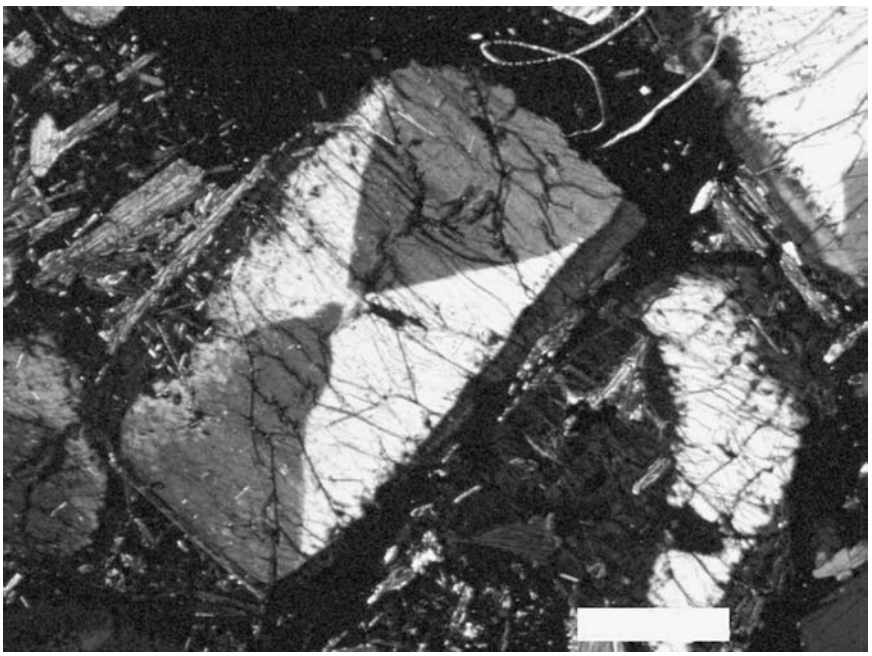

Figure 1.7. Growth sector zoning in birefringence in eudialyte ($Na_4(Ca, Ce, Fe, Mn)_2ZrSi_6O_{17}(OH, Cl)_2$) related to variations of chemical composition. Scale bar = 0.88 mm (see Color Section following page 254)

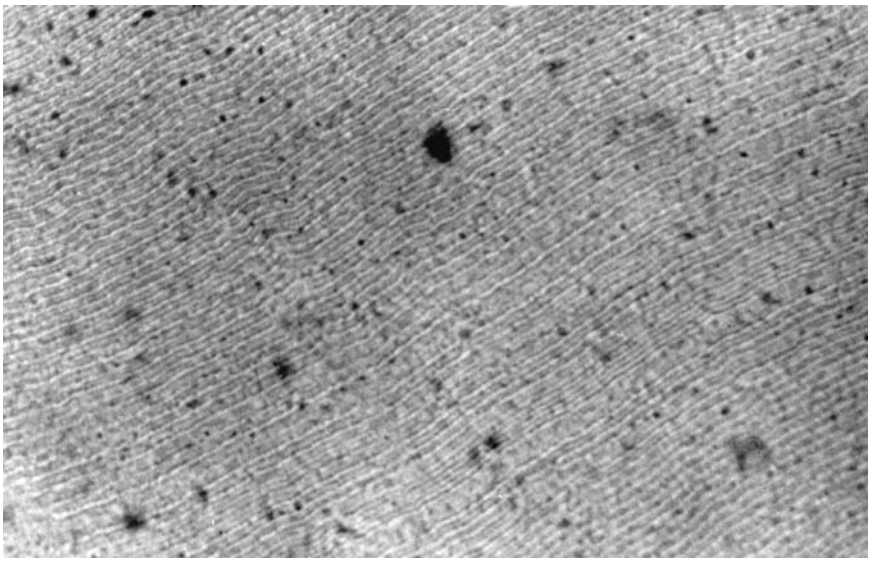

Figure 1.8. Rhythmic zoning in chalcedony (SiO_2) spherulite in linearly polarized light

Figure 1.8 shows the rhythmic zoning observed in quartz related to periodic changes in content of Al and OH (Frondel, 1985). This is the result of the cyclic interplay between diffusion and growth rate.

1.4.2. Macroscopic Deformations of Crystals

Distortions of the indicatrix due to macroscopic deformations are not considered genuine optical anomalies. If we put a crystal in a thumb screw, it is obvious that distortions in the optical indicatrix are a consequence of the stresses imposed upon it *externally*. On the other hand, *internal* stress resulting in strain from isomorphous impurities or dislocations, may have non-obvious etiologies and associated anomalies do indeed fall within the bounds of our discussion.

External deformations can originate from tectonic forces or crystallization pressure. They can be continuous or discontinuous. Continuous deformation manifests itself in wavy extinction as in quartz from metamorphic rocks (Korago and Kozlov, 1988). Discontinuous deformations can be seen in block structures and recrystallization substructures. As distinct from wavy extinction, blocks are marked by sudden changes of optical indicatrix orientation. Mechanical twinning is a special consequence of twinned lamellae with constant misorientation angles produced by stress as occurs in calcite, feldspar, pyroxene, and many other minerals. Similar optical structures can be induced by thermoelastic and ferroelastic transformations (Boiko *et al*., 1991; Salje, 1991). Optical anomalies due to internal strain will be treated fully in Chapter 2. If this internal strain and stress produce

macroscopic deformations of the crystal, distorted optical patterns can be observed due to misorientations of the crystal parts. For example, the mica crystal (ferrous muscovite $(K(Al, Fe, Mg)_2(AlSi_3O_{10})(F, OH)_2)$ shown in Figure 1.9 reveals the growth bending from internal stress relaxation. The curved crystal exhibits wavy extinction, so that only a narrow extinction stripe is observed for any stage orientation.

Weird optical micrographs of so-called *banded spherulites*, a variety of polycrystalline substances that grow radially with concentric extinction bands, are shown in Figures 1.10 and 1.11 for hippuric acid ($C_6H_5CONHCH_2COOH$) and chalcedony (Frondel, 1978), respectively. Substances of this kind were first observed by the irrepressible Brewster (1849–1853). Many such substances like this were described by Bernauer (1929). It is now generally believed that the optical banding is a consequence of the fact that crystallites, as they grow radially, twist helically, thereby turning the optical indicatrix successively in and out of the extinction position. The origin of twisting is not well understood. But, so long as we associate the optical properties with some well-defined process they are no longer anomalous. The banded spherulites in Figure 1.10 and chalcedony Figure 1.11 are certainly growth anomalies but we would not necessarily describe them as optical anomalies.

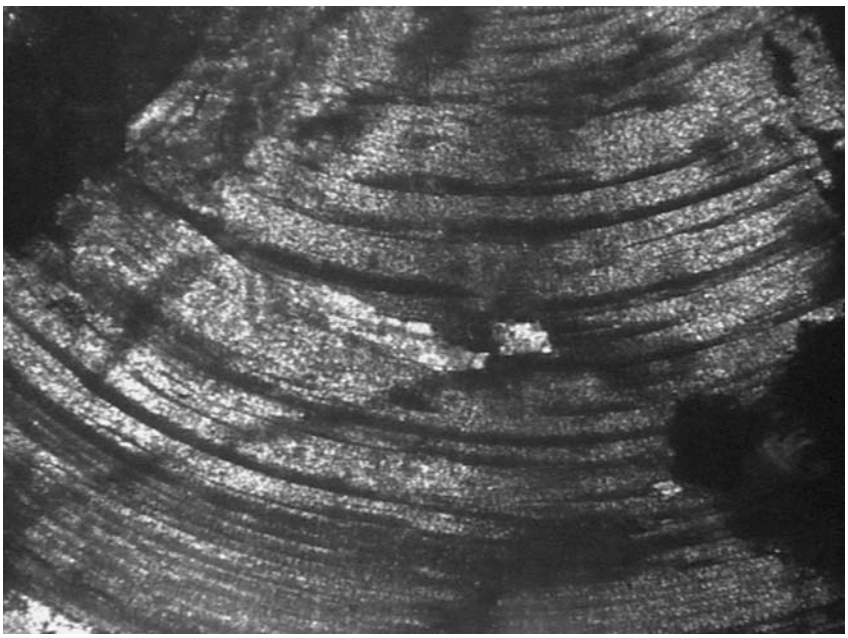

Figure 1.9. Wavy extinction in mica crystal curved due to relaxation of internal stress. Extinction is observed only in stripes, in which vibration directions in the crystal are parallel to vibration directions in the crossed polarizers oriented vertically and horizontally (see Color Section following page 254)

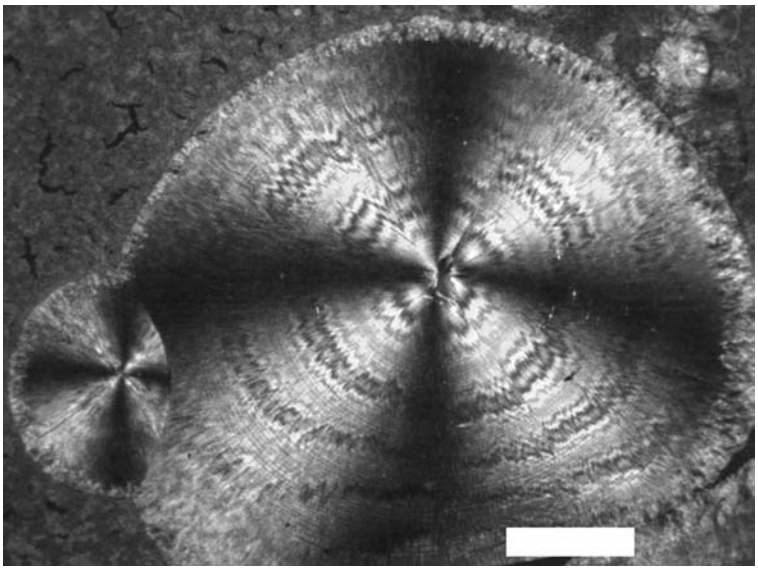

Figure 1.10. Hippuric acid ($C_6H_5CONHCH_2COOH$) spherulites between crossed polarizers. An extinction cross, typical for spherulites, arises when the refracting components are parallel with either the crossed polarizer or analyzer. The concentric banding is best accounted for by assuming fibrous crystallites twisting about the radius. Scale bar = 0.44 mm (see Color Section following page 254)

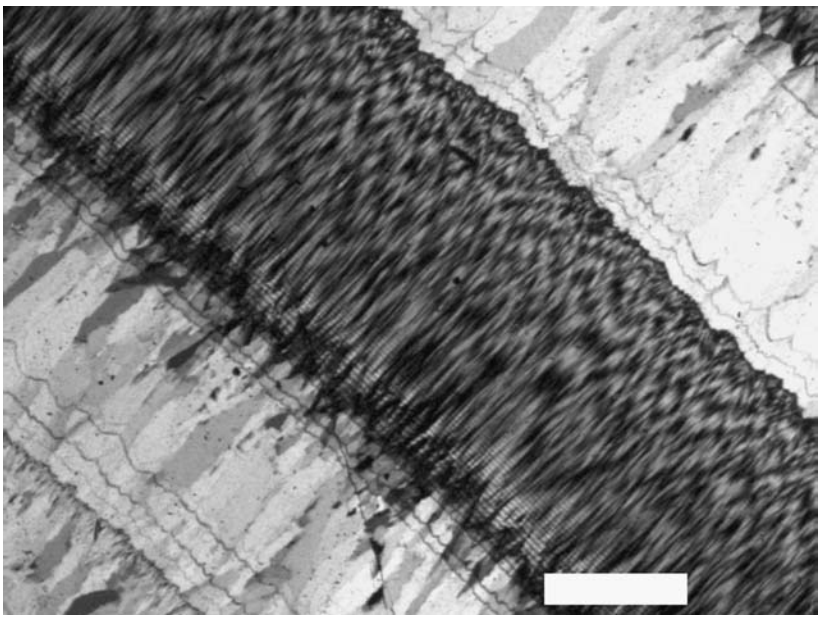

Figure 1.11. Chalcedony (fibrous SiO_2) spherulites between crossed polars. Twisting of crystalline fibers gives rise to rhythmic bands of extinction. Since the distance between bands is variable the twisting period is not constant. Scale bar = 0.88 mm (see Color Section following page 254)

1.5. ABUNDANCE OF OPTICAL ANOMALIES

How common are genuine optical anomalies in crystals? We have assembled in Appendix 2 more than 100 such compounds described in the scientific literature. Optical anomalies are found in natural and synthetic crystals grown over the greatest range of conditions imaginable. Nevertheless, some substances are more susceptible to the display of anomalous optical properties. If a compound has a high capacity to incorporate isomorphous structural units and form solid solutions, it is likely a good candidate for the study of optical anomalies. This results from the fact that most optical anomalies are controlled by chemical inhomogeneities of one kind or another. The possibility of finding optical anomalies strongly depends on the crystal size as well as on the ideal optical symmetry. Optical anomalies in big well-shaped crystals are much easier to detect than in small shapeless aggregates. Investigators usually do not search for optical anomalies they rather find them accidentally while studying something else. Certainly, if a compound stimulates a strong interest and is studied in much detail optical anomalies will be found, even in small crystals. For example, there is a great number publications devoted to anomalous birefringence in diamonds (see e.g. Orlov and Tatjanina, 1973; Frank *et al*., 1990, and references therein). Anomalous birefringence in cubic crystals or along the optic axis of a uniaxial crystal is visible even when evidenced by very small phase shifts. On the other hand, detection of optical anomalies in biaxial crystals of solid solutions is much more problematic. Of the optically anomalous compounds listed in Appendix 2 24% are cubic, 51% are hexagonal, trigonal, or tetragonal, and 25% are orthorhombic, monoclinic or triclinic. On the other hand, only 12% of minerals are cubic, 26% are hexagonal, trigonal, or tetragonal and 62% are orthorhombic, monoclinic or triclinic (Yushkin *et al*., 1987). Larsen and Berman (1934) give comparable figures for non-opaque minerals, 15%, 22% and 63% respectively. For non-opaque synthetic inorganic compounds, Winchell and Winchell (1964) report values of 29%, 25% and 46% respectively. These statistics show unambiguously that the optical anomalies are more likely detected in crystals possessing a high symmetry.

CHAPTER 2

STRESS INDUCED OPTICAL ANOMALIES

2.1. INTRODUCTION

The evaluation of stress, force per unit area, has long been a theme in optically anomalous crystal research. Brewster (1815) discovered in jellies the photoelastic effect, the change in refractive indices of a material under stress. The next year, he showed that mechanical compression or dilatation of fluorite (CaF_2) among other isotropic substances, induced birefringence in those bodies (Brewster, 1816) Brewster then showed that some cubes of fluorite not under compression or dilatation already possessed double refraction (Brewster, 1818b). It was thus presumed that these optically anomalous crystals had been stressed sometime during their history. Later researchers including Klein and Brauns (Brauns, 1891) argued the relative merits of external stress and internal stress, respectively, in producing anomalous birefringence. Stress remains a major source of optical anomalies in crystals because the influence of stress can be hidden in plastic deformations and dislocations. In the words of Nye (1949a) «stress remains locked up in the interior.»

Neumann (1841) made the first quantititive investigation of photoelasticity, work that underlies his contributions to the Neumann-Curie principle. Today, the study of the quantitative relationship between changes in birefringence and applied stress in crystals is a major subject in its own right (Sirotin and Shaskolskaya, 1982; Narasimhamurty, 1981).

2.2. PHENOMENOLOGICAL DESCRIPTION OF PIEZOOPTIC EFFECTS

A material body and its associated optical indicatrix will deform under the application of stress (Nye, 1985; Shuvalov, 2005). Elastic stress will reversibly distort the optical indicatrix. The temporary, stress-induced change of the optical indicatrix is called the piezooptic or photoelastic efffect. Strictly speaking, distortions of the optical indicatrix are the result of strain induced (elasto-optic) rather than stress-induced (piezo-optic) phenomena. Strain is the fractional change in the length of a body under stress. Optical indicatrix distortions are the consequence of the displacement of atoms, the deformation of the crystal structure resulting from

strain. However, it is more convenient to calculate stress than strain. The rigorous connection between stress and strain through Hooke's law permits us to frame indicatrix distortions as piezo-optic in nature.

2.2.1. Piezooptic and Elastooptic Coefficients

Refractive indices are directly related to the dielectric impermittivity ($\eta = n^{-2}$). The characteristic surface of the dielectric impermittivity tensor η_{ij} is the optical indicatrix $\eta_{ij}x_ix_j = 1$ (see section 1.1.2). Under elastic stress, the mutual displacement of atoms leads to distortions of bond lengths, valence angles, and attendant electronic structure. Lattice constants change, too. As a result, the absolute values of anisotropic polarizabilities change, affecting the impermittivity tensor and the optical indicatrix.

Elastic stress, described by a symmetric second-rank tensor σ_{ij}, adds a small symmetric tensor ζ_{ij} to the dielectric impermittivity:

$$\zeta_{ij} = \pi_{ijkl}\sigma_{kl} \qquad i, j, k, l = 1, 2, 3, \tag{2.1}$$

where π_{ijkl} is the fourth rank piezooptic tensor. In abbreviated notation, Equation (2.1) has the form

$$\begin{aligned} &\zeta_\lambda = \pi_{\lambda\mu}\sigma_\mu, \text{ where} \\ &\zeta_\lambda = \zeta_{ij} \quad ij \leftrightarrow \lambda = 1, 2, ..6 \\ &\sigma_\mu = \sigma_{kl} \quad kl \leftrightarrow \mu = 1, 2, ..6 \\ &\pi_{\lambda\mu} = \begin{cases} \pi_{ijkl} & ij \leftrightarrow \lambda = 1, 2, ..6\ kl \leftrightarrow \mu = 1, 2, 3 \\ 2\pi_{ijkl} & ij \leftrightarrow \lambda = 1, 2, ..6\ kl \leftrightarrow \mu = 4, 5, 6 \end{cases}. \end{aligned} \tag{2.2}$$

The relationship between indices is written using the following convention:

11	22	33	23, 32	13, 31	12, 21
1	2	3	4	5	6

.

Piezooptic coefficients have the units of area/force (m^2N^{-1}) with typical values of $10^{-12}m^2N^{-1}$ (10^{-11} cm^2dyn^{-1}). The number of independent components depends on the intrinsic symmetries of the σ_{ij} and ζ_{ij} tensors and reaches 36 for triclinic crystals. Most generally, fourth-rank tensors should have $3^4 = 81$ independent coefficients. However, symmetry reduces this number. π_{ijkl} is always symmetrical with respect to (ij) and (kl) permutations. For more symmetric crystals, the numbers of independent components are fewer: 20 for monoclinic crystals, 12 for orthorhombic crystals, and just 3 in the cubic crystal classes with four-fold axes, 432, $\bar{4}3m$ and $m\bar{3}m$ (Appendix 3).

The elastooptic effect is characterized by the small addition to the impermittivity tensor, ζ_{ij}, that is a consequence of elastic strain ε_{ij},

$$\zeta_{ij} = p_{ijkl}\varepsilon_{kl} \qquad i, j, k, l = 1, 2, 3 \tag{2.3}$$

where p_{ijkl} is the elastooptic tensor. Elastooptic coefficients are dimensionless and take values of about 0.1. The tensor p_{ijkl} has the same symmetry as the piezooptic tensor (Appendix 3). For simplicity and consistency only the piezooptic coefficients are used below.

The generalized Hooke's law gives the proportionality between the stress and the strain tensors (Nye, 1985; Shuvalov, 2005):

$$\sigma_{kl} = c_{klij}\varepsilon_{ij} \qquad i, j, k, l = 1, 2, 3 \tag{2.4}$$

or

$$\varepsilon_{ij} = s_{ijkl}\sigma_{kl} \qquad i, j, k, l = 1, 2, 3 \tag{2.5}$$

where c_{ijkl} and s_{ijkl} are the elastic stiffness and the elastic compliance tensors, respectively.

Using expressions (2.1), (2.3), (2.4), and (2.5), we obtain the relation between elastooptic and piezooptic coefficients

$$\pi_{ijkl} = p_{ijmn}s_{mnkl} \qquad i, j, k, l, m, n = 1, 2, 3 \tag{2.6}$$

$$p_{ijkl} = \pi_{ijmn}c_{mnkl} \qquad i, j, k, l, m, n = 1, 2, 3. \tag{2.7}$$

2.2.2. Piezooptic Phenomena in Amorphous Solids

The optical indicatrix of an amorphous substance is a sphere, characterized by the refractive index n_0. The piezooptic tensor in this case has only two independent components π_{11} and π_{12}.

$$\pi_{\lambda\mu} = \begin{bmatrix} \pi_{11} & \pi_{12} & \pi_{12} & 0 & 0 & 0 \\ \pi_{12} & \pi_{11} & \pi_{12} & 0 & 0 & 0 \\ \pi_{12} & \pi_{12} & \pi_{11} & 0 & 0 & 0 \\ 0 & 0 & 0 & \pi_{11} - \pi_{12} & 0 & 0 \\ 0 & 0 & 0 & 0 & \pi_{11} - \pi_{12} & 0 \\ 0 & 0 & 0 & 0 & 0 & \pi_{11} - \pi_{12} \end{bmatrix}. \tag{2.8}$$

The simplest stresses, hydrostatic and uniaxial, will be treated in turn.

1. *Hydrostatic stress* (compression, P). The stress tensor in this case is

$$\sigma_{ij} = \begin{bmatrix} -P & 0 & 0 \\ 0 & -P & 0 \\ 0 & 0 & -P \end{bmatrix} \text{ or } \sigma_{\lambda} = \begin{bmatrix} -P \\ -P \\ -P \\ 0 \\ 0 \\ 0 \end{bmatrix}. \tag{2.9}$$

Then, using Equation (2.2), one can write the small ζ_λ added to the impermittivity:

$$\zeta_\lambda = \begin{bmatrix} \pi_{11} & \pi_{12} & \pi_{12} & 0 & 0 & 0 \\ \pi_{12} & \pi_{11} & \pi_{12} & 0 & 0 & 0 \\ \pi_{12} & \pi_{12} & \pi_{11} & 0 & 0 & 0 \\ 0 & 0 & 0 & \pi_{11}-\pi_{12} & 0 & 0 \\ 0 & 0 & 0 & 0 & \pi_{11}-\pi_{12} & 0 \\ 0 & 0 & 0 & 0 & 0 & \pi_{11}-\pi_{12} \end{bmatrix} \begin{bmatrix} -P \\ -P \\ -P \\ 0 \\ 0 \\ 0 \end{bmatrix} = \begin{bmatrix} -P(\pi_{11}+2\pi_{12}) \\ -P(\pi_{11}+2\pi_{12}) \\ -P(\pi_{11}+2\pi_{12}) \\ 0 \\ 0 \\ 0 \end{bmatrix}. \tag{2.10}$$

Since for $\lambda = 1, 2, 3$

$$\zeta_\lambda = \eta_\lambda - \eta_0 = n_\lambda^{-2} - n_0^{-2} \approx \frac{2}{n_0^3}(n_0 - n_\lambda) \tag{2.11}$$

therefore,

$$n_\lambda - n_0 = -\frac{n_0^3}{2}\zeta_\lambda = \frac{n_0^3}{2}P(\pi_{11}+2\pi_{12}). \tag{2.12}$$

Hydrostatic compression of amorphous solids changes the refractive index uniformly; birefringence does not arise. An increasing refractive index under compressive stress is consistent with the Lorentz-Lorenz formula (1.19); stress increases density. It is also possible to show that the hydrostatic stress does not distort the shape of the optical indicatrix for anisotropic crystals.

2. *Uniaxial stress*, compression σ along the axis x_1, is described by the stress tensor:

$$\sigma_\lambda = \begin{bmatrix} -\sigma \\ 0 \\ 0 \\ 0 \\ 0 \\ 0 \end{bmatrix}. \tag{2.13}$$

Correspondingly, the tensor ζ_λ is written as follows:

$$\zeta_\lambda = \begin{bmatrix} \pi_{11} & \pi_{12} & \pi_{12} & 0 & 0 & 0 \\ \pi_{12} & \pi_{11} & \pi_{12} & 0 & 0 & 0 \\ \pi_{12} & \pi_{12} & \pi_{11} & 0 & 0 & 0 \\ 0 & 0 & 0 & \pi_{11}-\pi_{12} & 0 & 0 \\ 0 & 0 & 0 & 0 & \pi_{11}-\pi_{12} & 0 \\ 0 & 0 & 0 & 0 & 0 & \pi_{11}-\pi_{12} \end{bmatrix} \begin{bmatrix} -\sigma \\ 0 \\ 0 \\ 0 \\ 0 \\ 0 \end{bmatrix} = \begin{bmatrix} -\pi_{11}\sigma \\ -\pi_{12}\sigma \\ -\pi_{12}\sigma \\ 0 \\ 0 \\ 0 \end{bmatrix}. \tag{2.14}$$

The expression obtained shows that the impermittivity depends on the orientation; optical anisotropy arises. Since two of three principal values of the impermittivity tensor are equivalent the optical indicatrix becomes an ellipsoid

of revolution with the optic axis directed along the applied stress x_1. According to the Equation (2.11) the stress-induced birefringence is equal to

$$\Delta n = n_1 - n_2 = \left(n_0 - \frac{n_0^3}{2}\zeta_1\right) - \left(n_0 - \frac{n_0^3}{2}\zeta_2\right) = \frac{n_0^3}{2}(\zeta_2 - \zeta_1) = \frac{n_0^3}{2}\sigma(\pi_{11} - \pi_{12}). \quad (2.15)$$

Thus, the birefringence is directly proportional to the stress. The coefficient of proportionality, called Brewster's constant, contains the piezooptic constants and the average refractive index n_0. As seen from expression (2.15), under compressive stress the sign of Δn coincides with the sign of $\pi_{11} - \pi_{12}$. As a rule $(\pi_{11} - \pi_{12}) < 0$, therefore, the optic sign is usually negative and the refractive index along the loading axis is less than the refractive index in any perpendicular direction. The optic sign follows the sign of the applied stress.

3. *Triaxial stress* is defined by three unique non-zero principal values of the stress tensor. As required by symmetry, the optical indicatrices of orthorhombic, monoclinic, or triclinic crystals are triaxial ellipsoids with principal axes directed parallel to the principal axes of the stress tensor. In amorphous solids under load, the principal axes of the indicatrix are parallel to the principal stress directions. The birefringence is proportional to the difference in the so-called quasi-principal stress values, the eigenvalues of the two dimensional stress tensor acting in the section plane which gives the maximal shear stress acting in the plane of the wave front.

2.2.3. Piezooptic Phenomenon in Cubic Crystals

Although in the absence of stress cubic crystals are also isotropic, their organized structures result in more complicated behaviors under elastic stress; the loading direction plays a role. Here again, we consider the archetypal situations.

1. *Hydrostatic stress* does not induce optical anisotropy as for amorphous substances.
2. *Uniaxial stress* (compression σ along the axis x_1) has the form of (2.13).
   For most symmetric cubic crystal classes (432, $\bar{4}3m$ and $m\bar{3}m$, see Appendix 3) x_1 corresponds to the proper or improper four-fold axis. The piezooptic tensor has three independent components.

$$\zeta_\lambda = \begin{bmatrix} \pi_{11} & \pi_{12} & \pi_{12} & 0 & 0 & 0 \\ \pi_{12} & \pi_{11} & \pi_{12} & 0 & 0 & 0 \\ \pi_{12} & \pi_{12} & \pi_{11} & 0 & 0 & 0 \\ 0 & 0 & 0 & \pi_{44} & 0 & 0 \\ 0 & 0 & 0 & 0 & \pi_{44} & 0 \\ 0 & 0 & 0 & 0 & 0 & \pi_{44} \end{bmatrix} \begin{bmatrix} -\sigma \\ 0 \\ 0 \\ 0 \\ 0 \\ 0 \end{bmatrix} = \begin{bmatrix} -\pi_{11}\sigma \\ -\pi_{12}\sigma \\ -\pi_{12}\sigma \\ 0 \\ 0 \\ 0 \end{bmatrix} \quad (2.16)$$

The result is the same for amorphous solids with similar expectations of optic sign. As a rule $(\pi_{11} - \pi_{12}) < 0$ whereby compression along the four-fold axis results in a negative optic sign; tension produces a positive optic sign. Such

behavior is observed in halite, fluorite, and diamond. The opposite situation $(\pi_{11} - \pi_{12}) > 0$ holds for sylvite (KCl). The birefringence should be calculated in accordance with Equation (2.15).

Loading along the three-fold axis leads to a different result:

$$\zeta_\lambda = \begin{bmatrix} \pi_{11} & \pi_{12} & \pi_{12} & 0 & 0 & 0 \\ \pi_{12} & \pi_{11} & \pi_{12} & 0 & 0 & 0 \\ \pi_{12} & \pi_{12} & \pi_{11} & 0 & 0 & 0 \\ 0 & 0 & 0 & \pi_{44} & 0 & 0 \\ 0 & 0 & 0 & 0 & \pi_{44} & 0 \\ 0 & 0 & 0 & 0 & 0 & \pi_{44} \end{bmatrix} \begin{bmatrix} 0 \\ 0 \\ 0 \\ -\sigma \\ 0 \\ 0 \end{bmatrix} = \begin{bmatrix} 0 \\ 0 \\ 0 \\ -\pi_{44}\sigma \\ 0 \\ 0 \end{bmatrix} \tag{2.17}$$

As for loading along the four-fold axis, the optical indicatrix becomes uniaxial. The birefringence is:

$$\Delta n = n_\parallel - n_\perp = \left(n_0 - \frac{n_0^3}{2}\zeta_\parallel\right) - \left(n_0 - \frac{n_0^3}{2}\zeta_\perp\right) = \frac{n_0^3}{2}\pi_{44}\sigma \tag{2.18}$$

where $n_{||}$ and $n_\perp$ are the refractive indices for the electric vibrations parallel and perpendicular to the loading direction [111], respectively. The coefficient π_{44} is more often negative, but it can be positive as in fluorite. Expression (2.18) transforms to (2.15) if $\pi_{44} = \pi_{11} - \pi_{12}$. Uniaxial loading of cubic crystals in any other direction results in optical biaxiality.

A more complicated situation pertains to the lower symmetry cubic crystal classes (23 and $m\bar{3}$, see Appendix 3) that are characterized by four independent components of the piezooptic tensor. Uniaxial loading along x_1, parallel to the two-fold axis, provides the following expression for ζ_λ:

$$\zeta_\lambda = \begin{bmatrix} \pi_{11} & \pi_{12} & \pi_{21} & 0 & 0 & 0 \\ \pi_{21} & \pi_{11} & \pi_{12} & 0 & 0 & 0 \\ \pi_{12} & \pi_{21} & \pi_{11} & 0 & 0 & 0 \\ 0 & 0 & 0 & \pi_{44} & 0 & 0 \\ 0 & 0 & 0 & 0 & \pi_{44} & 0 \\ 0 & 0 & 0 & 0 & 0 & \pi_{44} \end{bmatrix} \begin{bmatrix} -\sigma \\ 0 \\ 0 \\ 0 \\ 0 \\ 0 \end{bmatrix} = \begin{bmatrix} -\pi_{11}\sigma \\ -\pi_{21}\sigma \\ -\pi_{12}\sigma \\ 0 \\ 0 \\ 0 \end{bmatrix} \tag{2.19}$$

Such loading leads to biaxiality. The birefringence depends not only on the stress direction, but also on the direction of observation in the plane x_2x_3.

3. *Triaxial stress* results in optical biaxiality and complicates relations between the resulting biaxial optical indicatrix and the stress tensor.

The deformation of the optical indicatrix under various loadings follows the Neumann-Curie principle (Nye, 1985) which states that a crystal under an external influence will exhibit only those symmetry elements that are common to the unperturbed crystal and the perturbation (see Foreword). For example,

uniaxial stress can be described by the point group ∞/mmm with an infinite order axis. A crystal will be optically uniaxial if the stress is directed along either the three-fold or four-fold axis, otherwise it will be optically biaxial.

In cubic crystals, the axial angle $2V$ has a complicated stress dependence. For example, the uniaxial compression of a cubic crystal (class 23) along [100] provides the following value of the axial angle:

$$\tan V = \sqrt{\frac{\zeta_{11} - \zeta_{22}}{\zeta_{22} - \zeta_{33}}} = \sqrt{\frac{\pi_{12}\sigma - \pi_{21}\sigma}{\pi_{21}\sigma - \pi_{11}\sigma}} = \sqrt{\frac{\pi_{12} - \pi_{21}}{\pi_{21} - \pi_{11}}}. \tag{2.20}$$

This expression shows that the biaxial angle, which can reach tens of degrees, is independent of the applied stress σ. Rather than modulating the axial angle, stress spreads the isochromes away from the center of the increasingly black field of view. Thus, the axial angle is not an aid in the study of elastic stress in cubic crystals. Much more information can be obtained from the anomalous birefringence of a crystal.

2.2.4. Piezooptic Phenomenon in Uniaxial Crystals

The phenomenological description of the piezooptic effect becomes more complicated for uniaxial crystals (trigonal, tetragonal, and hexagonal) whose piezooptic tensor is characterized by 7–13 independent components. The main features of the phenomenon can be summarized as follows.

1. *Hydrostatic stress* does not change the shape of the indicatrix.
2. *Uniaxial stress* preserves uniaxial symmetry and changes the birefringence $n_\omega - n_\varepsilon = \Delta n$ (n_ω and n_ε denote refractive indices of the ordinary and of the extreme value of the extraordinary rays, respectively; $n_\omega = n_\gamma$ in optically negative crystals and $n_\varepsilon = n_\gamma$ in optically positive ones).
3. *Any other loading* transforms the uniaxial indicatrix to a biaxial indicatrix. In uniaxial crystals it is convenient to characterize the stress using the axial angle $2V$ ($2V_\gamma$ in optically positive and $2V_\alpha$ in optically negative crystals), evaluated as follows:

$$\tan V = \sqrt{\frac{\zeta_{(1)} - \zeta_{(2)}}{n_\omega^{-2} - n_\varepsilon^{-2}}} \tag{2.21}$$

where $\zeta_{(1)}$ and $\zeta_{(2)}$ are eigenvalues of the tensor ζ_{ij} in the section perpendicular to the wave vector (see next section). In this case, $2V$ is diagnostic of applied stress.

2.2.5. The General Case

Here, we consider crystals of any symmetry under any elastic load. Let us introduce a special coordinate basis not necessarily coincident with the crystal physical basis, in which x_3 coincides with the wave vector with x_1 and x_2 parallel to the vibration

directions of two plane-polarized waves traveling along x_3 through a stress free crystal. When x_3 is a direction where $\Delta n = 0$, axes x_1 and x_2 are chosen for reasons of symmetry. Under elastic stress the dielectric impermittivity tensor consists of two parts: The first describes the optical indicatrix of the stress-free crystal η_{ij}, and the second describes a small addition ζ_{ij}, related to the action of elastic stress. The resulting indicatrix is expressed as:

$$(2.22) \qquad \left(\eta_{ij} + \zeta_{ij}\right) x_i x_j = 1 \; i, j = 1, 2, 3.$$

For a section normal to the wave front x_3 in the special coordinate system, Equation (2.22) transforms to

$$(\eta_{11} + \zeta_{11}) x_1 x_1 + (\eta_{22} + \zeta_{22}) x_2 x_2 + (2\zeta_{12}) x_1 x_2 = 1.$$

Diagonalizing this two-dimensional tensor, yields the refractive indices of two plane-polarized waves (n_1 and n_2)

$$(2.23) \qquad n_{1,2}^{-2} = \frac{\eta_{11} + \eta_{22} + \zeta_{11} + \zeta_{22}}{2} \pm \sqrt{\zeta_{12}^2 + \frac{\left(\eta_{11} - \eta_{22} + \zeta_{11} - \zeta_{22}\right)^2}{4}}$$

and orientations of their vibration directions with respect to the special coordinate frame

$$(2.24) \qquad \tan 2\varphi = \frac{2\zeta_{12}}{\eta_{11} - \eta_{22} + \zeta_{11} - \zeta_{22}}.$$

Rotations ($\varphi > 0$) are counterclockwise, i.e. from x_1 to x_2.

Calculation of ζ_λ from σ_μ with Equation (2.2) requires transformation of the piezooptic tensor $\pi_{\lambda\mu}$ to the special basis. In practice it is easier to transform the stress tensor to the crystal physical basis (Appendix 4), calculate tensor ζ_λ, and then return to the special basis.

The important cases are considered below.

1. $\eta_{11} = \eta_{22} = {n_0}^{-2}$. This condition is applicable for any cubic crystal section and for the section normal to the optic axis of uniaxial crystals. In this case, Equations (2.23) and (2.24) are simpler:

$$(2.25) \qquad n_{1,2}^{-2} = n_0^{-2} + \frac{1}{2}\left[\zeta_{11} + \zeta_{22} \pm \sqrt{(2\zeta_{12})^2 + (\zeta_{11} - \zeta_{22})^2}\right]$$

$$(2.26) \qquad \tan 2\varphi = \frac{2\zeta_{12}}{\zeta_{11} - \zeta_{22}}.$$

In such a section, the choice of x_1 and x_2 is arbitrary. The birefringence in such a section $\Delta n = |n_1 - n_2|$ is equal to

$$(2.27) \qquad \Delta n \approx \frac{n_0^3}{2}\left(n_1^{-2} - n_2^{-2}\right) = \frac{n_0^3}{2}\sqrt{(2\zeta_{12})^2 + (\zeta_{11} - \zeta_{22})^2}.$$

These expressions show the proportionality of the birefringence and the maximal shear stress.

In practice, we usually need to solve the inverse problem, that is to find the stress tensor from the axial angle and birefringence. This problem can be solved directly for some symmetries. In the simplest case, sections of trigonal and hexagonal crystals (classes 32, $3m$, $\bar{3}m$, 622, $6mm$, $\bar{6}2m$ and $6/mmm$) cut perpendicular to the optic axis, the special basis is chosen to coincide with the crystal physical basis.
Then

$$n_1^{-2} - n_2^{-2} = \sqrt{(2\zeta_6)^2 + (\zeta_1 - \zeta_2)^2} = \sqrt{(2\pi_{6\mu}\sigma_\mu)^2 + ((\pi_{1\mu} - \pi_{2\mu})\sigma_\mu)^2}, \mu = 1, 2, ..6.$$

Using the symmetry of piezooptic tensor $\pi_{\lambda\mu}$ (Nye, 1985, see Appendix 3) one can get

$$\zeta_{(1)} - \zeta_{(2)} = \sqrt{[(\pi_{11} - \pi_{12})(\sigma_1 - \sigma_2)]^2 + (2\pi_{66}\sigma_6)^2} =$$
$$= (\pi_{11} - \pi_{12})\sqrt{(\sigma_1 - \sigma_2)^2 + (2\sigma_6)^2} = (\pi_{11} - \pi_{12})(\sigma_{(1)} - \sigma_{(2)}),$$

where $\sigma_{(1)}$ and $\sigma_{(2)}$ are the so-called quasi-principal stress values. Then

$$\tan V = \sqrt{\frac{(\pi_{11} - \pi_{12})(\sigma_{(1)} - \sigma_{(2)})}{n_\omega^{-2} - n_\varepsilon^{-2}}} \tag{2.28}$$

and

$$2\tau_{\max} = \sigma_{(1)} - \sigma_{(2)} = \frac{n_\omega^{-2} - n_\varepsilon^{-2}}{\pi_{11} - \pi_{12}} \tan^2 V. \tag{2.29}$$

Orientation of one principal stress direction corresponds to the optic axial plane. The value of the maximal shear stress can also be obtained from the birefringence in the initially isotropic section

$$2\tau_{\max} = \sigma_{(1)} - \sigma_{(2)} = \frac{2\Delta n}{(\pi_{11} - \pi_{12})\, n_o^3}. \tag{2.30}$$

2. For biaxial crystals, and sections of uniaxial crystals not perpendicular to the optic axis, where the wave vector x_3 coincides with the axis of the indicatrix axis Z and x_1 coincides with X, rewriting Equations (2.23) and (2.24) for the section normal to the x_3 direction yields

$$n_{(1),(2)}^{-2} = \frac{n_\alpha^{-2} + n_\beta^{-2} + \zeta_{11} + \zeta_{22}}{2} \pm \sqrt{\zeta_{12}^2 + \frac{\left(n_\alpha^{-2} - n_\beta^{-2} + \zeta_{11} - \zeta_{22}\right)^2}{4}} \tag{2.31}$$

$$\tan 2\varphi = \frac{2\zeta_{12}}{n_\alpha^{-2} - n_\beta^{-2} + \zeta_{11} - \zeta_{22}}. \tag{2.32}$$

The birefringence is then

$$\Delta n = \frac{n_\alpha^2 n_\beta^2}{2\left(n_\alpha + n_\beta\right)} \sqrt{(2\zeta_{12})^2 + \left(n_\alpha^{-2} - n_\beta^{-2} + \zeta_{11} - \zeta_{22}\right)^2}. \tag{2.33}$$

The axial angle $2V_\gamma$ is found from

$$\tan V = \sqrt{\frac{{n_\alpha}^{-2} - {n_\beta}^{-2} + \zeta_{11} - \zeta_{22}}{{n_\beta}^{-2} - {n_\gamma}^{-2} + \zeta_{22} - \zeta_{33}}}. \tag{2.34}$$

The similar expressions can be written for any other orientation of the optical indicatrix with respect to the special coordinate basis. It is not difficult to calculate the distorted optical indicatrix from the stress tensor and in some cases we can solve the inverse problem. Substituting Equation (2.1) into (2.21), (2.27), (2.33), and (2.34) shows that changes in birefringence and axial angles are defined by the *shear* stress. On the other hand, hydrostatic compression will not induce optical anomalies but rather only slightly and proportionally change the refractive indices.

2.2.6. Example: Piezooptic Effect in $PbMoO_4$

Directional stress will cause variations in micrographs as illustrated by tetragonal $(4/m)$. Crystals of lead molybdate ($PbMoO_4$) and lead tungstate ($PbWO_4$) were grown from the melt by the Czochralski method (Hurle, 1993). They show distinct anomalous biaxiality ($2V \sim 3.5°$) originating from *thermoplastic* stress (see section 2.6) and easily visualized in (001) sections. Since the crystals are usually pulled from the melt along [100], (001) sections of the ingot are longitudinal, permitting the observation of the stress-induced biaxiality along the growth direction and simultaneously along the crystal radius.

The relation between stress and stress induced optical anomalies in the special coordinate frame x_1, x_2 and x_3 (wave vector) parallel to [100], [010] and [001], respectively, requires no transformation of the piezooptic tensor. Using symmetry (see Appendix 3) one can write the components of the supplemental tensor

$$\begin{aligned} \zeta_1 &= \sigma_1\pi_{11} + \sigma_2\pi_{12} + \sigma_6\pi_{16} \\ \zeta_2 &= \sigma_1\pi_{21} + \sigma_2\pi_{22} + \sigma_6\pi_{26}. \\ \zeta_6 &= \sigma_1\pi_{61} + \sigma_2\pi_{62} + \sigma_6\pi_{66} \end{aligned} \tag{2.35}$$

Substituting these expressions into Equations (2.21) and (2.26), minding the formula $\zeta_{(1)} - \zeta_{(2)} = \sqrt{(\zeta_1 - \zeta_2)^2 + 4\zeta_6^2}$, one can express the measured optical characteristics

($2V_\alpha$ angle and orientation of the optic axial plane φ with respect to x_1) through the components of the stress tensor σ_μ

$$\tan V_\alpha = \sqrt{\frac{[\sigma_1(\pi_{11}-\pi_{21})+\sigma_2(\pi_{12}-\pi_{22})+\sigma_6(\pi_{16}-\pi_{26})]^2+4(\sigma_1\pi_{61}+\sigma_2\pi_{62}+\sigma_6\pi_{66})^2}{n_\varepsilon^{-2}-n_\omega^{-2}}} \tag{2.36}$$

$$\tan 2\varphi = \frac{2(\sigma_1\pi_{61}+\sigma_2\pi_{62}+\sigma_6\pi_{66})}{\sigma_1(\pi_{11}-\pi_{21})+\sigma_2(\pi_{12}-\pi_{22})+\sigma_6(\pi_{16}-\pi_{26})}. \tag{2.37}$$

In practice, we find components of the stress tensor from the optical data. Unfortunately, a rigorous solution is generally impossible since we have two Equations with three unknowns σ_μ. On the other hand, if we restrict ourselves to the difference between the principal stress values in the section, the maximal shear stress $2\tau_{\max} = \sigma_{(1)} - \sigma_{(2)}$, with orientation ψ with respect to x_1. Taking into account that

$$\sigma_{(1)} - \sigma_{(2)} = \sqrt{(\sigma_1-\sigma_2)^2+4\sigma_6^2}$$

and

$$\tan 2\psi = \frac{2\sigma_6}{\sigma_1-\sigma_2}$$

we deduce

$$\sigma_{(1)} - \sigma_{(2)} = \tan^2 V_\alpha \left(n_\varepsilon^{-2} - n_\omega^{-2}\right) K \tag{2.38}$$

where

$$K = \frac{\sqrt{(\pi_{66}-\pi_{16}\tan 2\varphi)^2+((\pi_{11}-\pi_{12})\tan 2\varphi-2\pi_{61})^2}}{\sqrt{\begin{array}{c}(\pi_{66}(\pi_{11}-\pi_{12})-4\pi_{16}\pi_{61}+2\pi_{16}(\pi_{11}-\pi_{12})\tan 2\varphi)^2 \\ +\tan^2 2\varphi(\pi_{66}(\pi_{11}-\pi_{12})-2\pi_{16}\pi_{61})^2\end{array}}}$$

and

$$\tan 2\psi = \frac{\tan 2\varphi(\pi_{11}-\pi_{12})-2\pi_{61}}{\pi_{66}-\pi_{16}\tan 2\varphi}. \tag{2.39}$$

The maximal shear stress is directly related to the axial angle, as qualitatively shown in the section 2.2.4. However, distinct from the special more symmetrical case considered in section 2.2.5 (see Equation (2.29)) the maximal shear stress now depends not only on the axial angle but also on the optic plane orientation (Figure 2.1). As seen from Equation (2.39), the orientation of the optic axial plane also differs from orientation of the principal stress direction in the section (Figures 2.1, 2.18). For some angular ranges (e.g. $\varphi = 20$–$40°$) the slight change of optic axial plane φ leads to a significant change in the principal stress orientation ψ. For this symmetry class, we were unable to determine whether the minimal or maximal stress is located along the direction given by the angle ψ. This problem can be solved with a fuller description of the stress distribution.

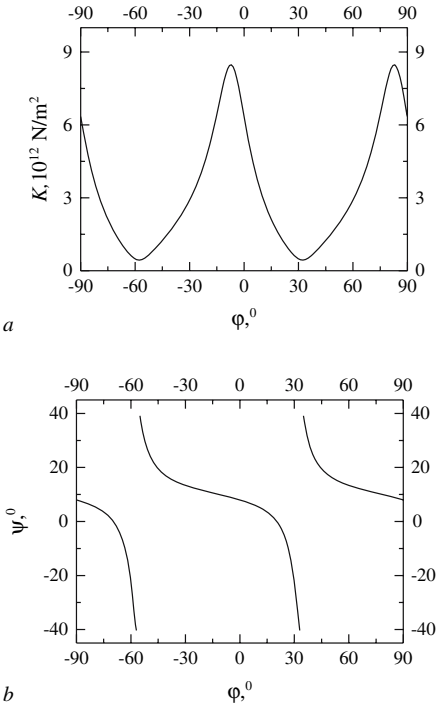

Figure 2.1. (*a*) The value of multiplier K in equation (2.38) and (*b*) the orientation of the principal axes of the stress tensor ψ as a function of orientation of the optic axial plane φ

2.3. NUMERICAL ESTIMATIONS OF STRESS AND STRESS-INDUCED OPTICAL ANOMALIES

Increasing stress in a crystal will ultimately lead to plastic or brittle deformation. Plastic materials flow only when a threshold stress has been exceeded, brittle materials fracture. The following estimates are useful: the tensile strength is approximately equal to $\sigma_{\text{tens.}} \approx 0.001E$, where E is the Young's modulus, the slope of the relationship between stress and strain; the compressive strength is usually in 6–20 times greater than the tensile strength (Petrophysics, 1992). Since both the tensile (lengthening) and compressive (shortening) stresses usually coexist, the maximum stress can be estimated from the tensile strength. Young's moduli are typically $2\text{–}5 \cdot 10^{10}$ N $\cdot$ m^{-2} for the water soluble salts, $(10\text{–}40) \cdot 10^{10}$ N $\cdot$ m^{-2} for silicates and oxides, and almost $100 \cdot 10^{10}$ N $\cdot$ m^{-2} for diamond (Shuvalov, 2005; Landolt and Börnstein, 1979). Thus, the maximum tensile stress σ_{lim} does not exceed $1 \cdot 10^{9}$ N $\cdot$ m^{-2}, consistent with experimental data on the internal stress in natural and synthetic crystals varying from 10^{6}–10^{9} N $\cdot$ m^{-2} (Punin, 1994).

To estimate the maximum birefringence, consider the simple, representative case of a uniaxial tension in a cubic crystal (class $m\bar{3}m$) along [111], a simple though illustrative case. The birefringence is equal to $\Delta n = \frac{n_0^3}{2}\pi_{44}\sigma_{\text{lim}}$. The piezooptic constants vary, in principle, from $0.3 \cdot 10^{-12}$ to $20 \cdot 10^{-12}$ m^2N^{-1}. In practice they are usually constrained in the range $0.5 \cdot 10^{-12}$ to $2 \cdot 10^{-12}$ m^2N^{-1} (Landolt and Börnstein, 1979; Narasimhamurty, 1981). Since the refractive index is usually about $n_0 = 1.5$, maximal stress-induced birefringence is about 0.04. For the typical values of piezooptic constants and Young's moduli, the maximal birefringence is equal to 0.002 for silicates, and 0.0002 for water soluble ionic compounds. Thus, the stress-induced birefringence is not high and even for the largest induced stresses should be barely detectable by ordinary compensator methods except in those cases where the section was initially isotropic.

On the other hand, the axial angle can vary widely. According to expressions (2.29) and (2.30), for the optically uniaxial crystals $\tan^2 V = \Delta n/|n_\omega - n_\varepsilon|$. For instance, in an isotropic section of a strongly birefringent substance with $n_\omega - n_\varepsilon = 0.1$, the maximal induced-birefringence of 0.002 leads to an axial angle of 16°.

Calculations show that elastic stress in biaxial crystals changes the axial angle by a few degrees at most. In cubic crystals, variations can be as large as tens of degrees but as shown in Equation (2.20) the values are independent of the stress. The axial angle is a suitable diagnostic only for uniaxial crystals, where it takes on relatively small values, can be reliably measured, and the optic axial plane is oriented with the quasi-principal stress in a crystal (see Equations (2.32) and (2.34)).

2.4. SOURCES OF STRESS

Stress can be applied to a crystal externally or internally. External stresses usually result from tectonic deformations of rock in the case of minerals, and crystallization pressure (Correns, 1949). Following relaxation of the load, external elastic stresses vanish. External elastic stresses are absent in single crystals of very high quality and in thin sections. More relevant to the problem of optical anomalies are internal stresses of the following etiologies:

1. Local stress associated with inclusions.
2. Stress on crystal defects such as dislocations, as well as block, grain, and twin boundaries.
3. Thermoelastic and thermoplastic stress.
4. Heterometry-induced stress related to compositional and phase lattice mismatch.

Below we consider the optical anomalies resulting from these stress sources.

2.5. INCLUSIONS

Small inclusions of another phase in a crystal commonly create internal stress. The causes of such stresses include the following:

1. Lattice mismatch between the crystalline host and an inclusion that precipitates from a solid solution.

2. Post-growth changes of temperature and pressure leading to local differences in thermal expansion coefficients or compressibilities.
3. Accumulation of stress from other sources at the inclusion.
4. Crystallization pressure acting during inclusion formation.

Suppose the strain on the boundary of a spherical inclusion in an initially isotropic matrix is ε, where the strain results from a difference in lattice constants a (Figure 2.2), then $\varepsilon = (a_{\text{matrix}} - a_{\text{inclusion}})/a$. As shown above, the anomalous birefringence is proportional to the maximal shear stress $2\tau_{\max} = \sigma_{rr} - \sigma_{\theta\theta}$, where σ_{rr} and $\sigma_{\theta\theta}$ are the principal stresses in the plane under consideration (the polar coordinate frame has been chosen for convenience). If the lattice constant of the included substance is larger than that of the matrix, σ_{rr} will generally be positive (compression) and $\sigma_{\theta\theta}$ will generally be negative (tension). Any central section of the inclusion is round, therefore, in the elastic isotropic solid, the stress distribution should be symmetric and $\sigma_{r\theta} = \sigma_{\theta r} = 0$. The problem of calculating stress in elastic isotropic media with concentric temperature gradients is well known from the theory of thermoelasticity (Boley and Weiner, 1960). Mathematically, our problem is the same. The maximal shear stress in the matrix decreases with the distance from the inclusion as follows:

$$2\tau_{\max} = \varepsilon \frac{E}{1+\nu} \frac{r_{\text{incl.}}^3}{r^3}, \tag{2.40}$$

where $r_{\text{incl.}}$ is the radius of the inclusion, $r \geq r_{\text{incl.}}$ is the distance from the center of inclusion, E is the Young's modulus, and ν is Poisson's ratio of contraction and extension strain. Inside the inclusion, $r < r_{\text{incl.}}$ $2\tau_{\max} = 0$. There should be no anomalous birefringence. Outside the inclusion, the birefringence for a given

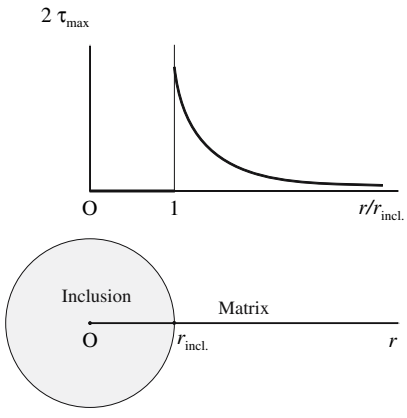

Figure 2.2. Distribution of maximal shear stress $2\tau_{\max}$ in a crystal with a spherical inclusion. r is the radial distance

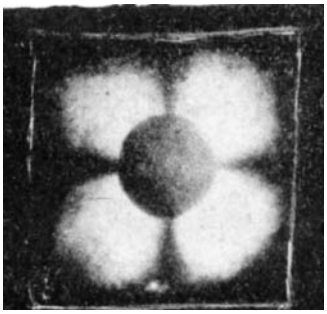

Figure 2.3. The birefringence rosette in a silicon-aluminum junction (after Indenbom, 1962; Nikitenko, 1962). Crystal size ~ 2 mm

direction in a crystal is proportional to the maximal shear stress. Birefringence decreases with a radial distance as r^{-3}, consistent with the experimental observations. Because of the radial stress distribution, the rosette of transmitted light observed under orthoscopic examination is similar to that from single dislocations (see section 2.6.1). It is important to note that the inclusion shape, as a rule, is not a sphere; both the matrix and the inclusion possess elastic anisotropy. This results in a more complicated optical pattern, however, the r^{-3} proportionality roughly holds.

The stress distribution around an inclusion is clearly illustrated by the junction of a silicon crystal with an aluminum wire (Indenbom and Nikitenko, 1962; Nikitenko and Indenbom, 1962; Figure 2.3). The round aluminum wire acts as an inclusion and the birefringence rosette appears around it.

This type of optical anomaly is characteristic of diamond crystals (see Figure 1; (Lang, 1967; Varshavsky, 1968; Orlov and Tatjanina, 1973; Zilbershtein, 1990). For example, Zilbershtein *et al.* (1995) studied diamond crystals with olivine $(Mg, Fe)_2SiO_4$ inclusions. The inclusions are presumed to form simultaneously with the diamond at high temperature and pressure but without stress at the interface. After crystal growth the temperature and the pressure decreased. Changes in lattice constants of olivine and diamond were no longer well-matched because of differences in thermal expansion coefficient (α_T) and in compressibility (β_P) resulting in strain, stress, and anomalous birefringence. Strain related to the change of temperature ΔT and pressure ΔP is equal to $\varepsilon = \Delta T(\alpha_{T1} - \alpha_{T2}) + \Delta P(\beta_{P1} - \beta_{P2})$. Taking anisotropy of elastic constants, thermal expansion coefficients, and compressibility into account for two different directions in a crystal, it is possible to obtain two Equations that connect changes in temperature and pressure with the elastic stress (and, respectively, with the birefringence). If the birefringence is known, we can obtain linear Equations with two variables ΔT and ΔP. Their solution gives the temperature and the pressure of the diamond formation. Similar calculations can be used to reconstruct growth conditions of other minerals.

The similar application of stress birefringence for estimation of crystallization temperature (piezothermometry) is well known in mineralogy and was carried out for quartz inclusions in garnet grains (Rosenfeld, 1969; Adams *et al*., 1975a,b).

2.6. DISLOCATIONS

Crystals, even under thermodynamic equilibrium, will always be imperfect. Such imperfections, argue Vainshtein *et al*. (1982) should never be regarded as defects but rather as elementary excitations of the idealized crystal structure from the ground state. Dislocations (Hirth and Lothe, 1968) are long range defects in crystals that result from well-defined linear displacements, around which structural units are misaligned. Naturally, dislocations have associated stress fields that have piezooptic consequences. The prototypical edge and screw dislocations have stress fields that are well described by the theory of elasticity. Their photoelastic consequences cannot be considered anomalies as such. However, single isolated dislocations with clearly resolved patterns of birefringence are a rarity. It is the superposition and interaction of stress fields from many dislocations that can be vexing to the microscopist.

2.6.1. Single Dislocations

The dielectric constant and refractive index are functions of the stress field in a crystal. Consequently, birefringence can be used to assess the stress field (Ming and Ge, 1990). The stress distribution around a single dislocation in a crystal is rather complicated. For edge dislocations in the cylindrical coordinate frame (Figure 2.4) the stress tensor components are written as follows (Landau and Lifshitz, 1986; Predvoditelev *et al*., 1986):

$$\sigma_{rr} = \sigma_{\theta\theta} = -C_D \frac{\sin\theta}{r}, \quad \sigma_{r\theta} = C_D \frac{\cos\theta}{r}, \quad \sigma_{zz} = -2C_D \nu \frac{\sin\theta}{r}. \tag{2.41}$$

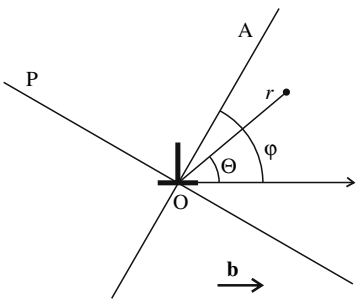

Figure 2.4. The edge dislocation in the cylindrical coordinate frame. **b** is the Burgers vector, P and A are the polarizer and analyzer, respectively

The angle θ is measured from the Burgers vector (the dislocation slip plane). In a Cartesian basis

$$\sigma_{11} = -C_D \frac{x_2\left(3x_1^2 + x_2^2\right)}{\left(x_1^2 + x_2^2\right)^2} \qquad \sigma_{22} = C_D \frac{x_2\left(x_1^2 - x_2^2\right)}{\left(x_1^2 + x_2^2\right)^2}$$

(2.42)

$$\sigma_{12} = \sigma_{21} = C_D \frac{x_1\left(x_1^2 - x_2^2\right)}{\left(x_1^2 + x_2^2\right)^2} \qquad \sigma_{33} = \nu\left(\sigma_{11} + \sigma_{22}\right) = -2C_D\nu \frac{x_2}{x_1^2 + x_2^2}$$

In these expressions $C_D = \frac{Gb}{2\pi(1-\nu)}$, where G is the shear modulus, and b is the Burgers vector.

Poisson's ratio, given by ν, is the ratio of transverse contraction strain to longitudinal extension in the direction of stretching force. Tensile deformation is considered positive and compressive deformation is considered negative. By convention Poisson's ratio contains a minus sign so that most materials have a positive ratio. For elastic anisotropic media G and ν are defined by a combination of elastic constants (Sirotin and Shaskolskaya, 1982). The work just cited contains expressions for the shear modulus for the different slip systems in a number of natural and synthetic compounds. For the sake of simplicity we will restrict ourselves to an isotropic approximation.

Consider an edge dislocation in elastic isotropic medium. The dislocation line lies normal to the section plane and parallel to the light direction (Figure 2.4). In such a section $\sigma_{rr} = \sigma_{\theta\theta}$ and $\sigma_{rr} - \sigma_{\theta\theta} = 0$, therefore, the *maximal birefringence* is defined only by the stress component $\sigma_{r\theta}$ and is equal to

$$\Delta n = C_F C_D \frac{\cos\theta}{r}, \tag{2.43}$$

where C_F is a combination of piezooptic coefficients. The observed birefringence will be proportional to the projection of $\sigma_{\theta r}$ on the directions of the crossed polarizers. If the angle between Burgers vector and analyzer is equal to φ, measured from the slip plane to the analyzer, the birefringence decreases by $\cos 2(\theta - \varphi)$. Thus, the *observed birefringence* is equal to

$$\Delta n = \frac{C_F C_D}{r} \cos\theta \cos 2\left(\theta - \varphi\right). \tag{2.44}$$

Here, θ fixes the point studied, and φ defines the stage rotation from the position where the Burgers vector is parallel to one of the cross hairs. As a result, the birefringence is described by a rosette (Figure 2.5) that satisfies to the following Equation

$$r = \text{const} \cdot \cos\theta \cos 2\left(\theta - \varphi\right). \tag{2.45}$$

Since Equation (2.45) includes φ, the shape of the rosette changes with stage rotation (cf. Figures 2.5*a* and 2.5*b*). Equation (2.45) shows that the birefringence is absent

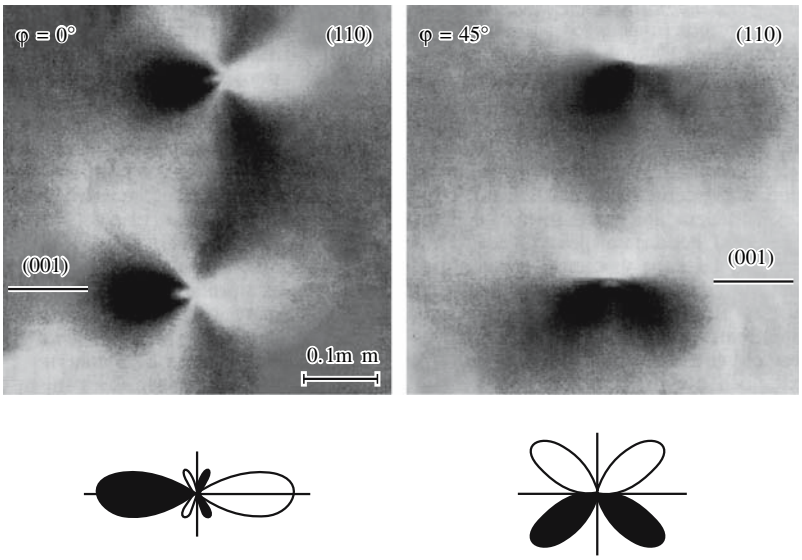

Figure 2.5. Birefringence rosettes around edge dislocation outcrops in silicon single crystal for two different orientations of the slip plane (Burgers vector) with respect to the crossed polarizers. Bright and dark fields correspond to different signs of stress (after Nikitenko and Osip'yan, 1975). The figure on the left corresponds to that case where the slip plane is aligned with the coordinate system of the microscope. The figure on the right is a consequence of rotating the sample by 45°

if $\theta = \pm\frac{\pi}{2}$. The dark line moves with θ by rotating the sample stage. This line is perpendicular to the slip plane and associated Burgers vector. The birefringence is also absent if $\theta = \varphi \pm \frac{\pi}{4}$. The corresponding lines of zero birefringence are diagonal to the cross hairs and do not move with stage rotation. Thus, the birefringence rosette establishes the orientation and magnitude of the Burgers vector.

The maximal birefringence at the distance of r from the dislocation occurs if $\theta = 0$ and $\theta = \varphi$. For a cubic crystal the birefringence is equal to $\Delta n = \dfrac{n_0^3}{2}\pi_{44}\dfrac{Gb}{2\pi(1-\nu)r}$ (we choose a crystal orientation so that a combination of piezooptic coefficients inserted into the formula for the calculation of birefringence is as simple as possible). Alum ($KAl(SO_4)_2 \cdot 12H_2O$), for example, has a low shear modulus $G = 0.8 \cdot 10^{10}\ \mathrm{N \cdot m^{-2}}$, and yttrium aluminum garnet ($Y_3Al_5O_{12}$), has a relatively high shear modulus $G = 11.5 \cdot 10^{10}\ \mathrm{N \cdot m^{-2}}$. For alum, the birefringence 0.1 mm from a single dislocation will be $1.2 \cdot 10^{-8}$. This value cannot be detected reliably even in thick sections. The corresponding value in yttrium aluminum garnet is equal to $2.7 \cdot 10^{-7}$. This value is also small but measurable (Figure 2.5). Birefringence rosettes are usually observed in relatively thick crystals with large elastic constants. The best known examples are semiconductors Si, Ge, GaAs (observed in infrared light) and synthetic garnets (Indenbom and Nikitenko, 1962; Nikitenko, 1966; Nikitenko and Osip'yan, 1975; Vainshtein *et al.*, 1982).

For a screw dislocation, the corresponding non-zero components of the stress tensor in the cylindrical and Cartesian coordinate frames are written as (Landau and Lifshitz, 1986; Predvoditelev *et al*., 1986):

$$\sigma_{\theta z} = \sigma_{z\theta} = \frac{Gb}{2\pi r}, \qquad \sigma_{13} = -\frac{Gb}{2\pi}\frac{x_2}{x_1^2 + x_2^2}, \quad \sigma_{23} = \frac{Gb}{2\pi}\frac{x_1}{x_1^2 + x_2^2}. \tag{2.46}$$

These Equations predict that the stress and its associated birefringence should be absent in elastic isotropic media when viewed along a dislocation line. The birefringence in sections normal to the dislocation line is absent only if the material possesses elastic as well as photoelastic isotropy, a rare occurrence. Ge *et al*. (1993) showed that stress birefringence can be observed in barium nitrate, as well as in yttrium aluminum and gallium gadolinium garnets even for screw dislocations parallel to the wave vector.

Birefringence is evident for any type of dislocation viewed normal to the dislocation line. However, as shown above, this birefringence is not large and discrete dislocations are rarity. Stress birefringence induced by a single dislocation can be observed only in rather perfect crystals with very low dislocation densities.

2.6.2. Dislocation Ensembles

Natural as well as synthetic crystals contain a significant number of dislocations. Typical dislocation densities are in the range of 10^4–10^{10} cm^{-2}. At the higher end dislocations form bundles and two dimensional dislocation ensembles, including plane ensembles (slip planes) and dislocation walls (Hirth and Lothe, 1968).

2.6.2.1. Dislocation bundles

Bundles consist of many closely spaced, approximately parallel dislocations and are widespread. They often originate from inhomogeneities and serve as a step source when the crystal growth is controlled by the spiral dislocation mechanism (Chernov, 1984; Klapper, 1998). Dislocation bundles complicate stress distributions. Principal stresses vary across the bundle obviating sharp extinction in orthoscopic examination. Optically anomalous stripes mark the dislocation bundles. They are typically localized near the bundle axis. The total Burgers vector of most dislocation bundles is zero (Predvoditelev, 1975). Long-range stress fields do not arise as evident in the anomalous birefringence in potassium alum crystals (Van Enckevort, 1982), mixed potassium-ammonium alum crystals (Figure 2.6 Shtukenberg *et al*., 2001b), and grossular-andradite garnets (Figure 2.7; section 2.8.2.4).

2.6.2.2. Dislocation rows

Consider a row of parallel edge dislocations having the same Burgers vector b and lying in a common plane in an isotropic medium (Figure 2.8*a*) with neighboring

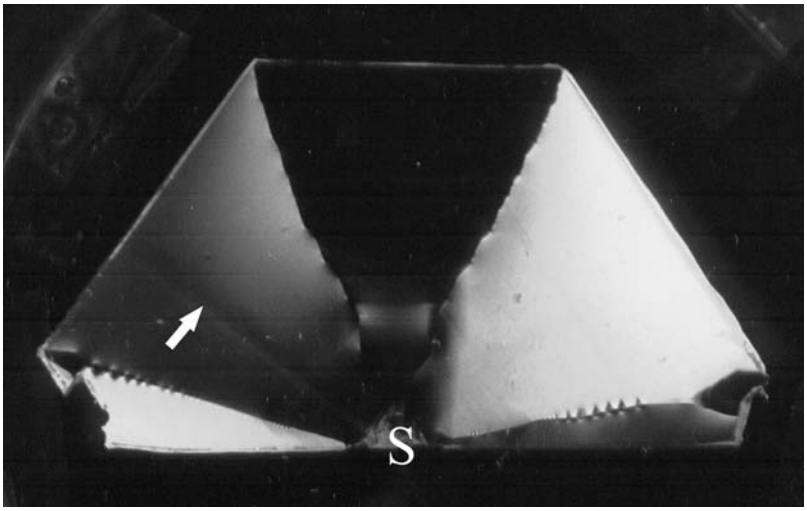

Figure 2.6. Birefringence bands (shown by arrow) related to a dislocation bundle in alum $(K_{0.5}(NH_4)_{0.5})Al(SO_4)_2 \cdot 12H_2O$. This bundle, formed at the seed (S), lies perpendicular to the growth front (111) and to the growth zones. The variation of indicatrix orientations in growth sectors is a consequence of growth dissymmetrization (see Chapter 3)

dislocations separated by distance d. Such a distribution is common for slip bands resulting from plastic deformation (Shuvalov, 2005). Analytical expressions for the stress tensor of such an ensemble are given by Predvoditelev *et al.* (1986) (see the next section). They show that far from the dislocation row ($x_2 >> d$):

$$\sigma_{22} = \sigma_{12} = 0, \ \sigma_{11} = \frac{Gb}{d\,(1-\nu)}. \tag{2.47}$$

Thus, the long-range stress field appears in the plane perpendicular to the dislocation lines. It is described by only one component of the stress tensor σ_{11}. The sign of the stress will be different above and below the plane of dislocation lines, so the half space with $x_2 < 0$ will be under compressive stress and the half space with $x_2 > 0$ will be under tensile stress. The dislocation plane divides the crystal into two parts with lattice constants a_1 and a_2. Correspondingly, the strain at this boundary is equal to $\varepsilon = \dfrac{a_2 - a_1}{a_1} = \dfrac{b}{d}$ (section 2.8.1). The maximal shear stress, $\tau_{\max} = \sigma_{11}/2$, produces optical anomalies far from the slip plane. For example, the birefringence along x_3 in a cubic crystal (class $m\bar{3}m$) (Figure 2.8) induces the birefringence equal to $\Delta n = n_0^3\,(\pi_{11} - \pi_{12})\,\tau_{\max}$.

In reality, the crystal is bounded by free surfaces that result in partial stress relaxation. If the crystal is an infinite band directed along x_2 and having a width $2A$ (Figure 2.9), the stress component σ_{11} changes along the x_2 direction and for

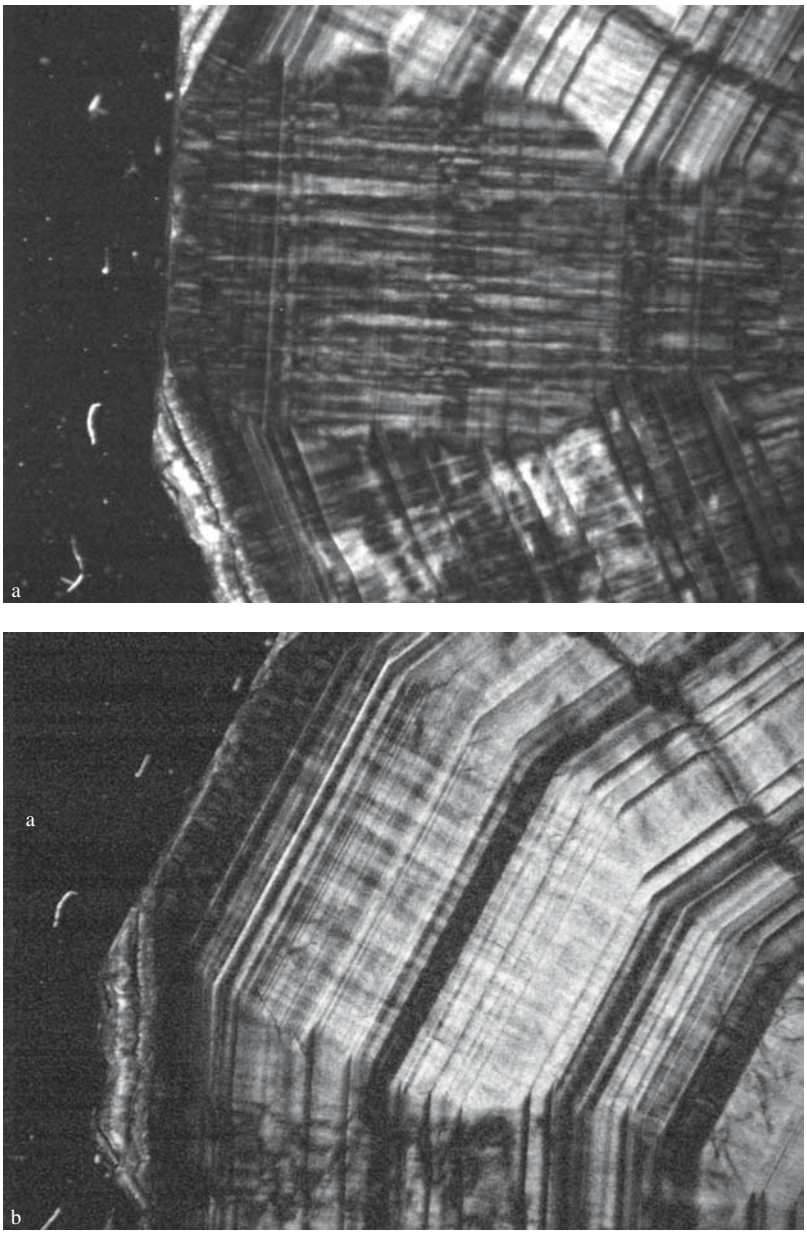

Figure 2.7. Birefringence bands in garnet $Ca_3(Al, Fe)_2(SiO_4)_3$ from the Dalnegorsk mine, Far East, Russia. These bands originate from elastic stress on dislocation bundles and are directed normal to the growth front. (*a*) and (*b*) correspond to different crystal orientations relative to the crossed polarizers directed vertically and horizontally, respectively. The growth front positions are marked by numerous concentric zoning boundaries. Birefringence more or less homogeneously distributed over concentric zones is caused by growth desymmetrization (see Chapter 3). The sample was kindly provided by P.B. Sokolov (see Color Section following page 254)

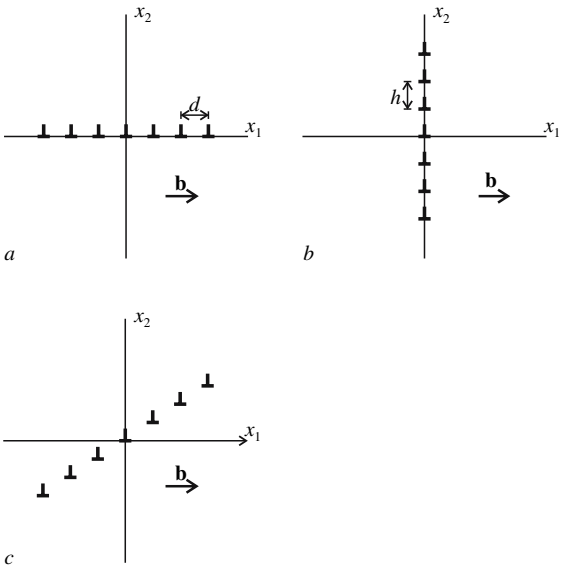

Figure 2.8. (*a*) Dislocations in a plane ensemble, as well as in (*b*) symmetric and (*c*) asymmetric dislocation walls

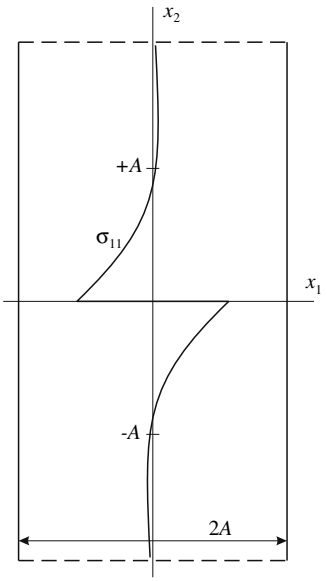

Figure 2.9. Distribution of the stress component σ_{11} in an infinitely long band along x_2, with width $2A$ along x_1 containing a single plane dislocation ensemble at $x_2 = 0$ (after Indenbom, 1960; Nye, 1949)

the line $x_1 = 0$ according to following expression (Nye, 1949b):

$$\sigma_{11} = \frac{4Gb}{\pi(1-\nu)\,d}\int_0^{\infty}\frac{\sinh u + u\cosh u}{u(\sinh 2u + 2u)}\sin\frac{ux_2}{A}\,du - \frac{Gb}{(1-\nu)\,d} \tag{2.48}$$

where u is the integration variable. The result of simulation is schematically shown in Figure 2.9.

At distances from 0 up to $0.91A$ from the slip plane, the stress decreases from the maximal value given by Equation (2.47) down to zero. Further from the dislocation plane, the stress appears again but it is smaller and of opposite sign. The calculation for this simple case well agrees with the experimental data. For example, birefringence at a point 100 μm from a row of edge dislocations ($d \approx 100$ μm) in a silicon crystal was measured at $1.15 \cdot 10^{-5}$, whereas the theoretical value was $0.9 \cdot 10^{-5}$ (Nikitenko, 1966).

Single dislocation rows arise in the course of stress relaxation in heteroepitaxial films (Chernov, 1984) but more often they appear in slip bands (Indenbom, 1960; Shuvalov, 2005), one or more systems of close parallel dislocation rows (Figure 2.10). The neighboring planes can contain dislocations of the same or of different signs (orientations of the Burgers vector). The resulting stress pattern will contain regions with alternation of compression and tension (Figure 2.11) on either side of the slip plane. As a result, alternation of bands with mutually perpendicular

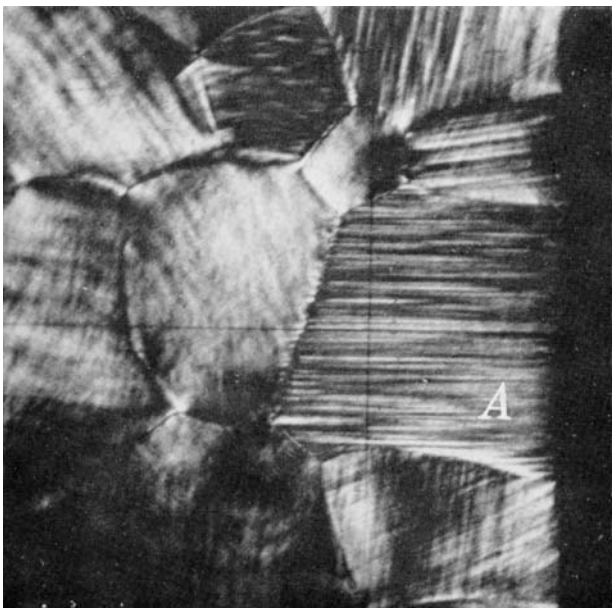

Figure 2.10. Anomalous birefringence in the slip bands of silver chloride grains (after Nye, 1949b). Orientation of crossed polarizers is shown by thin, mutually perpendicular black lines

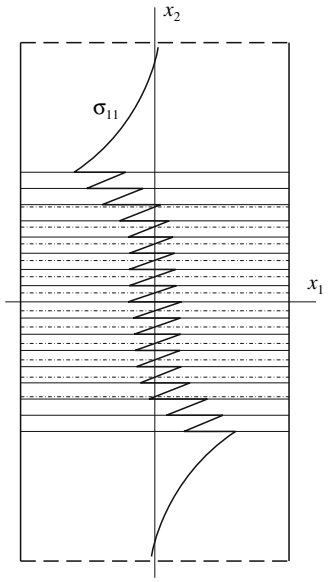

Figure 2.11. Distribution of the stress component σ_{11} for the case of large number of parallel plane dislocation ensembles (after Nye, 1949)

orientations of Z and X, separated by dark neutral lines with zero birefringence (ideally located in the middle between the slip bands) should be observed. If a conventional polarizing microscope is used such an alternation can be easily visualized with a gypsum plate.

Stress birefringence provides the most powerful tool for detection and study of the slip bands in crystals having undergone growth and post growth deformations, including the following: corundum (Indenbom and Tomilovskii, 1957a; Indenbom, 1960), silver chloride (Nye, 1949b), sodium chloride (Oberimov and Shubnikov, 1926; Mendelson, 1961), fluorite (Cheredov, 1993), and ammonium chloride (Figure 2.12), among others.

The stress distribution for a slip band consisting of screw dislocations is given in Predvoditelev *et al*. (1986). Distribution of stress and birefringence are approximately the same for the two dimensional dislocation networks formed in the course of heteroepitaxial growth (Predvoditelev *et al*., 1986). Far from the dislocation net, dislocation lines lie in the plane x_1x_3 and there are two non-zero components of the stress tensor $\sigma_{11} = \sigma_{33} = \sigma'_{11}(1+\nu)$, where σ'_{11} is defined by Equation (2.47).

It is important to note that the dislocation rows considered above induce strong long-range stress fields and, therefore, they lead to larger anomalous birefringence than those related to single dislocations.

Using expressions for a single edge dislocation (2.42), given below, we give a more stringent consideration of the stress distribution in the plane dislocation ensemble shown in Figure 2.8*a* by summing the stress fields of all dislocations in the row:

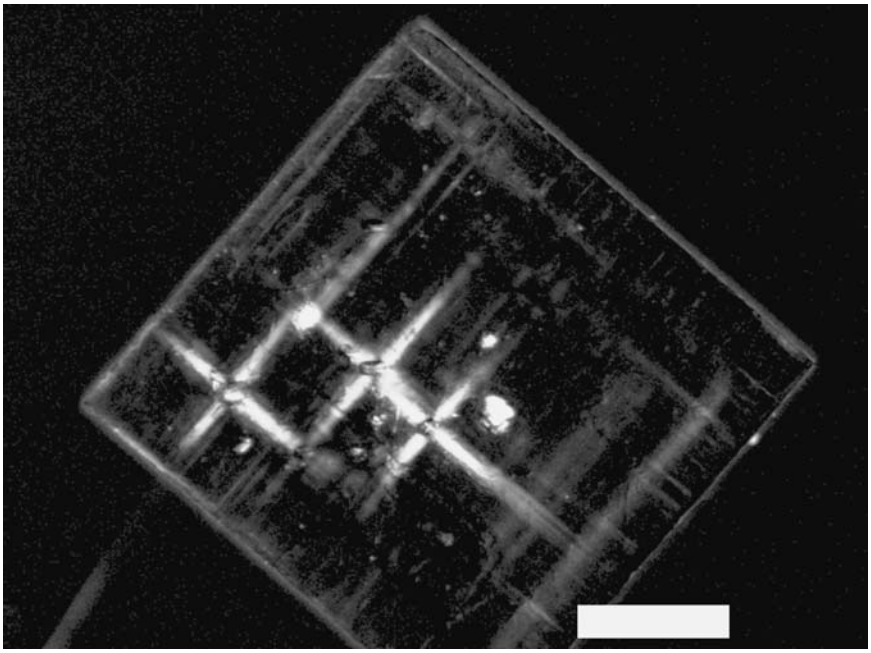

Figure 2.12. Slip bands in ammonium chloride induced by pricking the crystal surface with a needle. Scale bar= 0.88 mm (see Color Section following page 254)

$$\sigma_{11} = -C_D \sum_{n=-\infty}^{\infty} \frac{x_2\left[3\,(x_1+nd)^2 + x_2^2\right]}{\left[(x_1+nd)^2 + x_2^2\right]^2} \tag{2.49}$$

$$\sigma_{22} = C_D \sum_{n=-\infty}^{\infty} \frac{x_2\left[(x_1+nd)^2 - x_2^2\right]}{\left[(x_1+nd)^2 + x_2^2\right]^2} \tag{2.50}$$

$$\sigma_{12} = \sigma_{21} = C_D \sum_{n=-\infty}^{\infty} \frac{(x_1+nd)\left[(x_1+nd)^2 - x_2^2\right]}{\left[(x_1+nd)^2 + x_2^2\right]^2}. \tag{2.51}$$

These sums can be calculated with the method described previously (Predvoditelev *et al.*, 1986), which gives a rigorous solution for any point in space through combination of cumbersome trigonometric and hyperbolic functions. Since the dislocation spacing d is tens of microns or less compared with millimeter sized crystals, the discrete distribution of dislocations can be replaced by a continuous distribution with the same ratio of the Burger's vector (**b**) to the dislocation spacing: b/d. This operation is valid for any point in the crystal that is no closer to the slip plane than d. In this case, summation in Equations (2.49)–(2.51) can be replaced

by integration along the respective coordinate directions (Hirth and Lothe, 1968). The limits of integration A_1 and A_2 are equal to $\pm\infty$ if the summation is performed over an infinite dislocation row or to certain values of coordinates if the stress is calculated for the bounded dislocation row. The integration gives

$$\sigma_{11} = -C_D x_2 \int_{A_1}^{A_2} \frac{3(x_1 - x_1')^2 + x_2^2}{\left[(x_1 - x_1')^2 + x_2^2\right]^2} dx_1' = C_D \left[\arctan \frac{x_1 - x_1'}{x_2} - \frac{(x_1 - x_1')\, x_2}{(x_1 - x_1')^2 + x_2^2} \right] \Bigg|_{A_1}^{A_2} \tag{2.52}$$

$$\sigma_{22} = C_D x_2 \int_{A_1}^{A_2} \frac{(x_1 - x_1')^2 - x_2^2}{\left[(x_1 - x_1')^2 + x_2^2\right]^2} dx_1' = -C_D \frac{(x_1 - x_1')\, x_2}{(x_1 - x_1')^2 + x_2^2} \Bigg|_{A_1}^{A_2} \tag{2.53}$$

$$\sigma_{12} = C_D \int_{A_1}^{A_2} \frac{(x_1 - x_1')\left[(x_1 - x_1')^2 - x_2^2\right]}{\left[(x_1 - x_1')^2 + x_2^2\right]^2} dx_1' = -\frac{C_D}{2} \ln \left[(x_1 - x_1')^2 + x_2^2\right] \Big|_{A_1}^{A_2}. \tag{2.54}$$

For the infinite dislocation row $A_1 = -\infty$ and $A_2 = +\infty$, respectively, expressions (2.52)–(2.54) are transformed to (2.47).

2.6.2.3. Dislocation walls

Vertical rows of edge dislocations form dislocation walls (Figure 2.8*b*, *c*), that are wide spread in crystals and form so-called tilt block boundaries. The mutual misorientation of the neighboring blocks is defined by angle $\tan^{-1} b/h$, where h is the dislocation separation in the wall. To calculate the stress distribution around the wall, the stress fields of all dislocations in the ensemble should be summed using expressions similar to (2.49)–(2.51). The solution obtained by Predvoditelev *et al.* (1986) shows that the well ordered dislocation wall does not induce long-range stress fields. Not far from the wall the stress is equivalent to that produced by a single dislocation, but already at distances more than h the stress approaches zero. For this reason birefringences induced by dislocation walls are slight and resemble those from single dislocations.

The dislocation wall is not necessarily an ideal vertical row as shown in Figure 2.8*b*. Often the Burgers vector is not perpendicular to the tilt boundary (Figure 2.8*c*). Such an arrangement suggests the presence of an edge component parallel to the wall resulting in a long-range stress field as for the dislocation rows. These boundaries become visible under optical examination as in the well known example of so-called *irrational twinning* of sodium chloride and other halogenides in which preferred deformation-induced glide systems in different parts of a plate affect a rotation between them (Indenbom, 1960; Klassen-Nekludova, 1960; Urusovskaya, 1962; Vainshtein *et al.*, 1982). Dislocations in walls may not be well ordered or equally spaced. They can form "thick" multiples with varying Burger's vectors. Finally, very strong long-range stress fields are induced by the truncated dislocation wall or by so-called partial disclinations (Vladimirov and Romanov, 1986).

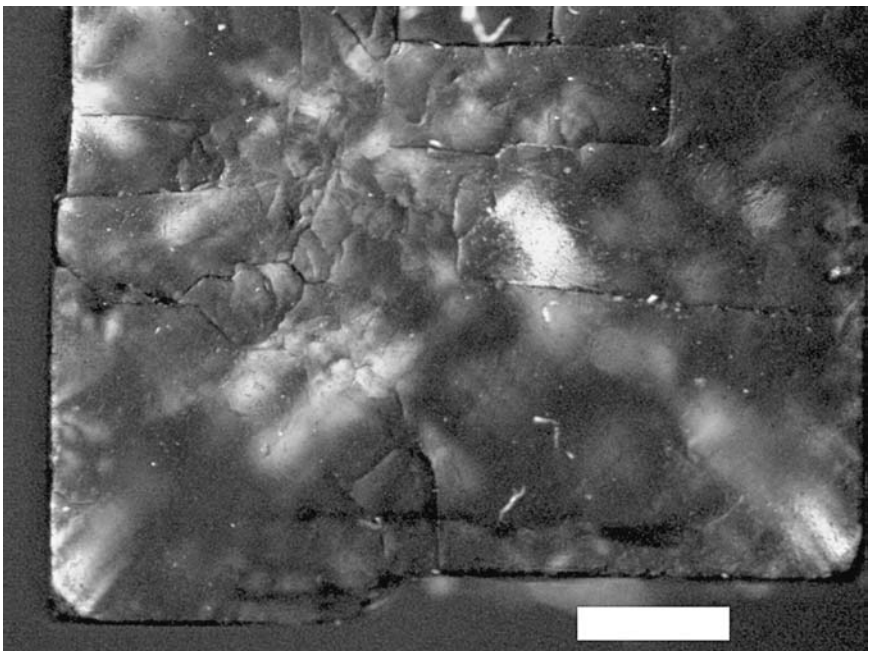

Figure 2.13. Anomalous birefringence in potassium chloride originating from stress on the block boundaries. Scale bar= 0.88 mm (see Color Section following page 254)

2.6.3. Macroblocks, Grain, and Twin Boundaries

Grain, twin, macro-block and other high-angle boundaries usually contain more or less ordered dislocation ensembles that induce long-range stress fields and optical anomalies. These ensembles approximate irrational twinning considered above. Deviations of the twin boundary from the twin plane results in macroscopic stress fields. Twin junctions can be described by a set of "twinning dislocations". The resulting stress field can be calculated as for dislocation ensembles (Vainshtein *et al*., 1982).

High-angle boundaries can be accompanied by other stress sources. Optical anomalies appear when twins and blocks near one another are restricted in their growth at an induction boundary creating crystallization pressure. The block crystal of potassium chloride shown in Figure 2.13 illustrates this phenomenon as does lead molybdate $PbMoO_4$ (Figure 2.14) showing anomalous biaxiality only in and around the growth macro-block whereas the rest of the crystal remains optically uniaxial.

2.7. THERMOELASTICITY AND THERMOPLASTICITY

Temperature induced stress is rare in minerals but not so in synthetic crystals grown from the melt where temperature gradients are required for crystal growth.

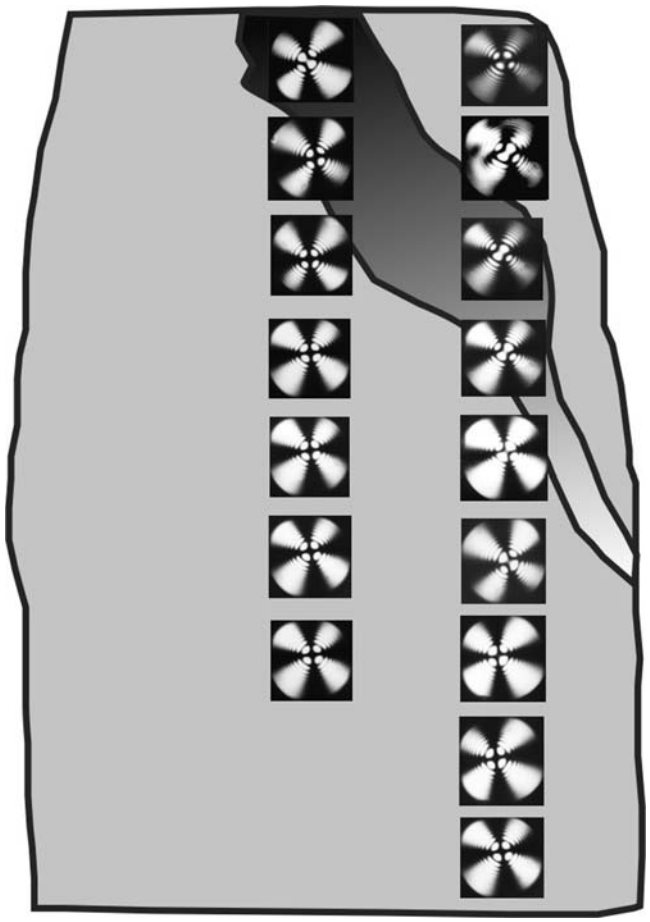

Figure 2.14. Anomalous biaxiality in Czochralski-grown lead molybdate ($PbMoO_4$). The biaxiality arises only in the growth block and around it. Crystal height= 20 mm. Figure kindly provided by A.V. Denisov

Non-uniform thermal expansion causes *thermoelastic* stress. After growth and temperature equilibration, thermoelastic stress vanishes. However, near the melting point thermoelastic stress can relax plastically by formation of dislocation ensembles and the redistribution of point defects. As a consequence the new stress arises after the crystal cooling. This stress is called *thermoplastic* or *residual* stress. During growth the crystal adjusts the distribution of defects to the non-uniform temperature field in order to mitigate thermoelastic stress. The persistent residual stresses are usually of opposite sign. Below we consider the most important sources of optical anomalies related to thermoelastic and thermoplastic stress (Chernov, 1984; Indenbom and Nikitenko, 1962).

Quench stress in crystals. The outside of a spherical crystal cools faster than the inside. Consequently the outer parts are under tensile stress and the inner parts are under compressive stress. If a crystal has a high degree of plasticity these stresses can be compensated by newly-formed dislocations such that after cooling, the inner parts will be stretched and outer parts will be compressed. This can be realized in the solidification of small portions of a melt taken from the surface, as is common in mineral formation in volcanic bombs, masses of lava ejected from a vent. Calculations show that the quench stress in the plagioclase crystal lapillies formed during the B. Tolbatchek volcano eruption (1975–1976; Kamchatka, Russia) attained a stress of $5 \cdot 10^8$ N $\cdot$ m^{-2}. The reverse process, cooling from the crystal center thereby reversing the stress distribution, is realized during some industrial crystal growth procedures such as the Kyropoulos method in which a crystal is grown into the melt.

Thermoelastic stress arising during crystal cooling from the surface is proportional to the radial temperature gradients. Since the temperature usually depends parabolically on the crystal radius (Figure 2.15), the thermoplastic stress should be distributed parabolically as well. The value of anomalous birefringence in the longitudinal section (for simplicity a cubic crystal is considered) is proportional to the difference $(\sigma_z - \sigma_r)$ and changes quadratically from the periphery to the center. At a certain crystal radius the stress changes sign and the birefringence falls away. Correspondingly, the optical indicatrix has mutually perpendicular orientations on either side of this neutral boundary. In the cross section the birefringence is proportional to the $(\sigma_r - \sigma_\theta)$ and decreases parabolically from the rim to the core (Figure 2.16*a*).

If the crystal has a low degree of plasticity the residual stress and optical anomalies appear only at the periphery (Figure 2.16*b*). In the limit of no plastic deformation there is a high probability of brittle deformation, since the stress can well exceed the breaking point.

Residual stress in a cylindrical crystal rod growing from the end. This case is realized in Verneuil, Czochralski, and Stockbarger-Bridgman methods as well as in zone melting (Hurle, 1993). These methods are accompanied by radial as well as axial temperature gradients. The stress distribution strongly depends on the crystal plasticity.

If a crystal has a high plasticity over a wide temperature range and the axial temperature gradient is modest, the plastic region will penetrate deeper into a crystal than is the crystal diameter. In this region, the thermoelastic and residual stresses are mainly defined by the radial temperature gradients (Figure 2.15). The crystal undergoes compressive theromoelastic stress in the center and tensile thermoelastic stress at the periphery. Residual stresses have opposite signs; the crystal core is stretched and the rim is compressed. This has been observed in semiconductor crystals (Indenbom and Nikitenko, 1962; Nikitenko and Indenbom, 1962; Chernov, 1984) and in synthetic fluorite (Dressler, 1986a,b; Cheredov, 1993).

In orthoscopic examination of the ingot cross section grown along an optic axis, a dark extinction cross is observed, invariant with respect to stage rotation. This suggests an axial stress distribution. The principal stresses act along the radii of the

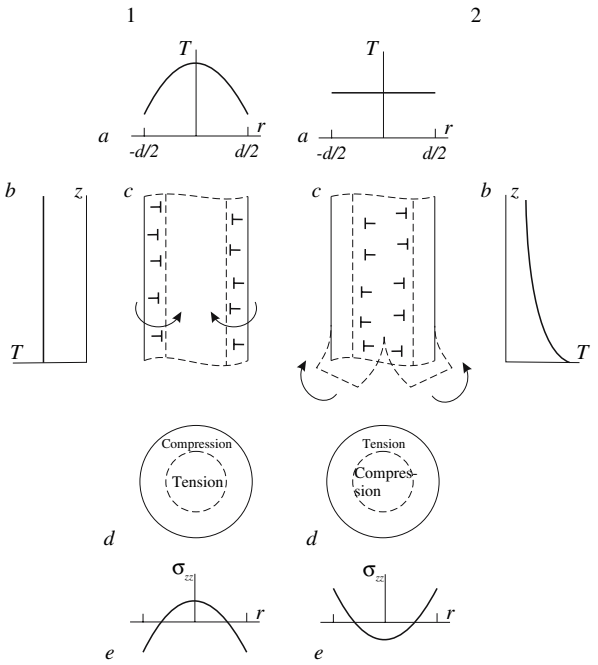

Figure 2.15. Formation of residual stress in cylindrical crystal rod of diameter d grown from the bottom end with wide (1) and narrow (2) regions of high plasticity. Quench stress corresponds to case (1). (*a*) Radial and (*b*) axial distributions of the temperature and the residual stress (*c*, *d*) in a crystal rod. Surface of zero birefringence is shown by a dashed line (*c*, *d*). Figures *c* shows newly-formed dislocations in the rim (1) and core (2). The radial distribution of residual axial stress σ_{zz} and the respective birefringence distribution in a longitudinal section after the cooling is shown in (*e*). After (Chernov, 1984) with kind permission of Springer Science and Business Media

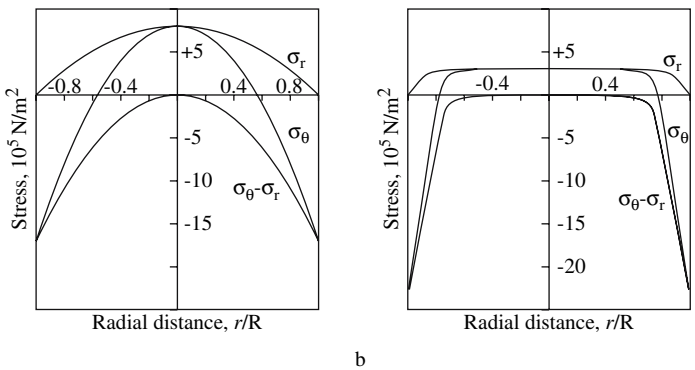

Figure 2.16. Thermoplastic stress distribution in the cross section for the case of (*a*) high and (*b*) low plasticity (after Nikitenko and Indenbom, 1962)

ingot perpendicular to the pulling axis. The birefringence increases parabolically from the center (Figure 2.16*a* Indenbom and Nikitenko, 1962). If, however, the growth direction does not correspond to an optic axis, the dark cross is transformed during the stage rotation into two hyperbolas. This pattern resembles the conoscopic interference figure of biaxial crystals in a section perpendicular to the acute bisectrix. Such behavior originates with the elastic anisotropy of the crystal (Dressler, 1986a). For example, fluorite pulled along the three-fold or four-fold axis at any stage orientation displays a dark cross as in uniaxial crystals in conoscopic illumination, whereas a crystal grown along the two-fold axis displays the dark cross that is transformed into two hyperbolas during the stage rotation (Figure 2.17).

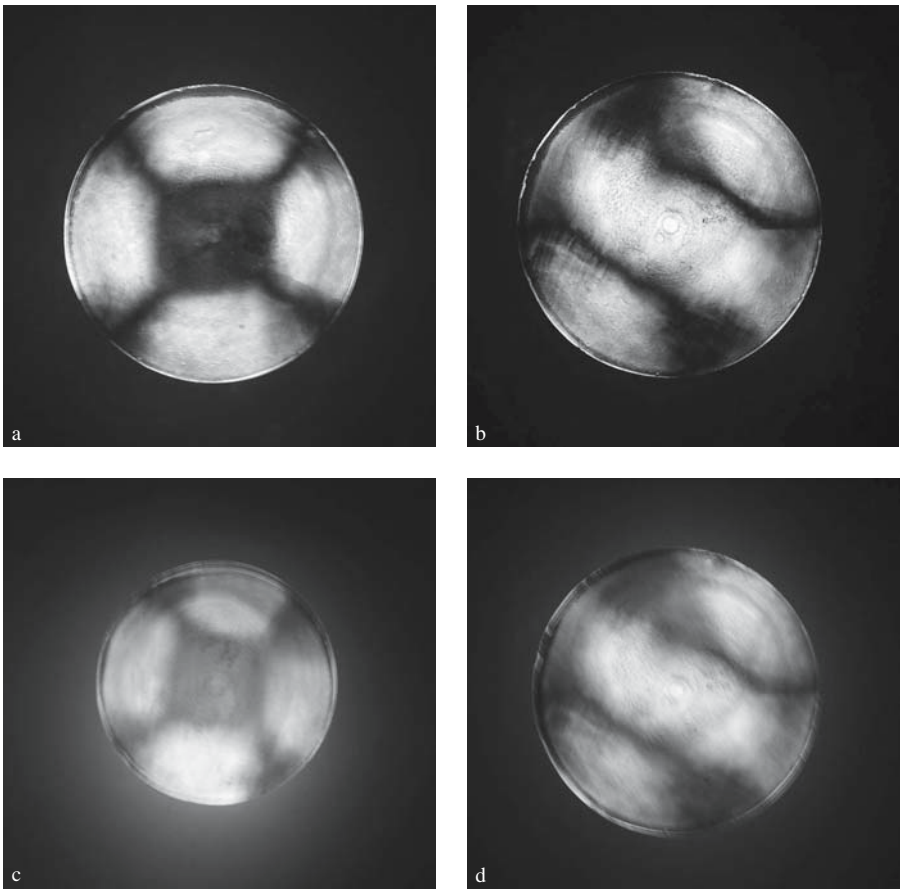

Figure 2.17. Orthoscopic optical pattern of anomalous birefringence in fluorite grown by Stockbarger method. The axis of illumination coincides with the ingot axis (two-fold axis). Rotation of the microscope stage by 45° transforms the dark cross in (*a*) into two hyperbolas in (*b*). (*c*, *d*) The same images taken with a first order red retarder. Polarizer and analyzer have diagonal orientations. Pictures kindly provided by L.A. Pyankova (see Color Section following page 254)

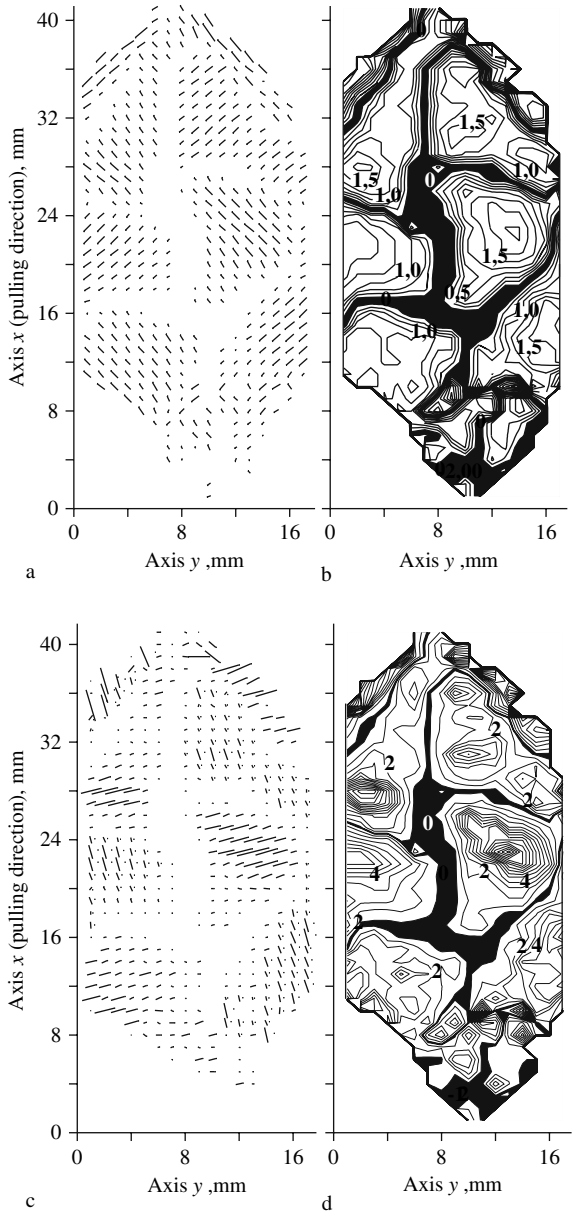

Figure 2.18. (*a*, *b*) Thermoplastic stress and (*c*, *d*) anomalous biaxiality (numbers denote values of 2*V* angles) in lead molybdate. Figure kindly provided by A.V. Denisov

In the sections cut parallel to the ingot axis the stress distribution is slightly more complicated and is similar to that observed for quench stress in cylindrical crystals. The stress changes parabolically from the center to the periphery. The center is stretched, whereas the periphery is compressed. Dark lines with zero birefringence appear at a certain distance from the crystal axis (Indenbom and Nikitenko, 1962).

For high plasticity in a narrow temperature range, the relaxation of thermoelastic stress through dislocation formation occurs only in a region that is much narrower than the crystal diameter and adjoins the growth front. If the front curvature is gradual, this narrow region is characterized by radial temperature gradients that are smaller than the axial gradients. As a result, the narrow plastic region has a higher temperature than the non-plastic remainder. The problem reduces to the growth of a thin layer with a large lattice constant onto a rigid substrate with a smaller lattice constant. Relaxation of the thermoelastic stress via dislocation formation and subsequent cooling are followed by residual tensile stress in the core and compressive stress in the rim (Figure 2.15). Such a stress distribution is a characteristic of corundum crystals grown by the Verneuil method. It sometimes induces the longitudinal splitting of the ingot (Indenbom and Tomilovskii, 1958). The optical pattern will resemble that involving crystals of high plasticity with exception of the stress sign.

The optical patterns considered above correspond to idealized and relatively simple cases. Under real growth conditions the crystals grown from the melt may display much more complicate optical patterns (see for e.g. Denisov *et al*., 2006a,b, Figure 2.18).

2.8. COMPOSITIONAL HETEROMETRY

2.8.1. What is Heterometry?

Compositional inhomogeneity resulting in a non-uniform distribution of lattice constants is called *compositional heterometry* or simply *heterometry*. This term was introduced by Shternberg (1962) to account for quartz cracking induced by inhomogeneous impurity distributions. Crystals manifesting heterometry undergo non-uniform, quasi-plastic deformation. Some authors refer to *lattice misfit* or *mismatch* when speaking of heterometry, however, this language is usually restricted to discussions of thin semiconductor films with abrupt compositional boundaries. Heterometry is a common source of internal stress and, consequently, of optical anomalies, especially in minerals. It is also found in synthetic crystals grown from solution and from the melt. Although heterometry induced by crystal growth in non-uniform temperature fields (*temperature heterometry*, see previous section) or by accretion of different crystalline phases (*phase heterometry*) can be distinguished as well, these parenthetical terms are used less frequently. Compatibility in heterometric systems requires adjustments of lattice constants, causing elastic strain and in turn optical anomalies.

There are several types of compositional inhomogeneities: concentric zoning, sector zoning, sub-sector zoning, concentration of impurities at dislocations as well as block and twinning boundaries. These inhomogeneities are present in nearly all the crystals, especially minerals.

Compositional heterometry can be described by gradients of unit cell dimensions because of "chemical" quasi-plastic deformation of the crystal lattice, $\varepsilon = \frac{1}{a}\frac{\partial a}{\partial C}\delta C = \alpha_C \delta C$, where δC represents the changes of the crystal composition, and the tensor of the chemical deformation α_C is similar to the tensor of thermal expansion coefficients. Here, temperature is replaced with chemical composition. Unfortunately, chemical deformation is not additive and it cannot be represented as a sum of deformations from different components. Therefore, the study of the compositional heterometry requires either a detailed study of composition/lattice constant relationships or measurement of lattice constants at different points of the crystal. Knowledge of the lattice constant distribution enables the calculation of the stress and stress induced distortions of the optical indicatrix.

As a rule, crystal composition changes abruptly at concentric zone, sector zone, sub-sector zone boundaries. Such discontinuities are evident optically.

Unlike thermoelastic stress, compositional heterometry-induced stress does not relax for most crystals, especially those grown at low temperature. It prevents plastic deformation. If the stress is too high, crystals usually relax by fracture.

The simplest case is the boundary between two layers or regions with different lattice constants. In a first approximation the stress tensor σ_i can be estimated from the generalized Hooke's law (see also Equations (2.4), (2.5) Nye, 1985; Shuvalov, 2005)

$$\sigma_i = c_{ij}\varepsilon_j \; i, j = 1, 2, \ldots 6, \tag{2.55}$$

where c_{ij} are the elastic stiffness constants and ε_j is the strain at the boundary. Tabulations of the elastic properties of minerals and synthetic compounds can be found in (Belikov, 1970; Landolt and Börnstein, 1979; Bass, 1995). Strain is calculated as the difference in lattice constants Δa, which lie in the plane of the boundary layer divided by the average value of the lattice constant $\varepsilon_j = \left(\Delta a / a\right)_j$. Expression (2.55) does not provide accurate values of the stress. Moreover, it does not give the stress distribution in the crystal volume. Rather it is simply a way to reliably estimate the stress on an isolated boundary.

2.8.2. Zoning

The main reasons for compositional heterometry and related optical anomalies are *concentric zoning* and *growth sector zoning*.

Layers or zones deposited at different times during crystal growth often have different compositions, especially when the composition of the growth medium is not constant. This results in a concentric distribution of compositions and lattice constants. Qualitative relationships between optical anomalies and compositional zoning were established for many compounds such as tourmaline, $Na(Al, Fe, Li, Mg, Mn)_3Al_6(Si_6O_{18})(BO_3)_3(OH, F)_4$ (Karnojitzky, 1891a), diamond (Varshavsky, 1968), beryl, $Be_3Al_2(SiO_3)_6$ (Graziani *et al.*, 1990), synthetic spinel, $MgAl_2O_4$ (Malinin *et al.*, 1973), synthetic garnets (see Appendix 1

for formulas and nomenclature) (Kitamura *et al*., 1986a,b) and germanium (Indenbom and Nikitenko, 1962) among others. However, a quantitative description of such optical anomalies has not been given.

Optical anomalies in crystals are typically observed in thin plates. Therefore, the general elastic problem reduces to the plane stress problem because normal components of the stress tensor are absent on free surfaces. Although the accurate calculation of internal stress is difficult because of complicated polygonal shapes of typical sections, corresponding elastic problems have been solved for most of the cases that can be geometrically well approximated. Mathematically these problems are very close to thermoelastic problems where the temperature plays the role of concentration and the thermal expansion coefficient stands in for the chemical deformation coefficient.

2.8.2.1. Plane zoning

Consider the thermoelastic stress in a rectangular beam of length L, thickness l, and width $2h$, so that $L >> l$ and $L >> 2h$ (Figure 2.19). The temperature is assumed to be only a function of coordinate $z(T = T(z))$. The solution of this one-dimensional problem in an isotropic approximation has been given (Boley and Weiner, 1960; Timoshenko and Goodier, 1982):

$$\begin{cases} \sigma_{zz} = \sigma_{xz} = 0 \\ \sigma_{xx} = \alpha E \left[\dfrac{1}{2h} \int\limits_{-h}^{h} T dz + \dfrac{3z}{2h^3} \int\limits_{-h}^{h} T z dz - T \right], \end{cases} \tag{2.56}$$

where α is the thermal expansion coefficient and E is Young's modulus. Replacing the continuous temperature distribution by a series of discrete zones with fixed temperatures we get in each zone:

$$\begin{cases} (\sigma_{zz})_j = (\sigma_{xz})_j = 0 \\ (\sigma_{xx})_j = \alpha E \left[\frac{1}{2h} \sum\limits_{i=1}^{N} T_i (z_i - z_{i-1}) + \dfrac{3z_j}{2h^3} \sum\limits_{i=1}^{N} T_i \dfrac{z_i^2 - z_{i-1}^2}{2} - T_j \right]. \end{cases}$$

Here, the subscript $j = 1, 2, \ldots, N$ donates the jth zone. The same subscript is used for z indicating the distance from $z = -h$ to the jth zone boundary ($j = 0$ for the lower edge of the beam and $j = N$ for the upper edge).

Replacing the temperature (T_i) with the lattice constant (a_i) gives an expression for the single non-zero stress component

$$(\sigma_{xx})_j = \frac{E}{a} \left[\frac{1}{2h} \sum_{i=1}^{N} a_i (z_i - z_{i-1}) + \frac{3z_j}{2h^3} \sum_{i=1}^{N} a_i \frac{z_i^2 - z_{i-1}^2}{2} - a_j \right] \tag{2.57}$$

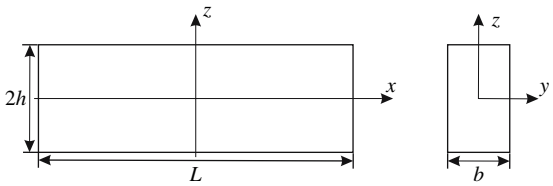

Figure 2.19. Geometry associated with the plane zoning problem

where a is the average value of the lattice constant. Elsen and Ettenberg (1978) treated heteroepitaxial films similarly. Their solution for zero crystal curvature gives the single non-zero stress component

$$(2.58) \qquad (\sigma_{xx})_j = \frac{E}{2h}\sum_{i=1}^{N} h_i \varepsilon_{ij} = \frac{E}{2h}\sum_{i=1}^{N} h_i \frac{a_i - a_j}{a}$$

where $h_i = z_i - z_{i-1}$ is the width of the ith zone. Equation (2.57) reduces to (2.58), if the second term, the crystal bending, is neglected. This simplified solution is also valid for the plates ($L \approx l, L >> 2h$) with $T = T(z)$. In this case, there are two non-zero stress components $\sigma_{xx} = \sigma_{yy} = \dfrac{\sigma'_{xx}}{1-\nu}$, with σ'_{xx} defined from Equation (2.56) or (2.57). For the calculation of optical anomalies we usually need to know the maximal shear stress calculated as $(\tau_{\max})_j = (\sigma_{xx})_j / 2$. With (2.58) we can compute the stress in massive crystals with plane zoning (thin, planar zones), whereas Equation (2.57) is applicable to crystals of acicular habit. The optical anomalies can be calculated from the stress distribution using the phenomenological description of piezooptic phenomena (see section 2.2). The isotropic approximation is adequate. Accounting for anisotropy is more accurate but also more cumbersome. Sirotin and Shaskolskaya (1982) have treated thermoelastic stress in the anisotropic plate.

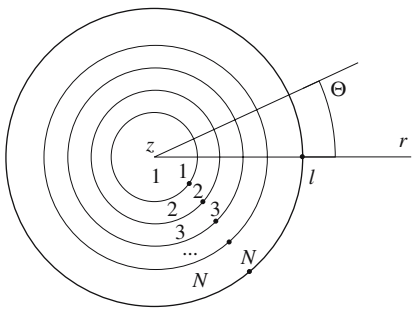

Figure 2.20. Geometry of the concentric zoning problem

2.8.2.2. Concentric zoning

Understanding heterometric stress in crystals with a concentric zoning begins with thermoelastic stress in a round plate. Given a plate of radius l and thickness $2h$, so that $l >> 2h$ (Figure 2.20) with temperature only a function of the crystal radius ($T = T(r)$), the plane stress ($\sigma_{zz} = \sigma_{rz} = \sigma_{\Theta z} = 0$) in a cylindrical frame is characterized by the following boundary conditions on the free cylindrical surfaces $\sigma_{rr} = 0$ at $r = l$. For isotropic media, the solution is given in (Boley and Weiner, 1960; Timoshenko and Goodier, 1982)

$$\begin{cases} \sigma_{rr} = \alpha E \left[\dfrac{1}{l^2} \int\limits_0^l Trdr - \dfrac{1}{r^2} \int\limits_0^r Trdr \right] \\ \sigma_{\Theta\Theta} = \alpha E \left[\dfrac{1}{l^2} \int\limits_0^l Trdr + \dfrac{1}{r^2} \int\limits_0^r Trdr - T \right] \\ \sigma_{r\Theta} = 0 \end{cases} \tag{2.59}$$

Once again, replacing the continuous temperature distribution with a discrete distribution, and associating with each temperature a lattice constant (a_i) we turn the integration into a summation:

$$\begin{cases} (\sigma_{rr})_j = \dfrac{E}{a} \left[\dfrac{1}{2l^2} \sum\limits_{i=1}^{N} a_i \left(r_i^2 - r_{i-1}^2 \right) - \dfrac{1}{2r_j^2} \sum\limits_{i=1}^{j} a_i \left(r_i^2 - r_{i-1}^2 \right) \right] \\ (\sigma_{\Theta\Theta})_j = \dfrac{E}{a} \left[\dfrac{1}{2l^2} \sum\limits_{i=1}^{N} a_i \left(r_i^2 - r_{i-1}^2 \right) + \dfrac{1}{2r_j^2} \sum\limits_{i=1}^{j} a_i \left(r_i^2 - r_{i-1}^2 \right) - a_j \right] \\ (\sigma_{r\Theta})_j = 0 \end{cases} \tag{2.60}$$

where $(\sigma)_j$ denotes stress in the jth zone at its outer jth boundary, and r_i is the radius of the outer boundary of the ith zone (Figure 2.20). For calculation of the optical anomalies the maximal shear stress is required:

$$(\tau_{\max})_j = \frac{(\sigma_{rr})_j - (\sigma_{\Theta\Theta})_j}{2} = \frac{E}{2a} \left[a_j - \frac{1}{r_j^2} \sum_{i=1}^{j} a_j \left(r_i^2 - r_{i-1}^2 \right) \right] \tag{2.61}$$

which can be transformed to the formula obtained in by Punin (1992)

$$(\tau_{\max})_j = \frac{E}{2} \sum_{i=0}^{j} \varepsilon_i \frac{r_i^2}{r_j^2} \tag{2.62}$$

where $\varepsilon_i = (a_i - a_{i-1})/a$ is the strain at the inner surface of the ith zone. The averaged value of $\tau_{\max}$ can be estimated by averaging $\tau_{\max}$ at inner and outer boundaries of the jth zone as it was carried out by Gorskaya *et al.* (1992)

$$(\tau_{\max})_j = \frac{E}{4} \sum_{i=1}^{j} \frac{a_i - a_{i-1}}{a} \left(\frac{r_{i-1}^2}{r_j^2} + \frac{r_{i-1}^2}{r_{j-1}^2} \right) (a_0 = a_1) \tag{2.63}$$

Transformation of the plane stress problem (thin round plate) to the plane deformation problem (long round cylinder) requires only the multipication of the stress components found from Equations (2.59)–(2.63) by the factor $1/(1-\nu)$ and the addition of a non-zero stress component $\sigma_{zz} = \sigma_{rr} + \sigma_{\Theta\Theta}$.

This problem is of great importance for the description of optical anomalies in crystals with concentric zoning. Although an ideal circular cross section rarely occurs, crystals frequently have more or less isometric habits and the shape is often close to circular. Crystals with prismatic or tabular habits can display isometric cross sections as well. Thus, the above approach is a good approximation for many real crystals. The isotropic approximation is usually sufficient for the calculation of stress. The anisotropic problem for the round and elliptical cylinders was solved by Sirotin (1956). Below we consider some examples of heterometry-induced optical anomalies.

2.8.2.3. Model system: potassium-ammonium dihydrogen phosphate

The theory developed above was verified by creating discrete, artificial zones in crystals of potassium-ammonium dihydrogen phosphate (Shtukenberg *et al*., 1994a,b). The internal stress in the crystals was calculated from the anomalous biaxiality and from the lattice constant distribution. The results were compared in order to analyze relationships between anomalous biaxiality and compositional, heterometry-induced stress.

Optical anomalies. Potassium dihydrogen phosphate (KDP) KH_2PO_4 and ammonium dihydrogen phosphate (ADP) $NH_4H_2PO_4$ are isomorphous crystals in the tetragonal system, space group $I\bar{4}2d$. They form a continuous series of solid solutions (Yasuhiro *et al*., 1987). The crystals exhibit the prism {100} and dipyramid {101} faces. The end members of the series are well-known for their anomalous biaxiality (Shamburov and Kucherova, 1966). The axial angle $2V$ can be as large as 30° in the prism sectors. It is usually smaller in the pyramid sectors Stepanova (1970). The optic axial plane usually displays four different orientations in the prism faces (the corresponding angles are 0°, 45°, 90°, and 135°. In {101} growth sectors, all four orientations are observed, whereas in {100} growth sectors only the first is observed (Fridman, 1972). As the axial angle increases from 0°, the orientation of the axial angle switches among the positions indicated (Belyustin and Stepanova, 1981). Both uniaxial and biaxial regions display distorted conoscopic figures (Leonova and Beskolova, 1977).

The value of the axial angle is proportional to the solution pH and inversely proportional to the growth temperature and solution storage time before the start of crystallization (Stepanova and Belyustin, 1975). On the other hand, the angle $2V$ is nearly independent of the impurity concentrations, growth rate, and the origin and size of the seed (Stepanova, 1970). DeYoreo and coworkers found that compositional heterogeneities cause spatial variations in the refractive index and induce a distortion of the transmitted-wave front, while groups of dislocations cause strain-induced birefringence leading to beam depolarization (De Yoreo and Rek, 1996). It is commonly assumed that anomalous biaxiality is induced by internal

stress related to the colloidal inclusions of Fe^{3+}, Cr^{3+}, and Al^{3+} phosphates. Suvorova and Chernov (1994) have argued that the internal stress is a consequence of the low-temperature, orthorhombic phase.

De Yoreo and coworkers (De Yoreo and Woods, 1993) also studied the effects of isotopes on anomalous birefringence. Crystals of the isotopomer of KDP, KD_2PO_4 (known sometimes as KD*P or DKDP) show significantly higher levels of strain. In a (0001) plate of $KD_{0.94}H_{0.6}PO_4$, the birefringence was most pronounced at the boundaries between growth sectors. Strain increases with the level of deuteration (Belouet *et al*., 1975; Belouet, 1980). Several sources of strain were identified including those associated with dislocations emanating from the seed cap, lattice mismatch strain (heterometry) as a consequence of trivalent cation impurities at the 10–100 ppm level (Petroff *et al*., 1975), as well as heterometry resulting from the fact that the cell parameters and orientations of the PO_4 tetrahedra in hydrogen rich and deuterium rich regions are measurably different (Nelmes *et al*., 1987). For such effects to manifest themselves, the segregation of the isotopes must exceed distances longer than the wavelength of the light. However, the segregation coefficient in the KDP-KD*P system is greater than one and therefore a diffusion profile will exist at the interface. Slight changes in growth conditions may affect this profile leading to the phase segregation.

Crystal growth and optical measurements. Crystals of KDP, ADP, and homogeneous mixed crystals (K,A)DP were grown from aqueous solutions while cooling from 35–24 °C. Sections 1.7–3.5 mm thick were cut from the crystals perpendicular to [001] and polished (Figure 2.21). The angle $2V$ was measured by Mallard's method (section 1.2). It was typically found to be small (1–1.5°) and invariant over the section area. The orientations of optic axial plane are both parallel and perpendicular to [100] and [010] in adjacent sectors. In crystals with two zones of different composition the angle $2V$ is usually higher, up to 3.5°. The orientations of optic axial plane are different but diagonal directions [110] are preferred (Figure 2.22*a*).

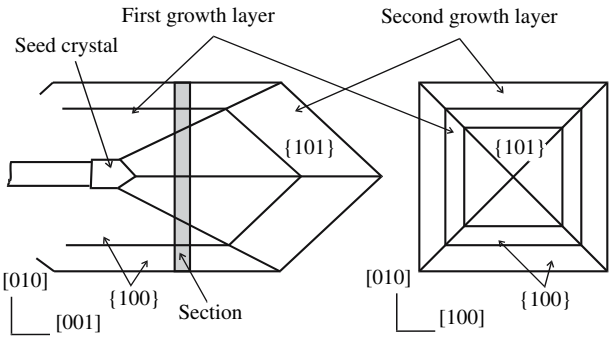

Figure 2.21. Morphology of $(K, NH_4)H_2PO_4$ plates used for the optical measurements. Sections of the crystal in the (100) (left) and (001) (right) planes

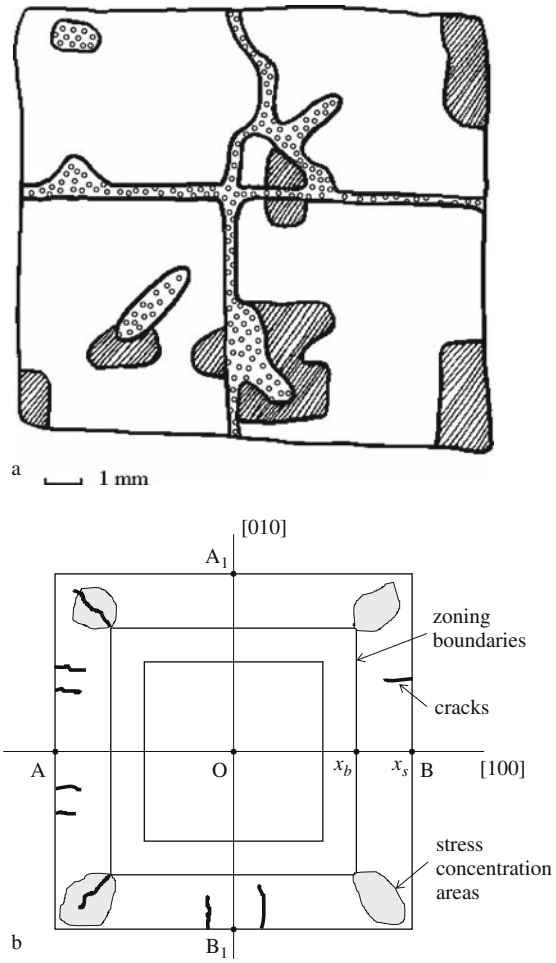

Figure 2.22. (*a*) Orientation of isoclinic fringes in $(K, NH_4)H_2PO_4$. Circles: isoclines are parallel (perpendicular) to corresponding {100} faces. Blank field: isoclines form an angle of 45° to < 100 >. Skew hatching: other orientations of isoclines. (*b*) The preferred crack orientations and fields of stress concentrations in the same section. The smallest square denotes the sector zone boundary

Slight birefringence in (001) sections is visible under orthoscopic examination. It is most pronounced around inclusions, cracks, and in the outer zone near the crystal corners (Figure 2.22*b*). Sometimes the thin zoning with alternation of Z' and X' orientations can be detected as well. These observations suggest that internal stress is the main cause of optical anomalies in (K,A)DP solid solutions.

Internal stress calculated from optical data. Optical measurements on (001) sections give the axial angle $2V_\alpha$, and the orientation φ of the vibration directions with respect to x_1 and x_2 of the physical coordinate frame. According to Equations (2.21)

and (2.26), and taking into account the crystal symmetry (point group $\bar{4}2m$), these values are expressed through the stress tensor components as follows:

$$\tan V_\alpha = \frac{\sqrt[4]{(2\pi_{66}\sigma_6)^2 + ((\pi_{11}-\pi_{12})(\sigma_1-\sigma_2))^2}}{\sqrt{\varepsilon^{-2}-\omega^{-2}}} \tag{2.64}$$

$$\tan 2\varphi = \frac{2\pi_{66}\sigma_6}{(\pi_{11}-\pi_{12})(\sigma_1-\sigma_2)}. \tag{2.65}$$

Simultaneous solution of these Equations with respect to $\sigma_1 - \sigma_2$ and σ_6 gives the value and orientation of the quasi-principal stress components $\sigma_{(1)}$ and $\sigma_{(2)}$, in other words, the principal components of two-dimensional stress tensor. The cumbersome expression obtained can be substantially simplified if the stress is calculated only along the coordinate axes (x_1 and x_2) through the crystal center

$$2\tau_{\max} = \sigma_{(1)} - \sigma_{(2)} = \frac{n_\varepsilon^{-2} - n_\omega^{-2}}{\pi_{11}-\pi_{12}} \tan^2 V_\alpha \approx \frac{2(n_\omega - n_\varepsilon) V_\alpha^2}{n_o^3 (\pi_{11}-\pi_{12})} \tag{2.66}$$

($\tan^2 V \approx V^2$ for small angles $V = 0-2°$). The angle φ in this case is obviously zero.

The maximal shear stress was calculated for the measured values of the axial angle for the points approximately along the "radii" OA, OB, OA_1 and OB_1 (Figure 2.22*b*).

Internal stress as calculated from the lattice constant. The lattice constants were measured for separate zones of the crystal by powder x-ray diffraction.

The sections studied are thin enough that they are assumed to be under plane stress. They are squares with two zones of different composition. Although the quantitative evaluation of the stress is rather complicated in this case, qualitatively the crystals (Figure 2.22) can be compared with a quenched, tetragonal glass plate (the same geometry of the sample but with a continuous distribution of the thermoplastic stress (Figure 2.23 Lebedev, 1937)). This comparison shows the satisfactory correspondence of the orientations of isoclinic (null) fringes, and loci of equivalent optic axial plane orientations with respect to crystal edges.

The simple quantitative stress calculation is possible only for lines AB going through the crystal center and midpoints of the crystal faces. For this case the model of concentric zoning predicts the following expressions for the maximal shear stress:

$$\begin{cases} 2\tau_{\max} = \dfrac{\Delta a}{a} c_{11} \dfrac{x_b^2}{x^2} & x_b \le x \le x_s, \\ 2\tau_{\max} = 0 & 0 \le x < x_b \end{cases} \tag{2.67}$$

where x is the distance from the crystal center to the given point, x_b is the distance from the crystal center to the zone boundary, x_s is the distance from the crystal center to the outer boundary of crystal (points A and B) and c_{11} is the elastic stiffness constant (Figure 2.22*b*). The results of calculations for one crystal are shown in Figure 2.24.

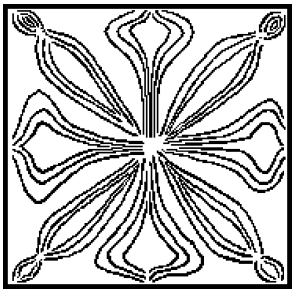

Figure 2.23. Orientation of isoclinic fringes in tetragonal quenched glass plate (after Lebedev, 1937)

Discussion. Weak anomalous biaxiality, a property of homogeneous (K,A)DP crystals, seems to be related to colloidal inclusions. The maximal shear stress calculated from the 2V angle is $\sim 6.2 \cdot 10^6\ \mathrm{N \cdot m^{-2}}$. This level of stress can be taken as a background and subtracted from the additional stress calculated from lattice mismatch. Data analysis shows the following:

1. The absolute values of observed and calculated stresses agree with one another. Larger stresses are likely related to deviations from the plane stress state since the sections are relatively thick.
2. The observed orientation of the optic axial plane in the outer zone corresponds to theoretical predictions. This is confirmed by the comparison with the quenched glass plate (see above) as well as by the crack distributions that reflect the compressive-tensile directions (Figure 2.22*b*).
3. The theory of concentric zoning predicts a zero shear stress in the inner zone of the crystal. This contradicts the experimental observations of strong shear stress in the inner zone reflecting the approximate nature of our model that does not account for deviations of the section from the circular ideal, deviations from the

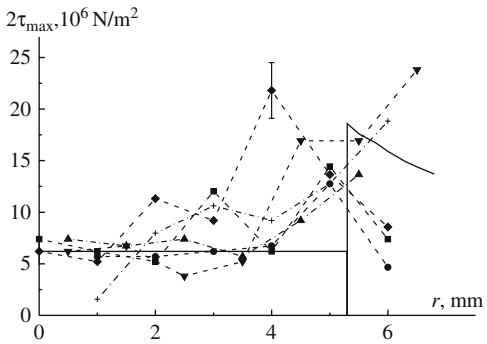

Figure 2.24. Experimental (dashed lines) and calculated (solid line) values of maximal shear stress in $(K, NH_4)H_2PO_4$. Symbols correspond to profiles OA, OB, OA_1 and OB_1 indicated in Figure 2.22b. Horizontal line corresponds to the "background" stress, vertical line denotes the zone boundary

plane stress state as a consequence of sector zoning-induced inhomogeneities in the distribution of lattice constants within one growth zone (Figure 2.22*b*), or deviations from partial stress relaxation associated with cracks or dislocations. This conclusion is supported by the fact that the optic axial plane rotates by 90° at the zoning boundary suggesting a change of the stress sign.

To verify the elastic nature of the anomalous biaxiality, a piece of the outer zone was cut out along the zoning boundary. The stress calculated from the biaxial angle was reduced by a third from $1.9 \cdot 10^7$ N · m^{-2} to $6.7 \cdot 10^6$ N · m^{-2} before and after cutting, respectively. This also confirms that the observed anomalous biaxiality in (K,A)DP crystals originates from the compositional heterometry-induced stress.

2.8.2.4. Grossular-andradite garnets

Grossular-andradite garnets (grandites, see Appendix 1 for garnet nomenclature, $Ca_3(Al, Fe)_2(SiO_4)_3$, cubic space group $Ia\bar{3}d$) are widespread in skarns (calc-silicate deposits) and some types of metamorphic rocks. They usually display a strong inhomogeneity in Fe/Al distribution. Compositional heterometry-induced stress and optical anomalies are common. (Growth desymmetrization is another source of optical anomalies described in Chapter 3). We studied a series of garnets of a composition $(Ca_{2.9–3.0}Mn_{0.00–0.02}Mg_{0.00–0.06})^{VIII}(Al_{0.0–2.0}Fe_{0.0–2.0}Ti_{0.0–0.11})^{VI}(SiO_4)_3$ from limestone skarns in western Mali (Ivanova *et al*., 1998; Shtukenberg *et al*., 2001a) that were kindly provided by P.B. Sokolov. Crystals of good quality had the forms of rhombic dodecahedra 0.5–7 cm in diameter. Most of the crystals had coarse concentric zones (hundreds of microns) distinguished by color and chemical composition. Oscillations were easily discerned in thick zones. Zone boundaries were identified by the Becke line, the refractive index contrast at zone boundaries.

Figure 2.25 shows the anomalous birefringence at different points of the garnet cross section cut parallel to the (001) plane measured with a Berek compensator. Growth sector zoning is distinct.

The stress birefringence was calculated from compositional variation between different zones. Concentrations of the chemical elements were determined at points on the crystal surface (Figure 2.26) with an electron microprobe.

The lattice constants were calculated in accord with the regression Equation (Novak and Gibbs, 1971)

$$a = 9.04 + 1.61\mathrm{R}^{\mathrm{VIII}} + 1.89\mathrm{R}^{\mathrm{VI}},$$

where $\mathrm{R}^{\mathrm{VIII}} = \dfrac{\sum_i \mathrm{R}_i{}^{\mathrm{VIII}} m_i}{\sum_i m_i}$, $\mathrm{R}^{\mathrm{VI}} = \dfrac{\sum_k \mathrm{R}_k{}^{\mathrm{VI}} m_k}{\sum_k m_k}$, and ionic radii $\mathrm{R}_i{}^{\mathrm{VIII}}$ and $\mathrm{R}_k{}^{\mathrm{VI}}$ were taken from (Shannon, 1976). The regression Equation was verified by comparison of calculated lattice constants with the values measured by powder diffraction. The maximal shear stress was calculated using the concentric zoning model (Equation (2.63), Figure 2.26). The birefringence was calculated for the profiles

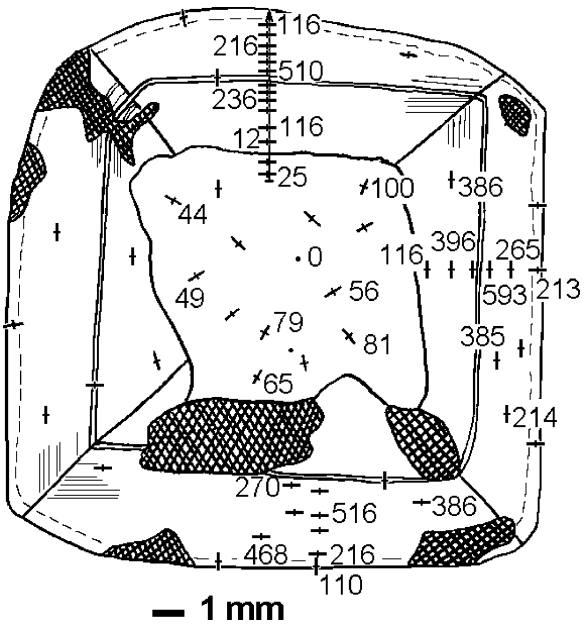

Figure 2.25. Anatomy of (001) garnet cross section. Crosses depict the vibration directions. The numbers represent birefringence $\times 10^{-6}$. Hatched fields correspond to inclusions. The main part of the section consists of the four growth sectors of a rhombic dodecahedron {110}. A fifth {110} growth sector is located in the inner part of the section and is characterized by chaotic orientations of vibration directions (a radial predisposition of Z' is nevertheless observed). Microprobe analysis was carried out along the vertical arrow in the upper sector

located along $< 110 >$ directions in the plane of (001) cross section from the formula

$$(\Delta n)_j = n_0^3 \pi_{44} (\tau_{\max})_j \,. \tag{2.68}$$

We used the piezo-optic coefficient $0.5 \cdot 10^{-12}$ m^2N^{-1} of synthetic garnets (Landolt and Börnstein, 1979).

The agreement between the measured and calculated distribution of birefringence is evident (Figure 2.26). Slightly higher values of calculated birefringence can be explained by brittle and plastic relaxation as evidenced by cracks and high dislocation density detected by x-ray diffraction topography, respectively.

An additional argument in favor of heterometry-induced stress is an alternation of zoning with mutually perpendicular Z' and X' orientations interpreted as an alternation of compressive and tensile stress in the neighboring zones (Figure 2.27). High internal stress is also confirmed by the presence of regular systems of cracks usually confined in zones (Figure 2.28).

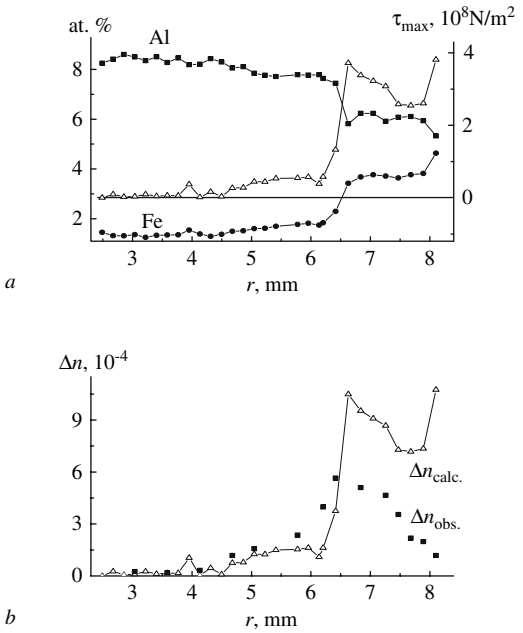

Figure 2.26. Compositional heterometry and anomalous birefringence in garnet as measured along the arrow in Figure 2.25. (*a*) Measured values of Al and Fe concentrations (solid symbols) and maximal shear stress (open symbols); (*b*) calculated (open symbols) and observed (solid symbols) birefringence

2.8.2.5. Polychrome tourmalines

Anomalous biaxiality of tourmalines (trigonal space group $R3m$) was studied in the Nineteeth Century (Karnojitzky, 1891a; Brauns, 1891). Tourmalines have complex compositions. They are characterized by isomorphous replacement at four different sites and can be described by a general formula $XY_3Z_6(BO_3)_3Si_6O_{18}(O, OH, F)_4$, X = Ca, Na, K; Y = Al, Li, Fe^{2+}, Mg, Mn; Z = Al, Cr, Fe^{3+}, V. Polychrome tourmalines are often inhomogeneous. Heterometry gives rise to internal stress-induced optical anomalies in turn.

Tourmaline crystals from rare-metal pegmatites, course grained igneous formations located in the Ural mountains and Transbaikalia region of Russia, are formed by four main minerals: elbaite, olenite, tsilaisite and schorl having the general formula $Na(Al, Li, Fe, Mn)_3Al_6(BO_3)_3Si_6O_{18}(O, OH, F)_4$. The crystals reveal complex concentric zoning and growth sector zoning manifest in composition variation, anomalous birefringence, and growth defect distributions. A typical (0001) section is shown in Figure 2.29. The optic axial planes were found to have regular orientations with respect to concentric zone and growth sector boundaries. The axial angle reaching 6° varies over the cross section (Figure 2.30). The lattice constants were measured for different zones by powder x-ray diffraction (Figure 2.30). The values are in agreement with the chemical composition

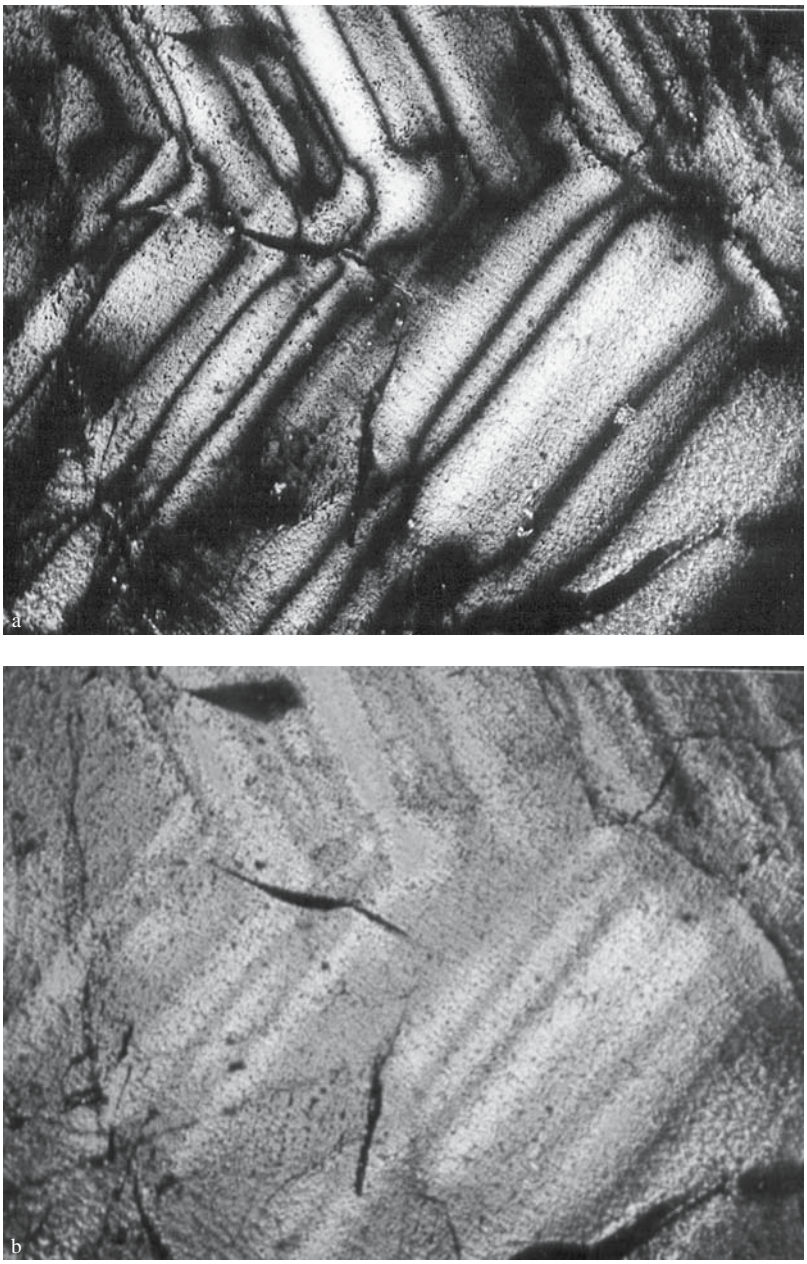

Figure 2.27. (*a*) Photomicrograph of grossular-andradite garnet between crossed polarizers with alternation of Z' and X' orientations between the neighboring zones. Boundaries between zones in two adjacent {211} growth sectors seen as narrow black lines. (*b*) The same picture taken with a first order red retarder. Picture size = 0.44 mm. Sample kindly provided by P.B. Sokolov (see Color Section following page 254)

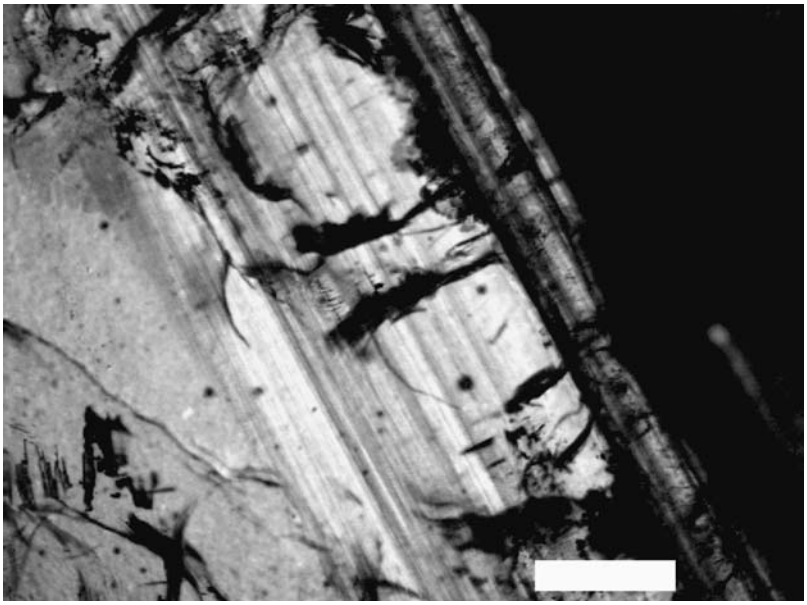

Figure 2.28. Photomicrograph of grossular-andradite garnet in polarized light (no analyzer inserted) with zones visible by color. At the boundaries of outer darker zones, regular systems of cracks appear. These cracks caused by compositional heterometry-induced stress are directed either normal or diagonal to the growth front and run well into the crystal. Scale bar = 0.88 mm. Sample kindly provided by P.B. Sokolov (see Color Section following page 254)

determined for some zones by electron microprobe analysis. Assuming a circular section and using the plane stress approximation, the stress distribution can be calculated from the varying lattice constant a and the concentric zoning model (see Equation (2.63)). For such a section $2\tau_{\max} = \sigma_{(1)} - \sigma_{(2)} = \dfrac{n_\varepsilon^{-2} - n_\omega^{-2}}{\pi_{11} - \pi_{12}} \tan^2 V_\alpha \approx \dfrac{2(n_\omega - n_\varepsilon)V_\alpha^2}{n_\omega^3(\pi_{11} - \pi_{12})}$, therefore, the calculated maximal shear stress $2\tau_{\max}$ should be proportional to the experimentally determined value $(2V)^2$ (Figure 2.30). In reality, the qualitative correspondence between these values is good. However, using the experimental value $\dfrac{n_\omega^3(\pi_{11} - \pi_{12})}{2(n_\omega - n_\varepsilon)}$ we predict $2.35 \cdot 10^{-10}\,\mathrm{m^2N^{-1}}$ (Gorskaya *et al.*, 1992), a smaller axial angle than calculated. This difference can be accounted for by brittle relaxation (Figure 2.29). The crack distribution agrees with orientation of the tensile stress (cf. Figure 2.29 and Figure 2.30). Small crystals without cracks show a greater correspondence with theory.

2.8.2.6. Beryl

Optical anomalies. The anomalous biaxiality of beryl also has a long history (Tschermak, 1884; Karnojitzky, 1891b; Brauns, 1891; Zemyatchensky, 1900). The

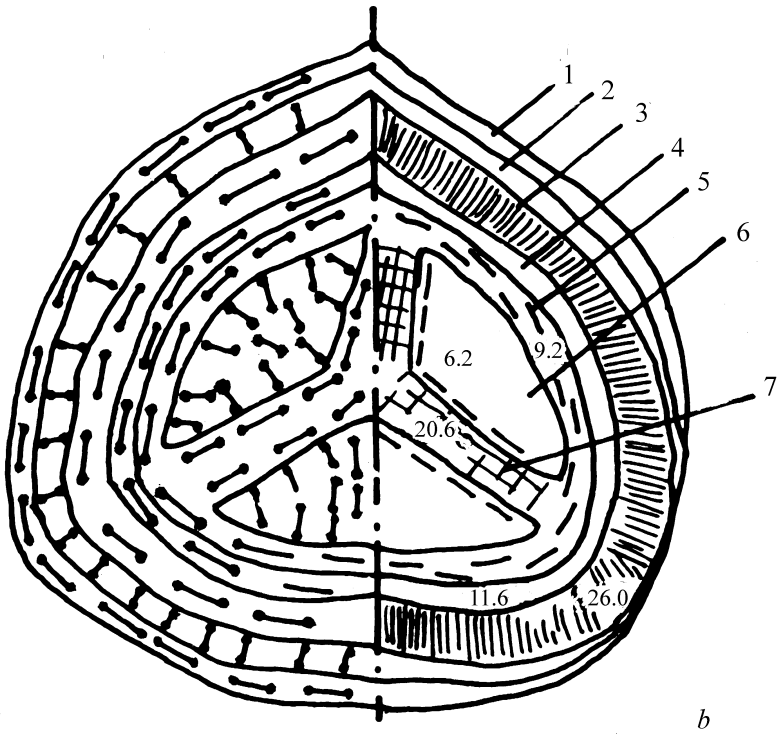

Figure 2.29. (*a*) Orientation of the optic axial plane and (*b*) preferable crack orientations in a zoned (0001) polychrome tourmaline section (after Gorskaya *et al*., 1992). The cracking coefficient (cracks per unit volume) is shown for the inner zones. Zones are numbered at right

axial value varies from 0–18° (Scandale *et al*., 1984), and can reach 26° (Vardanyants, 1941). Optical concentric and growth sector zoning (see e.g. Figure 2.31 and Figure 2.32) is evident. Pinacoid growth sectors observed in the centers of (0001) sections are optically isotropic, whereas the prism growth sectors are biaxial with the optic axial plane usually perpendicular or parallel to the growth front, though frequently not so oriented (Figure 2.31); sometimes even wavy extinction is observed (Zemyatchensky, 1900). The central part of the crystal can be optically biaxial, consisting of irregular spots with different orientations of the optic axial plane and axial angles (Zemyatchensky, 1900).

The following hypotheses have been put forward to account for optical anomalies in beryl:

1. Inhomogeneous, ordered distribution of impurities over the crystallographic sites reduces symmetry and creates optical anomalies (this theme is more fully explored in Chapter 3). N. Yu. Ikornikova (1939) confirmed this hypothesis with Laue images taken along [0001] direction, a rare instance where early x-ray studies did indeed predict anomalous birefringence. Although the patterns have

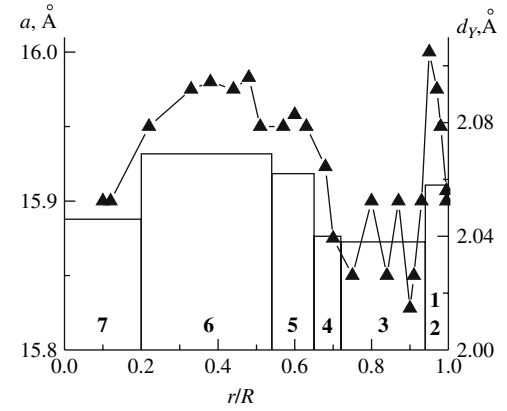

a

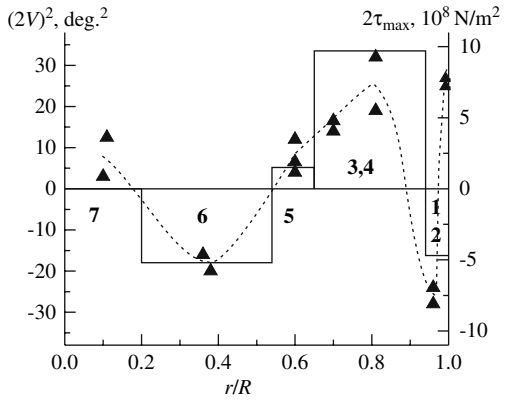

b

Figure 2.30. (*a*) Heterometry-induced stress in a polychrome tourmaline cross section. r/R is the normalized radial distance. The numbers identify zones in Figure 2.29 (after Gorskaya *et al*., 1992). The lattice constants a in each zone are the horizontal line segments. The cation-oxygen bond length d_Y, calculated from microprobe analysis, are represented by connected triangles. (*b*) Internal stress. The value of $(2V)^2$ = triangles connected by a dashed line; maximal shear stress $2\tau_{max}$ = solid line. The values of $(2V)^2$ were positive if the optic axial plane was parallel to the zone boundary and negative if it was perpendicular to the zone boundary

identical arrangements in different part of the crystal, Bragg peaks can show variable shape and size breaking the hexagonal symmetry (Figure 2.32). Two of six $33\bar{6}1$ reflections are elliptical, the others irregular; two of six $60\bar{6}1$ reflections are round, the others elliptical. In the biaxial zone, the asymmetry manifests itself not only in the spot shapes but also in their sizes. Unfortunately, the Laue spots are affected by the crystal shape and imperfections rendering judgment less equivocal than we might hope.

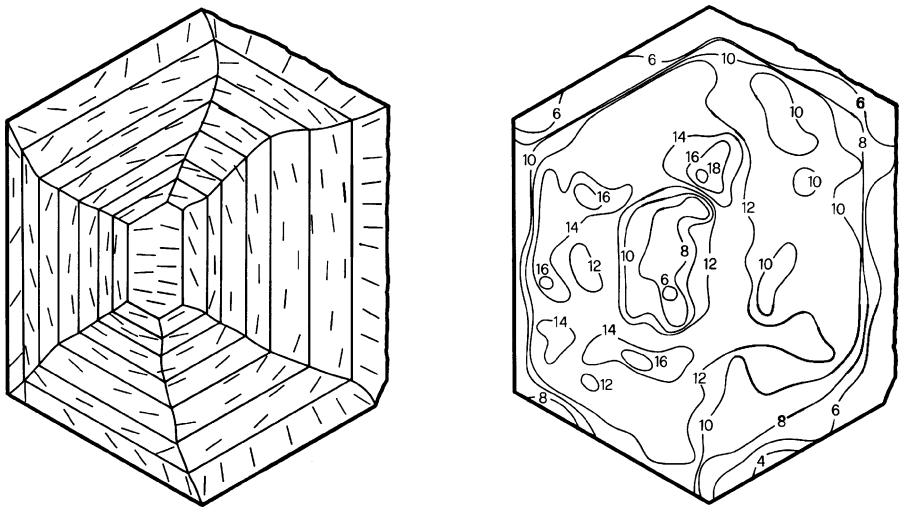

Figure 2.31. Orientation of the optic axial plane (short lines) and values of 2*V* angles (isolines with numbers) for the (0001) section of beryl. After (Graziani *et al*., 1990) with kind permission of Springer Science and Business Media

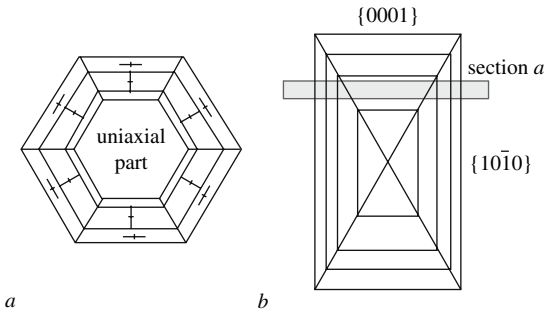

Figure 2.32. The anatomy of beryl. (*a*) (0001) section, (*b*) section parallel to [0001]. Crosses indicate orientation of the optic axial planes

2. As suggested by Scandale *et al*. (1984), the optical anomalies result from heterometry-induced stress. This hypothesis embraces all experimental observations. The inner part of the (0001) section is uniaxial, since only one thin, relative homogeneous zone of a (0001) growth sector appears in the field of view (Figure 2.32). In the rim with zone boundaries perpendicular to the section, the optic axial plane is perpendicular or parallel to the growth front depending on the stress sign. Growth sector zoning stress is added to that from concentric zoning complicating the optical pattern.

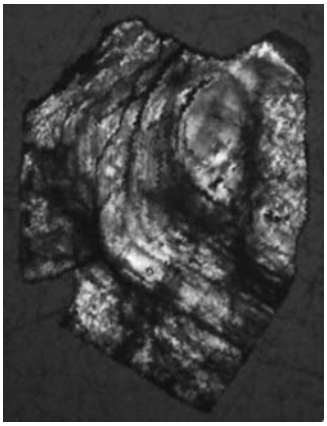

Figure 2.33. Anomalous birefringence in (0001) section of beryl, schematically shown in Figure 2.34. Birefringence changes at zone boundaries and cracks are visible (see Color Section following page 254)

Sample and optical measurements. Beryl crystals, described by Barabanov *et al*. (1975) and kindly supplied by him, from the quartz-topaz-ferberite vein at Schorl mountain, Transbaikalia, Russia with the general formula $(Be_{2.94-2.98}K_{0.01}Na_{0.01-0.02}Ca_{0.00-0.03})_3(Al_{1.95-1.98}Mg_{0.01-0.03}Fe^{3+}{}_{0.00-0.01})_2(Si_{5.93-5.97}Al_{0.02-0.05})_6(O_{17.83-17.87}OH_{0.17-0.13})_{18}$ (Li fraction in Be sites < 0.0025) were green-blue hexagonal prisms $\{10\bar{1}0\}$ with a few main concentric zones (1–5 mm thick). The outer cloudy, fissured zone is separated from the inner part by a crack. Numerous thin (< 0.1 mm) zones can be distinguished by changes of refractive index (Becke line relief).

The orientation of the optic axial plane φ and $2V$ were measured in a polished, 4 mm thick (0001) plate (Figure 2.33). The remainder of the crystal was used for lattice constant measurements (Figure 2.34).

Calculation of optical anomalies from the lattice constants. The calculation was carried out for a crystal well described within the concentric zoning model (diameter $>>$ thickness, circular shape). To calculate the heterometry-induced stress we need only the lattice constant a measured by powder diffraction. The maximal shear stress was calculated from Equation (2.63). The axial angle was calculated using (2.28). It follows from the symmetry that the optic axial plane always coincides with the orientation of the principal shear stress.

Results. Figure 2.35 shows that the calculated value of the axial angle is close to that measured, but the distribution of $2V$ does not always correspond to the observed optical pattern. At the same time, the observed orientation of the optic axial plane agrees with that calculated in most cases. Thus, the compositional heterometry-induced stress seems to be the main reason for the anomalous biaxiality in this beryl crystal. The reason for the observed disagreement in $2V$ values is likely to the conditional nature of the zone differentiation. Since the powder diffraction

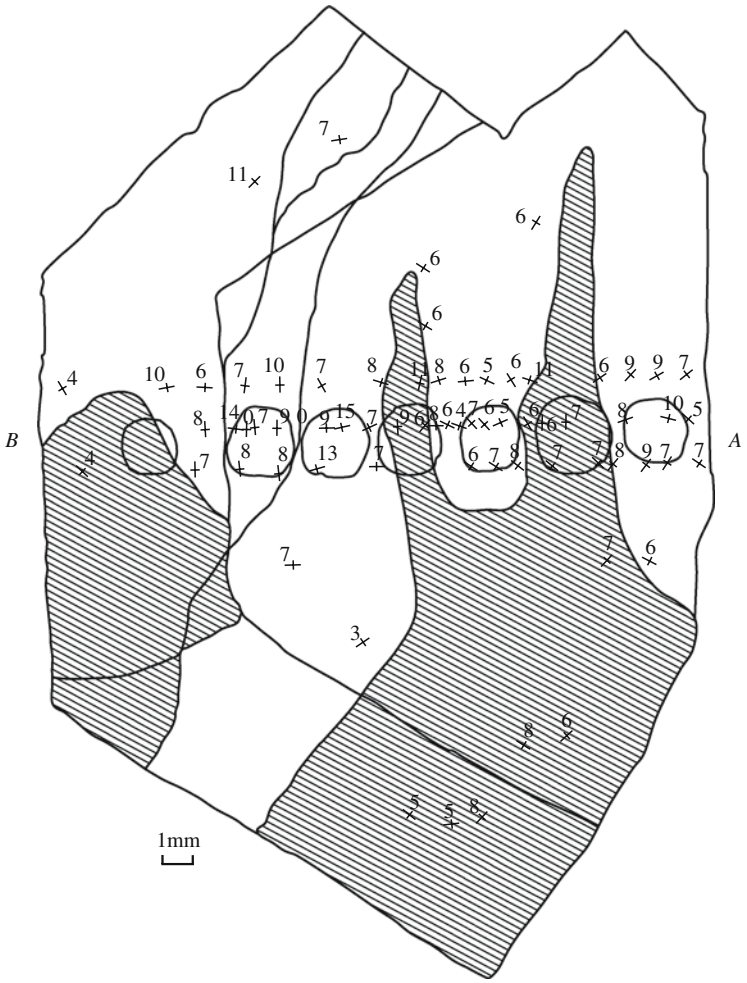

Figure 2.34. The measured values of axial angle $2V$ (numbers) and optic axial planes (long segments of crosses) in beryl (Figure 2.33). Circles depict the areas where the lattice constants were measured. The line AB is directed along $[10\bar{1}0]$, φ was measured between the optic axial plane and AB. Hatching denotes the areas with inclusions; thick lines correspond to cracks

analysis requires relatively large samples, measured "points" are relatively large (Figure 2.34) and may include several compositional zones.

2.8.3. Growth Sector Zoning

A polyhedral crystal nucleated at some internal point whose habit was constant during growth may be divided into a number of growth sectors or growth pyramids, sub-volumes each corresponding to growth through a particular

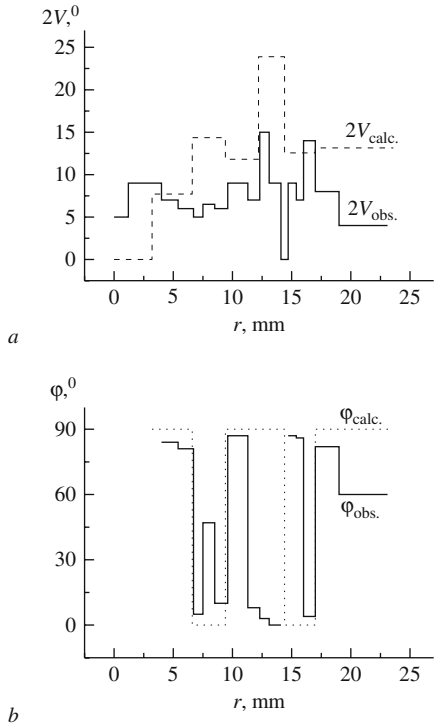

Figure 2.35. (*a*) Calculated and measured values of $2V$ and (*b*) of optic axial plane φ along AB in Figure 2.34. φ is the angle between $[10\bar{1}0]$ and the optic axial plane (orientation of X' in the (0001) section)

facet of the polyhedron. These pyramids are co-joined at the nucleation point (Figures 2.36, 2.37). Symmetry independent faces have different structures. They will have distinct selectivities for impurities and additives. This leads to differences in lattice constants (compositional heterometry) and to internal stress accompanied by optical anomalies whose spatial distribution will be bounded by the growth sectors. Sector specific stress in yttrium aluminum garnet (Chernov, 1984) is a good illustration to this type of optical anomaly. Optical sector zoning as a consequence of sector specific stress is common in crystals of minerals and synthetic crystals grown from solution and from the melt but may have also other etiologies as will be shown below.

2.8.3.1. Stress calculation

Complex geometries complicate the calculation of sector zoning stress as compared with concentric zoning stress. Stress at the sector zoning boundary can be roughly approximated with (2.55) but this Equation provides no information about the stress distribution. A proper calculation needs to account for free surface relaxation (stress tensor components normal to the crystal surface should be zero) but according

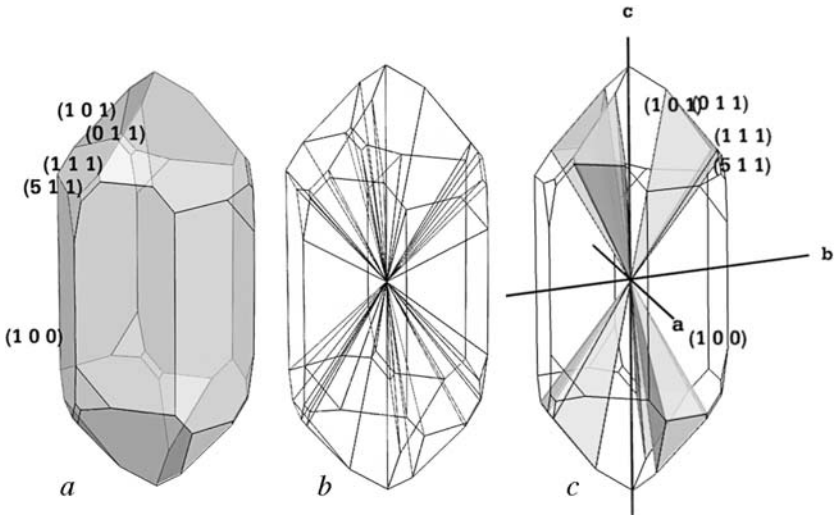

Figure 2.36. (*a*) Quartz crystal habit. (*b*) Same as (*a*) with all of the growth sectors delineated. (*c*) (011) growth pyramids only shaded. Illustration made with WinXMorph (Kaminsky, 2005)
Source: Figure courtesy of Professor Werner Kaminsky, Department of Chemistry, University of Washington.

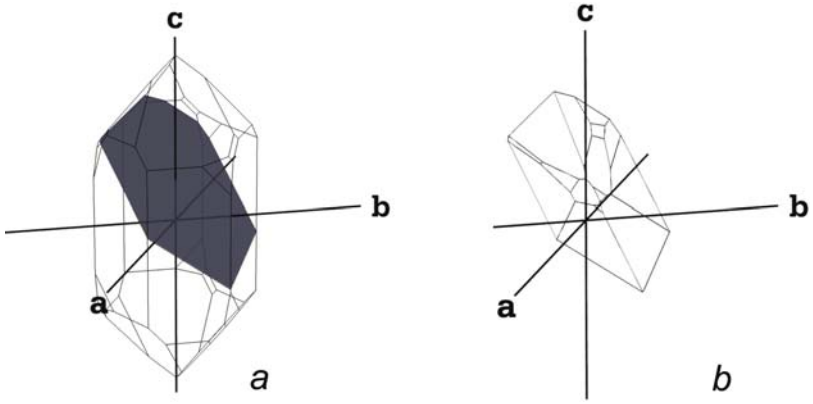

Figure 2.37. (*a*) Quartz habit with (123) slice shaded in gray. (*b*) Slice with cross sections of growth sectors delineated
Source: Figure courtesy of Professor Werner Kaminsky, Department of Chemistry, University of Washington.

Indenbom (1964), Indenbom and Kroupa (1979), and Härtwig (1981) the free surface relaxation decreases rapidly inside the crystal and can be often neglected. The stress in the crystal volume far from the free surface can be calculated using the model of plane dislocation ensembles. Consider a growth sector in the infinite two-dimensional crystal bounded by lines OA = OB = R with the internal angle

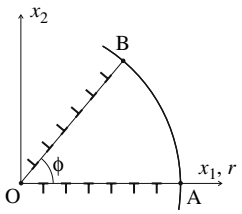

Figure 2.38. Representaion of sector boundaries by plane dislocation ensembles

ϕ (Figure 2.38). The substance inside and outside the sector has different lattice constants leading to strain and stress. The sector zoning boundary can be considered a plane dislocation ensemble (slip line) with the Burgers vector b and dislocation separation d, so that the strain is equal to $\varepsilon = \dfrac{a_2 - a_1}{a_1} = \dfrac{b}{d}$, with a_1 and a_2 the lattice constants in the neighborhood of the growth sectors. Dislocations in ensembles A and B have opposite signs. The stress field of these dislocation ensembles can be found from expressions (2.52)–(2.54) keeping in mind the boundary conditions $A_1 = 0$ and $A_2 = R$. For each ensemble the stress tensor is calculated in the Cartesian coordinate frame. It should be transformed into the polar coordinate frame where the stress fields are summed. The resulting components of the stress tensor are equal to $\sigma_j(r, \theta) = \sigma_j^A(r, \theta) - \sigma_j^B(r, \theta - \phi)$ $j = rr, \theta\theta, r\theta$. The solution ignores stress relaxation at the crystal surface. It is meaningless near the points A and B but is a reasonable approximation near the apex of the growth sector where the condition $r << R$ holds. The stress distribution in the growth sector, which has a larger lattice constant than the rest of the crystal and which has an internal angle $\phi = 50°$ is shown in Figure 2.39. As expected, the sector acts as a wedge tearing the crystal. The stress concentration at the sector apex O follows the logarithmic law.

2.8.3.2. Some examples

Reliable examples of optical anomalies related to sector zoning stress are few. This statement should not imply that such anomalies are not common. Rather, such anomalies are difficult to be distinguish from the stronger growth sector zoning related to growth ordering of structural units (see Chapter 3).

Pentaerythritol. Crystals of pentaerytrithol, $C(CH_2OH)_4$ (tetragonal crystal class $\bar{4}$) grown from low-temperature aqueous solutions usually contain impurities of other organic substances like dipentaerythritol and *ortho*-phthalic acid. Inhomogeneous distribution of impurities throughout the crystal produces zoning and sector zoning, heterometry-induced stress and anomalous biaxiality (Punin *et al*., 1986; Punin, 1992). Figure 2.40 shows the orientation of optic axial planes and values of the angle $2V$ in the growth sector boundaries. Qualitatively, the stress distribution corresponds to that calculated theoretically (Figure 2.39), however, the maximal shear stress found from the anomalous biaxiality is approximately ten times less than the stress calculated from the lattice constant distribution. This discrepancy is

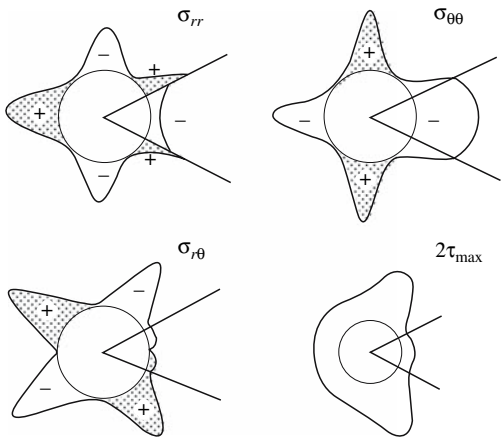

Figure 2.39. Stress distribution in sector zoned crystal, schematically shown in Figure 2.38. The corner angle ϕ is equal to 50°; the calculation was performed for $r/R = 0.01$

likely related to strong plastic relaxation of the elastic stress, since the pentaerythritol crystals reveal a high degree of plasticity even at room temperature, and dislocation densities can reach $2 \cdot 10^4\,\mathrm{cm}^{-2}$ (Punin *et al*., 1986).

Alum. Solid solutions of alum crystals grown from aqueous solutions often display complicated compositional zoning and growth sector zoning leading to anomalous birefringence (Brauns, 1891; Shtukenberg *et al*., 1994b; Crundwell, 1997; Shtukenebrg *et al*, 2001b). As will be shown below, the main part of the birefringence results from the growth ordering of atoms (see Chapter 3). After annealing, the optical anomalies of this type vanish completely and the stress birefringence becomes visible. For example, the cube growth sector {100} of the crystal $(K, NH_4)Al(SO_4)_2 \cdot 12H_2O$ (Figure 2.41) is slightly enriched by ammonium ions compared with the neighboring {111} octahedral sector having a smaller lattice constant. The anomalous birefringence is concentrated at the kinks of the sector boundary (B). Figure 2.41 also shows a crack (F) formed during the crystal growth. In the (111) growth sector between the crack and sector boundary the birefringence is distributed more or less homogeneously. At the same time, it is nearly absent outside this region. As expected, the stress field does not spread across the crack. In Figure 2.41, thin zones alternate with varying optical characteristics. These fine zones were formed by different growth step sources and, therefore, they probably have a different composition resulting in the stress birefringence (Shtukenberg *et al*., 2001b).

Tourmaline. The tourmaline crystal shown in Figure 2.29 has two inner parts 6 and 7 of different composition from growth sectors $\{10\bar{1}1\}$ and $\{02\bar{2}1\}$, respectively. The lattice constants a in these sectors and in the neighboring $\{10\bar{1}0\}$ growth sectors are shown in Figure 2.30*a*. The calculated values of maximal shear stress are shown in Figure 2.30*b*. The changes of the axial angle as well as of the optic axial plane

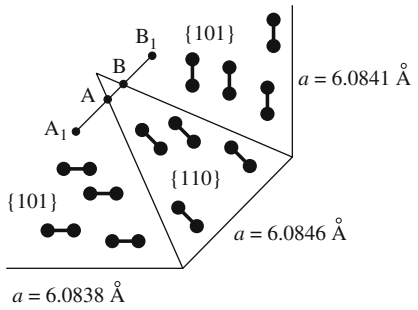

a

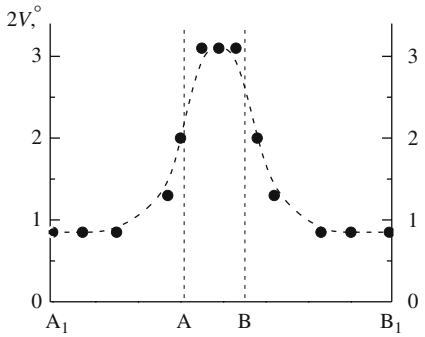

b

Figure 2.40. (*a*) Orientation of the optic axial planes in (001) cleavage section of pentaerythritol. The accuracy of the lattice constant *a* is 0.0003 Å. (*b*) The value of the optic angle as measured along the line A_1ABB_1

along the sector zoning boundaries (Figure 2.30*a*) were found to agree with the maximal shear stress calculated from the lattice constants and observed in the crack distribution (Figure 2.30*b*).

2.8.4. Sub-Sector Zoning

Surfaces of crystals grown at lower supersaturation often propagate through dislocations that produce growth spirals or hillocks, shallow stepped pyramids with single or multiple dislocations at the apex. Polygonization of hillocks partitions faces into vicinal regions, each having slightly different inclinations. Impurity partitioning among vicinal slopes, *intrasectoral zoning* or *sub-sector zoning*, results from the selective interactions of impurities with particular stepped hillock slopes. Sub-sector compositional inhomogeneity is a consequence of tangential selectivity (section 3.3.2). Other mechanisms that can lead to impurity partitioning within a single growth sector include high index microfaceting approximating a flat surface, and minor crystallite twinning leading to slightly mis-oriented blocks or domains.

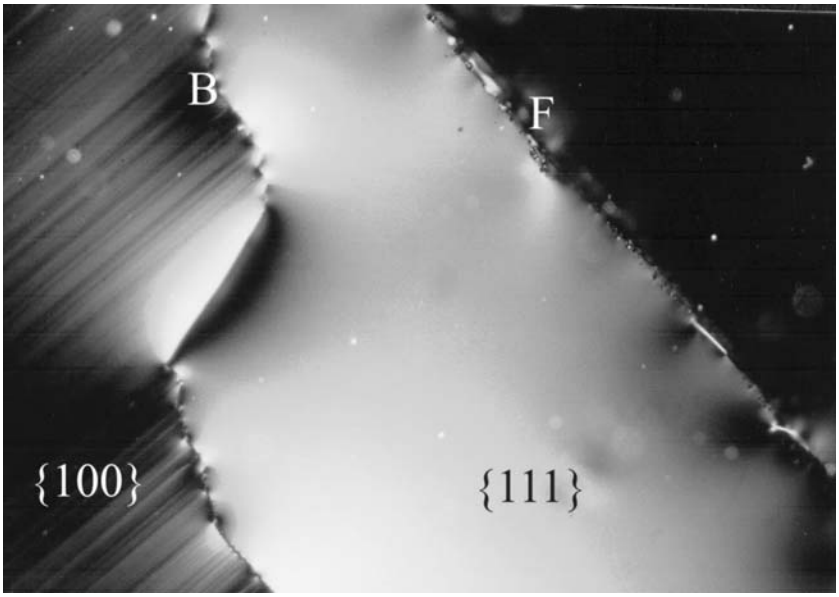

Figure 2.41. Anomalous birefringence in alum $(K, NH_4)Al(SO_4)_2 \cdot 12H_2O$. B is the sector boundary, F is a crack. Horizontal = 6.5 mm

During crystal growth all these elements can form regions with different chemical composition within one growth sector—"parasitic" growth pyramids according to the terminology by Lemmlein (1948). Stress calculations meet significant difficulties in such cases, but the stress can be estimated once again from Equation (2.55) if the compositions giving rise to different lattice constants in the main and parasitic growth pyramids are known. Optical anomalies from such sources are usually slight.

2.8.5. Effect of Growth Conditions on the Stress-Induced Optical Anomalies

Growth conditions do not affect optical anomalies directly. They can influence stress by creating compositional or temperature inhomogeneities.

The situation is relatively simple for thermoplastic stress—the temperature gradients are mainly defined by the furnace design and thermal properties of the melt. As shown above, the crystal plasticity near the melting point plays an important role. On the other hand, the effect of growth conditions on compositional inhomogeneity and heterometry can be severe. Above all, the compositional inhomogeneity (especially concentric zoning) is controlled by instability of growth conditions (temperature, pressure, composition, hydrodynamics). Even under essentially stable

external conditions the spatial inhomogeneity of crystals can be pronounced (sector zoning, sub-sector zoning, thin oscillating zoning).

Given stable growth conditions, sectoral inhomogeneity increases as the growth temperature and growth rate (supersaturation) decrease (Punin, 2000). Growth sectors and sub-sectors not related by symmetry adsorb impurities differently. Thus they have different distribution coefficients. The differences are inversely correlated to temperature and growth rate. Internal stress will therefore be greater with low temperatures and slow rates.

On the other hand, strong deviations from equilibrium (high growth rates) are much more likely to be accompanied by strong variations of the growth rate (de-supersaturation or self-oscillations). This leads to crystal zoning via changes of distribution coefficients and to strong sub-sector zoning via change of the vicinal relief.

In crystals of solid solutions with positive mixing energy albeit insufficient for ex-solution, the optical anomalies and imperfections usually increase in the middle of the series. The possible reason for such behavior is a segregation of components at the micro scale followed by internal stress. The typical examples studied by us are the crystals of $(K, NH_4)H_2PO_4$, $(K, NH_4)_2SO_4$, and $Na(Cl, Br)O_3$.

The effect of the growth medium on composition is not as simple as expected at first glance. Highly paradoxical phenomena can be observed. For example, adding impurities to the growth medium can reduce the level of internal stress while excessive purification can significantly increase it. A well-known substance exhibiting this behavior is potassium dihydrogen phosphate. Highly pure solutions will increase growth rates of both the prism and pyramid faces thereby producing stress at the growth sector boundaries.

Growth-induced internal stress can partially or completely relax during or after crystal growth. Brittle as well as plastic stress relaxation decreases and redistributes optical anomalies. Under some conditions when the heterometry-induced stress exceeds the breaking point or the yield strength, the most inhomogeneous parts of the crystal can be free of the optical anomalies since the stress has relaxed. This paradoxical situation is observed for example for grossular-andradite garnets from the Dalnegorsk mine (Far East, Russia), Figure 2.7. The difference in lattice constants between the neighboring crystal zones can reach 0.025 Å significantly exceeding the yield strength. The crystals therefore do not exhibit the anomalous birefringence as a consequence of heterometry-induced stress because this is relaxed by a high dislocation density (Figure 2.7).

The capacity of a material to undergo plastic deformation depends on growth conditions, especially temperature. The nucleation rate, multiplication, and motion velocity of dislocations exponentially increases with the temperature (Poirier, 1985). Note that while plastic deformations reduce optical anomalies related to the compositional heterometry they give rise to optical anomalies related to residual stress (section 2.7).

More often the internal stress relaxes by means of crack formation. The brittle relaxation is affected in particular by crystal size. The larger the crystal the more

probable is cracking. For example, larger polychrome tourmaline crystals of similar compositional inhomogeneity are characterized by smaller axial angles and greater fissuring (Gorskaya *et al*., 1992).

The brief discussion above shows that depending on the substance and set of growth conditions one and the same factor can oppositely affect the value and distribution of elastic stress in a crystal. The experimental data on the direct relationships between optical anomalies and growth conditions are few. The anomalous biaxiality of pentaerythritol increases at higher supersaturation and lower growth temperature (Punin *et al*., 1986). In the potassium dihydrogen phosphate crystals the anomalous biaxiality decreases with temperature but does not depend on the growth rate (Belyustin and Stepanova, 1981). Furthermore, transition from natural convection to strong solution stirring also decreases the optical anomalies (Fridman, 1972). In a similar manner the stirring of the melt (rotation of a crystal) lessens thermal convection and thereby reduces impurity striations (zoning) that can also give rise to optical anomalies. The sector zoning birefringence related to the so-called "facet effect" is also reduced by a strong stirring of the melt. For additional data on thermoplastic stress-induced optical anomalies see the following: Urusovskaya (1962), Nikitenko (1962), Cheredov (1993), and Denisov *et al*. (2006a).

CHAPTER 3

KINETIC ORDERING-DISORDERING

3.1. INTRODUCTION

Order-disorder transitions in crystals induced by the thermodynamic variables of temperature and pressure are widespread. Not only do we expect changes in optical properties accompanying transitions from one equilibrium phase to another, changes that qualify as optical anomalies can arise as a consequence of kinetic aspects of order-disorder phase transformations (Chernov, 1970). The term *kinetic phase transformation* emphasizes processes governed by rates, not by thermodynamic variables.

A necessary condition for a kinetic order-disorder transformation is the presence of sites occupied in the crystal structure by different kinds of structural units. In the disordered phase, these units are distributed randomly among lattice sites that are related by symmetry. In the ordered phase, they distribute themselves non-statistically thereby breaking the symmetry relationships between or among the formerly equivalent sites. Such phenomena are observed for fully miscible Al and Fe in grandite garnets ($Ca_3(Al, Fe)_2(SiO_4)_3$) as well as slightly miscible Al and Si ions in quartz. Kinetic order-disorder phenomena can occur between compounds that are known to undergo thermodynamic phase transformations (e.g. orthorhombic-hexagonal cordierite, $Mg_2Al_3(AlSi_5O_{18})$) and also between those that do not (e.g. orthorhombic-triclinic topaz).

Orientational ordering of dissymmetric structural units is also possible. Such thermodynamic phase transformations are known (e.g. Mookherjee *et al*., 2002 and references therein). Kinetic transformations are also possible. However, there are fewer examples of such transformations (For an exception see section 3.4.2) and we will restrict ourselves to order-disorder among distinct crystallographic sites.

3.1.1. Kinetic Ordering

Tammann (1917) first proposed atom ordering as the basis for anomalous birefringence, followed by Yoder (1950). More than half a century ago, compounds with non-random distributions of impurities among nominally equivalent sites were revealed by electron paramagnetic resonance spectroscopy. These impurities include

Gd^{3+} in synthetic corundum, Al_2O_3 (Geschwind and Remeika, 1961), and Fe^{3+} in calcite, $CaCO_3$ (Marshall and Reinberg, 1963), Fe^{3+} in amethyst (Barry and Moore, 1964; Barry *et al*., 1965). Non-equivalence of sites on crystal faces differentially occupied by impurities during growth was thus established but not explained. Shubnikov (1961) formulated the idea of growth ordering independently. Detailed mechanisms were first considered in quartz (Tsinober and Samoilovich, 1975), zinc selenate (Nizamutdinov *et al*., 1977) and sodium kröhnkite, $Na_2Cd(SO_4)_2 \cdot 2H_2O$ (Vinokurov *et al*., 1977). Similar mechanisms were later suggested by Akizuki to account for optical anomalies in adularia, $KAlSi_3O_8$ (Akizuki and Sunagawa, 1978), apatite, $Ca_5(PO_4)_3(OH, F)$ (Akizuki *et al*., 1994), garnet (Akizuki, 1984), apophyllite, $KCa_4(Si_4O_{10})_2(F, OH) \cdot 8H_2O$ (Akizuki and Terada, 1998), topaz, $Al_2SiO_4(OH, F)_2$ (Akizuki *et al*., 1979), analcime, $NaAlSi_2O_6 \cdot H_2O$ (Akizuki, 1981b), chabazite, $Ca_2Al_4Si_8O_{24} \cdot 13H_2O$ (Akizuki, 1981c), brewsterite, $(Sr, Ba)_2Al_2Si_{12}O_{32} \cdot 10H_2O$ (Akizuki, 1987c; Akizuki *et al*., 1996), edingtonite $BaAl_2Si_3O_{10} \cdot 4H_2O$ (Akizuki, 1986; Tanaka *et al*., 2002b), yugawaralite, $CaAl_2Si_6O_{16} \cdot 4H_2O$ (Akizuki, 1987b; Tanaka *et al*., 2002b) among others.

The essence of the kinetic ordering of atoms (growth desymmetrization phenomenon) is as follows: Positions related by symmetry in the bulk of a crystal may be—and most often are—structurally and energetically non-equivalent on a growing surface. These differences give rise to an ordered distribution of structural units in the surface layer. The ordered distribution is then overgrown and buried in the metastable state. The crystal would have a lower free energy were the guests statistically distributed among bulk sites having the same potential energy. Nevertheless, the metastable state can persist indefinitely because of the slow diffusion in solids. Thus the crystal symmetry is reduced, resulting in optical anomalies in favorable cases. In addition to anomalous birefringence, optical anomalies can manifest themselves as anomalous pleochroism (section 3.4.4), detected in, for example, smoky quartz and amethyst (Tsinober and Samoilovich, 1975; Partlow and Cohen, 1986).

Crystal growth can occur via step motion across a crystal face (*tangential growth*) or via normal displacement of a whole face (*normal growth*). The inequivalence arising from both growth mechanisms is shown in Figure 3.1

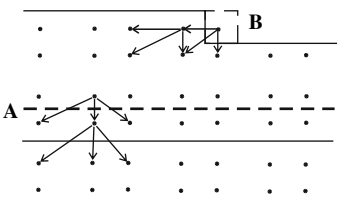

Figure 3.1. Equivalent atoms in the volume of a crystal become geometrically non-equivalent relative to growth front (after Vinokurov *et al*., 1977). **A** – normal selectivity, **B** – tangential selectivity. The solid and dashed lines show two successive positions of the growth front. Arrows show nearest neighbors at the moment of attachment to the crystal surface

(Vinokurov *et al*., 1977). The relationship between kinetic ordering and growth face structure is discussed in greater detail in section 3.4.6.

3.1.2. Kinetic Disordering

The reverse of kinetic ordering—kinetic disordering—is also possible as described theoretically by Chernov (Chernov and Lewis, 1967; Chernov, 1970). Corresponding data are few (Akizuki and Sunagawa, 1978; Carpenter and Putnis, 1985). Given a solid solution characterized by a certain degree of ordering in equilibrium with a growth medium, the attachment of structural units into similar crystal sites is a dynamic process that involves statistical selection. In the course of this selection the units attach and detach at possible sites. The statistical selection required to give a certain degree of ordering requires time that depends on the detachment rate. As the growth rate increases, the time required for the site selection decreases with a concomitant decrease in the degree of ordering. In the limit of very rapid growth the structural units are statistically disordered. For example, in potassium feldspar (microcline, $KAlSi_3O_8$, triclinic, point group $\bar{1}$) aluminum atoms occupy only one of four tetrahedral sites ($4T_1(o)$); they are eschewed by sites $4T_1(m)$, $4T_2(o)$, and $4T_2(m)$ fully occupied by silicon. With fast growth, fully disordered monoclinic feldspar (sanidine, $KAlSi_3O_8$, monoclinic point group $2/m$) is crystallized; all four sites have 0.25 Al occupancies (The Encyclopedia...1981). If growth rates of different faces are very different the corresponding growth sectors can have different degrees of ordering leading to optical inhomogeneities and/or optical anomalies. Such a kinetic model was offered as the etiology of optical anomalies in adularia, $KAlSi_3O_8$ (Akizuki and Sunagawa, 1978).

3.2. CRYSTAL SYMMETRY

3.2.1. The Neumann-Curie Principle

The connection between ordering, growth face structure, and the resulting optical indicatrix is found in the symmetry of the growth face (normal selectivity) and/or in the symmetry of steps (tangential selectivity). This follows from the Neumann-Curie principle (Shubnikov and Kopstik, 1974; Nye, 1985) which states that a medium under an external influence will exhibit only those symmetry elements that are common to the medium without the influence and the influence without the medium (see Foreward). The Neumann-Curie Principle is here generally formulated. For our purposes, we can replace *medium* by *crystal*. Classical crystal symmetry is represented by 32 point groups. The symmetry of the influence, in our case of crystal growth, is either the point group of the material flux toward the face (symmetry of a cone, ∞mm) or the point group of the plane material flux toward the step on the face (point group m). Shubnikov (1961) identified ten point groups that describe the symmetries of a growth pyramid after desymmetrization via normal selection. They are 1, 2, 3, 4, 6, m, $2mm$, $3m$, $4mm$, and $6mm$. In other words,

the resulting crystal contains only the symmetry operations that are included in the symmetry of the cone, mirror planes and axes normal to the growth face. For example, growth ordering via normal selectivity by attachment to the octahedron face {111} (cubic crystal point group $m\bar{3}$, Figure 3.2) is accompanied by symmetry reduction to the trigonal point group 3. For the rhombic dodecahedron face {110} the resulting symmetry corresponds to the monoclinic group *m*.

Step growth (tangential selectivity) results in two possible point groups – 1 and *m*, since the resulting symmetry is defined not only by the face symmetry but also by a polar direction in the plane of the face, perpendicular to the growth step. For the group $m\bar{3}$ considered above the crystal symmetry is reduced to triclinic 1 when growth steps are not perpendicular to the mirror plane or monoclinic *m* when they are.

Rationales for desymmetrization based on arguments of this sort were applied to analcime (Akizuki, 1981b), grossular garnet (Akizuki, 1989), chabazite (Akizuki, 1981c), sodium chlorate-bromate (Gopalan *et al.*, 1993; Crundwell, 1997; Shtukenberg *et al.*, 2004), long chain carboxylic acid derivatives (McBride and Bertman, 1989), and benzene derivatives (Kahr and McBride, 1992; Vaida *et al.*, 1988; Shimon *et al.*, 1993). For example, in the course of topaz (*mmm*) desymmetrization a (010) growth sector bounded by a growing face of symmetry *2mm* remains orthorhombic, {*hk*0} growth sectors (face symmetry *m*) become monoclinic and {*hkl*} growth sectors (face symmetry 1) become triclinic (Akizuki *et al.*, 1979). This approach does not take into account the site symmetry of the substituted units. Symmetry reduction is not always realized. For example, normal selectivity on the cube {100} face of alum (point group $m\bar{3}$, Figure 3.2) should result in the orthorhombic symmetry 2*mm*, however, in reality this growth sector remains cubic (section 3.2.2). Nevertheless, if symmetry reduction does occur, it is constrained by the scheme outlined above.

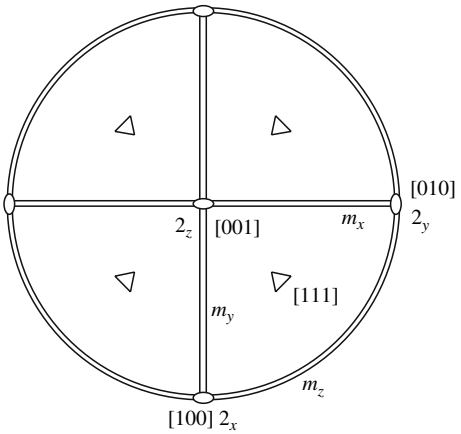

Figure 3.2. Stereographic projection of alum, symmetry $m\bar{3}$. The inversion center is not shown

3.2.2. Application of Group Theory

Often it is easy to determine by inspection of models of crystal surfaces and steps how many subsets there are of symmetry related bulk sites that are inequivalent during normal or tangential growth. Likewise, the degeneracies of these subsets can be deduced from models. However, a rigorous, systematic description of desymmetrization requires the theory of groups (Hall, 1959). Such an approach was applied to the analysis of the desymmetrization of crystals of zinc selenate and sodium kröhnkite (Nizamutdinov *et al*., 1976a,b; Vinokurov *et al*., 1977; Anufriev *et al*., 1980; Bulka *et al*., 1980) when grown in the presence of paramagnetic Cu^{2+} ions, among others. The authors showed that the intensities of peaks in electron paramagnetic resonance spectra were controlled by the distribution of paramagnetic impurities over systems of translationally equivalent positions with respect to the symmetry of growth steps.

Here, we illustrate the application of this approach to the analysis of normal selectivity in {111} growth sectors of alum mixed crystals and then apply it to alums (Table 3.1) and garnets (Table 3.2). Before moving on to examples, it is necessary to first review some concepts of group theory and their manifestation of desymmetrization phenomenon.

If group $H = \{h_1, h_2 \ldots\}$ is a subset of group $G = \{g_1, g_2 \ldots\}$ then H belongs to $G (H \subset G)$. H is thus a *subgroup* of G. For any subgroup H we may define a *coset*

$$g_i H = \{g_i h_1, g_i h_2 \ldots\}$$

where g_i is an element of G not in H. $g_i h_1$, $g_i h_2 \ldots$ are then different elements in G. After forming a coset, if there are any elements left in G not in H, we can select one and form a new coset until every element of G belongs to a coset. In this way, H partitions G into cosets. The coset concept can be used to carry out an operation important in the analysis of desymmetrization, the *decomposition of a group with respect to a subgroup*. This process is tantamount to enumerating the elements of a group according to the unique cosets to which they belong. The number of unique cosets needed to enumerate the elements of G is called the *index* of the subgroup H. Finally, if G has two subgroups H and L, then $H_g L$ is a double coset of G if g_i is an element of G.

We define the following symmetries:

$G_k =$ point group of the crystal.

$G_\alpha =$ site symmetry in the bulk of a structure undergoing substitution.

$G_\Gamma =$ symmetry of a crystallographic face.

$G_\beta =$ symmetry of a step on a crystallographic face. $G_\beta = \sum_{j=1}^{g_\beta} a_j$,

Then, g_k, g_α, g_Γ, and g_β are the orders, or number of symmetry elements, of G_k, G_α, G_Γ, and G_β respectively.

All the sites, which can be obtained from a given site using only elements of the translation group T form the system of translationally equivalent positions.

Table 3.1. Occupancies of translationally equivalent positions, theoretically predicted crystal systems and experimentally observed optical indicatrices for the alums

	Normal selectivity		Tangential selectivity		
Growth sector	Site occupancies, face symmetry	Suggested crystal system	Site occupancies, step symmetry	Suggested crystal system	Observed optical indicatrix
{111}	$o_1 \neq o_2 = o_3 = o_4$ 3 $G_\Gamma = 1 + 3_1 + 3_2$	Trigonal, three-fold axis $\perp$ to growth face (111)	$o_1 \neq o_2 \neq o_3 \neq o_4$ 1 $G_\beta = 1$	Triclinic	Biaxial, close to uniaxial with optic axis || to growth direction [111]
{110}	$o_1 = o_2 \neq o_3 = o_4$ m $G_\Gamma = 1 + m_x$	Monoclinic	$o_1 = o_2 \neq o_3 = o_4$[#] m $G_\beta = 1 + m_x$	Monoclinic or triclinic[#]	Biaxial
{100}	$o_1 = o_2 = o_3 = o_4$ $2mm$ $G_\Gamma = 1 + 2_z + m_x + m_y$	Cubic	$o_1 = o_2 \neq o_3 = o_4$[#] m $G_\beta = 1 + m_x$	Monoclinic or triclinic[#]	Often isotropic, sometimes biaxial

[#] Resultant symmetry depends on the growth step orientation. If the step is not perpendicular to mirror plane, all the occupancies are different and the point symmetry is triclinic

Table 3.2. Observed optical indicatrices for grandite garnet growth sectors compared with theoretical indicatrices and distributions of occupancies o_i over octahedral sites (site symmetry $\bar{3}$)

Growth sector Face symmetry	Observed optical indicatrix	Theoretical optical indicatrix Distribution of occupancies
Cube {100} 4*mm*	Sphere	Sphere $o_1 = o_2 = o_3 = o_4 = o_5 = o_6 = o_7 = o_8$
Octahedron {111} 3*mm*	Uniaxial ellipsoid, optic axis ⊥ to (111) face	Uniaxial ellipsoid, optic axis is ⊥ to (111) face $o_1 = o_5 \neq o_2 = o_3 = o_4 = o_6 = o_7 = o_8$
Rhombic dodecahedron {110} 2*mm*	Biaxial ellipsoid, $n_\gamma \| \| [\bar{1}01]$; $n_\beta \| \| [010]$; $n_\alpha \| \| [101]$; (⊥ to the face)	Biaxial ellipsoid, principal axes are || to [010], $[\bar{1}01]$ and ⊥ to (101) face $o_1 = o_4 = o_5 = o_6 \neq o_2 = o_3 = o_7 = o_8$
Icositetrahedron {211} *m*	Biaxial ellipsoid, $n_\alpha \| \| [211]$ (normal to the face); optic axial plane || to *m*	Biaxial ellipsoid, one of the main sections || to *m* $o_1 = o_5 \neq o_2 = o_8 \neq o_3 = o_7 \neq o_4 = o_6$
Tetrahexahedron {210} *m*	Biaxial ellipsoid, normal to the face without correspondence to any principal vibration direction; optic axial plane || to *m*	Biaxial ellipsoid, one of the main sections is parallel to the mirror plane *m* $o_1 = o_5 \neq o_2 = o_8 \neq o_3 = o_7 \neq o_4 = o_6$
Hexakisoctahedron {321} 1	Biaxial ellipsoid, oblique orientation of the indicatrix	Biaxial ellipsoid, oblique orientation of the indicatrix $o_1 \neq o_2 \neq o_3 \neq o_4 \neq o_5 \neq o_6 \neq o_7 \neq o_8$

Transitions between different systems can be realized by means of elements of the factor group $F = G_0/T$, where G_0 is the space group of the crystal. The factor group F is isomorphous to the point group of the crystal G_k.

Each regular system of points can be divided into K_α systems of translationally equivalent positions. The number K_α is found as an index of subgroup G_α in G_k, or in other words, as a number of cosets in decomposition of the point group G_k with respect to the group of local symmetry of the position G_α, thus $K_\alpha = g_k/g_\alpha$.

The normal or tangential selectivity orders additives at site G_α with respect to a surface or step (point groups $G_\Gamma = \sum_{j=1}^{g_\Gamma} a_j$, and where g_Γ and g_β are the numbers of symmetry elements a_j in these groups—their orders). To find a number of populations (distinct occupancies) a coset decomposition of G_k with respect to G_α is required:

$$G_k = \sum_{i=1}^{K_\alpha} a_i G_\alpha$$

The operation should be repeated until the cosets from decomposition of G_k with respect to G_α exhausts the elements of G_k. In order to reckon normal or tangential selectivity, we then need to perform a *double coset decomposition* of the group G_k with respect to (G_Γ, G_α) or (G_β, G_α):

$$G_\Gamma G_k = \sum_{i=1}^{l_{\Gamma\alpha}} n_{\Gamma l\alpha} G_\Gamma a_l G_\alpha,$$

$$G_\beta G_k = \sum_{i=1}^{l_{\beta\alpha}} n_{\beta l\alpha} G_\beta a_l G_\alpha \text{ and}$$

$$\sum_{l=1}^{l_{\Gamma\alpha}} n_{\Gamma l\alpha} = K_\alpha,$$

$$\sum_{l=1}^{l_{\beta\alpha}} n_{\beta l\alpha} = K_\alpha,$$

where $l_{\beta\alpha}$ and $l_{\Gamma\alpha}$ are the number of non-equivalent orientations and $n_{\Gamma l\alpha}$ are the multiplicity of the degeneracy of the ith nonequivalent orientation. In other words, $n_{\Gamma l\alpha}$ is the number of equivalent elements $G_\Gamma a_i G_\alpha$, and $n_{\beta l\alpha}$ is the number of equivalent elements $G_\beta a_i G_\alpha$.

According to the Neumann-Curie principle the symmetry group of each physical property G_I should include all elements of the crystal point group G_k. Mathematically this statement can be written as $G_k \subseteq G_I$. Thus, after dissymmetrization the resulting optical indicatrix may not correspond to the initial crystal symmetry but rather to the point group of the crystal after dissymmetrization G'_k. More accurately

the optical indicatrix should correspond to the symmetry of the growing face or to the symmetry of the step on the face, that is $G'_k \subseteq G_I$.

Alums $A^+M^{3+}(SO_4)_2 \cdot 12H_2O$, $A^+ = K, NH_4, Rb..$, $M^{3+} = Al, Fe, Cr\ldots$ belong to the cubic crystal class $G_k = m\bar{3}$, $g_k = 24$ (Figure 3.2). They are known for the optical anomalies related to kinetic ordering of structural units. Let us consider the atomic ordering over A^+ and M^{3+} sites (special sites 4(*b*) and 4(*a*), respectively, with multiplicity 4)

$$G_\alpha = \bar{3} = 1 + \bar{1} + 3^1 + 3^2 + \bar{3}^1 + \bar{3}^2;\ g_\alpha = 6.$$

For the normal selectivity on the {111} faces of alum, we have

$$G_\Gamma = 3 = 1 + 3^1 + 3^2;\ g_\Gamma = 3.$$

The double coset decomposition of G_k with respect to $(G_\alpha,\ G_\Gamma)$ in this case is as follows:

$$G_\Gamma G_k = G_\Gamma G_\alpha + G_\Gamma m_x G_\alpha + G_\Gamma m_y G_\alpha + G_\Gamma m_z G_\alpha$$

Since $G_\Gamma \subset G_\alpha$, one can write $G_\Gamma G_\alpha = 1 + \bar{1} + 3^1 + 3^2 + \bar{3}^1 + \bar{3}^2$. $G_\Gamma m_x G_\alpha$ includes all other elements of the group G_k, therefore, $G_\Gamma m_x G_\alpha = G_\Gamma m_y G_\alpha = G_\Gamma m_z G_\alpha$. Finally

$$G_k = G_\alpha + ([m_x G_\alpha] + 3^1[m_x G_\alpha] + 3^2[m_x G_\alpha]).$$

As a result, there are two different occupancies for sites o_i, $(i = 1, ..4)$:

$$o_1 \neq o_2 = o_3 = o_4.$$

The results of comparable calculation for all the growth sectors of alum are shown in Table 3.1. The observed optical symmetry is in accord with the symmetry reduction related to the growth ordering of cations A^+ or M^{3+}. The group theoretical analysis usually gives the same optical symmetry as the symmetry of the face or growth steps on the face. In particular, growth by the octahedron face (point group 3) results in trigonal symmetry, whereas the growth by a step on the octahedron face (point group 1) results in triclinic symmetry. However, differences are also possible. For example, the faces of the cube have orthorhombic symmetry 2*mm* but the theory for normal selectivity predicts the cubic symmetry—no desymmetrization occurs. This agrees with the experimental observations.

3.3. OPTICAL INHOMOGENEITY OF CRYSTALS

Becke (1894) recognized that a polyhedral crystal is not a monolith but rather an assemblage of *growth pyramids* or *growth sectors* whose bases correspond to growth

faces and whose coincident apices mark the site of crystal nucleation. Shubnikov recognized that such pyramids would naturally be of reduced symmetry in the presence of suitable impurities "feeding" the faces (Shubnikov, 1961). As shown in the previous section, the symmetry of the growth front has a major influence on crystal desymmetrization and consequent optical anomalies. However, growth sector zoning is only one of a variety of inhomogeneities real crystals can display. Various kinds of inhomogeneities are considered below including sub-sector zoning which is a consequence of the selective adsorption of impurities to vicinal facets that emerge on growth hillocks, as well as concentric zoning, a crystallographic response to changing growth conditions.

3.3.1. Sector Zoning

Growth sectors often have distorted optical indicatrices as a consequence of unidirectional growth in any one sector. The refractive indices of sectors associated with growth faces of different simple forms usually differ in magnitudes and directions. Symmetry related faces often have the same eigenvalues but different eigenvectors. This spatial inhomogeneity is a signature of an optically anomalous crystal.

A simple, prototypical example is that of mixed crystals of $NaClO_3$ and $NaBrO_3$. Such crystals grow as cubes that are best represented as six square pyramids created by dissecting the cube along all four-body diagonals. Despite the fact that the ensemble still has 23 symmetry at the point where the pyramids are co-joined, the individual sectors are optically biaxial (Brauns, 1898; Gopalan *et al.*, 1993). The intermediate refractive index n_β is perpendicular to each growth face while n_α and n_γ establish the vibration directions along the diagonals of each growth face. An exaggerated optical indicatrix and its orientation in each sector is illustrated in Figure 3.3.

Between crossed polarizers, optically anomalous crystals look like twins or intergrowths as in jeremejevite, $Al_6B_5O_{15}(F, OH)_3$ (Figure 3.4). Apophyllite is another spectacular example discovered by Brewster (Brewster, 1821). When Brewster lifted a tetragonal plate from a square prism he was astonished by the fine tessellation of components (Figure 3.5*a*). The origin of the individual tiles is obvious from the square bi-pyramidal habit of a whole crystal. A new optical structure is generated for each facet that grows through the plane of Brewster's slice (Figure 3.5*b*).

Mixed crystals of alums (general formula $\mathbf{A^+M^{3+}(SO_4)_2 \cdot 12H_2O}$). Figure 3.4 shows a (110) section of an alum ($(K_{0.5}(NH_4)_{0.5})Al(SO_4)_2 \cdot 12H_2O$) crystal that consists of four {111} octahedron growth sectors, one {100} cube sector, and two growth sectors of the rhombic dodecahedron {110} (see also Figure 3.6). Despite the cubic symmetry of potassium or ammonium alum, the mixed crystals are birefringent. When pairs of opposing {111} sectors have unique extinction positions.

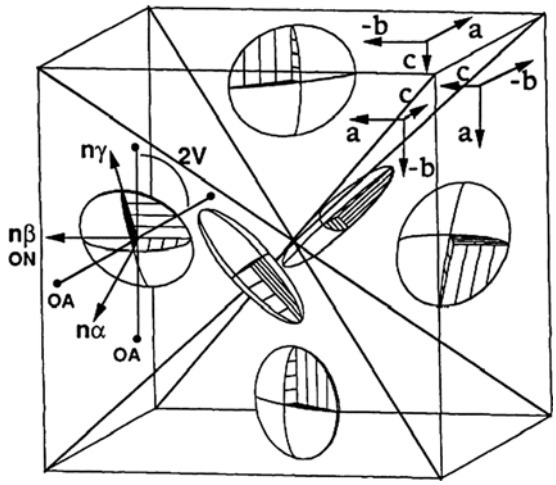

Figure 3.3. Cube of $Na(Cl, Br)O_3$ divided into six growth sectors. Each sector is optically biaxial although the ensemble has the 23 symmetry of the optically normal end members of the mixed crystal series. Indicatrices of each sector are represented; differences in the dimensions of the principal directions are exaggerated such that their relative orientations may be perceived. In crystals with composition $NaCl_{0.80}Br_{0.20}O_3$: $2V = 90°$, optic axes (**OA**) are within 2° of *b* and c and n_α (1.512) and n_γ (1.532) are diagonally oriented in the plane of the growth face, while the optic normal (**ON**), n_β (1.522), is perpendicular to it

Source: Reprinted with permission from Gopalan, P., Peterson, M.L., Crundwell, G., Kahr, B. (1993). Reevaluating Structures for Mixed Crystals of Simple Isomorphous Salts: $NaBr_xCl_{1-x}O_3$, *J. Am. Chem. Soc. 115,* p. 3366–3367. Copyright 1993 American Chemical Society.

Octahedral growth sectors are the most birefringent $\Delta n_{\{111\}} \sim 0.0001 >> \Delta n_{\{110\}} \geq \Delta n_{\{100\}}$. To a first approximation, the optical indicatrix is an ellipsoid of revolution. The optical sign is negative (oblate ellipsoid) for solid solutions with substitution at A^+ sites, and positive (prolate ellipsoid) for substitution at M^{3+} sites. These facts were established for seven isomorphous series as indicated in Table 3.7. The optic axis ε coincides with the growth front direction [111] in each of eight {111} growth sectors (Figure 3.6). Accurate measurements nevertheless reveal that the optical indicatrix is actually a biaxial ellipsoid, though nearly uniaxial, with the following axial ratios:

1. $(K, NH_4)Al(SO_4)_2 \cdot 12H_2O - (n_\gamma - n_\alpha)/(n_\gamma - n_\beta) = 15–20$;
2. $(K, Rb)Al(SO_4)_2 \cdot 12H_2O - (n_\gamma - n_\alpha)/(n_\gamma - n_\beta) = 5–15$;
3. $K(Al, Cr)(SO_4)_2 \cdot 12H_2O - (n_\gamma - n_\alpha)/(n_\beta - n_\alpha) = 5–10$.

From these values, axial angles ($2V$) of 26–30°, 30–53°, and 37–53°, respectively, were calculated. The axis $Z(X)$ is aligned with the [111] growth direction to within 5°.

Rhombic dodecahedral sectors are slightly birefringent $\Delta n < 2 \times 10^{-5}$ (usually 5×10^{-6}). The optical indicatrix can be biaxial or uniaxial. In (110) sections, either Z' (series $(K, NH_4)Al(SO_4)_2 \cdot 12H_2O$ and $(K, Rb)Al(SO_4)_2 \cdot 12H_2O$) or X' (series

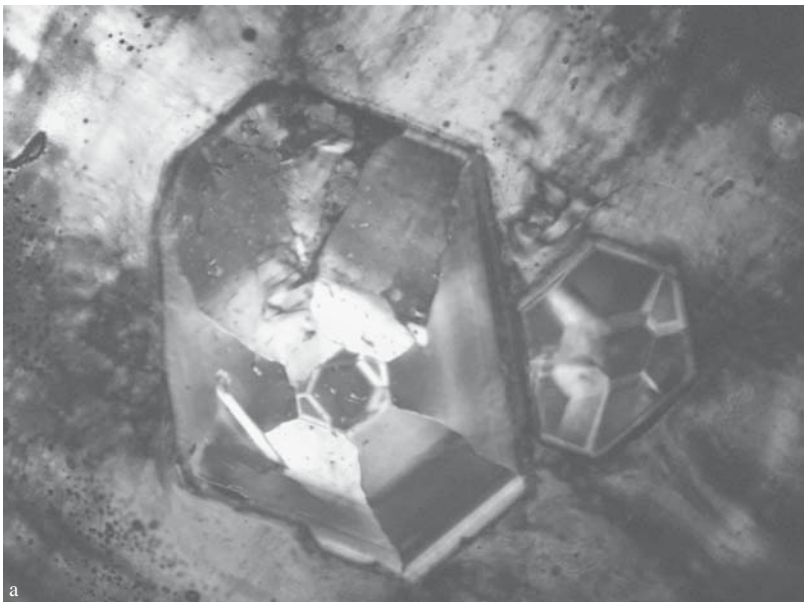

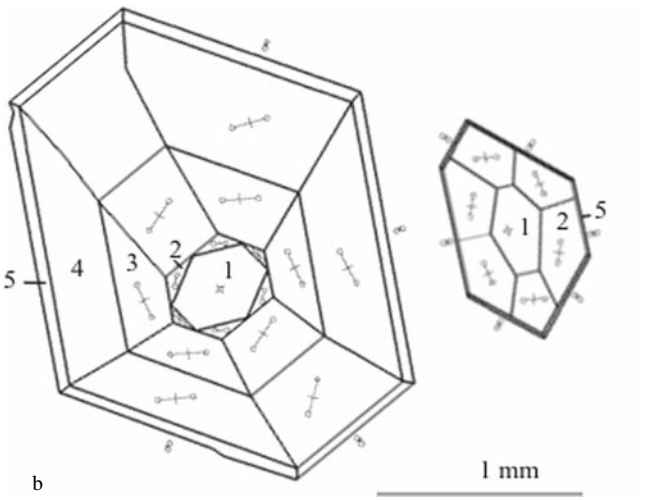

Figure 3.4. Optical sector zoning in jeremejevite $Al_6B_5O_{15}(F, OH)_3$ (0001) section (two crystals). (*a*) Photomicrograph; (*b*) Idealization after (Zolotarev *et al*., 2000). Growth sectors: (1) pinacoid {0001} $2V = 0°$, (2–4) hexagonal dipyramid, $2V = 3°$, (5) hexagonal prism, $2V = 10–18°$. The samples were kindly provided by V.A. Mikhailov (see Color Section following page 254)

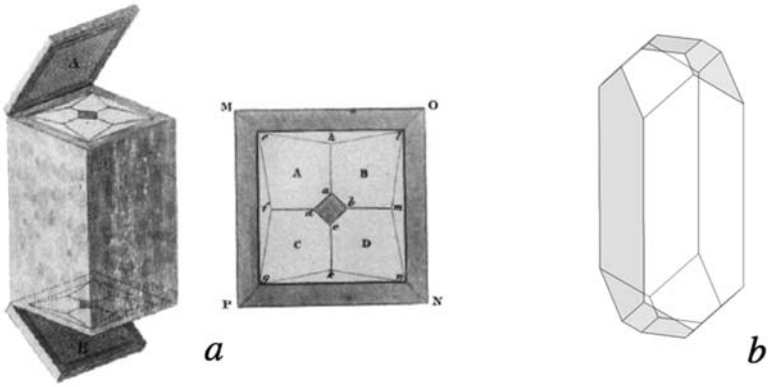

Figure 3.5. Apophylite $KCa_4(Si_4O_{10})_2(F, OH) \cdot 8H_2O$. (*a*) Brewster's (1821) slice revealing tessellation of growth sectors. (*b*) Square bi-pyramidal habit from which growth sectors originate
Source: Reprinted with permission from Kahr, B., McBride, J.M. "Optically Anomolous Crystals" *Angewandle Chemie, International. Edition in English*, 1992, *31* p.1–26. Copyright 1992 Wiley-VCH, STM.

$K(Al, Cr)(SO_4)_2 \cdot 12H_2O$) vibration directions are parallel to the growth direction, however other orientations are also observed.

Cube sectors {100} are less birefringent than {111} and {110} growth sectors. Often they are even optically isotropic. Otherwise, the indicatrix is usually biaxial with eigenvalues and eigenvectors varying unpredictably throughout the sector. These observations, along with data on crystal annealing (section 3.4.5.3), argue for a significant contribution of elastic stress to the optical anomalies in alum {100} sectors.

Theoretical analysis of the crystal symmetry after desymmetrization (Table 3.1) well-agrees with the data. The normal selectivity seems to dominate in {111} growth sectors. In {100} growth sectors the desymmetrization—if evident—arises through tangential selectivity. In {110} growth sectors desymmetrization can occur via normal as well as tangential selection.

Optical anomalies in **ugrandite garnets** ($(Ca_3(Al, Fe, Cr)_2(SiO_4)_3$, ideal point group $m\bar{3}m$) were studied in detail by Brauns (1891), and more recently by Akizuki *et al.*, (1998), Andrut and Wildner (2001), and Shtukenberg *et al.*, (2001a)—Table 3.2, Figure 3.7.

3.3.2. Sub-Sector Zoning

Sector zoning is often complicated by sub-sector zoning (see also section 2.8.4).

Many crystals that commonly manifest growth desymmetrization precipitate from aqueous solutions. Such crystals typically grow by means of a dislocation-spiral mechanism (Sunagawa, 2005) so long as supersaturation is low. New layers are formed by step propagation across the crystal surface. The optical indicatrix should be controlled by the tangential selectivity of structural units. Spiral hillocks may

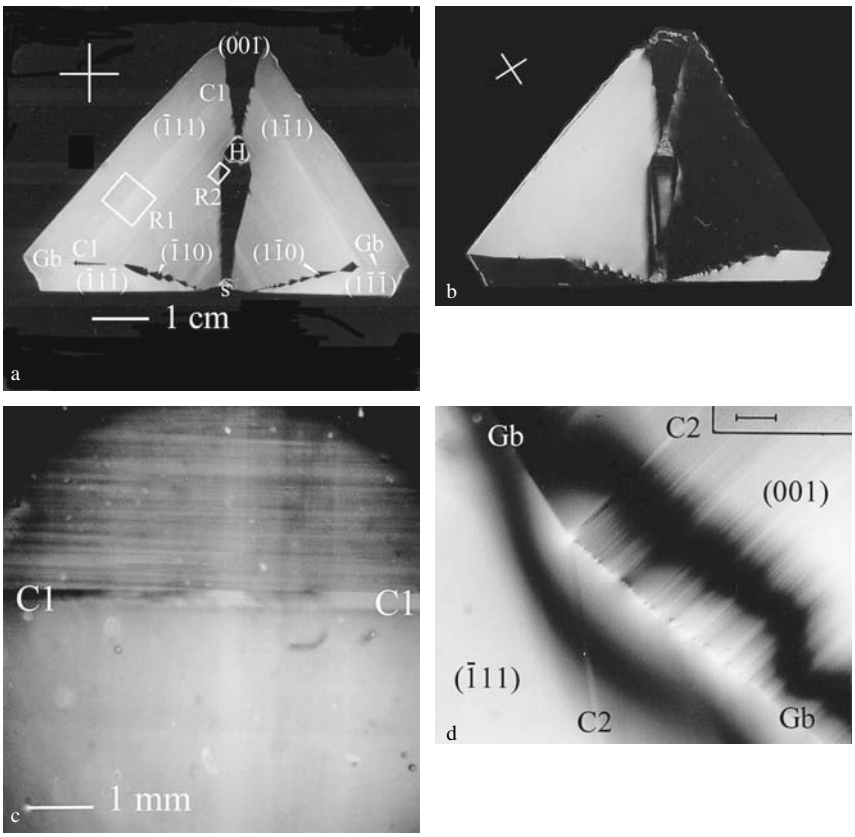

Figure 3.6. Optical inhomogenetiy of alum, $(K_{0.5}(NH_4)_{0.5})Al(SO_4)_2 \cdot 12H_2O$. The (110) section was cut through the center of the crystal. (*a*) and (*b*) have different orientations with respect to the crossed polarizers. Optical orientations are indicated by crossed white lines. The birefringence is strong in {111} growth sectors and weak in {110} and {100}. In {111} growth sectors, the *X* vibration direction is always normal to the growth front direction. Some growth sector boundaries are marked by Gb, S = seed crystal, H = solution inclusion. Regions R1 and R2 are magnified in (*c*) and (*d*), respectively. They display fine zoning related to unstable growth and changes of step sources. Horizontal stripes in (*c*) are associated with dislocation stresses. The boundaries C1-C1 and C2-C2 mark a supersaturation jump and the cessation of crystal rotation for one hour, respectively. Scale bar in (*c*) = 0.38 mm

be rounded or they may become polygonal. Polygonal hillocks have discrete step orientations. Thus, the optical properties will likewise vary in discrete steps. In rounded hillocks, these properties may change continuously.

For example, the growth hillocks on the octahedron faces of alums have the shape of shallow trigonal pyramids (point symmetry of the octahedron face is 3), therefore, each hillock forms three equivalent sub-sectors evident in cross sections cut parallel to the {111} growth face. This pattern is characteristic of the ideal case in which there is a single growth active hillock. In reality, several hillocks

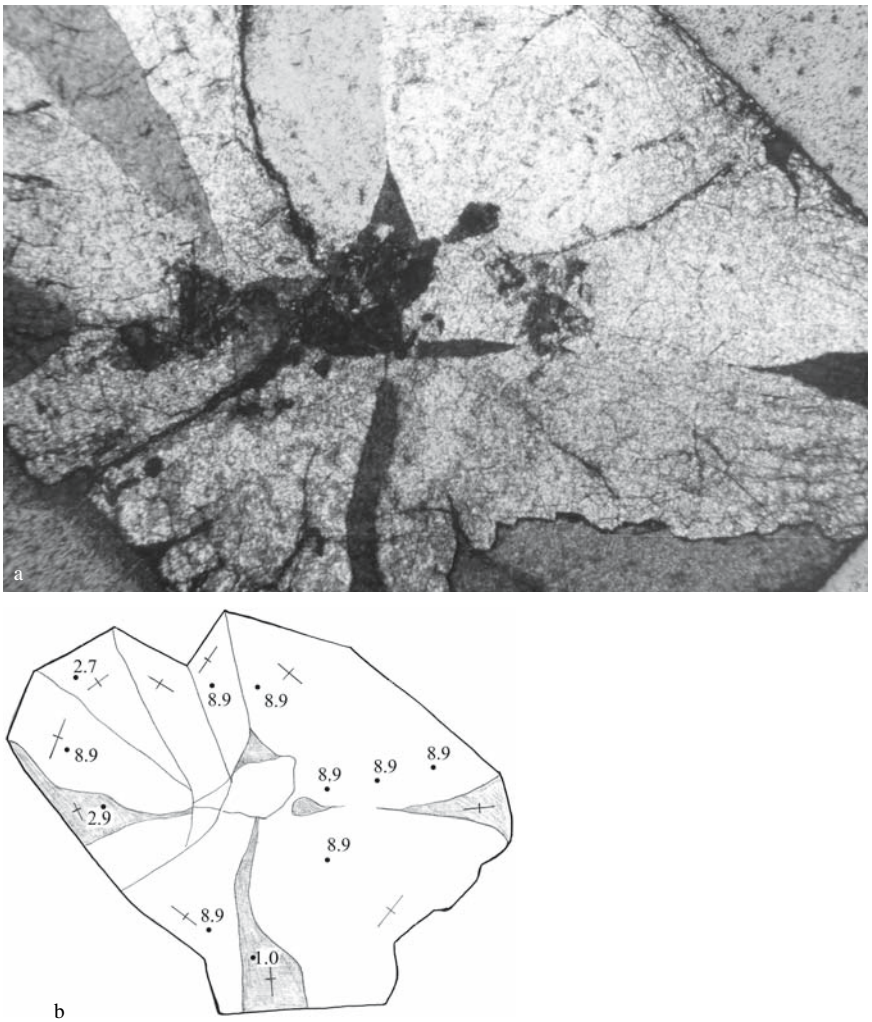

Figure 3.7. Grossular-andradite garnet from the Bazhenovo mine (Ural mountains, Russia) between the crossed polarizers with a first order red retarder. (*a*) Photomicrograph and (*b*) Cartoon based on (*a*). The {110} growth sectors of different orientations are visible. Crosses denote orientations of vibration directions X' and Z'. Numbers indicate birefringence $\times 10^{-3}$. Crystal size ~ 1 cm. The growth direction [110] in hatched and unhatched growth sectors form distinct angles with respect to the section plane (see Color Section following page 254)

may be operative giving rise to a corresponding number of overlapping triplets of sub-sectors (Figure 3.8*a*, 3.9). The point co-joining a triplet of sub-sectors often corresponds to the apex of the vicinal hillock observed on the crystal face (Figure 3.8*a*, 3.9) (Shtukenberg *et al.*, 2001b).

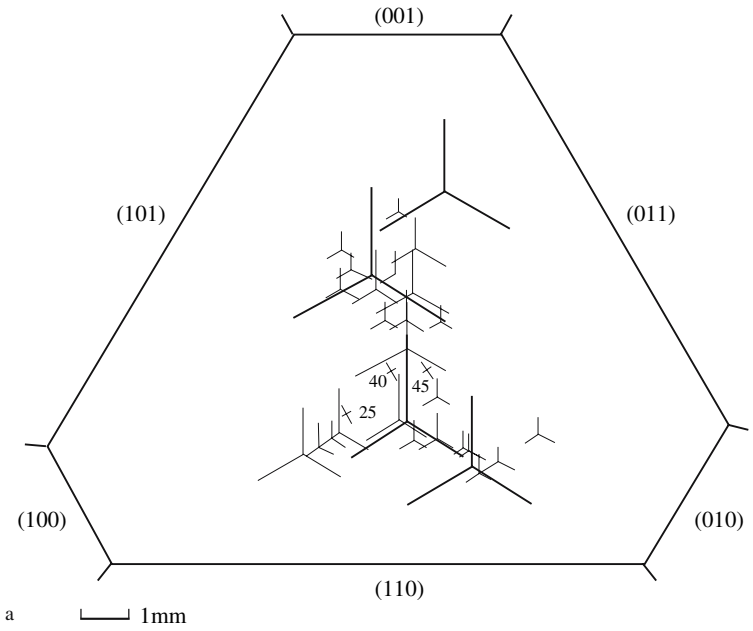

Figure 3.8. (*a*) Subsector zoning in alum $(K_{0.77}Rb_{0.23})Al(SO_4)_2 \cdot 12H_2O$ {111}, section parallel to (111) growth face. Sub-sector boundaries shown by bold lines are the boundaries between different vicinal faces on the crystal surface. Sub-sector boundaries shown by thin lines are observed between crossed polarizers. Numbers denote birefringence $\times 10^{-7}$. (*b*) The same crystal with section through the center of (111) face parallel to the growth direction [111] between crossed polarizers and with a first order red retarder. White line marks position of (111) face (see Color Section following page 254)

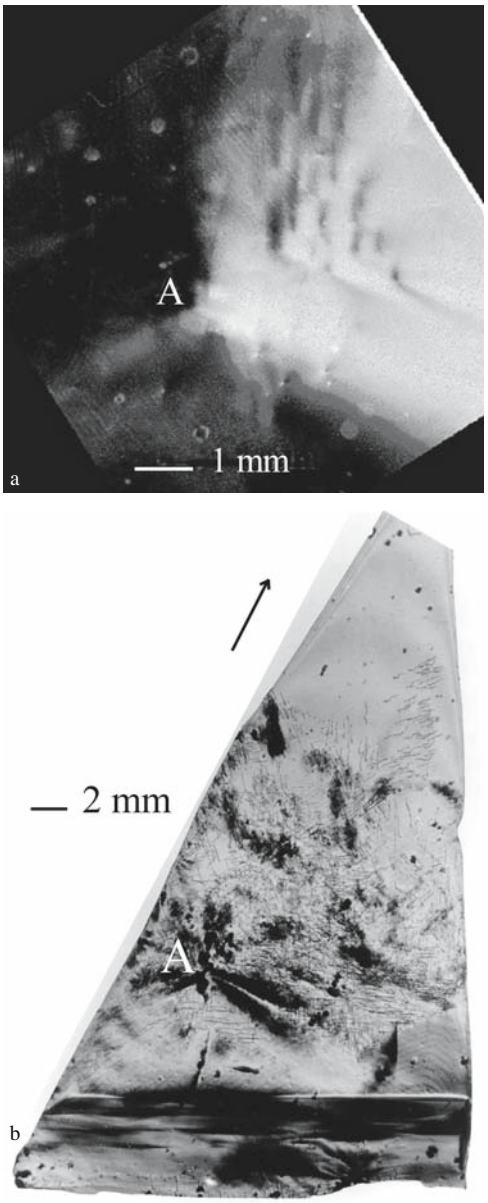

Figure 3.9. Sub-sector zoning in alum $(K_{0.5}(NH_4)_{0.5})Al(SO_4)_2 \cdot 12H_2O$ section parallel to the (111) growth face. (*a*) Anomalous birefringence around the apex of vicinal hillock (**A**). (*b*) X-ray diffraction topograph. The arrow indicates diffraction vector **g** for reflection 220

This complexity of overlapping growth hillocks can be readily seen in crystals of potassium hydrogen phthalate (conventionally abbreviated KAP for potassium acid phthalate, $C_6H_4 \cdot COOH \cdot COO^-K^+$, space group $Pca2_1$) (Bullard *et al*., 2004). KAP is easily grown from aqueous solution as large {010} plates with well-defined growth hillocks. Because the [001] direction is polar, the steps that propagate in the $+c$ and $-c$ directions are different in structure (Figure 3.10*a*). Differential recognition of additives for these distinct steps leads to intrasectoral or sub-sector zoning on (010). Luminescent molecules (Figure 3.10*b*) that bind, say, to the "fast" steps (Figure 3.10*a*) that are widely spaced in preference to the "slow" steps that are closely spaced reveal themselves in patterns of light bounded by the perimeters of the fast slopes (Figure 3.10*c*); the vertices of the colored chevrons mark the cores of the screw dislocations.

In real crystals, not all once-active growth hillocks survive at the surface to be observable in reflected light. However, some fluorescent dyes may be incorporated within the crystal throughout the growth process. Thus, even after subsequent overgrowth, the luminophores create a record of hillock evolution in patterns of light that can be revealed by successive cleavage or with a confocal luminescence microscope. Confocal laser scanning microscopy (CLSM) produces optical sections of the sample by restricting the collected light to a single diffraction-limited point with a variable pinhole. Due to its ability to eliminate out-of-focus light, confocal microscopy can be used to image a "fossil record" of dyed hillocks throughout the crystal, even those that are no longer growth-active on the surface.

Differences in birefringence in the fast and slop vicinal slopes were recorded outside of the absorption band and found to be slight, on the order of 0.004 (Bullard *et al*., 2004).

This kind of sub-sector zoning was observed in apatite (Akizuki *et al*., 1994) (Figure 3.11), grossular-andradite garnets (Akizuki, 1984), analcime (Akizuki, 1981b), chabazite (Akizuki, 1981c), edingtonite (Akizuki, 1986) and other compounds. In all cases, the optical sub-sector zoning correlates with the vicinal relief of the growth face. The optical symmetry agrees with the local symmetry of the faces or the local symmetry of the vicinal slopes of the hillocks on the faces.

For sections cut parallel to the growth direction, regions formed by the slopes of the same vicinal hillock can be distinguished. The x-ray diffraction topograph in Figure 3.12 shows the presence of a dislocation bundle acting as a growth steps source on the octahedron face. The position of the bundle coincides with the optical boundary that divides the growth sector into sub-sectors with discrete extinctions. If the growth face is formed by several vicinal hillocks, each controls some area of the crystal surface and forms its own sub-sectors that are divided by inter-vicinal boundaries. Optical characteristics of growth sectors can also differ because of different orientations, heights and velocities of growth steps forming sub-sectors. For example, growth of the alum octahedron face (Figure 3.12) was controlled by one vicinal hillock at first. Then, the growth sector of a cube face tapered out producing a dislocation bundle that gave rise to new, competing vicinal hillocks that

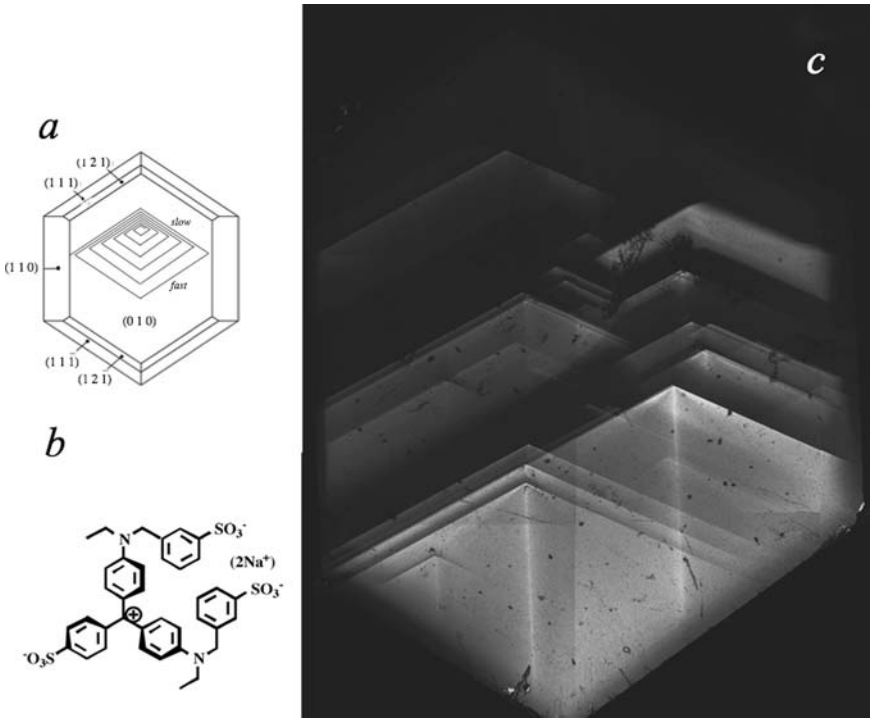

Figure 3.10. Potassium hydrogen phthalate (KAP) hillocks. (*a*) Idealized view of KAP crystal habit, viewed down [010], with (010) growth hillock and absolute indices. The orientation of the fast and slow moving slopes of a growth hillock on (010) face are indicated. (*b*) Structure of luminescent dye light green SF yellowish (LGSFY) [Color Index #42095]. (*c*) Confocal slice of KAP with LGSFY. Luminescence develops on the fast slopes of (010) growth hillocks, with vertices marking the dislocation core. (Bullard *et al*., 2004)

Source: Reprinted with permission from Bullard, T., Kurimoto, M., Avagyan, S., Jang, S.H. and Kahr, B. "Luminescence Imaging of Growth Hillocks in Potassium Hydrogen Phthalate" *Am. Cryst. Assn. Trans*. 2004, *39*. Copyright 2004 American Crystallographic Association, Inc. http://aca.hwi.buffalo.edu/index.htm.

after a short time took control over most of the face. This resulted in a sub-sector boundary (Figure 3.12). Magnification of the boundary shows a complex structure especially in the late stages of the growth (Figure 3.13).

Instability of the dominant step source often leads to fine oscillatory sub-sector zoning patterns that can be observed in alum crystals (Figure 3.6). The growth sectors of cubes are usually free of screw dislocations. Growth is controlled by edge dislocations, colloidal particles, and crystal edges that are able to produce growth steps in then absence of any strong and stable step source (Van Enckevort, 1982; Ristic *et al*., 1991; Shtukenberg *et al*., 2001b). As a result, the leading step source constantly changes location with concomitant changes of step character. Sometimes, helter-skelter optical contrast can also be observed in growth sectors

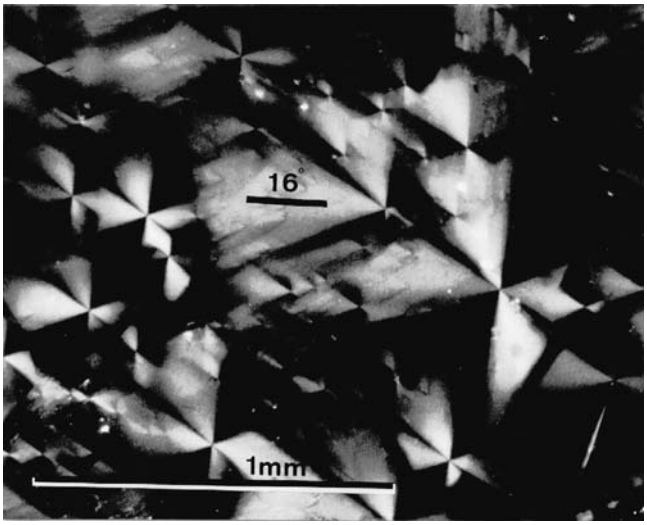

Figure 3.11. Optical sector-zoning in apatite cross sections cut perpendicular to the axis [0001] (Akizuki *et al*., 1994). Reproduced with kind permission of the Mineralogical Society of Great Britain and Ireland. The growth hillocks observed on the crystal surface often but not always have the same location as the optical "vicinals"

of the octahedron if numerous hillocks simultaneously start to produce steps (Figure 3.8*a*). The leading step source is defined by the competition between these hillocks. Numerous fine pseudo-zoning boundaries appear (Figure 3.8) in mixed alums when growth conditions are not tightly controlled. This process can be also related to formation of macrosteps.

3.3.3. Sector Zoning vs Sub-Sector Zoning

As shown above, growth desymmetrization is accompanied by pronounced optical growth sector zoning, also called *intra-growth sectoral zoning* or more succinctly *intra-sectoral zoning*. The observed optical indicatrix is often consistent with normal selectivity in the distribution of isomorphous components. Optical sub-sector zoning reflects tangential selectivity in the distribution of isomorphous components but it is not always evident. Even when growth proceeds by step motion, the optical anomalies are often paradoxically more consistent with normal selectivity.

A few hypotheses have been put forward to account for this conundrum. First, if the face grows through steps of variable orientation associated with distinct hillocks then the averaged optical indicatrix should reflect normal selectivity and correspond to the symmetry of the face. A version of this hypothesis was formulated by Gali (1983). Yet, the growth of many crystals is governed by a few (usually 1 or 2) vicinal hillocks controlling large areas of a given face so

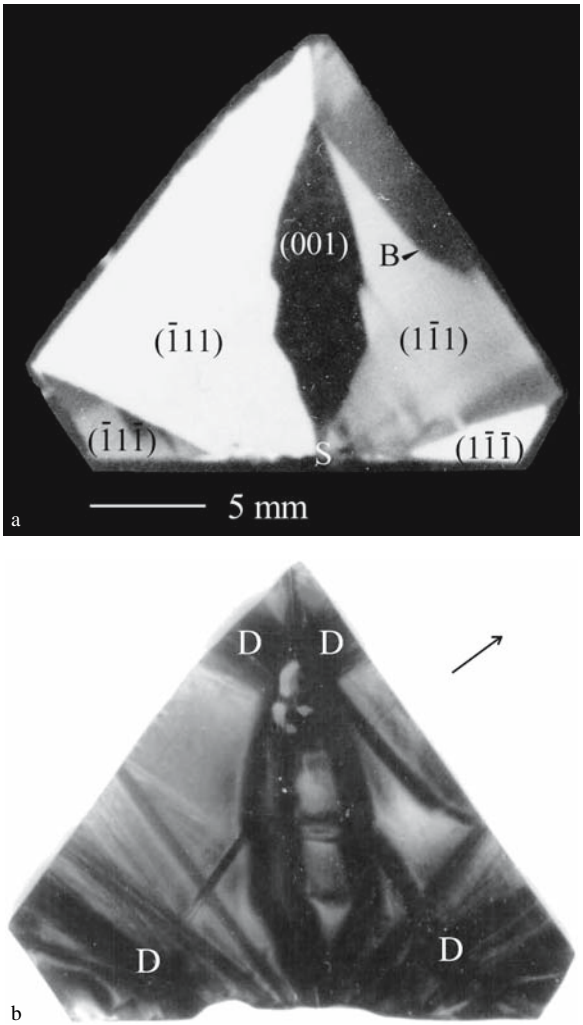

Figure 3.12. Sub-sector zoning in alum ($K(Al_{0.5}Cr_{0.5})(SO_4)_2 \cdot 12H_2O$). S = seed, B = sub-sector boundary that separates two regions formed by steps from different vicinal hillocks. (*a*) Anomalous birefringence. (*b*) X-ray diffraction topograph. The arrow indicates the diffraction vector **g** for reflection 333. D - bundles of dislocations originating from the seed and solution inclusions

that substantial sub-volumes are formed by steps of the same orientation (see e.g. Figure 3.12), thus obviating the averaging mechanism. Alternatively, we may presume that distortions induced by tangential selectivity are similar to those formed by normal selectivity because the principal differences in energy between the lattice sites arise from their non-equivalence with respect to the growth face and any additional non-equivalence imposed by the growth step is slight. Thus,

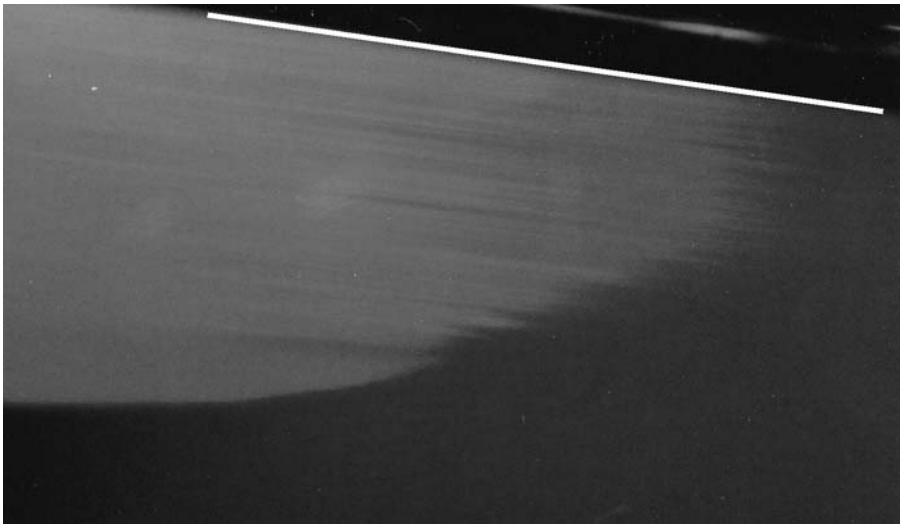

Figure 3.13. Photomicrograph of the sub-sector boundary marked by B in Figure 3.12. White line marks position of (111) face. Horizontal = 4 mm

the optical anomalies only appear to be controlled by normal selectivity when in reality they result from the tangential selectivity. This is plausible but not terribly satisfying.

Tangentially selected structural units can ultimately occupy positions expected by normal selectivity through diffusional relaxation discussed in section 3.4.7.

3.3.4. Concentric Zoning

Variable crystal growth conditions such temperature, hydrodynamics, supersaturation, solution composition, and micromorphology of the growth faces can affect growth ordering and associated optical anomalies (see section 3.5). Growth condition related inhomogeneities were observed in mixed alums (Shtukenberg *et al*., 1994b), strontium-lead nitrates (Shtukenberg, 2005) and grossular-andradite garnets (Figure 3.14). Figure 3.14*a* shows garnet with a distribution of aluminum and iron evident as differences in the transmitted light spectrum as well as in the interference colors between crossed polarizers (Figure 3.14*b*). Stress induced birefringence plays a minor role so the optical indicatrix in adjacent zones has largely the same orientation.

3.3.5. Anomalous Progression of Anomalous Birefringence

In some crystals such as mixed alums, anomalous optical inhomogeneity is manifest as the gradual increase of birefringence from the crystal center to the periphery (Figure 3.15). The birefringence either abruptly increases at the beginning of growth

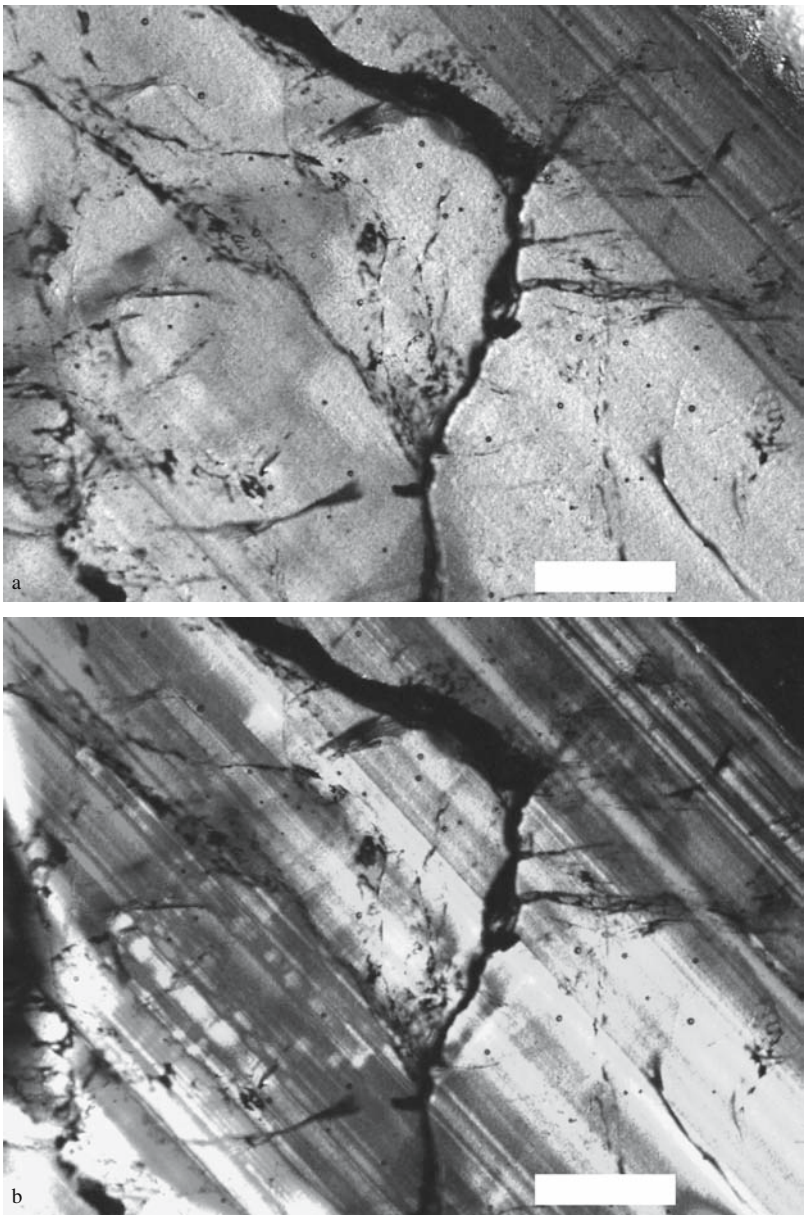

Figure 3.14. Optical zoning in {110} growth sector of grossular-andradite garnet. (*a*) In polarized light without analyzer. (*b*) Between crossed polarizers with a first order red retarder. Scale bar = 0.88 mm (see Color Section following page 254)

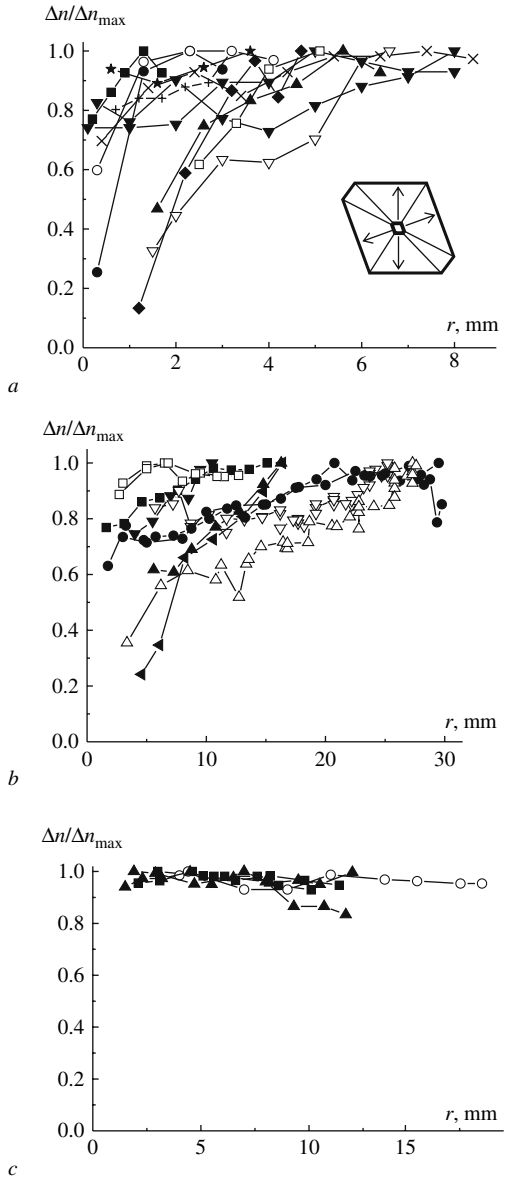

Figure 3.15. Birefringence (Δn) as a function of the radial distance from the seed r. Symbols denote different crystals. Data points in some cases represent crystals grown simultaneously. Δn_{max} is the maximum birefringence for the given profile. Insert shows the typical (110) section with four large {111} growth sectors and two small {100} sectors. The arrows indicate the directions along which the birefringence was measured. (*a*) $K(Al_{0.98-0.92}Cr_{0.02-0.08})(SO_4)_2 \cdot 12H_2O$ grown at $T = 25$–$35\,^{\circ}C$ under free convection, (*b*) $(K_{0.5}(NH_4)_{0.5})Al(SO_4)_2 \cdot 12H_2O$ grown at $T = 40$–$54\,^{\circ}C$ under strong stirring (40–60 rpm), (*c*) $K(Al_{0.4-0.6}Cr_{0.6-0.4})(SO_4)_2 \cdot 12H_2O$ grown at $T = 36$–$38\,^{\circ}C$ under strong stirring (40–60 rpm)

and then gradually approaches a constant value (Figure 3.15*a*) or it increases with constant rate (Figure 3.15*b*). These examples contrast sharply with optically anomalous crystals whose birefringence (Figure 3.15*c*) is constant with the radial distance from the seed or nucleus. These progressive changes do not appear to be related to the crystal composition, growth temperature, growth rate, micromorphology of the growth face, growth and post-growth annealing, or internal stress. The progression of anomalous birefringence can be mitigated by slowing growing crystals from seeds under carefully controlled conditions with strong stirring.

The following hypothesis (Shtukenberg and Punin, 2003) was suggested to explain progressive anomalous birefringence: At the beginning of growth, the degree of growth ordering η_0 may be slight because of peculiarities of the *seed regeneration*.

Seed regeneration is a mysterious though well established process for some crystals. On KDP and ADP seeds cut from larger crystals, growth begins first by regeneration or by "restoration". The quotation marks are given by Chernov (1984). A highly defective regeneration zone can clearly be seen in x-ray topographs (Fishman, 1970) that resolves itself before near perfect growth is reestablished.

After a regeneration stage in alums, crystals should have a degree of ordering $\eta_{\max}$ corresponding to a given composition and set of growth conditions. The degree of ordering at any radial distance η is defined by the competition between the maximum degree of ordering controlled by external growth conditions $\eta_{\max}$ and ordering inherited from the seed crystal and first deposited layers η_0. This competition can be simply formulated in terms of the change of the ordering in the surface layer $\Delta\eta = (\eta_{\text{new layer}} - \eta_{\text{previous layer}})$ and the deviation from the stationary value $(\eta_{\max} - \eta)$. Given that $\dfrac{d\eta}{dr} \approx \dfrac{\Delta\eta}{h}$ where h is the height of the elementary step, one can derive the following:

$$\frac{d\eta}{dr} = \alpha\,(\eta_{\max} - \eta)\,. \tag{3.1}$$

In this Equation α is a constant, and r is the radial distance from the seed crystal. Solving Equation (3.1) with the initial condition $\eta_{r=0} = \eta_0$ and assuming a proportionality between degree of ordering and the birefringence $\Delta n \sim \eta$ gives

$$\frac{\Delta n}{\Delta n_{\max}} = 1 + \left(\frac{\Delta n_0}{\Delta n_{\max}} - 1\right)\exp(-\alpha r)\,. \tag{3.2}$$

Here Δn_0 and $\Delta n_{\max}$ are the initial and maximum values of birefringence, respectively. The function (3.2) can fit the data (Figure 3.15). For the first progression (Figure 3.15*a*), $\Delta n_0 = (0.1 - 0.7)\Delta n_{\max}$, $\alpha = 0.8 - 1.3\,\text{mm}^{-1}$; for the second (Figure 3.15*b*) $\Delta n_0 = (0.2 - 0.8)\Delta n_{\max}$, $\alpha = 0.1 - 0.2\,\text{mm}^{-1}$; and for the third (Figure 3.15*c*, constant birefringence) $\Delta n_0 = \Delta n_{\max}$.

A similar progression of anomalous birefringence was seen in crystals of grossular-andradite garnets, although here it is impossible to rule out changes in growth conditions (Shtukenberg and Punin, 2003).

3.4. KINETIC ORDERING AND CRYSTAL STRUCTURE

3.4.1. Experimental Analyses

1. *Diffraction*. Single crystal x-ray, electron, or neutron diffraction were used to detect growth ordering in topaz (Ribbe, 1980), grossular-uvarovite garnets (Wildner and Andrut, 2001), sodium chlorate-bromate (Gopalan *et al.*, 1993; Crundwell *et al.*, 1997; Shtukenberg *et al.*, 2004), lead-barium nitrate (Gopalan and Kahr, 1993), lead-barium-strontium nitrate (Shtukenberg *et al.*, 2006a), pollucite $(Cs, Na)_2Al_2Si_4O_{12} \cdot H_2O$ (Frank-Kamenetskaya *et al.*, 1995), vesuvianite, $Ca_{19}(Mg, Fe, Al)_{13}Si_{18}O_{68}(O, OH, F)_{10}$; (Tanaka *et al.*, 2002a), yugawaralite (Tanaka *et al.*, 2002b), elbaite-liddicoatite tourmalines and alums (unpublished data). Growth ordering has even be detected in powder x-ray diffraction data for cordierite (Demina, 1980) and edingtonite (Akizuki, 1986).
   Unfortunately, x-ray scattering is not sensitive to slight differences in site occupancies and slight ordering presents difficulties in routine crystal structure refinement. Accurate diffractometry is essential otherwise the most appropriate space group cannot be identified (Seiler, 1992; Frank-Kamenetskaya and Rozhdestvenskaya, 2004). The proper determination of small differences in site occupancies is still a subject of discussion (see e.g. Kirfel, 1996; Kroll *et al.*, 1997; Merli *et al.*, 2000). The following criteria are used: 1. Distortions of unit cell dimensions (usually slight); 2. Differences in intensities of otherwise symmetry related reflections; 3. Appearance of systematically absent reflections. The detection of symmetry reduction by the aforementioned criteria is then supported by refinement of the crystal structures in a series of space groups. Application of x-ray diffraction to the desymmetrization of grossular-andradite solid solutions is illustrated in the next section. As described in the Foreword, the application of x-ray scattering to the analysis of desymmetrization in optically anomalous crystals was reviewed by Baur and Fischer (2003).
2. *Electron spin resonance (ESR) and nuclear magnetic resonance (NMR) spectroscopies* can accurately determine mixed atom occupancies in crystals. Naturally, paramagnetic ions or magnetic nuclei are requisite for ESR and NMR, respectively.
   Most contributions to the spin Hamiltonian in a magnetic resonance experiment such as the Zeeman interaction with the applied field, dipole-dipole interactions, spin-orbit coupling, quadrupolar interactions, scalar couplings, and electron shielding, for example, are anisotropic: they depend on the orientations of the crystal with respect to an applied magnetic field (Carrington and McLachlan, 1967). Thus, spectra associated with unpaired electrons or magnetic atoms at sites that are nominally related by symmetry in a crystal will be distinct so long as the crystal is in a general orientation with respect to the applied magnetic field. If these sites have different occupancies, the associated spectra will have different intensities. The variation in spectral intensity for sites otherwise symmetry related is strong evidence for kinetic ordering.

ESR was applied to the analysis of Al^{3+} in quartz (Tsinober *et al*, 1975), Cu^{2+} in zinc selenate (Anufriev *et al*., 1980; Bulka *et al*., 1980), Cu^{2+}, Gd^{3+}, and V^{4+} in kröhnkite, $Na_2Cd(SO_4)_2 \cdot 2H_2O$ (Vinokurov *et al*., 1977). NMR was applied to Al/Si ordering in cordierite (Putnis and Angel, 1985).

Anomalous biaxiality has been observed in a variety of quartz samples also subject to ESR analysis (Barry *et al*., 1965; Tsinober and Samoilovich, 1975). Relative ESR spectral intensities are well predicted by the site symmetry associated with faces bounding individual growth sectors. ESR spectra of synthetic smoky quartz (Tsinober and Samoilovich, 1975) showed that oxygen atoms belonging to three different SiO_4 tetrahedra form three spectra that are magnetically inequivalent for a general orientation with respect to the applied magnetic field. Moreover, intensities vary indicative of differing occupancies. The sectors formed by pinacoid faces ($\{0001\}$ surface symmetry 3) have three ESR spectra of equal intensity. The prism sectors ($\{10\bar{1}0\}$ surface symmetry 2) have two groups of lines with equal intensities while the third group is unique, and the rhombohedral sectors ($\{01\bar{1}1\}$ surface symmetry 1) have three distinct spectral intensities. Since the intensity of ESR transitions is proportional to the concentration of holes, the intensity dependencies confirm the desymmetrization. As a result, pinacoid growth sectors remain trigonal, prism sectors become monoclinic, and rhombohedral sectors become triclinic.

3. *Infrared and Raman spectroscopy*. Infrared (IR) dichroism was used to assay OH dipole orientations and OH/F ordering in topaz (Shinoda and Aikawa, 1994a,b), grossular garnet (Rossman and Aines, 1986), and apophyllite (Akizuki and Terada, 1998). Vibrational spectroscopy in polarized light was also used to establish Al/Si ordering in adularia (Akizuki and Sunagawa, 1978). IR spectroscopy is most effectively applied to high concentrations of isomorphous components. Al/Fe ordering in grossular-andradite garnets was too slight to be detected by infrared spectroscopy (McAloon and Hofmeister, 1993, 1995), although it was found by others (Takéuchi *et al*., 1982; Shtukenberg *et al*., 2002, see also next section). On the other hand, IR micro-spectroscopy is suited to smaller domains (Putnis and Bish, 1983).
4. *High-resolution transmission electron microscopy (HRTEM) and scanning electron microscopy (SEM)* sometimes can detect growth ordering in crystals if the degree of ordering is high and the guests induce appreciable distortions of the crystal structure as in cordierite (Putnis and Bish, 1983), calcite ($CaCO_3$) and dolomite ($(Ca, Mg)CO_3$) (Reeder, 1992) and prehnite (Akizuki, 1987a). If the degree of ordering is slight as in calcic garnets EM is usually not sensitive enough (Allen and Buseck, 1988).

3.4.2. Desymmetrization by X-Ray Diffraction

Optical anomalies in **grossular-andradite solid solutions** (grandites, $X_3Y_2(ZO_4)_3$, $X = Ca$, $Y = Al$, Fe, $Z = Si$, cubic space group $Ia\bar{3}d$) are common and pronounced (see sections 2.6.2.1 and 2.8.2.4). Birefringence of just 0.015 gives

rise to detectable phase differences even in thin sections. Although heterometry-induced stress contributes to anomalous birefringence it cannot account for large deviations from optical isotropy. A number of groups during the last 30 years attempted to find ordering in garnets by x-ray diffraction (Takéuchi and Haga, 1976; Takéuchi *et al*., 1982; Allen and Buseck, 1988; Kingma and Downs, 1989; Griffen *et al*., 1992; Wildner and Andrut, 2001; Shtukenberg *et al*., 2002, 2005), however, the precise nature of the organization was questionable until recently.

Three birefringent grandite samples cut from rhombic dodecahedral growth sectors (Table 3.3) were ground to spheres to obviate absorption corrections. Full spheres of data were collected with an automated four-circle diffractometer (Table 3.3).

The *unit cell* was pseudo-cubic with slight, yet significant, deviations of the β angle from 90° (Table 3.3), arguing for symmetry reduction to the monoclinic or even triclinic system. The complete set of reflections was divided into groups of equivalents with respect to particular symmetry operations (3 four-fold axes, 4 three-fold axes and 9 mirror planes). Intensities of reflections otherwise equivalent in the Laue group $m\bar{3}m$ were then compared. If the difference in intensities between the strongest and weakest reflections within the group $I_{max} - I_{min}$ exceeded $4\sigma_I$, where σ_I is the estimated standard deviation, the symmetry was assumed to be violated.

In one sample (Baz-1) from the Bazhenovskoe mine in the Ural mountains, Russia, the expected equivalences are imperfect and the differences are distributed among all classes of reflections (Figure 3.16) but these differences do not rise above the expected noise. For two other crystals, violations are greater (Figure 3.16) especially for particular symmetry operations. The mirror relationships (010), (101) and ($\bar{1}$01) are slightly violated suggesting orthorhombic (Laue class *mmm*) or triclinic (pseudo-orthorhombic Laue class $\bar{1}$) symmetry.

The clearest evidence of symmetry reduction is appearance of reflections forbidden in the ideal space group $Ia\bar{3}d$ (Table 3.4). Multiple scattering, a common cause of violations of extinction conditions evident in garnets (Rossmanith and Armbruster, 1995), was ruled out by comparing intensities using different scanning geometries.

In summary, analysis of the diffraction pattern suggests that the crystal structure distortions of Baz-1 are slight. The crystal is effectively cubic (space group $Ia\bar{3}d$). The symmetry of another sample (Baz-2) from the Bazhenovskoe mine is orthorhombic (space group *Fddd*) or triclinic (space group $I\bar{1}$). Likewise, a garnet from Mali (Mali) is triclinic (pseudo orthorhombic, space group $I\bar{1}$).

The crystal structures of all three samples were refined in $Ia\bar{3}d$, *Fddd* and $I\bar{1}$ (Tables 3.3–3.5).

For the sample Baz-1 the chemical composition and crystal structure were found to be very close to cubic grossular with the ideal formula $Ca_3Al_2(SiO_4)_3$. In other words, concentrations of minor ions in the X and Y sites were small, minimizing the possibility of kinetic growth ordering. Refinement of the crystal structure shows that Baz-1 is almost cubic (space group $Ia\bar{3}d$), irrespective of optical anomalies.

Table 3.3. Grossular-andradite garnet samples studied

Sample	Baz-1	Baz-2	Mali
Fe/(Fe + Al)	0.078	0.58	0.23
Birefringence, Δn	0.0002(1)	0.0089(1)	0.0066(1)
Density, g/cm^3	3.597(4)	3.703(2)	3.698(4)
μ, cm^{-1}	27.91	42.54	33.94
Unit cell dimensions			
Triclinic axes			
a, Å	11.856(4)	11.984(2)	11.892(2)
b, Å	11.853(4)	11.979(2)	11.889(2)
c, Å	11.857(4)	11.980(2)	11.892(2)
α, °	90.00(0)	90.00(2)	90.00(2)
β, °	90.00(3)	89.71(2)	90.12(2)
γ, °	90.00(0)	89.99(2)	90.03(2)
$< a >$, Å	11.855	11.981	11.891
Orthorhombic axes			
a, Å	16.760(5)	16.901(2)	16.810(5)
b, Å	11.856(3)	11.979(2)	11.895(5)
c, Å	16.768(5)	16.987(2)	16.848(5)
Number of measured reflections ($I > 2\sigma_I$)	8065	10619	9238
Number of unique reflections ($F > 4\sigma_I$)			
$Ia\bar{3}d$	314	325	482
Fddd	1853	1904	2193
$I\bar{1}$	-	7002	6773
R, %			
$Ia\bar{3}d$	2.81	2.64	4.49
Fddd	4.36	2.74	3.44
$I\bar{1}$	-	3.70	3.26
R_w, %			
$Ia\bar{3}d$	4.97	-	6.02
Fddd	5.16	4.63	3.82
$I\bar{1}$	-	5.07	3.80

Weight scheme: $w = 1/[\sigma_F{}^2 + kF_{obs.}{}^2]$, $k = 0.0010$–0.0068

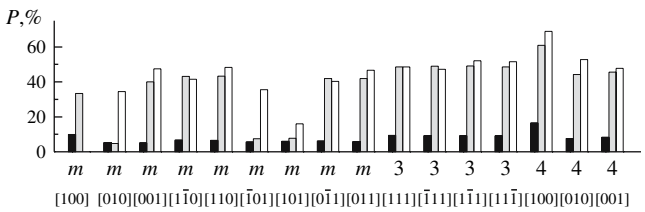

Figure 3.16. Percent of cubic-equivalent reflections that violate ($\Delta I > 4\sigma_I$) the given symmetry operations for the garnets (samples: solid bars – Baz-1, grey bars – Baz-2, open bars – Mali)

Table 3.4. Analysis of reflection conditions for the cubic space group $Ia\bar{3}d$.

Sample	Baz-1	Baz-2				Mali
Reflection conditions, Symmetry operations	Number of forbidden reflections	Number of forbidden reflection	Number of forbidden reflections verified by ψ-scans	Forbidden reflections whose presence was confirmed by ψ-scans Number	%	Number of forbidden reflections
hkl: $h+k+l=2n$ Translation $a/2+b/2+c/2$	0	0	–	–	–	0
$0kl$: $k=2n,\ l=2n$ b or c glide plane (100)	0	105	22	19	86	36
$h0l$: $h=2n,\ l=2n$ a or c glide plane (010)	0	5	5	0	0	7
$hk0$: $h=2n,\ k=2n$ a or b glide plane (001)	0	107	11	9	82	49
hhl: $2h+l=2n$ d glide plane (011)	0	81	22	13	59	41
hkh: $2h+k=2n$ d glide plane (110)	0	12	12	0	0	28
hkk: $2k+h=2n$ d glide plane (101)	0	81	16	10	63	35
Total number of forbidden reflections	0 (0%)	391 (4%)	–	–	–	196 (2%)

Refinement of the crystal structure of samples Baz-2 and Mali were consistent with substantive Fe concentrations and Al/Fe ordering over Y-octahedra (Table 3.5) accompanied by corresponding changes of the average cation-oxygen bond lengths $< Y-O >$.

Table 3.5. Y site Fe occupancies

		Space group $I\bar{1}$				Space group *Fddd*		
Site		Baz-2	Mali	Munam*		Baz-2	Mali	Munam*
0 0 0	Y1	0.830(5)	0.471(5)	0.41(1)	Y1	0.861(5)	0.344(6)	0.433(3)
$^1/_2$ 0 0	Y2	0.830(5)	0.241(5)	0.45(1)				
$^1/_4{}^1/_4{}^1/_4$	Y3	0.868(5)	0.258(5)	0.45(1)				
$^3/_4{}^3/_4{}^1/_4$	Y4	0.878(5)	0.340(5)	0.49(1)				
0 $^1/_2$ 0	Y5	0.277(5)	0.073(5)	0.15(1)	Y2	0.308(5)	0.052(6)	0.237(3)
$^1/_2{}^1/_2$ 0	Y6	0.279(5)	0.126(5)	0.29(1)				
$^1/_4{}^3/_4{}^1/_4$	Y7	0.308(5)	0.032(5)	0.27(1)				
$^3/_4{}^1/_4{}^1/_4$	Y8	0.320(5)	0.00(1)	0.16(1)				

* in accordance with Takéuchi *et al*. (1982)

Refinement of Baz-2 in the orthorhombic space group shows that the difference in iron atom fractions between two octahedral sites Y1 and Y2 is equal to 0.55 (Table 3.5). Refinement in the triclinic space group reveals that 8 non-equivalent Y-octahedra divided into two quartets. Each quartet has near equal occupancies and average values close to the those in the orthorhombic crystal structure. The variation of $< Y-O >$ bond lengths within these quartets does not exceed one standard deviation whereas the variation between quartets exceeds four. Thus refinement of the crystal structure also argues for the orthorhombic space group *Fddd*.

The Mali refinement in the orthorhombic space group gives differences in occupancies of Y1 and Y2 sites of 0.29 (Table 3.5). Refinement in the triclinic space group shows that 8 non-equivalent Y-octahedra are divided into two quartets with relatively close occupancies within each quartet, however, the difference in occupancies within one quartet significantly exceeds the error and achieves 0.23 (Table 3.5). The symmetry of this sample can be considered triclinic though deviations from orthorhombic symmetry are small.

The results agree with the most reliable data on 9 crystal structures of grossular-andradite and grossular-uvarovite garnets with anomalous birefringence (Takéuchi *et al*., 1982; Wildner and Andrut, 2001).

Alum crystals displaying anomalous birefringence (section 3.3.1) were likewise analyzed with x-rays. According to the optical data (section 3.3.1), the group theoretical analysis of the symmetry (section 3.2.2), and a comparison of symmetry related reflections (Figure 3.17) the alum crystal $K(Al_{0.6}Cr_{0.4})(SO_4)_2 \cdot 12H_2O$ is trigonal. However, refinement of the crystal structure did not reveal deviations from the cubic structure (Euler *et al*., 1999; Crundwell, 1997). Growth ordering of atoms likely occurs in this case as well but is too slight to be detected by x-ray diffraction.

Topaz displays clear sector zoning in the distribution of optical anomalies (Akizuki *et al*., 1979). The single crystal neutron diffraction experiment indicates symmetry reduction from the orthorhombic space group *Pbnm* down to the triclinic

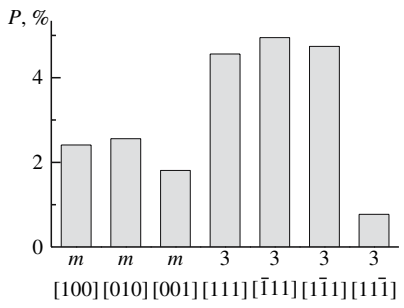

Figure 3.17. Percent of cubic equivalent reflections that violate $I_{max} - I_{min} > 2(I_{hkl} - I_{\overline{hkl}})_{max}$. The trigonal symmetry is supported by the slight violation of one three-fold axis compared with the other three-fold axes and also with all mirror planes

space group $P1$. Symmetry reduction is manifest in the appearance of forbidden reflections (Parise *et al*., 1980; Ribbe, 1980). Refinement of the crystal structure revealed that the partial ordering of OH^- groups might be responsible for the optical anomalies in topaz.

Growth sector zoning as a consequence of kinetic ordering is well illustrated in the x-ray analysis of **1,5-dichloro-2,3-dinitrobenzene** (DCDNB, $C_6H_2Cl_2(NO_2)_2$). This is an excellent illustration of the orientational ordering of dissymmetric structural units. Artini (1907) reported that although crystals of DCDNB from many solvents appeared to be tetragonal microscopy of square (001) sections showed division along the diagonals into four distinctly biaxial sectors related to one another by 90° rotation about [001], the apparent four-fold symmetry axis (Figure 3.18). In a reinvestigation Kahr and McBride (1992) refined lattice parameters from x-ray diffraction data from adjacent (011) growth sectors from a single plate.

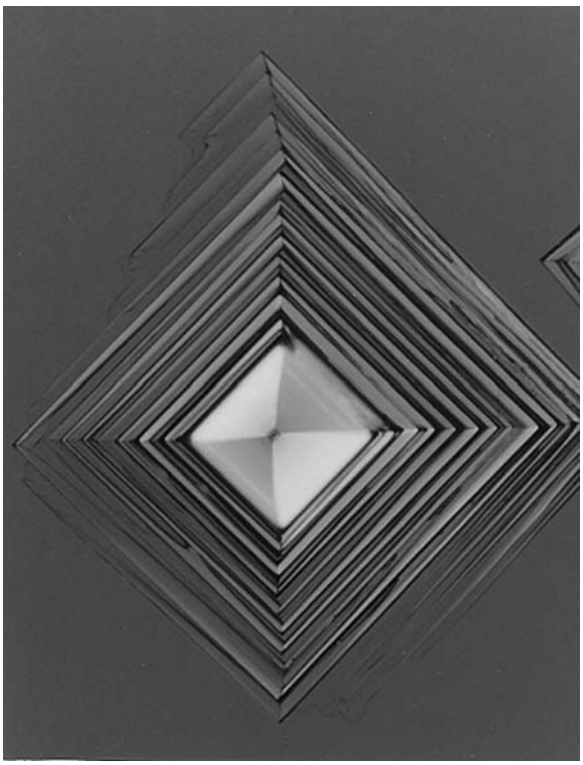

Figure 3.18. Photomicrograph of 1,5-dichloro-2,3-dinitrobenzene grown from chloroform. Crystal between crossed polarizers with a first order red retarder in the diagonal position. Diagonal width = 0.24 mm. Thickness = 0.024 mm at perimeter of central bright square
Source: Reprinted with permission from Kahr, B., McBride, J.M. "Optically Anomolous Crystals" *Angewandle Chemie, International Edition in English*, 1992, *31* p.1–26. Copyright 1992 Wiley-VCH, STM. (see Color Section following page 254)

This data showed a near orthorhombic cell with the principal axes in adjacent sectors rotated by 90° about [001]. At a superficial level the absence of four-fold symmetry mandates the biaxiality and resolves the anomaly, however refinement of the crystal structure revealed a mechanism for the symmetry reduction that exemplifies the type of molecular recognition during crystal growth that underlies the kinetic origin of many optical anomalies. An ordered crystal structure for DCDNB was refined to $R = 0.087$ in space group $P2_12_12$. This orthorhombic space group differs from the tetragonal group $P4_12_12$ by the absence of two-fold rotational axes along the molecular C2-C5 axes. Thus 5-chloro-1,2,3-trinitrobenzene (CTNB, $C_6H_2Cl(NO_2)_3$), the analogue of DCDNB in which the chlorine at position 1 has been replaced by a nitro group to actualize molecular two-fold rotation gives crystals in space group $P4_12_12$ that are isomorphous with DCDNB. CTNB does not show growth sector zoning or anomalous biaxiality. If the growing crystal of DCDNB were totally unable to distinguish between the 3-chloro and 1-nitro groups flanking the 2-nitro position, the molecule would be incorporated from solution with complete rotational disorder about the C2-C5 axis, and the additional effective molecular symmetry would make the crystal truly tetragonal. The residual electron density after x-ray refinement of the $P2_12_12$ structure showed peaks consistent with this kind of disorder. The degree of rotational disorder was refined independently in each of the four molecular sites which are nominally related by symmetry in space group $P2_12_12$. This five-parameter model gave much improved agreement with x-ray data collected from an untwinned crystal fragment ($R = 0.065$). The model showed that the minor molecular orientation was present in substantial amounts that varied from site to site: 32, 31, 15, and 18% (Figure 3.19).

These population differences lower the crystal symmetry to $P1$ and reflect how molecules from solution were incorporated during growth into the different "symmetry-related" sites. The differences can be visualized by examining how molecules are oriented in one of the four molecular layers which stack along [001], the approximate fourfold screw axis of the unit cell. The same pattern arises by the same mechanism in the other three molecular layers of the unit cell, except that each is rotated by the four-fold screw axis that passes through the center of the original square (Figure 3.20).

3.4.3. Kinetic Ordering and the Optical Indicatrix

X-ray diffraction reveals the ordering of atoms presumably related to growth desymmetrization, the likely etiology of many optical anomalies. However, the observation of desymmetrization does not establish a *causal* relationship. Afterall, distortions of the optical indicatrix can be related to internal stress and the optical consequences of desymmetrization could be subordinate to those piezo-optic distortions (section 2.2) of the indicatrix.

A more substantive demonstration of such a causal relationship would be the computation of the distorted optical indicatrix from the refined, dissymmetric crystal

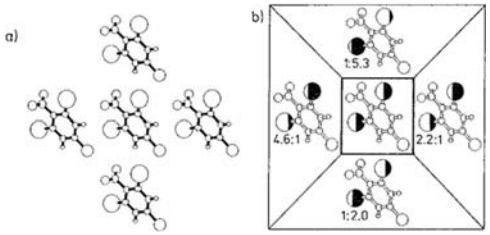

Figure 3.19. (*a*) Five molecules of 1,5-dichloro-2,3-dinitrobenzene in one layer with the identity of the 1- and 3-substituents (C1 or NO_2) undefined, represented as large unfilled circles. The molecules are related by [100] and [010] translations. (*b*) The central square symbolizes a growing crystal plate, and the four surrounding trapezoids represent the four growth sectors formed by adding molecules through the sides of the square. The average orientation of the molecules within each sector is indicated by the shading of the circles representing 1- and 3-substituents. The ratio of dark to light areas in a circle corresponds to the NO_2 to Cl occupancies. In the bottom and right sectors molecules are oriented so that chlorines contact the growth surface of the central square 2/3 of the time. At the top and left edges the bias is ca. 5 : 1 in the opposite direction, favoring contact of nitro with the growth surface. Apparently molecules from solution prefer to approach the bottom and right faces with their 1-chloro substituent toward the 5-chloro group of the surface molecules, and to approach the top and left faces with their 3-nitro group toward the 2-nitro group of the surface molecules
Source: Reprinted with permission from Kahr, B., McBride, J.M. "Optically Anomolous Crystals" *Angewandle Chemie, International Edition in English*, 1992, *31* p.1–26. Copyright 1992 Wiley-VCH, STM.

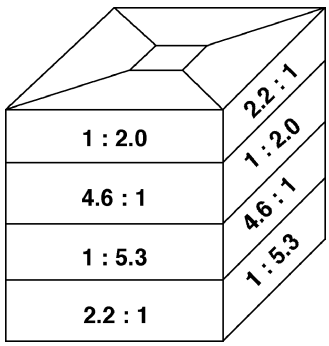

Figure 3.20. Stack of four successive layers of 1,5-dichloro-2,3-dinitrobenzene showing the sequence of chloro:nitro population ratios in the 1-position of molecules in each sector and layer. Each of the four sectors of the macroscopic 3-dimensional crystal is a stack of the same set of four different orientational populations in the same order, but from sector to sector the entire set is rotated by 90° and displaced by one layer
Source: Reprinted with permission from Kahr, B., McBride, J.M. "Optically Anomolous Crystals" *Angewandle Chemie, International Edition in English*, 1992, *31* p.1-26. Copyright 1992 Wiley-VCH, STM.

structure. Such calculations were performed within the framework of the point-dipole model (section 1.1.5.4) for ugrandite garnets (Shtukenberg *et al*., 2002, 2005) and solid solutions of sodium chlorate-bromate (Gopalan *et al*., 1997; Shtukenberg *et al*., 2004) and of lead-barium-strontium nitrate (Shtukenberg *et al*., 2006a).

Lattice constants, atom coordinates, site occupancies, and electronic polarizabilities are required input. The crystallographic parameters are known from diffraction. The electronic polarizabilities are assigned by comparison with related substances and to mimic the experimental refractive indices.

Garnets. For the calculation of the optical indicatrix we used two of our refined structures (section 3.4.2), three refinements from Takéuchi *et al*., (1982) and six from Wildner and Andrut (2001). The polarizabilities of Ca, Si, Al, Fe, Cr were chosen from the most typical values reported for the silicate minerals (Batsanov, 1966; Lasaga and Cygan, 1982; Lager *et al*., 1987; Abbott, 1993, 1994, 1996). The oxygen polarizability was variable for grossular, andradite, and uvarovite garnets. These values are given in Table 3.6. The calculations were performed using AnRef software by D.Yu. Popov.

The calculations performed for the pseudo-cubic coordinate frame have shown that 9 of 11 samples reveal the following orientation: $X \parallel [101]$, $Z \parallel [\bar{1}01]$ and $Y \parallel [010]$. Deviations from these directions are within 20° (Figure 3.21). This orientation is close to that observed for the most birefringent rhombic dodecahedral growth sectors of garnet (Table 3.2). The axial angle is equal to $90 \pm 10°$, close to the measured values. Thus, correspondence between the calculated and observed optical indicatrix confirms the relationship between anomalous birefringence and cation ordering in ugrandite garnets. Systematic underestimation of birefringence by 2-5 times is likely a consequence of uncertainties in polarizabilities as well as the infelicitous use of isotropic polarizabilities (Shtukenberg *et al*., 2002, 2005). Calculations based on the structures of Takéuchi *et al*. (1982) gave the incorrect indicatrix orientation (Figure 3.21).

Table 3.6. Electronic polarizabilities of ions α_i used for the calculation of the optical indicatrix of ugrandite garnets. Silicate data from Batsanov (1966), Lasaga and Cygan (1982), Lager *et al*., (1987), and Abbott (1993, 1994, 1996). $n_{obs.}$ and $n_{calc.}$ are the measured and calculated refractive indices

Polarizabilities α_i, Å^3	Data on silicates	Common values for most minerals	Final set		
			Grossular	Andradite	Uvarovite
Si^{4+}	0.0–0.71	0.0–0.32	0.20	0.20	0.20
Ca^{2+}	0.25–1.90	0.61–1.12	0.73	0.73	0.73
O^{2-}	0.93–1.60	1.16–1.60	1.36	1.48	1.49
Al^{3+}	0.13–0.65	0.13–0.42	0.27	–	–
Fe^{3+}	1.13	1.13	–	1.13	–
Cr^{3+}	0.58–1.00	0.58–1.00	–	–	0.80
$n_{obs.}$	–	–	1.734	1.887	1.855
$n_{calc.}$	–	–	1.7357	1.8865	1.852

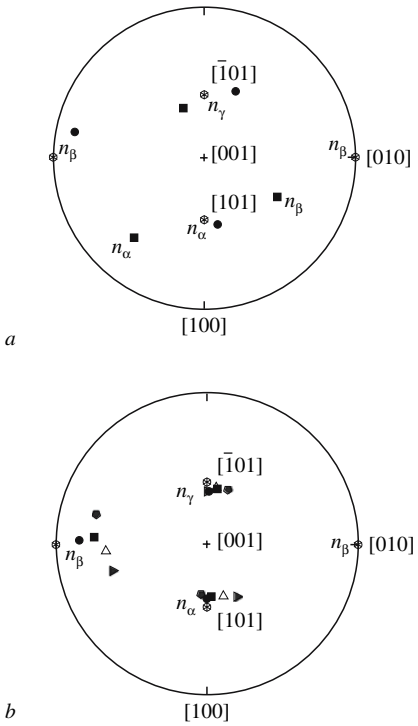

Figure 3.21. Orientation of the optical indicatrix in (*a*) grossular-andradite solid solutions and (*b*) grossular-uvarovite solid solutions. Sectored hexagons mark the observed optical indicatrix, open triangles represent calculations based on the orthorhombic crystal structure refinement, and other symbols represent calculations based on the triclinic crystal structure refinement. The orientation of the optical indicatrix is not shown for two crystals refined in the orthorhombic space group that display another indicatrix orientation

In the mixed **sodium halates**, $Na(Cl, Br)O_3$, the chlorate and bromate ions are non-statistically distributed among four symmetry related sites in the cubic space group $P2_13$. The optical indicatrix was calculated for the two samples, whose crystal structures were refined as both monoclinic ($P2_1$) and triclinic ($P1$) space groups (Gopalan *et al.*, 1993; Crundwell *et al.*, 1997; Shtukenberg *et al.*, 2004). The polarizabilities of ions Na^+, Cl^{5+}, Br^{5+} and O^{2-} equal to 0.32, 0.32, 0.8 and 1.52 Å^3, respectively, were taken from (Batsanov, 1966). The polarizabilities of anions O^{2-} were manipulated (1.36 Å^3 for $NaClO_3$ and 1.42 Å^3 for $NaBrO_3$) to match experimental refractive indices.

We tried to calculate the optical indicatrix for both the monoclinic and the triclinic structures, but failed to get any plausible results in the latter case. The calculated indicatrix for the monoclinic structure matched the observed indicatrix orientation (Figure 3.22). The calculated axial angle ($2V = 85$–$87°$) was close to the observed angle (90°), however, the calculated values of birefringence $\Delta n = n_\gamma - n_\alpha = 0.0061$

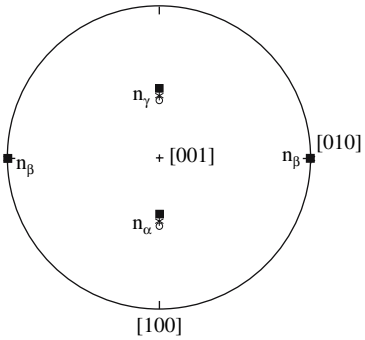

Figure 3.22. Orientation of the optical indicatrix in two solid solutions of $Na(Cl, Br)O_3$. Stars correspond to the observed optical indicatrix, circles and squares represent calculations

and 0.0080, respectively, were an order of magnitude larger than the observed values of 0.0007 and 0.0010. The discrepancy likely stems from the uncertainties in the electronic polarizabilities of atoms.

Munn (2000) calculated optical indicatrix of optically anomalous **1,5-dichloro-2,3-dintirobenzene** (DCDNB). Reliable calculations on refractive indices for molecular crystals have been hard to come by (Reis *et al*., 1998, 2000). Munn departed from the point-dipole model (section 1.1.5.4) which has been so successful for ionic compounds because he was dealing with an aromatic molecule with highly delocalized electrons. He therefore calculated molecular polarizabilities using *ab initio* molecular orbital calculations. To match the observed indicatrix, Munn then had to use the molecular polarizability to mimic the disordered structure. Several models were tried: 1. *Independent averaged planes*. The layers were given an average molecular polarizability based on the observed disorder. Dipole interactions between layers were precluded. 2. *Interacting averaged planes*. Nearest-neighbor planes were allowed to interact. 3. *Interacting pseudo-statistical planes*. The average polarizability over orientations in a plane was replaced with sequences of planes in major and minor orientations so as to reproduce the disorder. Munn found that the results were not very sensitive to the precise treatment of the disorder so long as neighboring interactions between layers were included in the susceptibility calculation.

3.4.4. Kinetic Ordering and Anomalous Pleochroism

The effects of kinetic ordering on the optical indicatrix, a representation of the real part of the dielectric susceptibility, are also reflected in the absorption ellipsoid, a representation of the imaginary part of the dielectric susceptibility. Kinetic ordering associated with a species that absorbs light gives rise to anomalous linear dichroism in conjunction with anomalous linear birefringence. Sometimes authors refer to anomalous *pleochroism*. Strictly speaking dichroism refers to a comparison

of two distinct axes of absorption while pleochroism or *trichroism* refer to a comparison between three such axes. However, dichroism and pleochroism are often used interchangeably.

We would expect that the absorption ellipsoid of colored quartz would obey the crystal symmetry. Therefore, amethyst and smoky quartz should be dichroic with one color associated with the ordinary ray and another with the extraordinary ray. Amethyst and smoky quartz (trigonal point group 32) have long been studied for their anomalous pleochroism which coexists with anomalous birefringence (Tsinober *et al*., 1967a,b; Rumyantsev and Novozhilov, 1980). In reality, symmetry distinct growth sectors have differentiable pleochroism and symmetry related growth sectors orient their absorption ellipsoids in different directions.

In many optically anomalous crystals, the absorption ellipsoid must undergo desymmetrization so as to follow the distortion of the indicatrix. However, the changes in the absorption for transparent crystals such as mixed halates, nitrates and some mixed alums, will be evident only in the deep ultraviolet part of the absorption spectrum. Such disymmetries will be hard to detect by absorption—and impossible to observe by microscopy unless all of the optical components are fashioned out of material such as fluorite that is transparent in the ultraviolet. A class of crystals that are rich in their anomalous absorption are so-called dyed crystals. These are crystals of simple substances grown from solutions containing organic dyes that absorb light in the visible part of the spectrum.

In the middle of the Nineteenth Century, Sénarmont (1854) contemplated whether pleochroism might be imparted to an otherwise transparent crystal if a colored material present in solution should stain the crystal during growth. Sénarmont was satisfied by red, pleochroic crystals of $Sr(NO_3)_2 \cdot 4H_2O$ that he grew from a solution containing a dye extracted from the logwood tree (Kahr *et al*., 1997).

Gaubert was the first to observe anomalous linear birefringence' in dyed crystals during his investigations of sodium and ammonium halides (Gaubert, 1915). Slavnova and others detected anomalous linear birefringence in dyed alkaline earth nitrates (Melankholin and Slavnova, 1959; Khlopin and Tolstaya, 1940). Figure 3.23*b* is a micrograph indicating direction of the absorption of methylene blue within crystals of $Ba(NO_3)_2$. The 60° relationships are to be expected between {111} sectors whose bounding facets are not normal to the wavevector. France and Davis (1936) observed anomalous linear dichroism in cubic alum crystals containing various dyes. Frondel (1940) observed anomalous linear dichroism in the cubic alkali fluorides.

Dyed, hexagonal crystals ($P6_3$) of $LiKSO_4$ were grown by slow evaporation at room temperature of aqueous solutions (10^{-4} M in the dye Chicago sky blue CSB (Colour Index No. 24410)) containing equi-molar quantities of Li_2SO_4 and K_2SO_4. The resulting crystals grew by spontaneous nucleation such that they were oriented with their unique [0001] axes $\perp$ or || to the bottom of the crystallization dishes (Figure 3.24*a*, *b*). The hexagonal bi-pyramidal habit (Figure 3.25) is a consequence of enantiomorphous twinning both $\perp$ and || to [0001]. The {0001} growth sectors

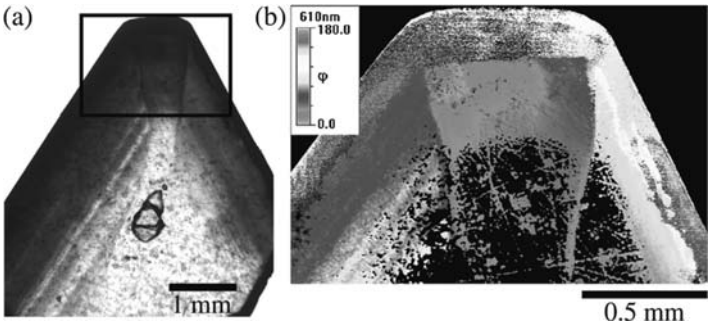

Figure 3.23. (*a*) Barium nitrate with {111} habit grown in the presence of methylene blue. (*b*) Map of the absorption of the most absorbing direction measured counterclockwise from the horizontal
Source: Originally published in Liu, X. Y. and De Yoreo, J.J. *Nanoscale Structure and Assembly at Solid-Fluid Interfaces*, 2004, 700 p., Copyright 2004 Springer (formerly Kluwer Academic Publishers, Boston) (see Color Section following page 254)

were heavily colored whereas the $\{01\bar{1}1\}$ growth sectors were less optically dense by a factor of 4. The birefringence of $LiKSO_4$ is very small ($n_\varepsilon - n_\omega = 0.0005$).

From the dichroic ratio for light polarized along the extinction directions in $LiKSO_4$ (n' and n''), we calculated that the CSB electric dipole transition moments, $\theta = \arctan[(\alpha'/\alpha'')^{1/2}]$ bisect n' and n'' of the host. However, we can not ordinarily determine for any one sector whether this deviation θ is clockwise or counterclockwise from say n' from measurements of absorption in linearly polarized as the electric field is constrained to projections on the eigenmodes. These possibilities would lead to very different models of guest association with the surfaces of the host crystal.

The *absolute orientations* – the clockwise or counterclockwise rotations with respect to a defined eigenmode – of the dipoles were evidence in the differential transmission of left and right circularly polarized light. the clockwise or counterclockwise rotation with respect to a defined eigenmode. This is a wholly new optical anomaly that is a consequence of desymmetrization and is detected with circularly polarized light. A non-zero differential circular transmission rules out a random distribution of dipoles, and the sign differentiates between clockwise and counterclockwise deviations from the n'' vibration direction. CSB molecules are distributed in the crystal as shown in Figure 3.26. The logic of this proof is as follows. The upper right $\{01\bar{1}1\}$ sector is red in Figure 3.24. This means that right circularly polarized light is more effectively transmitted than left circularly polarized light ($I_R > I_L$). Left circularly polarized light entering a quarter waveplate will yield linearly polarized light oriented at $+45°$ with respect to the fast direction of the crystal which is vertical in Figures 3.24–3.26. If the chromophores are oriented at $+45°$, they will absorb and attenuate left circularly polarized light. Likewise, in the upper left $\{01\bar{1}1\}$ sector, $I_L > I_R$, as indicated by the blue color in the micrographs in Figure 3.24.

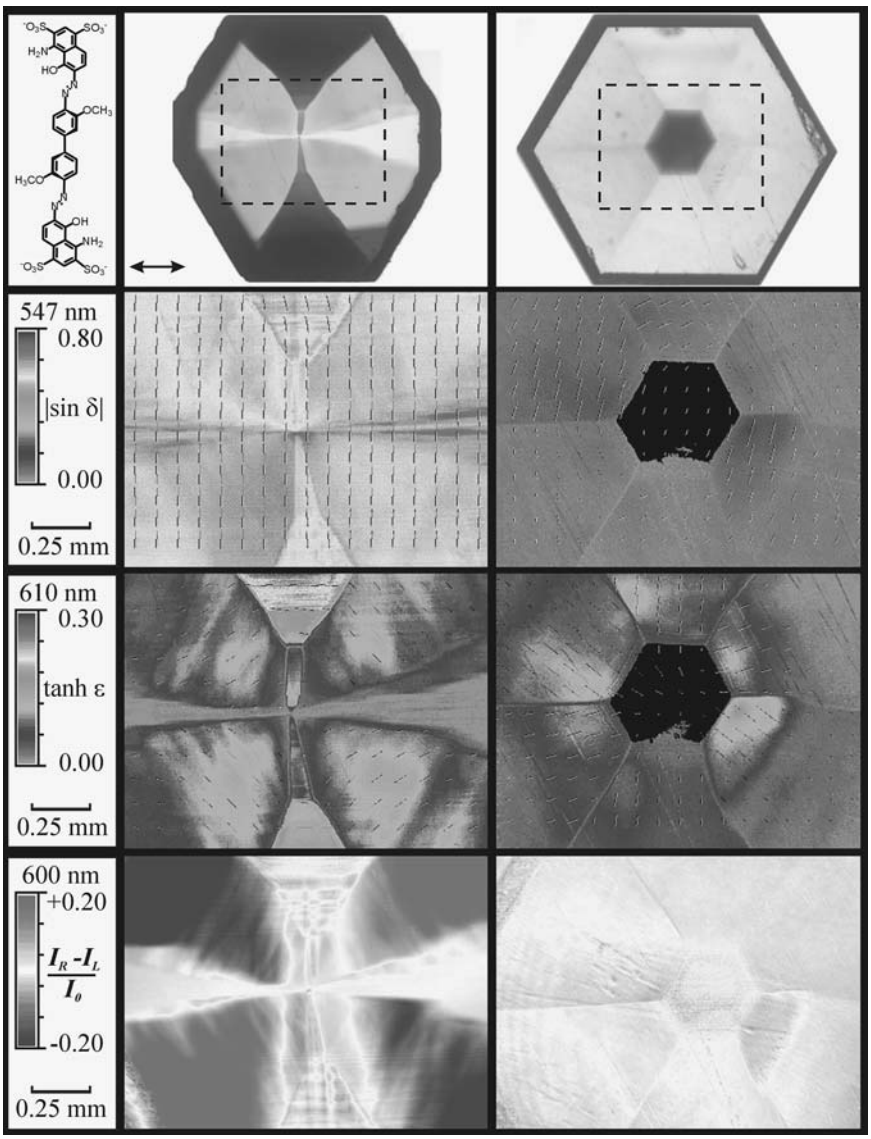

Figure 3.24. Chicago sky blue dyed $LiKSO_4$ crystals. Images in the left column are made along the [100] direction of 0.68 mm thick section, [001] is vertical. Images in the right column are made along the [001] of 0.38 mm thick section. (a, b) Photographs in light polarized along the arrow. Dotted, rectangular enclosures are imaged below. (c, d) Linear birefringence micrographs, $\delta = 2\pi L\Delta n/\lambda$. ($e$, f) Linear dichroism micrographs, $\tanh \varepsilon = 2(T' - T'')/(T' + T'')$. ($g$, h) circular extinction micrographs, $(I_R - I_L)/I_o$
Source: Reprinted with permission from Claborn, K., Chu, A.S., Jang, S.H., Su, F., Kaminsky, W. and Kahr, B. "Circular Extinction Imaging: Determination of the Absolute Orientation of Embedded Chromophores in Enantiomorphously Twinned $LiKSO_4$ crystals" *Cryst. Growth Des.* **2005,** *5*, p.2117–2123. Copyright 2005 American Chemical Society (see Color Section following page 254)

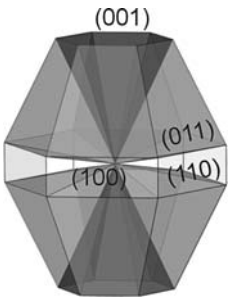

Figure 3.25. Idealized $LiKSO_4$ crystal habit, a consequence of ubiquitous enantiomorphous twinning, with shading representing the coloring by Chicago sky blue
Source: Reprinted with permission from Claborn, K., Chu, A.S., Jang, S.H., Su, F., Kaminsky, W. and Kahr, B. "Circular Extinction Imaging: Determination of the Absolute Orientation of Embedded Chromophores in Enantiomorphously Twinned $LiKSO_4$ crystals" *Cryst. Growth Des.* **2005,** *5*, p.2117–2123. Copyright 2005 American Chemical Society.

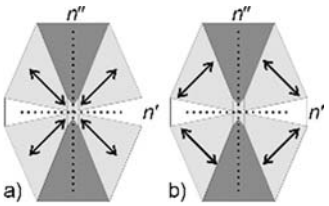

Figure 3.26. Idealized slices of dyed $LiKSO_4$ crystals. Dotted lines (n' and n'') are extinction directions of the host. Arrows in (*a*) and (*b*) represent two possible dispositions of adsorbed dipoles in the {011} sectors that are indistinguishable by polarized absorption measurements alone. Anomalous circular extinction data in Figure 3.24 indicate that Chicago sky blue dipoles are distributed as in (*a*)
Source: Reprinted with permission from Claborn, K., Chu, A.S., Jang, S.H., Su, F., Kaminsky, W. and Kahr, B. "Circular Extinction Imaging: Determination of the Absolute Orientation of Embedded Chromophores in Enantiomorphously Twinned $LiKSO_4$ crystals" *Cryst. Growth Des.* **2005,** *5*, p.2117–2123. Copyright 2005 American Chemical Society.

3.4.5. Metastability of Kinetic Ordering

3.4.5.1. General remarks

Solid solutions in which guests are non-statistically distributed among sites that would otherwise have the same potential energy are presumably not at equilibrium. Validation of the kinetic ordering model requires a demonstration of the metastability of optical anomalies. On the other hand, according to Hatch and Griffen (1989) the ordering in grossular-andradite garnets is a result of a temperature or stress driven order-disorder phase transformation. In their view, the birefringence is that of a non-cubic crystal phase at equilibrium under a given set of conditions.

In the kinetic ordering model, the non-statistical arrangement of structural units on a surface becomes metastable as soon as a newly formed layer with non-statistically distributed impurities is buried within the crystal volume. Diffusion, sluggish in solids at room temperature, then begins to slowly equalize the occupancies. At high temperatures ($T > 0.8T_{\text{melt.}}$) the diffusive redistribution of occupancies is considerably faster. Thus, if the ordering is kinetic in origin, annealing should significantly reduce the birefringence. This phenomenon has been observed for a number of crystals including the following: quartz (Samoilovich *et al.*, 1968; Tsinober and Samoilovich, 1975), brookite (TiO_2, Ikornikova-Lemmlein, 1946), topaz (Akizuki *et al.*, 1979), analcime (Náray-Szabó, 1938), ralstonite ($Na_xMg_xAl_{2-x}(F, OH)_6 \cdot (H_2O)$; Stepanov and Moleva, 1962), sodium chlorate-bromate (Gopalan *et al.*, 1993; Crundwell *et al.*, 1997), grossular-andradite garnets (Hariya and Kimura, 1978; Takéuchi *et al.*, 1982; Allen and Buseck, 1988), synthetic garnets $(Y_{0.53}Nd_{0.47})_3Ga_5O_{12}$ (Kitamura *et al.*, 1986a), and lead-strontium nitrate (Shtukenberg, 2005) among others.

For the grandite garnets (Allen and Buseck, 1988) and sodium chlorate-bromate solid solutions (Gopalan *et al.*, 1993; Crundwell, 1997; Crundwell *et al.*, 1997) the crystal structures of samples were refined before and after crystal annealing. The equalization of occupancies after the annealing was accompanied by the simultaneous disappearance of the optical anomalies. These experiments provide strong evidence for the origin of optical anomalies in the kinetics of mixed crystal growth and confirm the desymmetrization mechanism.

3.4.5.2. Annealing kinetics

Crystals containing two types of atoms or structural units, marked by superscript $[i] = [1],\ [2]$, may be ordered over two sites in the crystal structure. The concentration or occupancy (atomic fraction) of one component in the first site is $x^{[1]}$, and the second site is $x^{[2]}$. Generally, each site [1] has $n^{[1-1]}$ nearest neighbors of the type [1] and $n^{[1-2]}$ neighbors of type [2]. Assuming structural units randomly diffuse stepwise to neighboring positions, the kinetic equation describing time evolution of the concentration at the site [1] is:

$$\frac{dx^{[1]}}{dt} = \frac{n^{[1-1]}P_E x^{[1]} + n^{[1-2]}P_E x^{[2]}}{n^{[1-1]} + n^{[1-2]}} - P_E x^{[1]} =$$

$$= \frac{n^{[1-2]}}{n^{[1-1]} + n^{[1-2]}} P_E \left(x^{[2]} - x^{[1]}\right) = n^* P_E \left(x^{[2]} - x^{[1]}\right) \tag{3.3}$$

In this Equation t denotes time and P_E corresponds to the probability of a jump to a neighboring (vacant) site. The same result can be obtained considering site [2]. The solution of this Equation yields

$$\frac{x^{[2]} - x^{[1]}}{x_0^{[2]} - x_0^{[1]}} = \exp\left(-2n^* P_E t\right) = \exp\left(-\frac{2n^* D_v t}{h^2}\right) \tag{3.4}$$

where $x_0^{[2]} - x_0^{[1]}$ and $x^{[2]} - x^{[1]}$ denote the differences in occupancies before and after annealing for time t, h is the distance between the neighbor sites $[i]$, and $D_v = h^2 P_E$ is the self-diffusion coefficient. In Equation (3.4), average characteristic diffusion constants are used. If the birefringence Δn (or some other appropriate characteristic of anomalous crystal optics) is directly proportional to the difference in occupancies of one species at different sites, an assumption confirmed by modeling the optical indicatrix (section 3.4.3), then the reaction progress $1 - \xi$ can be found from

$$\xi = \frac{\Delta n}{\Delta n_0} = \exp\left(-\frac{2n^* D_v t}{h^2}\right) = \exp(-kt) \tag{3.5}$$

where subscript 0 refers to initial birefringence. The decrease of anomalous birefringence during high-temperature annealing obeys first order reaction kinetics, declining exponentially with the annealing time. This Equation contains the self-diffusion coefficient (D_v) which exponentially depends on the temperature

$$D_v = D_{v0} \exp\left(-\frac{E_d}{RT}\right) \tag{3.6}$$

where E_d is the activation energy, D_{v0} is the pre-exponential term and R is the universal gas constant. Correspondingly, the annealing rate should also increase exponentially with temperature.

If the growth ordering is well described, annealing kinetics of anomalous birefringence can be used to assess self-diffusion coefficients.

3.4.5.3. Selected examples

Quartz. The annealing kinetics of quartz crystals was previously studied (Samoilovich *et al*., 1968; Tsinober and Samoilovich, 1975). The activation energy for atomic disordering was 29 kJ/mol, a small amount of energy compared with activation barriers reported for other inorganic compounds (Lasaga, 1981b; Poirier, 1985) including oxygen self-diffusion in quartz (231 kJ/mol) and ions in alkali halogenides (90–120 kJ/mol). The probable reason for this discrepancy is the equalization of occupancies by filling holes which can significantly affect the EPR spectra. Obviously, it leads to errors in the values of activation energy found.

Alums. Annealing kinetics were measured for two isomorphous series $(K, NH_4)Al(SO_4)_2 \cdot 12H_2O$ and $K(Al, Cr)(SO_4)_2 \cdot 12H_2O$ (Shtukenberg *et al*., 1998). It shows a plot of $\ln \xi$ versus t (Figure 3.27) indicating first order annealing kinetics with a rate constant k: $\xi = \exp(-kt)$ (cf. with Equation (3.5)). The value of k does not depend on the initial birefringence Δn_0, further evidence of first order reaction kinetics. The value of k changes from one crystal to another with differences exceeding the experimental error (Figure 3.27). For any given crystal $k_{(111)} > k_{(100)}$ while $k_{(100)}/k_{(111)}$ varies from 0.24–0.72 with nine samples averaging 0.35.

As $\ln k$ is inversely proportional to the reciprocal temperature $1/T$ (Figure 3.28) the birefringence decrease is governed by Arrhenius kinetics $k = k_0 \exp(-E_d/RT)$

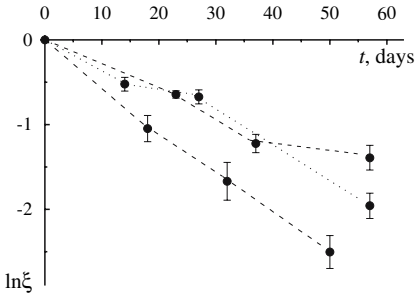

Figure 3.27. Decreasing birefringence of alum $(NH_4, K)Al(SO_4)_2 \cdot 12H_2O$ {111} growth sectors as a function of the annealing time at 50 °C

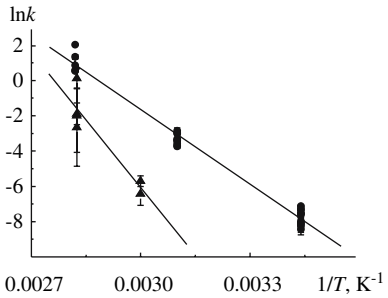

Figure 3.28. Arrhenius plot for the transformation from birefringent to isotropic {111} growth sectors in solid solutions of alums. Circles – series $(NH_4, K)Al(SO_4)_2 \cdot 12H_2O$; triangles – series $K(Al, Cr)(SO_4)_2 \cdot 12H_2O$

with the activation energies E_d equal to 116 ± 2 and $196 \pm 13\,\mathrm{kJ \cdot mol^{-1}}$ for the NH_4 and Cr isomorphous series, respectively. E_d is constant for different growth sectors, so that differences in k are contained within the pre-exponential term k_0.

The activation energies obtained are close to the activation energies of self-diffusion in ionic crystals $E_d = 70$–$250\,\mathrm{kJ \cdot mol^{-1}}$ measured at the comparable fractions of the melting temperatures $T/T_{\mathrm{melt.}} \approx 0.8$–$0.96$ (Nowick and Burton, 1975; Poirier, 1985). This supports the relationship between the diminution of birefringence and the diffusional redistribution of structural units. Based on the measured activation energy, the mean squared displacements of units can be found for the reaction progress variable $1 - \xi = 0.4$. The expression

$$\langle h^2 \rangle = D_v t = D_{v0} \exp\left(-E_d / RT\right) \cdot t \qquad (3.7)$$

contains the constant D_{v0}, unknown for alum. A rough estimate, neglecting entropy, gives $D_{v0} \approx \nu \frac{a^2}{2} \approx 0.1\,\mathrm{cm^2 \cdot s^{-1}}$, where $a = 12\,\text{Å}$ is the lattice constant, $\nu = 10^{12}\mathrm{s^{-1}}$ is frequency of vibrations, and the multiplier 1/2 takes into account the mutual location of A^+ or M^{3+} ions in accordance with the FCC lattice. Hence the value of

$\langle h^2 \rangle^{1/2}$ is equal to 2Å. Using the maximum literature value of $D_{v0} \approx 130\,\mathrm{cm}^2 \cdot \mathrm{s}^{-1}$ for KCl (Nowick and Burton, 1975; Poirier, 1985) the mean squared displacement is about 80Å. The birefringence decrease in alum solid solutions is associated with the diffusive redistribution of cations over several unit cells. The annealing process is a disordering. The higher activation energy found for the second series confirms the diffusive nature of the birefringence decrease. Indeed, mobility of K^+ and $NH_4{}^+$ ions as well as the probability of the vacancy formation at corresponding sites should be much higher compared with Cr^{3+} and Al^{3+} ions that form stronger chemical bonds with surrounding oxygen atoms.

Garnets. Garnets from Malian skarns ($Ca_3(Al_{0.9-0.5}Fe_{0.1-0.5})_2(SiO_4)_3$) were studied likewise. Others had already established the decrease in anomalous birefringence at above 600 °C (Hariya and Kimura, 1978; Takéuchi *et al*., 1982; Allen and Buseck, 1988). According to our data, the rate constant k strongly varies for different points in the sample. For example, in one crystal, the rim containing a higher concentration of water, titanium, and dislocations is characterized by rate constants 3.3 times larger than the core. The temperature dependence of k agrees with Arrhenius kinetics (Figure 3.29). The activation energy is constant within experimental error. Differences in rate constants are reduced to differences in the pre-exponential term k_0. Between 950–1090 °C the activation energy is $249 \pm 12\,\mathrm{kJ} \cdot \mathrm{mol}^{-1}$ (Figure 3.30). Above 1090 °C one of two crystals studied is characterized by significantly higher activation energy (Figure 3.30) arguing for a change of the diffusion mechanism. The diffusion coefficient at relative low temperatures can be limited by concentration of pre-existing vacancies. Higher annealing temperatures are accompanied by formation of thermal vacancies (Lasaga, 1981b; Poirier, 1985). This hypothesis explains not only the complicated temperature behavior of the activation energy but also its constancy in different crystals and different zones of the same crystal. The differences in the rate constant k are included in the pre-exponential term k_0 which depends on the vacancy concentration.

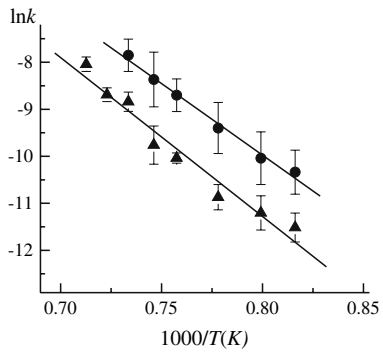

Figure 3.29. Arrhenius plot for the transformation from birefringent to isotropic {110} growth sectors of garnet $Ca_3(Al_{0.5-0.7}Fe_{0.5-0.3})_2(SiO_4)_3$. Circles – crystal core, triangles – crystal perimeter

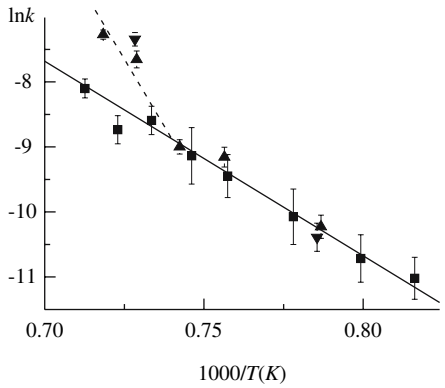

Figure 3.30. Arrhenius plot for the transformation from birefringent to isotropic {110} growth sectors of two grandite garnet crystals (squares and triangles, respectively)

Unfortunately, the self-diffusion coefficients of trivalent ions are not known for the garnets. Self-diffusion coefficients of divalent cations in pyralspite garnets (Chakraborty and Ganguly, 1992; Schwandt *et al.*, 1995, 1996; and references therein; Freer and Edwards, 1999) show that the activation energies E_d range from 155–290 $\mathrm{kJ \cdot mol^{-1}}$, and that most data correspond to a narrower range of $E_d =$ 250–290 $\mathrm{kJ \cdot mol^{-1}}$. These values agree with those from the annealing experiments and confirm the diffusive origin of the birefringence decrease.

The birefringence of **lead-strontium nitrate** solid solutions (Shtukenberg, 2005) also diminishes on heating with first order Arrhenius temperature dependence. The activation energies were 111(5) and 359(17) $\mathrm{kJ \cdot mol^{-1}}$ below 370 °C and above 400 °C, respectively. As in garnets, the presence of two activation energies is likely a consequence of a significant number of new vacancies only formed at elevated temperatures. At relatively low temperatures vacancies can move but they do not form.

Differences in rate constants k for different points within the same growth sector and for different crystals were observed as well. Unlike garnets and alums $k_{\max}/k_{\min}$ can be as high as 10^3. As activation energies measured for different points are comparable, differences must be attributed to the pre-exponential factor k_0. Rate constants increase significantly in the vicinity of cracks, liquid inclusions, and sometimes at growth sector boundaries and free surfaces.

Figure 3.31 shows the relative change in birefringence during three annealing runs at $T =$ 275–343 °C as a function of the distance from a crack, z. Such behavior suggests that the fresh crystal surface acts as a source of vacancies that diffuse into the crystal volume and accelerate the self-diffusion and equalization of cation occupancies. In this case, the birefringence should be controlled by the concentrations of vacancies $C_{\mathrm{vac}} \propto D_{v0}$ (see Equations (3.5) and (3.6)). Since annealing does not affect the homogeneous parts of the crystal, the assumption of negligible vacancy concentration in the beginning of the experiment seems to be reasonable.

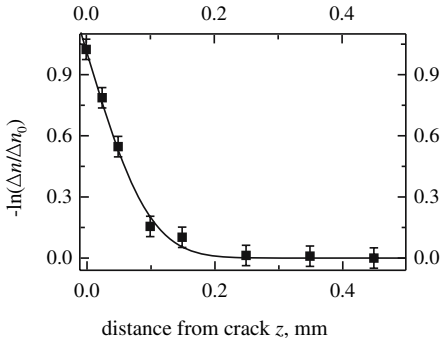

Figure 3.31. Changes in birefringence during annealing of $(Sr, Pb)(NO_3)_2$ {111} growth sector as a function of the distance from a crack. Points represent experiment, line fit to equation (3.8)

According to the semi-infinite medium solution to the Fick diffusion Equation (Lasaga, 1981b; Crank, 1975) the concentration of vacancies C_{vac} decreases with the distance from the crack as

$$C_{vac} = C_{vac0}\left(1 - \mathrm{erf}\left[\frac{z}{2\sqrt{D_{vac}t}}\right]\right) \tag{3.8}$$

where C_{vac0} denotes the concentration of vacancies at the free surface and D_{vac} is the vacancy diffusion coefficient. An excellent fit of the experimental profile with the function (3.8) (Figure 3.31) confirms the hypothesis and underscores the role of vacancies in the reduction of anomalous birefringence.

3.4.6. Kinetic Ordering *vs*. Structure of the Growing Surface

Geometrical analysis of the structure of growing faces supports the kinetic ordering model. As discussed in section 3.2.2, sites related by symmetry in the bulk can be dissymmetric on an exposed crystal surface. The nature of this dissymmetry was analyzed for particular materials including quartz (Barry *et al*., 1965; Tsinober and Samoilovich, 1975), cordierite (Tsinober *et al*., 1977), chabazite (Akizuki, 1981c), topaz (Akizuki *et al*., 1979), stilbite (Akizuki and Konno, 1985b), adularia (Akizuki and Sunagawa, 1978), yugawaralite (Akizuki, 1987b), garnets (Akizuki, 1984), brewsterite (Akizuki, 1987c), 11-bromoundecanoyl peroxide (McBride and Bertman, 1989), and 1,5-dichloro-2,3-dinitrobenzene (Kahr and McBride, 1992), among others.

Smoky quartz is illustrative. Tsinober and Samoilovich (1975) reckoned the ordering of the Al hole centers with various growth face structures illustrated in Figure 3.32. On the rhombohedron faces $\{01\bar{1}1\}$ there are three SiO_4 tetrahedra orientations. Accordingly, three oxygen sites reveal different occupancies by hole centers. The prism faces $\{\bar{1}\bar{1}20\}$ display two SiO_4 tetrahedra orientations and two of three oxygen sites have equal hole occupancies. Lastly, the pinacoid faces {0001}

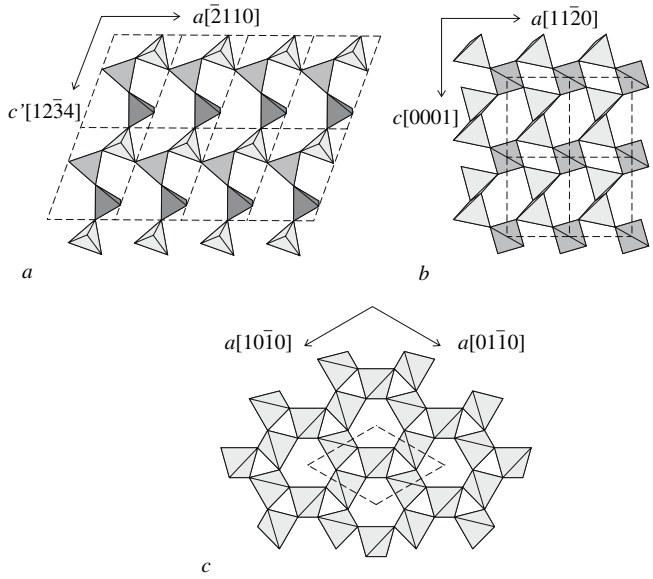

Figure 3.32. α-Quartz planes: (*a*) (01$\bar{1}$1), (*b*) ($\bar{1}\bar{1}$20) and (*c*) (0001) (Tsinober and Samoilovich, 1975). SiO_4 tetrahedra which are marked by different levels of the gray scale have different orientations with respect to growth face and different vacancy levels

reveal one SiO_4 orientation accompanied by equal oxygen occupancies. Correspondence between site occupancies and geometrical non-equivalence is well-established by these observations.

Anomalous birefringence of **ugrandite garnets** can be analyzed similarly. As discussed previously, the optical anomalies in these garnets result from cation (Al^{3+}, Fe^{3+} and Cr^{3+}) ordering over Y sites. The limiting cases of tangential and normal selectivity on the rhombic dodecahedron faces are discussed below.

Normal selectivity. The garnet structure has two different orientations of YO_6 octahedra on the (101) growth plane. In the first orientation (Y21, Y22, Y23, Y24 in Figure 3.33) two Y-O bonds are directed inward, two are in the surface, and two others are directed outward. For the other YO_6 orientations (Y11, Y12, Y13, Y14 in Figure 3.33) three bonds are directed inward and three outward. We know the orientation of the optical indicatrix with respect to growth face (Table 3.2). The crystal structure was refined (Andrut and Wildner, 2001; Wildner and Andrut, 2001). Differently occupied octahedral sites were recognized on (101). Normal selectivity reduces the crystal symmetry from cubic to orthorhombic (Table 3.2), space group *Fddd*. As a result, Y21, Y22, Y23 and Y24 octahedra (Figure 3.33) surrounded Y2 sites (Table 3.5), and Y11, Y12, Y13 and Y14 octahedra (Figure 3.32) surrounded Y1 sites (Table 3.5). In other words, differently occupied Y octahedra have different orientations with respect to the growth face (101).

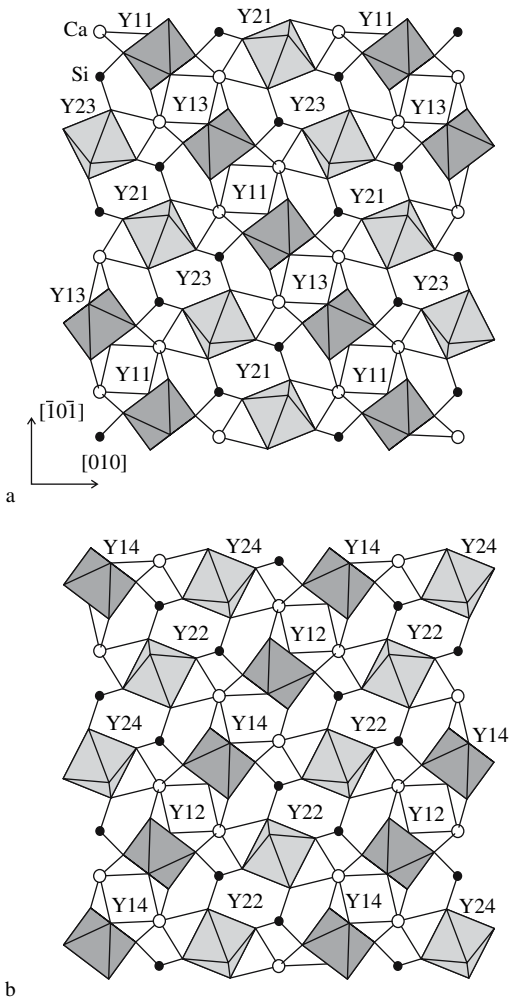

Figure 3.33. Garnet structure on $(\bar{1}01)$. (*a*) $z_{[\bar{1}01]} = 0 \pm 0.45 d_{101}$, (*b*) $z_{[\bar{1}01]} = d_{101} \pm 0.45 d_{101}$. Differently occupied types of YO_6 octahedra are shown by different gray levels. White and black balls denote Ca and Si atoms, respectively

Tangential selectivity. The similar treatment of the surface structure shows that all eight octahedra have different orientations with respect to growth steps that are usually parallel to < 112 > (Akizuki, 1984). Eight different occupancies in the triclinic system are expected from symmetry arguments (section 3.2.2) and eight were found experimentally for most of the ugrandites studied (Takéuchi *et al.*, 1982; Wildner and Andrut, 2001; Shtukeneberg *et al.*, 2002, 2005), see section 3.4.2.

The large size and aspect ratios of some organic molecules make selectivity on the basis of surface structure readily apparent. Di-11-bromoundecanoylperoxide

($Br(CH_2)_{10}C(O)O-O(O)C(CH_2)_{10}Br$) crystallizes in the space groups $P4_1$ and $P4_3$. Given the length of the molecule, and its inclination with respect to the screw axis, crystals grow with large undulations on the (100) and (010) surfaces (Figure 3.34). When crystals were grown in the presence of analogues having slightly different end groups (Cl, H, CH_3) on one or two of the chain ends, the guest molecules differentially compete with the host molecules for the concave and convex sites thus breaking the tetragonal symmetry in adjacent sectors and producing classically optically anomalous crystals with biaxial growth sectors (Figure 3.35; McBride and Bertman , 1989).

The anomalous pleochroism of **phthalic acid** ($C_6H_4(COOH_2)$) containing methyl red (MR, $(CH_3)_2N-C_6H_4-N=N-C_6H_5CO_2H$) can be well explained on the basis of surface structure and symmetry. Force-field calculations of MR bound to the lowest energy surfaces of (001) and (110) were conducted using a molecular replacement approach. Single phthalic acid molecules were removed from the 2D periodic surfaces of the relaxed cell and replaced with MR allowing for hydrogen bonding between COOH groups (Figure 3.36). The phthalic acid atomic positions were fixed and the energy of MR was minimized as a function of position with its geometry fixed. The (001) surface has a single phthalic acid molecule presentation. The (110) surface displays two phthalic acid molecules related by symmetry in the bulk but dissymmetric on the surface. These two sites are distinguished as I and II in (Figure 3.36). The long axis of MR is inclined 40° with respect to [010], parallel to phthalic acid hydrogen bonds, when docked to

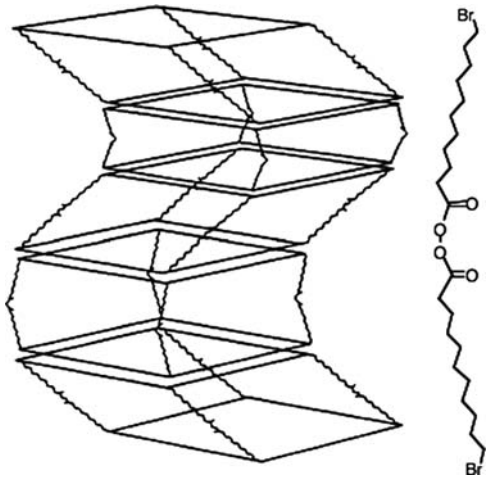

Figure 3.34. Four slabs of di-11-bromoundecanoylperoxide ($Br(CH_2)_{10}C(O)O-O(O)C(CH_2)_{10}Br$, structure at right) stacked along a four-fold screw axis. Each layer is a 10×10 molecule array. Only the corner molecules are drawn explicitly (McBride and Bertman, 1989)
Source: Figure courtesy of Professor Steven Bertman, Ph.D. Dissertation, Yale University, 1990, Figure 6–9, p.174.

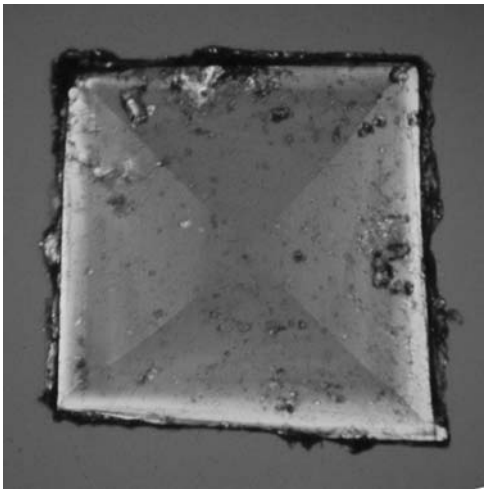

Figure 3.35. Growth sector zoning in crystal of di-11-bromoundecanoyl peroxide containing 15% of the corresponding compound in which one bromine atom was replaced with hydrogen. View along [001] between crossed polarizers with a first order red retarder
Source: Reprinted with permission from McBride, J.M. and Bertman, S.B. "Using Crystal Birefringence to Study Molecular Recognition" *Angewandle Chemie, International*, Edition in English, 1989, *28* p. 330–333. Copyright 1989 Wiley-VCH, STM (see Color Section following page 254)

(001) and position I on (110). When docked to position II on (110), MR is nearly parallel to [100]. Indeed, measured dichroic ratios were consistent with the average of two orientations (Benedict *et al*., 2006).

3.4.7. Relaxation by Diffusion

The occupancy of each site can be described by equilibrium distribution coefficients (section 3.5.1.2) that vary for the step, face, and volume of the crystal. The disordered equilibrium state may be achieved via diffusive exchange of structural units according to the relaxation mechanism depicted by Chernov (1984) for the non-equilibrium incorporation of isomorphous impurities. Here, we adapt this mechanism to growth ordering.

During the tangential selectivity of structural units, as soon as the kink is buried in the surface layer the ordering of units becomes metastable. From this moment, diffusive redistribution strives toward a new state, that expected as a result of normal selectivity. In the crystal volume, all the nominally symmetry related sites actually become equivalent by diffusive redistribution. However, this latter process requires overcoming a much higher activation barrier and proceeds only at very high temperatures (section 3.4.5).

The newly deposited metastable surface layer is not in equilibrium with the solution. Structural units can detach from the surface layer into growth medium

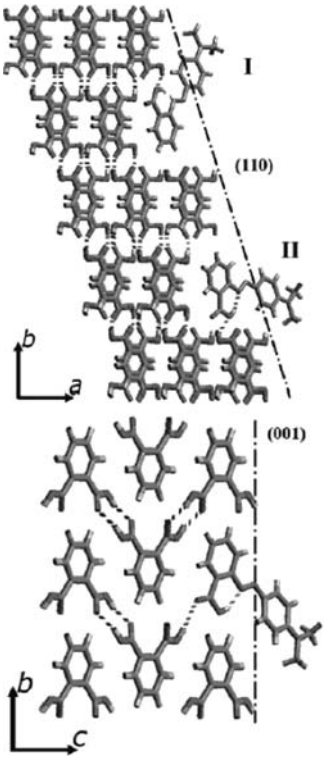

Figure 3.36. Simulations of methyl red ($((CH_3)_2N-C_6H_4-N=N-C_6H_5CO_2H)$) docking to two distinct sites (I) and (II) on the asymmetric (110) surface above and the one unique site on the (001) with local symmetry *m*. Black dashed lines denote lowest energy stable surfaces for the indicated facets *Source*: Reprinted with permission from Benedict, J.B., Cohen, D.E., Lovell, S., Rohl, A.L. and Kahr, B. "What is syncrystallization? States of pH indicator methyl red in single phthalic acid crystals" *J. Am. Chem. Soc,* 2006, *128*, p.5548–5559 Copyright 2003 American Chemical Society (see Color Section following page 254)

with the probability P_d. The vacant site i is then occupied by a unit from the growth medium. The occupancy x_i evolves to x_{fi} that characterizes the equilibrium of the face with the growth medium. The corresponding rates are given by the expression

$$\frac{dx_i}{dt} = \left(x_{fi} - x_i\right) P_d. \tag{3.9}$$

Detachment probability is $P_d = D_s/h^2$, where h is the elementary step height and D_s is the diffusion coefficient for detachment. Solution of this Equation yields

$$\frac{x_{fi} - x_i}{x_{fi} - x_{si}} = \exp\left(-\tau_{\mathrm{ML}} P_d\right),$$

where x_{si} is the initial occupancy of this site provided by tangential selectivity and corresponding to the equilibrium between the step and the growth medium.

The time required for covering the surface by a new monolayer (ML) is equal to $\tau_{ML} = h/V$ where V is the normal growth rate. The resulting occupancies can be found as follows:

$$x_i = x_{fi} + (x_{si} - x_{fi}) \exp\left(-\frac{D_s}{Vh}\right) \quad (3.10)$$

To a first approximation, the diffusion coefficient is equal to

$$D_s = \nu h^2 \exp\left(-\frac{E_s}{RT}\right), \quad (3.11)$$

where E_s is the activation energy for dissociation from the crystal surface into the growth medium, T is the absolute temperature, R is the universal gas constant, and $\nu = 10^{12}\,\mathrm{s}^{-1}$ is a vibrational frequency.

If the exponential term in Equation (3.10) is close to unity (the diffusion rate is low compared to the growth rate) $x_i = x_{si}$; no relaxation occurs. The resulting ordered state buried in the crystal volume should correspond to tangential selectivity. On the contrary, if the exponential term is close to zero (diffusion rate is high compared to the growth rate) $x_i = x_{fi}$. In this case, the redistribution proceeds fully and the resulting ordered state corresponds to normal selectivity.

Unfortunately, experimental E_s values are lacking. However, the activation energy of the detachment E_s is higher than the activation energy for crystal dissolution E_{ds} and less than the activation energy for self-diffusion in the crystal volume E_d. This relation results from the fact that detachment from a surface layer demands breaking a greater number of bonds than detachment from a kink (dissolution of crystal) and less than detachment from the crystal volume. Knowing E_{ds} and E_d, the lower and upper limit of E_s can be estimated. Two examples are described below.

Desymmetrization of **grossular-andradite garnets** results in either orthorhombic (ordering of cations over two sites that corresponds to the normal selectivity) or triclinic (ordering of cations over eight sites that corresponds to the tangential selectivity) symmetry (see section 3.4.2).

According to data (Lasaga, 1981a) for diopside ($CaMgSi_2O_6$), enstatite ($Mg_2Si_2O_6$), forsterite ($(Mg, Fe)_2SiO_4$), quartz, augite ($(Ca, Na)(Mg, Fe, Al)(Al, Si)_2O_6$) and kaolin (hydrated Al/Si oxide clay), E_{ds} range between 37 and $150\,\mathrm{kJ \cdot mol^{-1}}$. On the other hand, the activation energy for the growth of quartz, sodalite ($Na_4Al_3(SiO_4)_3Cl$), cancrinite ($Na_7CaAl_6Si_6O_{24}(CO_3)_2$), corundum ($Al_2O_3$), ZnO, and TeO_2 range between 33 up $130\,\mathrm{kJ \cdot mol^{-1}}$ (Kuznetsov, 1968). The activation energy for dissolution $E_{ds} = E_g + \Delta H$, where ΔH is the heat of crystallization, is $\sim 20\,\mathrm{kJ \cdot mol^{-1}}$ for the most compounds (Treivus, 1979; Chernov, 1984). Data on the growth and dissolution of pyralspite garnets (see Appendix 1 for garnet nomenclature) give $E_g \approx E_{ds} = 46$–$54\,\mathrm{kJ \cdot mol^{-1}}$ (Walther and Wood, 1986; Azimov, 2000; Azimov and Shtukenberg, 2003). By considering all the data we can estimate that $E_{ds} \sim 60\,\mathrm{kJ \cdot mol^{-1}}$. Dissolution usually proceeds through detachment of ions

from the step edges. For Y cations in grandite garnets, this requires breaking of two bonds. Detachment of a Y cation from the surface breaks 3 or 4 bonds depending on the Y octahedron orientation. Thus, the activation energy required can be roughly found as $E_s \approx 1.75E_{ds} = 105\,\mathrm{kJ \cdot mol^{-1}}$. Another approach to the evaluation of E_s is based on diffusion rates in solids. To migrate through garnet a Y cation must break 6 bonds. This jump from the Y site is characterized by the activation energy for self-diffusion E_d. Our experiments give $E_d = 249\,\mathrm{kJ \cdot mol^{-1}}$ (section 3.4.5.3), close to the activation energies of self-diffusion for different X cations in pyralspite garnets ($E_d = 155$–$285\,\mathrm{kJ \cdot mol^{-1}}$) (Schwandt *et al.*, 1995, 1996; and references therein). Hence, $E_s \approx 0.58E_d = 145\,\mathrm{kJ \cdot mol^{-1}}$, in relatively good agreement with the former estimate.

Data on garnet growth rates differ drastically from 1 cm per million years to a few cm per year. Recent studies argue strongly for the higher values (Wood and Walther, 1983; Walther and Wood, 1986; Gavrieli *et al.*, 1992; Azimov, 2000). According to these investigators, the normal growth rate of grossular and pyrope (see Appendix 1) can be evaluated in the usual way

$$V = \beta\sigma^n = \beta_0 \exp\left(-\frac{E_g}{RT}\right)\sigma^n \tag{3.12}$$

where the kinetic coefficient β is a function of temperature, a pre-exponential term $\beta_0 \approx 1.6 \cdot 10^{-7}\,\mathrm{m/s}$ and the activation energy for growth, $E_g = 50\,\mathrm{kJ \cdot mol^{-1}}$. The relative supersaturation σ varies, but we will use the upper limit of 0.3 (Azimov, 2000). The dislocation growth mechanism gives n close to 2. Substituting Equations (3.11) and (3.12) into (3.10) gives the following:

$$\eta = \frac{x_i - x_{fi}}{x_{si} - x_{fi}} = \exp\left(-\frac{\nu h}{k_0\sigma^n}\exp\left[-\frac{E_s - E_g}{RT}\right]\right). \tag{3.13}$$

Substitution of numerical values into (3.13) shows the effect of growth temperature on the occupancies (Figure 3.37). Unfortunately, the numerical values are roughly determined. $E_s - E_g$ seems to be in the range of 70–$100\,\mathrm{kJ \cdot mol^{-1}}$, whereas the product $\beta_0\sigma^n$ is likely to vary from $10^{-10} - 10^{-8}\,\mathrm{m \cdot s^{-1}}$. The transformation from the orthorhombic to the triclinic structure occurs between 150–350 °C. This falls into the temperature range for birefringent ugrandite garnet crystallization (150–700 °C). Crystallization at elevated temperatures leads to the more symmetric orthorhombic structure, in line with the general observation that temperature favors symmetry. On the other hand, the symmetry approaches orthorhombic as the growth rate (expressed as $\beta_0\sigma^n$) decreases. In summary, the diffusion relaxation mechanism can explain the existence of both orthorhombic and triclinic grandite garnets.

Desymmetrization of **sodium chlorate-bromate** solid solutions manifests itself as symmetry reduction from cubic space group $P2_13$ {111}. Normal selectivity would result in a monoclinic structure, space group $P2_1$. Tangential selectivity would result in a triclinic structure $P1$. The samples studied (Gopalan *et al.*, 1993; Crundwell *et al.*, 1997; Shtukenberg *et al.*, 2004) showed various deviations from monoclinic

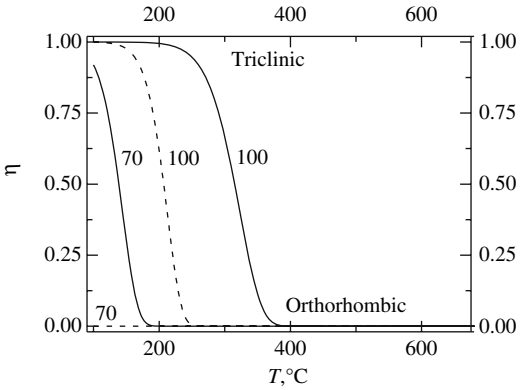

Figure 3.37. Calculated occupancy parameter η as a function of growth temperature T for the different $E_s - E_g$ activation energies (numbers at the curves, $\mathrm{kJ \cdot mol^{-1}}$) and for the different growth rates $\beta_0 \sigma^n = 10^{-10}$ (dashed lines) and $10^{-8} \mathrm{m \cdot s^{-1}}$ (solid lines) in the ugrandite garnets

symmetry. Rates, the heat of crystallization, and activation energies of crystal growth were established (Bliznakov *et al*., 1971; Treivus, 1979, 1987; Kitamura *et al*., 1982). The activation energy for dissolution varies from $35–40 \mathrm{kJ \cdot mol^{-1}}$. Detachment of halate anions $(\mathrm{Cl, Br})\mathrm{O_3}$ from kinks requires breaking 3–4 bonds, whereas detachment from the surface layer requires breaking 5 bonds. Hence, $E_s \approx 1.43 E_{ds} = 50–57 \mathrm{kJ \cdot mol^{-1}}$. Using of this value along with the typical value of the growth rate equal to $0.1–5 \mathrm{mm \cdot day^{-1}}$ gives either the monoclinic modification or the structure, which is very close to fully disordered triclinic modification.

3.5. FACTORS AFFECTING GROWTH ORDERING

3.5.1. Crystal Composition

3.5.1.1. General remarks

Three scenarios characterize the effect on composition of ordering. For stoichiometric compounds like the aluminosilicates (cordierite, zeolites, and adularia), the degree of ordering does not depend on composition and is only a function of growth conditions. The degree of ordering should be proportional to the micro-impurity ($\mathrm{Al^{3+}}$ and $\mathrm{Fe^{3+}}$ in quartz, $\mathrm{Cu^{2+}}$ in $\mathrm{ZnSeO_4 \cdot 6H_2O}$ *etc*.) content. Unfortunately, relevant data are not available. Finally, ordering in a system with *good miscibility* of components (complete isomorphous series of garnets, alums *etc*.) is more complicated. Obviously, the end members of the series should display undistorted optical patterns, whereas anomalies are most pronounced in the middle of the series.

3.5.1.2. Theory

Consider the growth ordering of two different cations over two non-equivalent positions in a regular lattice. These positions are denoted by the upper index

$[i] = [1], [2]$, each characterized by its own segregation coefficient $K^{[i]}$ (Balarew, 1987; Azimov and Shtukenberg, 2000)

$$\frac{x^{[i]}}{1-x^{[i]}} = K^{[i]}\frac{y}{1-y} \tag{3.14}$$

Here, $x^{[i]}$ is the mole fraction of component B, y is the mole fraction of this component in solution. Combination of two Equations (3.14) for different subsystems of points defines the so-called inter-site distribution coefficient K

$$\frac{x^{[2]}}{1-x^{[2]}}\frac{1-x^{[1]}}{x^{[1]}} = \frac{K^{[1]}}{K^{[2]}} = K \tag{3.15}$$

Difference in site occupancies are expressed as sum and differences of the average occupancies: $\overline{x} = (x^{[1]} + x^{[2]})/2,\ \delta x = (x^{[1]} - x^{[2]})/2 > 0$ with:

$$x^{[1]} = \overline{x} + \delta x \tag{3.16}$$

$$x^{[2]} = \overline{x} - \delta x. \tag{3.17}$$

Here, $x^{[1]} > x^{[2]}$ and $0 < K < 1$. Substitution of Equations (3.16) and (3.17) into (3.15) yields the quadratic Equation with respect to δx. Only one of the two roots is physically meaningful. Thus,

$$x^{[1]} - x^{[2]} = \frac{1+K}{1-K} - \sqrt{\left(\frac{1+K}{1-K}\right)^2 - 4\overline{x}\,(1-\overline{x})} \tag{3.18}$$

which can be simplified using the approximate formula for the square root

$$x^{[1]} - x^{[2]} \approx \frac{1-K}{1+K} 2\overline{x}\,(1-\overline{x})\,, \tag{3.19}$$

The difference in occupancies displays a parabolic dependence on the average crystal composition. Deviations from the solution of Equation (3.18) are greatest in the middle of the series and strongly depend on the distribution coefficient; K is close to unity for small deviations. For $K = 0.01$, differences are as high as 40%, for $K = 0.1$, 21%, for $K = 0.2$, 13%, and for $K = 0.4$, differences are less than 5% (Figure 3.38*a*). In the limit $K \to 1$, the parabolic relationship is maintained. The simplified expression is

$$x^{[1]} - x^{[2]} \approx (1-K)\,\overline{x}\,(1-\overline{x})\,. \tag{3.20}$$

The birefringence is proportional to the extent of ordering. The difference in sub-site occupancies ($\Delta n \sim \delta x$) can thus be taken as a measure of the birefringence. Such a dependence was observed in the calculated birefringence of grossular-andradite garnets (Figure 3.38*b*).

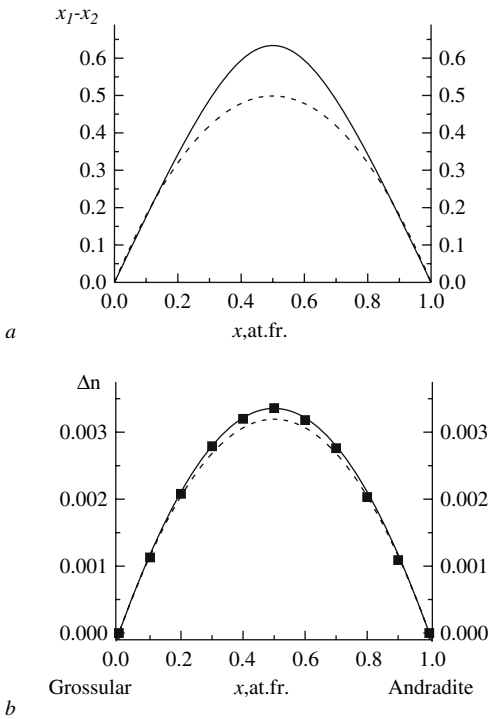

Figure 3.38. (*a*) Difference in occupancies as a function of average crystal composition. Solid line from equation (3.18), dashed line from equation (3.19). Inter-site distribution coefficient $K = 0.05$. (*b*) Calculated birefringence as a function of iron content in garnet $Ca_3(Al, Fe)_2(SiO_4)_3$ for the space group *Fddd* (squares). Solid line fit to equation (3.18); dashed line drawn after equation (3.19). for the same $K = 0.4$ and the same fitting variable in both cases. In contrast to (*a*) the difference between solid and dashed curves is slight

If we presume that the birefringence Δn is directly proportional to Δx ($\Delta n \propto \Delta x$) then expressions (3.18) and (3.19) provide the functional relationship between the anomalous birefringence and the crystal composition. Concomitant growth ordering over several sites leads to a more complex dependence of anomalous birefringence on crystal composition. Nevertheless, the magnitude of the effect will peak in the middle of the series.

The dependence of the inter-site distribution coefficient K on the crystal composition and the birefringence illustrates this complexity. For example, for non-ideal (regular) solid solutions the constant values $K^{[i]}$ in Equation (3.14) should be replaced with variables $K^{[i]} = K_0^{[i]}\ f_A^{[i]} / f_B^{[i]}$, where $K_0^{[i]}$ is a constant, $f_j^{[i]} = \exp\left[A^{[i]}\left(1 - x_j^{[i]}\right)^2\right]$ is the activity coefficient of component $j = A,\ B$ in the solid solution, $x_B^{[i]} = 1 - x_A^{[i]} \equiv x^{[i]}$ and $A^{[i]}$ is the dimensionless expression for the mixing

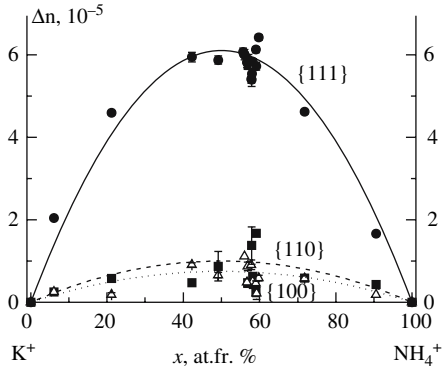

Figure 3.39. Anomalous birefringence in alums $(K_{1-x}(NH_4)_x)Al(SO_4)_2 \cdot 12H_2O$ as a function of the average crystal composition. Growth sectors: {111} = circles, {110} = squares, {100} = triangles. Lines represent parabolic fits

energy (Putnis and McConnell, 1980; Azimov and Shtukenberg, 2000). Then the inter-site distribution coefficient is written as

$$K = \frac{K_0^{[1]}}{K_0^{[2]}} \exp\left[A^{[1]}\left(2x^{[1]} - 1\right) - A^{[2]}\left(2x^{[2]} - 1\right)\right]. \quad (3.21)$$

Substitution into (3.18) provides an Equation that can be solved numerically with respect to $\overline{x}$. These elaborations of the model may shift the maximum on the plot Δn *vs.* $\overline{x}$ and slightly distort the parabolic shape of the function. Equation (3.18) also takes a more complicated form if the sites [1] and [2] have different muliplicities (Shtukenberg *et al.*, 2004), shifting the maximum of the $\Delta n\,(\overline{x})$ curve off-center.

3.5.1.3. Examples

Alums. The relationships above are born out in the optically anomalous alums. For three series ($(NH_4, K)Al(SO_4)_2 \cdot 12H_2O$, $K(Al, Cr)(SO_4)_2 \cdot 12H_2O$ and $NH_4(Al, Fe)(SO_4)_2 \cdot 12H_2O$) anomalous birefringence depends parabolically on crystal composition (see e.g. Figure 3.39)

$$\Delta n = 4\Delta n_{\max} x\,(1 - x)\,. \quad (3.22)$$

Here, x corresponds to the mole fraction of one component. This parabolic dependence is consistent with the prediction of Equation (3.19).

The birefringence is also *additive* with respect to isomorphous substitutions at different crystallographic sites. For the crystal $(NH_4)_{0.47}, K_{0.53})(Al_{0.885}, Cr_{0.115})(SO_4)_2 \cdot 12H_2O$ the birefringence before annealing Δn_0^{Σ} was equal to -236×10^{-7} (optically negative), after 7 days annealing at 60 °C it was equal

to $+283 \times 10^{-7}$ (optically positive). A knowledge of the rate of change of the birefringence during annealing, coupled with the assumption that $K \leftarrow NH_4$ and $Al \leftarrow Cr$ substitutions contribute independently to the perturbation of the optical properties, enable the computation of individual contributions to $\Delta n_0^{\Sigma} : \Delta n_0^{K-NH_4} = (-556 \pm 70) \times 10^{-7}$ and $\Delta n_0^{Al-Cr} = (+320 \pm 30) \times 10^{-7}$. Similar values can be obtained taking into account the compositional effect on the birefringence in binary solid solutions $\Delta n_0^{K-NH_4} = (-590 \pm 10) \times 10^{-7}$ and $\Delta n_0^{Al-Cr} = (+410 \pm 50) \times 10^{-7}$.

The crystals of **sodium chlorate-bromate** $Na(Cl, Br)O_3$ solid solutions should be optically isotropic. In reality, such crystals possess anomalous birefringence related to the Cl/Br growth ordering over four translationally nonequivalent sites (Gopalan *et al.*, 1993; Crundwell *et al.*, 1997; Shtukenberg *et al.*, 2004). The birefringence increases in the middle of the series forming the parabola-like function (Figure 3.40). The maximum of birefringence is actually shifted from the center ($Cl_{0.5}$, $Br_{0.5}$) position and corresponds to the compositions with *ca.* 65% of $NaBrO_3$. This deviation seems to originate in the strong non-ideality of $Na(Cl, Br)O_3$ solid solutions. The observed quasi-linear dependency $K(x)$ (Shtukenberg *et al.*, 2004) can be fitted with Equation (3.21) confirming the proposed hypothesis.

Grossular-andradite garnets $Ca_3(Al, Fe)_2(SiO_4)_3$ represent the most pronounced example of growth desymmetrization in minerals. However, the plot of birefringence versus average composition is not parabolic, it forms a field of points bounded at the bottom by $\Delta n = 0$ and on the top by a parabola-like curve with a maximum in the middle of the series (Figure 3.41). This complicated behavior can be explained by variations in growth conditions (section 3.5.3). Therefore, the maximum birefringence is attained only for a small fraction of samples plotted in Figure 3.41.

Some garnets reveal complex oscillatory zoning. Individual zones display a wide spectrum of Al/Fe ratios and birefringence. Assuming that the growth conditions (temperature, pressure) for all these zones are comparable, we can build the

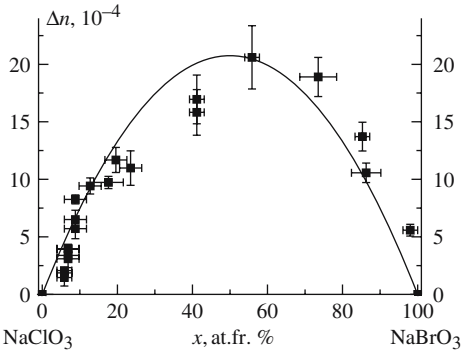

Figure 3.40. Anomalous birefringence in {100} growth sectors of sodium halate $Na(Br_xCl_{1-x})O_3$ solid solutions as a function of the average composition. Solid line is a parabola

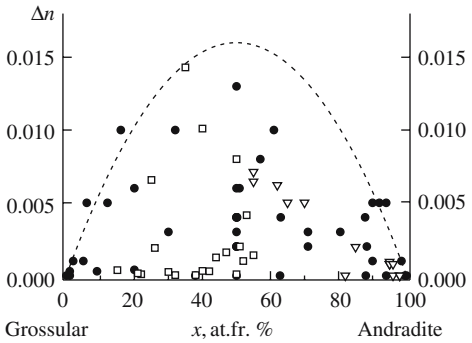

Figure 3.41. Anomalous birefringence in grossular-andradite garnets as a function of iron content x. Open symbols – our data; solid symbols from the following: (Kalinin, 1967; Murad, 1976; Hariya and Kimura, 1978; Fraga *et al*., 1982; Hirai *et al*., 1982; Takéuchi *et al*., 1982; Allen and Buseck, 1988; Kingma and Downs, 1989; Griffen, 1992; McAloon and Hofmeister, 1995). Dashed line is a parabola

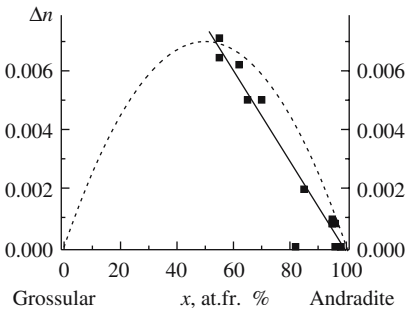

Figure 3.42. Anomalous birefringence in grossular-andradite garnets as a function of iron content x in crystal with a complex oscillatory zoning from the Dalnegorsk mine, Far East, Russia. Dashed line is a parabola

birefringence–composition plot for one and the same sample and, respectively, for constant growth conditions. Such a plot shown in Figure 3.42 demonstrates the linear relationships between the birefringence and the crystal composition. Despite the strong deviation from the parabola, this linear function is in agreement with the theoretical predictions of Eq. (3.18). If the inter-site distribution coefficient K strongly deviates from unity for the average crystal composition, the dependence is not parabolic and is described by a rather complicated curve with linear segments near the end members of the series (Figure 3.38*a*).

3.5.1.4. Isomorphous replacements

Some crystals—alum being the best among them – can tolerate numerous isomorphous replacements thus providing a family of related crystalline materials that can

be used to test the models above. Shtukenberg *et al*. (2000) studied the anomalous birefringence for 10 different isomorphous alum series (Table 3.7). The optical sign is determined by the type of isomorphous replacement. The maximum birefringence varies from one series to another. These differences are not simply correlated to lattice constants or ionic radii (Table 3.7).

3.5.1.5. Impurities

The degree of ordering of the principal components can be affected by adventitious impurities though data on these influences are sparse. A number of impurities (Be, Cs, Ca, Mn, Ti, Li, Cu, B, Sc, V, Cr, Fe) can affect the ordering in synthetic cordierite, $Mg_2Al_3(Si_5AlO_{18})$ (Demina, 1980a,b). The order-disorder transformation interchanging hexagonal (space group $P6/mcc$) and orthorhombic (space group $Cccm$) phases originates in Al ordering over three groups of tetrahedral sites (Tsinober *et al*., 1977). The transformation depends on the impurity concentration (Demina, 1990; Pecherskaya *et al*., 2003). Increasing the Be, Sc or B concentration in the charge of Al_2O_3 leads to decreased ordering. Cs, Rb, Li and Cr have the opposite effect. However, impurities affect not only the kinetic ordering but also the equilibrium phase transformations rendering their influences less than transparent.

In the mixed alum, $K(Al, Cr)(SO_4)_2 \cdot 12H_2O$, the partial (about 2/3) replacement of H_2O by D_2O strongly decreases the birefringence. The origin of the effect is unclear.

Table 3.7. Crystal chemical data and anomalous birefringence for alum {111} growth sectors

Series	Replacement site	Sign of Δn	Absolute value of Δn_{max}, 10^{-7}	Δa, Å	Δr, Å	Remark
$(NH_4, K)Al(SO_4)_2 \cdot 12H_2O$	A^+	–	600 ± 30	0.082	0.10	
$(Rb, K)Al(SO_4)_2 \cdot 12H_2O$	A^+	–	540	0.085	0.14	#
$(Rb, NH_4)Al(SO_4)_2 \cdot 12H_2O$	A^+	?	≈ 0	0.003	0.04	
$(NH_4, K)Cr(SO_4)_2 \cdot 12H_2O$	A^+	–	> 70	0.078	0.10	*
$(K, Rb)Cr(SO_4)_2 \cdot 12H_2O$	A^+	?	≈ 0	0.083	0.14	*
$K(Al, Cr)(SO_4)_2 \cdot 12H_2O$	M^{3+}	+	820 ± 30	0.038	0.09	
$NH_4(Al, Fe)(SO_4)_2 \cdot 12H_2O$	M^{3+}	+	550 ± 70	0.078	0.02	
$NH_4(Al, Cr)(SO_4)_2 \cdot 12H_2O$	M^{3+}	+	> 430	0.034	0.09	*
$NH_4(Fe, Cr)(SO_4)_2 \cdot 12H_2O$	M^{3+}	?	≈ 0	0.044	0.07	*
$NH_4(Al, Ga)(SO_4)_2 \cdot 12H_2O$	M^{3+}	+	> 130	0.027	0.09	*

Remarks: All crystals grown between 25–35 °C. (#) Δn_{max} was determined using one sample (with application of equation (3.22)).; (*) composition of crystal was unknown. Δa - difference between lattice constants for end members of the series; Δr - difference between ionic radii (Shannon, 1976) for admixed cations.

3.5.2. Composition of Growth Medium

The growth ordering of atoms is also affected by components of the growth medium that are not incorporated into the crystal. In grossular-andradite garnets grown hydrothermally (Kalinin, 1967), replacement of the $CaCO_3$ with CaO or $Ca(OH)_2$ in the charge reduces the anomalous birefringence. Na_2CO_3 solutions deposit more birefringent crystals than Na_2SiO_3 or $Na_2B_4O_7$ solutions. According to Hariya and Kimura (1978) CO_2 and H_2O affects the optical anomalies formed during garnet synthesis. Growth at 650 °C and 800 Kbar leads to optical anomalies if the charge contains 5–10% of water. Nevertheless, optical anomalies can appear even if the charge does not contain CO_2 and H_2O at all. The responsible mechanisms are unknown.

Additives can modify crystal habit and produce faces that were not otherwise present. In so doing, they generate surfaces with new structures, symmetries, and associated optical anomalies. $Na_2S_2O_3$ and $Na_2S_2O_6$ were used as habit-modifying impurities to produce $Na(Cl, Br)O_3$ with tetrahedral habits ($\{111\}$, and $\{\overline{1}\overline{1}\overline{1}\}$), rather than cubes (100) (Buckley, 1930; Sherwood *et al*., 1993, 1994). Diffraction data from $\{111\}$ and $\{\overline{1}\overline{1}\overline{1}\}$ growth sectors were refined in the trigonal space group $P3$ (Crundwell *et al*., 1997). In each case the pyramidal halate ion that was located on the special position was depleted in Br. Conoscopic optical investigations nevertheless showed that the crystals are biaxial with a small $2V$ (10–15 °), in marked contrast to the 90 ° angle in the optically anomalous $\{100\}$ crystals (see section 3.3.1).

3.5.3. Temperature and Pressure

A comprehensive picture of ordering of mixed crystal components must reckon the effect of temperature on occupancies δx and, consequently, on anomalous optics. The distribution coefficient usually depends exponentially on the growth temperature (Chernov, 1984)

$$K^{[i]} = \left(K^{\#}\right)^{[i]} \exp\left(-\frac{U^{[i]}}{RT}\right) \tag{3.23}$$

where $(K^{\#})^{[i]}$ is a constant and $U^{[i]}$ includes the strain energy and mixing energy of the solid solution. Substitution of Equation (3.23) into (3.18) gives a cumbersome expression even after making the approximation that $\left(K^{\#}\right)^{[1]} \approx \left(K^{\#}\right)^{[2]}$:

$$x^{[1]} - x^{[2]} \approx \frac{e^{\left(-U^{[2]}/RT\right)} + e^{\left(-U^{[1]}/RT\right)}}{e^{\left(-U^{[2]}/RT\right)} - e^{\left(-U^{[1]}/RT\right)}} - \sqrt{\left(\frac{e^{\left(-U^{[2]}/RT\right)} + e^{\left(-U^{[1]}/RT\right)}}{e^{\left(-U^{[2]}/RT\right)} - e^{\left(-U^{[1]}/RT\right)}}\right)^2 - 4\bar{x}(1-\bar{x})}. \tag{3.24}$$

One can show numerically that the difference in occupancies decreases as the temperature increases. A simpler relationship is evident if the differences in occupancies are slight and the distribution coefficient is close to unity. In this

case, simple rearrangement of Equation (3.20) predicts the reverse influence of temperature on occupancies

$$x^{[1]} - x^{[2]} \approx \overline{x}\,(1-\overline{x})\left(\frac{U^{[1]} - U^{[2]}}{RT}\right). \quad (3.25)$$

Theory predicts a decrease in optical anomalies with increasing temperature. At elevated temperatures the energy of thermal motion becomes comparable to the energetic differences between the non-equivalent sites. As a result the selectivity of incorporation of components becomes slight and finally vanishes leading to a decrease and ultimately a disappearance of optical anomalies.

The effect of growth temperature on the kinetic ordering and optical anomalies has been studied for alums (Figure 3.43) and quartz (Tsinober *et al.*, 1967; Tsinober and Samoilovich, 1975) (Figure 3.44). Hariya and Kimura (1978) did not observe optical anomalies at elevated growth temperatures in grossular-andradite garnets (Figure 3.45) while pressure caused slight increases in anomalous birefringence. Milke (2004) made similar observations regarding the effect of temperature on garnets as did Tsinober *et al*. (1977) for cordierite. The variation of pressure and temperature during growth probably obscures an otherwise sharp relationship between anomalous birefringence and crystal composition of grossular-andradite garnets (section 3.5.1.3, Figure 3.41). Only the maximum values of birefringence fall onto the theoretical parabola.

3.5.4. Growth Rate

3.5.4.1. Background

As growth rate increases, the kinetic ordering of atoms and related optical anomalies should decrease because the selection of atoms among dissymmetric surface sites

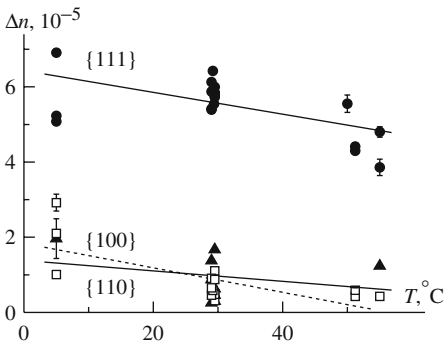

Figure 3.43. Anomalous birefringence in (110) sections of $K_{0.51-0.40}(NH_4)_{0.49-0.60}Al(SO_4)_2 \cdot 12H_2O$ as a function of growth temperature. The growth sectors intersected by the (110) section are indicated

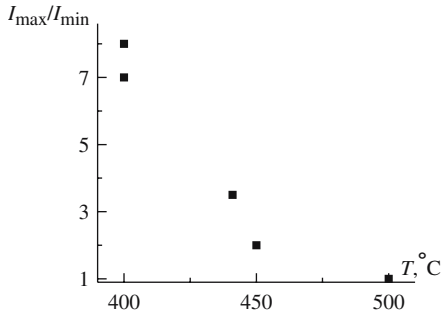

Figure 3.44. The ratio of maximum (I_{max}) and minimum (I_{min}) electron paramagnetic resonance (EPR) spectral intensities of Al hole centers in smoky quarty as a function of the growth temperature (Tsinober *et al.*, 1967b). Signal is proportional to the strength of optical anomalies. If $I_{max}/I_{min} = 1$, growth ordering and optical anomalies are absent

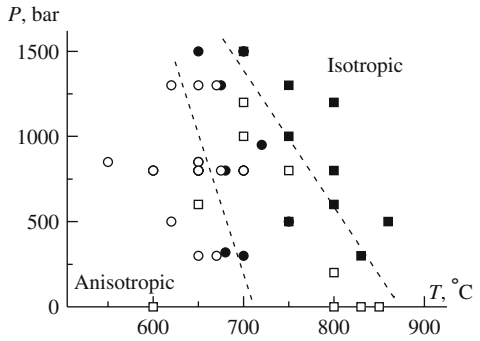

Figure 3.45. The stability fields of optically isotropic (solid symbols) and anisotropic (open symbols) grossular-andradite garnets as a function of growth temperature (T) and pressure (P) (Hariya and Kimura, 1978). Squares and circles correspond to natural and synthetic garnets, respectively

diminishes. Attachment of structural units is mainly controlled by trial and error statistics (Chernov, 1984); the components do not have enough time to order before they are buried in the crystal volume.

Decrease of anomalous birefringence with increasing growth rate was detected for analcime (Akizuki, 1981b). The influence of the growth rate on the birefringence of alum {111} growth sectors was by Shtukenberg *et al.* (2000). For $(K, NH_4)Al(SO_4)_2 \cdot 12H_2O$, no effect of growth rate on birefringence was observed whereas for $K(Al, Cr)(SO_4)_2 \cdot 12H_2O$ a linear decrease of anomalous birefringence with growth rate was observed (Figure 3.46, 3.47).

3.5.4.2. Comparison with theoretical estimations

The *kinetic disordering* phenomenon was treated theoretically for the crystallization from the vapor (Chernov, 1970) and experimentally for a number of minerals (Carpenter and Putnis, 1985) for which the usual equilibrium order-disorder phase

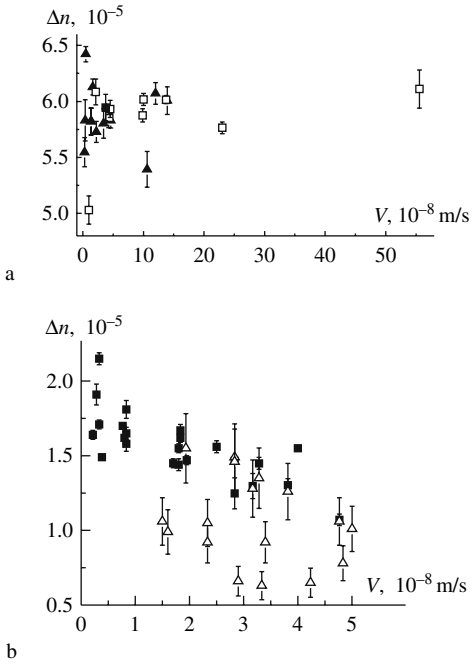

Figure 3.46. Anomalous birefringence in alum crystals as a function of growth rate. (*a*) Series $(K_{1-x}(NH_4)_x)Al(SO_4)_2 \cdot 12H_2O$, triangles correspond to $x = 0.55$–0.60 ($T = 28$–$30\,^\circ C$); squares correspond to $x = 0.36$–0.42 ($T = 29.5$–$32\,^\circ C$). (*b*) Series $K(Al_{1-x}Cr_x)(SO_4)_2 \cdot 12H_2O$, triangles correspond to $x = 0.03$–0.05 ($T = 24$–$37\,^\circ C$); squares correspond to $x = 0.04$–0.05 ($T = 34$–$36\,^\circ C$). Open symbols correspond to growth under free convection. Solid symbols correspond to growth under strong solution stirring (Reynolds number Re = 1400–3200)

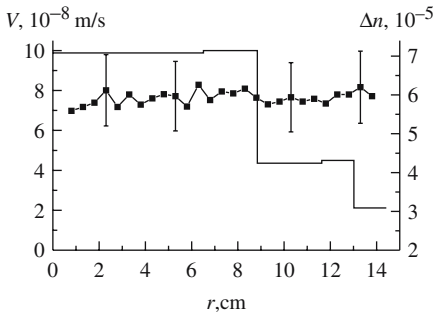

Figure 3.47. Evolution of growth rate (stepped line) and birefringence (squares) along the growth direction of $K_{0.63}(NH_4)_{0.37})Al(SO_4)_2 \cdot 12H_2O$ grown under free convection

transformations are known (feldspars, omphacite $(Ca, Na)(Mg, Fe^{2+}, Al)Si_2O_6$, dolomite). According to the theory of Chernov (Chernov and Lewis, 1967; Chernov, 1970) we consider growth from the vapor of a semi-infinite crystal with a single kink on a single step. Although Chernov considered the kinetic disordering we may apply this analysis to kinetic ordering. A crystal with a simple cubic lattice contains equal fractions of A and B atoms with the bond energies $\varepsilon_{AA} = \varepsilon_{BB}$, $\varepsilon_{AB} = \varepsilon_{BA} = \psi\varepsilon_{AA}$. The dimensionless temperature is $q = \exp(-\varepsilon_{AA}/k_B T)$, where T is the temperature, k_B is the Boltzmann constant and ε_{AA} is A-A bond energy in the crystal. Assume the attachment frequencies are constant and equal to ω_+ and detachment frequencies are expressed as $\omega_- = \exp\left[-\left(\varepsilon_{\alpha\beta} + \varepsilon_{\mu\beta} + \varepsilon_{\lambda\beta}\right)/k_B T\right]$. Here α, μ and λ are atom β's nearest neighbors; ε are the bond energies between the corresponding pairs of atoms. A crystal with the maximum degree of long-range order consists of two sub-lattices [1] and [2], each of which is fully occupied by atoms of A and B, respectively. Thus, the nearest neighbours of each A are only B atoms and *vice versa*. For the fully disordered crystal, both positions are equivalent and are randomly occupied by A and B. The degree of long-range order is $\eta = 2x_A^{[1]} - 1$, where x is a molar fraction of A in the sub-lattice [1]. Each growth temperature is characterized by an equilibrium η_e. However, at higher supersaturations, velocity of attachment of atoms is substantially greater then velocity of detachment. The degree of order may drop to zero, whereas the equilibrium degree of order may be equal to one.

The expression for the degree of long-range order near equilibrium (Chernov and Lewis, 1967) is

$$\eta = 1 - 2/\Omega^2 q^{2(\psi+2)}. \tag{3.26}$$

Here $\Omega = \nu/\omega_+$, where $\nu \approx 10^{12}\,\mathrm{s}^{-1}$ a vibrational frequency of the crystal. Substitution of the equilibrium temperature q_e into Equation (3.26) gives the equilibrium value of the long-range order η_e. To express the difference between the long-range ordered and equilibrium states supersaturation must be calculated. Supersaturated states are created by lowering the vapor temperature (change of q) and by increasing its pressure (change of ω_+, which is proportional to the vapor pressure P). In the first case,

$$\Delta\eta = \eta_e - \eta = \frac{2}{\Omega^2}\left(\frac{1}{q^{2(\psi+2)}} - \frac{1}{q_e^{2(\psi+2)}}\right) \approx \frac{4(\psi+2)}{\Omega^2 q_e^{2(\psi+2)}} \cdot \frac{\Delta q}{q_e}.$$

Following Chernov, assume $q_e \approx 0.1$ with a relatively high supersaturation $\Delta q/q_e = 0.3$. The value of $\omega_+ \approx 10^6$ for growth from vapor or from solution. Then, $\Delta\eta \approx 0.0005$. The significant supersaturation of about 0.3 leads to a negligible change of the ordering. In the second case,

$$\Delta\eta = \eta_e - \eta = \frac{2}{q^{2(\psi+2)}}\left(\frac{1}{\Omega^2} - \frac{1}{\Omega_e^2}\right) \approx \frac{4}{q^{2(\psi+2)}\Omega^2} \cdot \frac{\Delta\Omega}{\Omega}.$$

The relative supersaturation of the vapor is expressed through the change of the pressure $\frac{\Delta\mu}{RT} = \ln\frac{P}{P_e} \approx \frac{\Delta P}{P_e} = \frac{\Delta\omega_+}{\omega_{+e}} = \frac{\Delta\Omega}{\Omega}$. The subscripts e denote equilibrium values. Using the same initial values of all parameters $\Delta\eta \approx 0.0001$.

The validity of the near equilibrium condition that is necessary for the application of Equation (3.26) follows from fulfillment of the inequality $q^{1-\psi}(1-\eta) \approx 0.001 = 1$ (Chernov, 1970).

Since the crystallization from solution is similar to crystallization from the vapor, the growth ordering should not change significantly for supersaturations between 0 and 0.3, the range usually achievable for the alums. The growth rate is directly related to the supersaturation of the solution, therefore, the results outlined above can be easily adapted to model the relationship between the degree of ordering and growth rate. Thus, effect of growth rate seems to be slight. Nevertheless, the estimates provided above are rough. The steps and kink density and the value ψ, among other parameters, can deviate from those used.

3.5.5. Hydrodynamics and Mass Transfer

Data on the dependence of anomalous birefringence on hydrodynamics and mass transfer exist only for alum crystals (Shtukenberg *et al.*, 2000). For $(K, NH_4)Al(SO_4)_2 \cdot 12H_2O$ and $K(Al, Cr)(SO_4)_2 \cdot 12H_2O$ grown under different hydrodynamic conditions, no correlation with the mass transfer coefficient was observed. Stirring does not affect the birefringence. This suggests that the interface processes are deterministic, consistent with the growth desymmetrization mechanism.

At the same time the mass transfer can strongly modulate the *inhomogeneous* distribution of optical anomalies. Complex vicinal relief and sub-sector zoning is apparently linked to more complicated hydrodynamic conditions. Moreover, the stirring of the solution influences the anomalous progression of anomalous birefringence (Shtukenberg *et al.*, 2001b; Shtukenberg and Punin, 2003, see section 3.3.5).

CHAPTER 4

HETEROGENEOUS CRYSTALS

4.1. OPTICS OF HETEROGENEOUS CRYSTALS

Heterogeneous crystals often resemble single crystals via the regular intergrowth of different phases. The sizes of components can vary in scale from nanometers to centimeters. Domains $< 100\,\mu$m, too small to reasonably separate but larger than the wavelength of light form the subject of this chapter. Sub-wavelength heterogeneity can be too small to recognize directly in an optical microscope, but that is not to say that submicroscopic domains won't have a great effect on optical properties.

Heterogeneous crystals can be classified according to their dimensionality that essentially defines their optical properties.

1. *Zero-dimensional* - more or less isometric inclusions, such as colloidal particles captured during growth.
2. *One-dimensional* - rod-like inclusions of another phase.
3. *Two-dimensional* - layering of two or more phases as in polytype intergrowths. Anomalous optics have been most well studied in layered intergrowths.

Alternatively, we can classify heterogeneous crystals by composition:

1. *Components have the same composition and the same crystal structures*. This class of objects includes polysynthetic micro- and sub-microtwinning, as found in pyroxenes ($XM(Si, Al)_2O_6$), carbonates, and feldspars ($XAl_{(1-2)}Si_{(3-2)}O_8$).
2. *Components have different compositions and the same or nearly the same crystal structures*. This group includes crystals with fine oscillatory zoning, such as garnets and vesuvianite ($Ca_{10}(Mg, Fe)_2Al_4(SiO_4)_5(Si_2O_7)_2(OH)_4$). It also includes many ex-solution structures found in feldspars and pyroxenes.
3. *Components have the same composition and the different crystal structures*. The group includes polytype intergrowths, polymorphs that differ in the stacking of two-dimensional sheets such as the mica group ($M_{2-3}(X, Si)_4O_{10}(O, F, OH)_2$).
4. *Components have different compositions and different crystal structures*. This group covers syntactic intergrowths, oriented inclusions, or incorporated domains of another phase. *Syntaxy* can be defined as an intergrowth between two mineral species in which multiple unit cells coincide in size and shape.

It describes intergrowths of mixed-layer minerals such as biopyriboles (mixed talc-like and pyroxene-like crystals), carbonates, and oxides among others (Drits, 1997).

X-ray diffraction and electron microscopy are used in tandem to establish the nature of intergrowths. However, unlike light microscopy, they are ill suited to the rapid analysis of many crystals. Moreover, they are not sensitive enough to detect minor intergrowths that can nevertheless have drastic optical consequences. We reemphasize the conditional quality of optical anomalies. If the heterogeneity is obvious, the "anomalous" optical properties are undoubtedly a consequence of intergrowth. If the heterogeneity is not apparent—even though it may be suspected and ultimately detected through methods of analysis more subtle and sophisticated than polarized light microscopy—we may speak of "optical anomalies"

If the size of particles or thickness of layers in a heterogeneous crystal is less than the wavelength of light, the object may resemble a single crystal optically and morphologically. The complex structure of such an *optically homogeneous* system manifests itself as broad variations of orientation and shape of the optical indicatrix within and between crystallites in the ensemble. Optical properties are not well correlated to chemical composition in such cases. If the thickness of layers (or some other characteristic size) exceeds the wavelength of light the crystal becomes *optically heterogeneous*, with the loss of extinction and the distortion of interference (conoscopic) figures.

The overwhelming abundance of heterogeneous layered structures consisting of a great number of slabs of varying thickness, composition, and orientation is such that, unless otherwise specified, these two dimensional heterogeneities will be the focus of the following inquiry.

4.2. OPTICALLY HOMOGENEOUS SYSTEMS

4.2.1. Inclusions

4.2.1.1. Form birefringence

If the crystalline matrix contains non-isometric regularly oriented inclusions of some other phase whose size in at least one dimension is less than the wavelength of light, the corresponding distortions of the optical indicatrix are said to result from so-called *form birefringence* (Born and Wolf, 1980). Consider identical optically isotropic inclusions with refractive index n_2 having the shape of prolate (elongated) ellipsoids of revolution (axial ratio $h_{\parallel}/h_{\perp}$) similarly oriented, and located within an isotropic matrix of refractive index n_1. The volume fraction of inclusions f_2 is assumed to be small compared with the volume fraction of the matrix $f_1 : f_2 = 1 - f_1 \ll 1$. The latter assumption can be rejected if the difference between refractive indices is small. Generally, such a system acts as a uniaxial crystal with the optic axis directed along the axis of revolution of the inclusions. The difference in refractive indices

observed parallel $n_{\parallel} = n_{\varepsilon}$ and perpendicular $n_{\perp} = n_{\omega}$ to the axis of revolution can be calculated following Bragg and Pippard (1953):

$$n_{\varepsilon}^2 - n_{\omega}^2 = \frac{f_1 f_2 \left(n_2^2 - n_1^2\right)^2 \left(L_{\perp} - L_{\parallel}\right)}{n_1^2 \left[1 + f_1 \left(\frac{n_2^2 - n_1^2}{n_1^2}\right)\left(L_{\perp} + L_{\parallel}\right) + f_1^2 \left(\frac{n_2^2 - n_1^2}{n_1^2}\right)^2 L_{\parallel} L_{\perp}\right]}. \tag{4.1}$$

In this expression, variables L denote depolarization coefficients that can be found from $L_{\parallel} + 2L_{\perp} = 1$ and $L_{\parallel} = 1/\left[1 + 2(h_{\parallel}/h_{\perp})^{1.2}\right]$. If the inclusions are elongated along the axis of revolution, the optical sign is always positive. In the limiting case, $h_{\parallel}/h_{\perp} = \infty$. The difference of refractive indices is expressed as follows

$$n_{\varepsilon}^2 - n_{\omega}^2 = \frac{f_1 f_2 \left(n_1^2 - n_2^2\right)^2}{\left(1 + f_1\right) n_2^2 + f_2 n_1^2}. \tag{4.2}$$

This Equation (4.2) is also applicable to inclusions of cylindrical shape with a large aspect ratio, $h_{\parallel}/h_{\perp} \geq 10$. In the limiting case of $h_{\parallel}/h_{\perp} = 0$ in a system of parallel slabs, Equation (4.1) reduces to a simpler form,

$$n_{\varepsilon}^2 - n_{\omega}^2 = -\frac{f_1 f_2 \left(n_1^2 - n_2^2\right)^2}{f_1 n_2^2 + f_2 n_1^2}. \tag{4.3}$$

This is the limiting case of a layered heterostructure. In such a system, as well as in all the systems where inclusions have a disc shape $h_{\parallel}/h_{\perp} < 1$, the optical sign is always negative.

If the inclusions are isometric $h_{\parallel}/h_{\perp} = 1$ symmetry requires overall optical isotropy.

Form birefringence is widely used in biological microscopy to study shape, orientation, and volume fraction of, for example, viruses (Born and Wolf, 1980) and also in colloid chemistry in the study of thixotropy, the property of some gels of becoming fluid when stirred or shaken. If the particles are birefringent, refractive index matching oils/media can be used to distinguish the particles from the matrix.

During the optical examination of minerals, form birefringence is usually not taken into account. One exception is chalcedony (Correns and Nagelschmidt, 1933) with birefringence ($\Delta n < 0.006$) was significantly lower than that of quartz ($\Delta n \approx 0.009$). Positive form birefringence was assumed to compensate in part for the negative birefringence of fibers (although the quartz is optically positive the fibers are considered to be negative since the two-fold axis of quartz is directed along the fiber axis). This hypothesis was confirmed by impregnation of porous samples with liquids of varying refractive index, followed by comparison of measured and

calculated birefringence. The birefringence was calculated using an Equation like (4.2) that also accounts for the optical anisotropy:

$$n_{\parallel}^2 = f_1 n_1^2 + f_2 n_{2\parallel}^2$$
$$n_{\perp}^2 = n_1^2 \frac{(f_2+1)\, n_{2\perp}^2 + f_1 n_1^2}{(f_2+1)\, n_1^2 + f_1 n_{2\perp}^2}, \tag{4.4}$$

where the subscripts $\parallel$ and $\perp$ refer to the long fiber axis. Similar expressions permit the calculation of form birefringence for many substances.

Form birefringence can account for the higher birefringence of quartzine compared with chalcedony. Quartzine fibers are elongated along the three-fold axis so the form birefringence should increase the intrinsic birefringence as observed. The relatively high birefringence (up to 0.012) in layers of "amorphous" silica in some onyxes is likely form birefringence of lamellar quartz polymorphs, cristobalite and tridymite.

Generally, the form birefringence is more abundant than expected. High-resolution techniques reveal an increasing number of substances with microheterogeneous structures (Reeder, 1992; Merlino, 1997).

4.2.1.2. Anisotropic inclusions in an isotropic matrix

Isotropic matrices with sufficiently birefringent inclusions (with the volume fraction f_2) can usually be modeled without taking form birefringence into account. Then, the observed the birefringence is

$$\Delta n = f_2 \Delta n_2 \tag{4.5}$$

where Δn_2 is the birefringence of the second phase. If the isotropic matrix contains only 0.5% of the anisotropic phase with $\Delta n_2 = 0.001$, the birefringence will be visible routinely. Typically, phase analysis by x-ray diffraction (XRD) requires ≥ 5 volume percent of impurity. In other words, XRD will only detect the major component thereby missing the etiology of the birefringence. If $\Delta n_2 = 0.01$, even 0.05% of the second phase can be detected optically, far below the x-ray sensitivity threshold.

In practice, this approach was used to measure the volume fraction of the orthorhombic double salt $NH_4Cl \cdot CO(NH_2)_2$ in cubic ammonium chloride (Franke *et al*., 1987; Punin *et al*., 1993), section 4.2.7, Figure 4.13. The anomalous birefringence in ammonium chloride crystals induced by syntactic intergrowths with the double salts $CuCl_2 \cdot (NH_4Cl)_2 \cdot 2H_2O$ and $MnCl_2 \cdot (NH_4Cl)_2 \cdot 2H_2O$ is shown in Figures 4.1, 4.2, respectively.

4.2.1.3. Anomalous pleochroism

The problem of anomalous pleochroism produced by organic dyes was discussed in section 3.4.4. Gaubert questioned whether artificial pleochroism could be extended

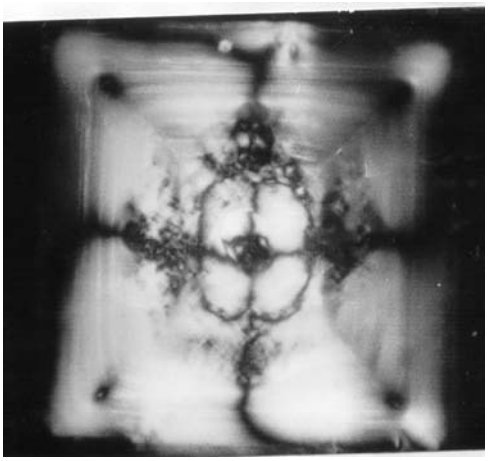

Figure 4.1. Anomalous birefringence in NH_4Cl related to syntactic intergrowth with $CuCl_2 \cdot (NH_4Cl)_2 \cdot 2H_2O$. Crystal size ~ 5 mm

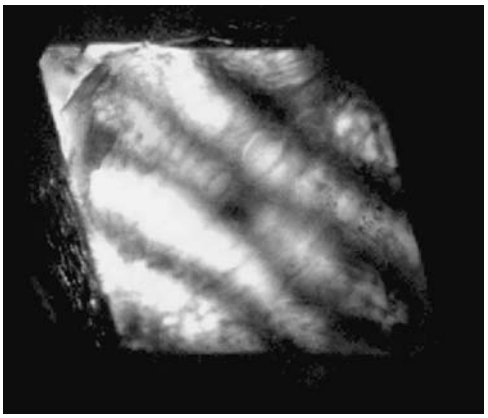

Figure 4.2. Anomalous birefringence in NH_4Cl related to syntactic intergrowth with $MnCl_2 \cdot (NH_4Cl)_2 \cdot 2H_2O$. Crystal size ~ 0.8 mm (see Color Section following page 254)

to isotropic hosts (Gaubert, 1894). He was the first to describe a *bona fide* anomalously pleochroic cubic crystal hosts: NaCl with murexide, and $NH_4Br(Cl)$ with tartrazine (Gaubert, 1915). Gaubert also invented crystals of $Ba(NO_3)_2$, $Pb(NO_3)_2$ and the isomorphous anhydrous $Sr(NO_3)_2$ containing methylene blue, $C_{16}H_{18}ClN_3S$ (Gaubert, 1900, 1930).

Through this work, Gaubert came to distinguish two types of inclusions. In the first kind, the colored molecules entered the crystal in whatever their degree of dilution, while in the second kind, the colored material was only taken up when it was saturated in the solution. Studies of the pleochroism of the resultant

colored crystals indicated that in the first case the colored molecules were as they would be in solution, mono-dispersed, while in the second case there was a regular grouping of crystalline dye particles within the colorless medium. Gaubert termed the latter phenomenon *syncrystallization* (Gaubert, 1905) For example, ponceau red and bismarck brown formed microcrystalline deposits in K_2SO_4 (Gaubert, 1912).

Gaubert's concept of syncrystallization, a term that predated x-ray diffraction, gave way to *epitaxy*, the oriented overgrowth of one crystalline substance on another. Neuhaus brought this highly restricted view of isomorphism to studies of dye inclusion crystals and thereby carried some of Gaubert's results into the post diffraction era. By measuring lattice constants of crystalline dyes and the salts with which they had syncrystallized Neuhaus was able to propose epitaxial relationships based upon the close matching of lattice dimensions (Neuhaus, 1942). This numerology, contrived in hindsight, was applied to those systems formerly studied by Gaubert and others (Neuhaus, 1941a,b). While it may make sense in a limited number of genuine syncrystals it is undoubtedly wrong in many other cases.

No dyed crystals have received more attention than the cubic alkaline earth nitrates, $Ba(NO_3)_2$ and $Pb(NO_3)_2$ stained with methylene blue and its congeners. Slavnova (Slavnova, 1959) carried out the most extensive and informative analyses of this nitrate mixed crystal family. Along with Vedeneeva, she advanced our understanding with the use of spectrophotometry, a method of analysis they earlier applied to dyes adsorbed in clays (Vedeneeva and Slavnova, 1952; Slavnova, 1956). In $Pb(NO_3)_2$, methylene blue absorbed at energies comparable to that of dilute solutions. On the other hand, the higher energy absorption in $Ba(NO_3)_2$ was characteristic of dimers or higher crystalline aggregates. At methylene blue concentrations higher than 5×10^{-3} M, $Pb(NO_3)_2$ no longer co-crystallized with the dye, while dye incorporation into $Ba(NO_3)_2$ only began at concentrations greater than 3×10^{-3} M (Slavnova, 1956, 1958) This puzzling behavior is further exemplified by methylene blue preferring {100} sectors of $Pb(NO_3)_2$ as opposed to {111} for $Ba(NO_3)_2$. The $Ba(NO_3)_2$ crystals typically exhibited strong linear dichroism (Khlopin and Tolstaya, 1940). This work was extended to methylene blue congeners (Melankholin and Slavnova, 1959; Slavnova, 1960). However, a clear picture of the physico-chemical interactions of methylene blue with the alkaline earth nitrates is outstanding.

4.2.2. Optically Homogeneous Heterostructures

In layered heterostructures the optical indicatrix consists of several types of lamellae whose thickness is less than the light wavelength. Here, we consider two layers, however the results can be generalized to any number. Each layer has its own optical indicatrix and volume fraction f: $f_1 + f_2 = 1$. Despite the seeming simplicity of this model system, the proper construction of the optical indicatrix can be vexing.

A simple and accurate solution can be obtained only for the simplest case—layering of *isotropic* lamellae with refractive indices n_1 and n_2. This is an example

of so-called form birefringence (Born and Wolf, 1980) considered in section 4.2.1.1, characterized by a uniaxial (negative) optical indicatrix with the optic axis directed normal to the lamellae. One can anticipate this arrangement in cubic crystals with thin oscillatory zoning such as the garnets studied by Ivanova *et al*. (1998).

For optically anisotropic components, three approximate approaches for constructing the optical indicatrix are used.

1. *Mallard's method* (Pockels, 1906). The optical indicatrices are averaged such that each radius vector of the optical indicatrix takes on an average value of the radius vectors of the individuals

$$r = f_1 r_1 + f_2 r_2. \tag{4.6}$$

   This method was criticized in 1898 by Fedorov (1953a) and then by Pockels (1906), since the resulting figure is not an ellipsoid. Nevertheless, it was successfully applied to the analysis of feldspar twinning (Marfunin, 1959a) and to polytype intergrowths and twinning of sheet compounds (Drits *et al*., 1966; Murav'ev and Drits, 1970). The smaller the difference between the principal refractive indices, the closer the figure to an ellipsoid.
2. *Fedorov's* (1953a) *and Pockels'* (1906) *method*. Mindful of the limitations of Mallard, alternatively, the dielectric impermittivity tensors may be averaged: $\eta = f_1\eta_1 + f_2\eta_2$. The radius vector of the new optical indicatrix is defined as follows:

$$\frac{1}{r^2} = \frac{f_1}{r_1^2} + \frac{f_2}{r_2^2}. \tag{4.7}$$

   This method was used in the description of the optical properties of plagioclase (Pockels, 1906; Fedorov, 1953a).
3. *Hauser's and Wenk's (1976) method*. The dielectric permittivity tensors are averaged: $\kappa = f_1\kappa_1 + f_2\kappa_2$. The radius vector of the new optical indicatrix is defined as follows:

$$r^2 = f_1 r_1^2 + f_2 r_2^2. \tag{4.8}$$

This method was used for analysis of polysynthetic calcite twinning and feldspar ex-solution structures (Hauser and Wenk, 1976).

Methods 2 and 3 result in ellipsoids, albeit still approximate. Indeed, averaging $1/\kappa$ implies the constancy of displacement vector **D** in both the components, whereas the averaging of κ implies the constancy of the electric field E. Neither average is strictly correct since at the boundary of layers with different refractive indices the normal component of **E** and as well as the tangential component of **D** are discontinuous (Born and Wolf, 1980). The maximum relative error κ_{aver}. obtained for the direction in calcite with $n_\gamma - n_\alpha = 0.172$ using method 3 is about 1%; it decreases as the birefringence increases. Fedorov's error is twice as large; the error in Mallard's method is even slightly smaller. Mallard's method

is the simplest and therefore it is convenient for the construction of the optical indicatrix of heterogeneous, but locally optically homogeneous crystals. Its main advantage is in determining the volume fractions of components from the optical measurements.

4.2.3. Heterostructures of Polytype Modifications

Consider the common situation where one axis of the optical indicatrix of each component is perpendicular or nearly perpendicular to the lamellae. Let all the components have the same eigenvalues n_a, n_b and n_c mutually rotated around the common axis n_c by an angle ψ. This is a characteristic of many polytype compounds including sheet silicates such as micas, synthetic fluorphlogopite ($Mg_3K(AlF_2O(SiO_3)_3)$) and potassium ferrocyanide trihydrate ($K_4Fe(CN)_6 \cdot 3H_2O$). Polytype crystals are built from two-dimensional structural units superimposed on each other in different orientations. Various layer stackings can lead to twinning, syntactic intergrowths of polytypes, ordered polytypes with different numbers of layers, and one-dimensional disordered crystals. Generally speaking we have order-disorder (*OD*) crystals (Dornberger-Schiff and Grell, 1982). Components of such heterogeneous crystals are parallel two-dimensional sheets. Two potassium ferrocyanide and three mica components can be integral. If concentrations of components change periodically with dimensions smaller than the wavelength of light, the crystals will be optically homogeneous, described by a common indicatrix. Since the mutual rotation of components occurs only around one axis n_c, the elliptical sections are averaged. For a two-component system, the problem reduces to the geometrical summation of two similar ellipses with the axial ratio for the corresponding axes equal to f_1/f_2 and the angle ψ between these corresponding axes. The resulting retardation is defined as a vector sum of the components, hence the principal refractive indices in the given section n'_a and n'_b and the extinction angle of the heterogeneous crystal φ with respect to one of the components can be found as

$$n'_{a,b} = \frac{n_a + n_b}{2} \pm \frac{n_a - n_b}{2} \left[f_1^2 + f_2^2 + 2 f_1 f_2 \cos 2\psi \right]^{1/2} \quad \text{and} \tag{4.9}$$

$$\cot 2\varphi = \cot 2\psi + \frac{f_1}{f_2} \frac{1}{\sin 2\psi}. \tag{4.10}$$

Obviously, if the components have the same fractions $f_1 = f_2 = 0.5$, the resulting optical indicatrix will be located symmetrically with respect to the component indicatrices and its principal axes will lie along the bisectors of angles formed by corresponding axes of the components. The principal refractive indices can be calculated from

$$n'_{a,b} = \frac{n_a + n_b}{2} \pm \frac{n_a - n_b}{2} \cos \psi. \tag{4.11}$$

This formula can be useful in determining the optical constants of some polytype modifications of sheet minerals (Drits *et al*., 1966; Murav'ev and Drits, 1970) or polysynthetic twins (Marfunin, 1959a).

4.2.4. The Reverse Problem for the Polytype Intergrowths

4.2.4.1. Two-component systems

From experiment, it is easy to find the following crystal optical characteristics: an extinction angle φ of the system with respect to extinction position of one component, the birefringence $(n_b - n_a)_r$ in the stacking plane, and the axial angle $2V_r$. The angle φ is defined by expression (4.10). Two other characteristics can be found from (4.9). Hence

$$(4.12) \qquad (n_b - n_a)_r = \left(f_1^2 + f_2^2 + 2f_1 f_2 \cos 2\psi\right)^{1/2} (n_b - n_a) \equiv Q\,(n_b - n_a)\,,$$

$$(4.13) \qquad \sin^2 V_r \approx \frac{Q \sin^2 V}{1 - \frac{1-Q}{2} \sin^2 V},$$

where $2V$ is the axial angle for each component. It is important to know the value of φ exactly, $(n_b - n_a)_r$, and $2V_r$ with accuracy comparable to Fedorov or Hauser and Wenk.

In a two-component crystal $f_1 + f_2 = 1$, the fraction of components can be found from each of three parameters using the expressions (4.10), (4.12) and (4.13). However, determination of the extinction angle requires a crystallographic reference point (faceting, zoning, etch figures *etc*.) sometime but not always present. The measurement of birefringence requires accurate knowledge of path length (crystal thickness), therefore, axial angle measurements are the easiest way to assay component fractions.

A good example of a two-component system is **potassium ferrocyanide trihydrate** ($K_4Fe(CN)_6 \cdot 3H_2O$) grown from low-temperature aqueous solutions. Brewster had long ago recognized the anomalous biaxiality of these apparently tetragonal crystals (Brewster, 1818a). Brauns (1885) likewise studied these crystals.

In the crystal structure, two-dimensional units can stack in two ways, with a shift of the layers in one of two mutually perpendicular directions. This corresponds to the mutual rotation of components by $\psi = 90°$ (Punin *et al*., 1982). The compound has two polytype modifications: monoclinic $2M$ (For notation, refer to Appendix 1, Mica Nomenclature) with $f_1 = 1$ and tetragonal $4Tr$ with $f_1 = f_2$. It forms *OD*-crystals with any f_1/f_2 ratio.

For the case of $\psi = 90°$, measurement of the extinction angle φ does not give any additional information since the Equation (4.10) results in indeterminate forms of type $(\infty - \infty)$. For $f_1 > f_2$ and $f_1 < f_2$, one gets $\varphi = 0°$ and $\varphi = 90°$, respectively. The extinction position does not change as a function of component concentratons.

The ratio $f_1 = f_2$ corresponds to an isotropic section. As a result, for $\psi = 90°$ Equations (4.12) and (4.13) are simplified to

$$(4.14) \qquad (n_b - n_a)_r = (f_1 - f_2)(n_b - n_a),$$

$$(4.15) \qquad \sin^2 V_r \approx \frac{(f_1 - f_2)\sin^2 V}{1 - f_2 \sin^2 V},$$

where it is assumed that $f_2 < f_1$. Thus the volume fraction of component 2 can be found from the birefringence or from the axial angle of the heterogeneous crystal

$$(4.16) \qquad f_2 = \frac{1}{2} - \frac{(n_b - n_a)_r}{2(n_b - n_a)} = \frac{\sin^2 V - \sin^2 V_r}{\sin^2 V\left(2 - \sin^2 V_r\right)}.$$

The expressions obtained were used for analysis of polytype composition in potassium ferrocyanide trihydrate (Punin and Zhogoleva, 1980; Punin and Kotelnikova, 1983). The fraction of different polytypes for a given growth condition varies widely. At 25 °C, the crystals (Figure 4.3) are closer to monoclinic modification and at 50 °C to tetragonal (Kotelnikova *et al*., 1989). The change of growth conditions (concentration of impurities, supersaturation) not only shifts the average polytype composition (Figure 4.3) but also changes the distribution of polytype compositions (Punin and Zhogoleva, 1980; Punin, 1987; Kotelnikova *et al*., 1989). Variations in polytype concentrations occur not only among crystals in ensembles but even within one crystal among growth sectors or zones (Punin *et al*., 1982). In these cases, *OD*-crystals form according to the deformation-growth mechanism (Punin, 1987, 1994, 2002) whereby impurities produce stresses that cause twinning or splitting. Stacking faults can intersect the zoning and sector zoning boundaries accompanied by formation of complex superimposed structures (Figure 4.4).

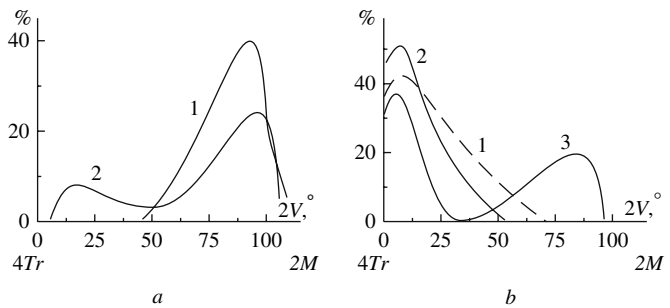

Figure 4.3. Effect of the growth temperature on the polytype composition of potassium ferrocyanide trihydrate crystals found from the value of the axial angle $2V$. Growth temperature: (*a*) 50 °C, (*b*) 25 °C. 1 - no additivities; 2 and 3 - with impurities of KOH and K_2CrO_4, respectively (after Kotelnikova *et al*., 1989)

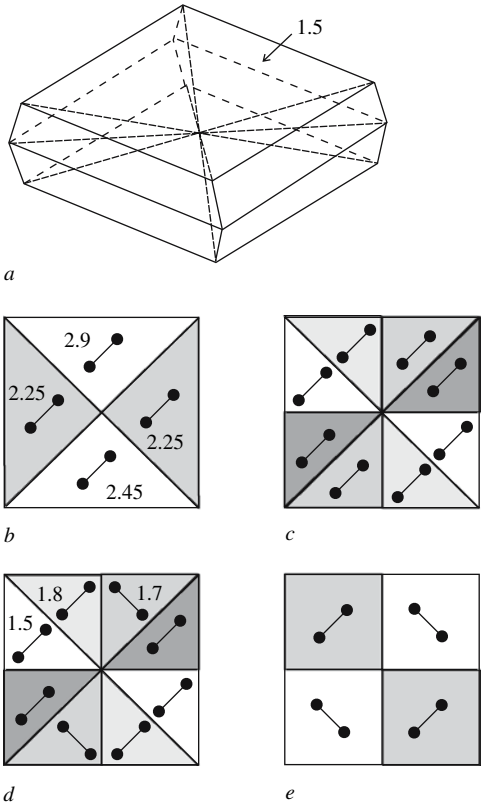

Figure 4.4. Sector zoning of potassium ferrocyanide trihydrate. (*a*) idealized {001} plates with growth sectors delineated, (*b–e*) sector zoning in (001) sections. (*b*) shows the typical situation in which the optical sector zoning corresponds to growth sector zoning. (*e*) illustrates the unusual situation lacking a correspondence between optical sectors and growth sectors. (*b*, *c*) represent intermediate variants. The optical patterns shows both the "true" growth sectors and additional growth sectors induced by deformation-growth processes (Punin, 1987, 1994, 2002). Numbers denote the birefringence $\Delta n \times 10^{-3}$, dumbbells indicate orientation of the optic axial plane, and colors denote parts of the crystal with discrete birefringences

4.2.4.2. Multicomponent systems

For multicomponent systems, Mallard's construction reduces to the geometrical summation of N similar ellipsoids with the ratio between the principal axes $f_1/f_2/f_3/\ldots$ and the condition

$$\sum_{i=1}^{N} f_i = 1. \tag{4.17}$$

The ellipses are rotated with respect to the first component by the angle ψ_i. Obviously $\psi_1 = 0$. The resulting retardation is found from the vector sum of each

component leading to the following expressions:

$$\tan 2\varphi = Q_y / Q_x, \tag{4.18}$$

$$(n_b - n_a)_r = \left(Q_x^2 + Q_y^2\right)^{1/2} (n_b - n_a) \equiv Q\,(n_b - n_a)\,, \tag{4.19}$$

$$\sin^2 V_r \approx \frac{Q \sin^2 V}{1 - \frac{1-Q}{2} \sin^2 V}, \tag{4.20}$$

where

$$Q = \left(Q_x^2 + Q_y^2\right)^{1/2}\,,\ Q_x = \sum_{i=1}^{N} f_i \cos 2\psi_i,\ Q_y = \sum_{i=1}^{N} f_i \sin 2\psi_i. \tag{4.21}$$

Thus, we can calculate the optical characteristics of a crystal comprised of any number of components. However, the reverse problem cannot be solved for more than three components since there are only two independent optical parameters that can be easily and reliably measured. The birefringence and axial angle $2V$ are interrelated (see Equations (4.19) and (4.20)). For a three component system, two independent Equations contain two variables f_i. The third unknown fraction can be found from Equation (4.17).

4.2.4.3. Mica: an example of a three component system

The optics of three component systems have been studied for synthetic fluorphlogopite and natural lithium-aluminum micas (see Appendix 1 for mica nomenclature) from rare-metal pegmatites, course-grained igneous formations. As is well known, micas consist of two-dimensional units mutually misoriented by multiples of 60°. Since the optical indicatrix always has a center of symmetry, we can restrict our consideration to three misorientations of 120° multiples. The indicatrix axis X is normal to the lamellae or makes a negligibly small angle to the normal. The indicatrix always rotates around $n_c = X$.

As mentioned above, to measure the fractions of a three component heterogeneous crystal it is necessary to know simultaneously the values of either φ, and $(n_b - n_a)_r$ or $2V_r$. Estimates of the deviation of a given heterogeneous structure from the pure polytype modification although not sufficient for an accurate determination of all volume fractions can be made from axial angle measurements.

The parameter Q in Equation (4.20) can take the same value for different fractions. If f_1 is assumed to be the major component (i.e. $1/3 \le f_1 \le 1$) the dependence of Q *vs.* f_1 can be drawn (Figure 4.5). Generally, decreasing f_1 from 1 to 1/3 is accompanied by a decrease of Q, and $2V$. However, the measured Q corresponds not to the single value f_1 but to some range. The greatest ambiguity corresponds to $Q = 0.5$; f_1 can vary in the range of 0.5–0.67 depending on the relationship between f_2 and f_3. The presence of this optical ambiguity should lead to the appearance of a satellite maximum on the $2V$ distribution curves as observed for crystals of fluorphlogopite. The stable modification $1M$ is characterized by $2V = 16°$.

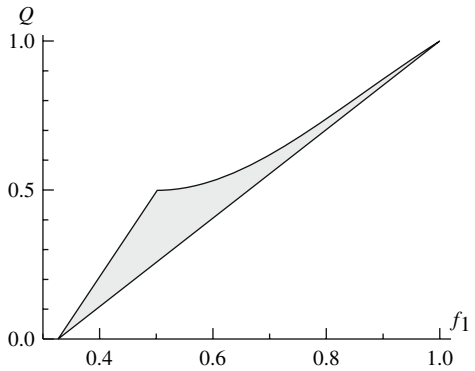

Figure 4.5. The optical ambiguity field for *OD*-micas. Depending on the relationship between fractions f_2 and f_3 one and the same value of Q corresponds to the certain range of the fraction f_1 contained within the shaded region

However, as seen in Figure 4.6, on the distribution curve this principal maximum is accompanied by additional maximum in the range of $2V = 9 - 12°$ (the value $Q = 0.5$ corresponds to $2V = 11°$). This satellite maximum does not argue for a polytype modification but results from the uncertainty between the axial angle and fractional distribution of components. This conclusion is confirmed by x-ray diffraction (Punin *et al.*, 1985a,b).

The stable polytype modification $1M$ of trioctahedral mica contains only one component. $2V$ distributions reflect the average *OD*-composition as well as dispersion in component concentrations (taking the satellite maximum into account). Variations in such distributions reflect the action of different growth conditions on

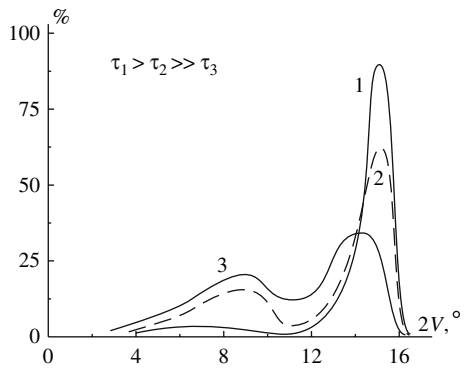

Figure 4.6. Distribution of fluorphlogopite ($Mg_3K(AlF_2O(SiO_3)_3)$ $2V$ values for varying synthesis times (τ). τ decreases (growth rate increases) from curve 1 to 3

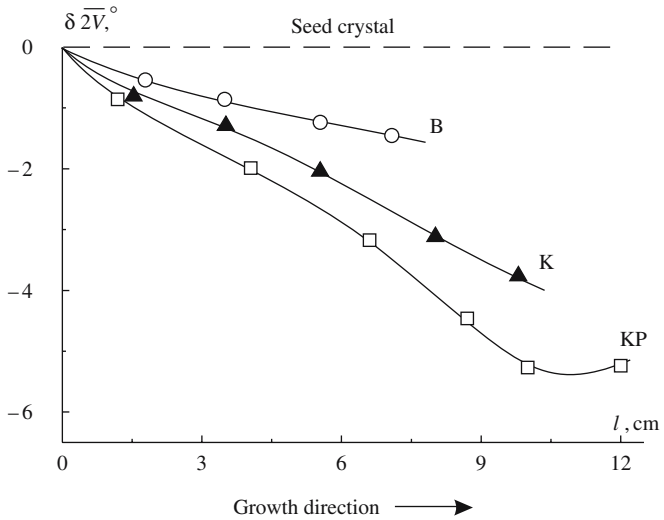

Figure 4.7. Decreasing axial angle $2V$ during the growth of synthetic fluorphlogopite ($Mg_3K(AlF_2O(SiO_3)_3)$) by the directional crystallization technique. B – cylindrical rotating crucible, K – cylindrical pendulous crucible, KP – plane pendulous crucible

the layer disorder (Punin and Kotelnikova, 1983; Punin, 1987). Figure 4.6 shows the evolution of the $2V$ distributions with increasing of growth rate. Figure 4.7 shows the decrease of the axial angle $2V$ and increase of layer disorder compared with the seed for the fluorphlogopite crystals grown by the directional crystallization technique (Punin *et al*., 1989). The concentration of stacking faults and the degree of microheterogeneity increases as the symmetry of the crucible-dependent thermal field decreases.

For dioctahedral and di-trioctahedral micas the situation is more complicated (Punin, 1989a; Punin *et al*., 1989, 1997). Stable modifications are usually two-component structures: $2M_1$ (muscovite—$KAl_2(AlSi_3O_{10})(F, OH)_2$) and $2M_2$ (lepidolite—$KLi_2Al(Al, Si)_3O_{10}(F, OH)_2$). The axial angle is not sensitive to distortion in stacking disorder and to the appearance of a third layer orientation as it was for trioctahedral mica.

Moreover, distinct from the $1M$ modification, where the $2V$ distribution is restricted to small axial angles (Figure 4.6), the $2V$ distribution is broadened on the high and low sides.

Figure 4.8 shows variations of the average axial angle $2V$ and its dispersion for the muscovite-polylithionite micas from the rare-metal pegmatites as a function of Li_2O concentration (Sokolov *et al*., 1987; Punin *et al*., 1989, 1997). Depending on the crystal composition, lepidolites of $2M_1$ and $2M_2$ modifications are characterized by $2V$ ranges from 24 to 40°, with an average value of 33° (Lapides *et al*., 1977). The axial angles of muscovites range from 35–50°. For the lepidolite (polylithionite) $1M$ modification, $2V$ varies from 35–60° with the average value of 42°. The

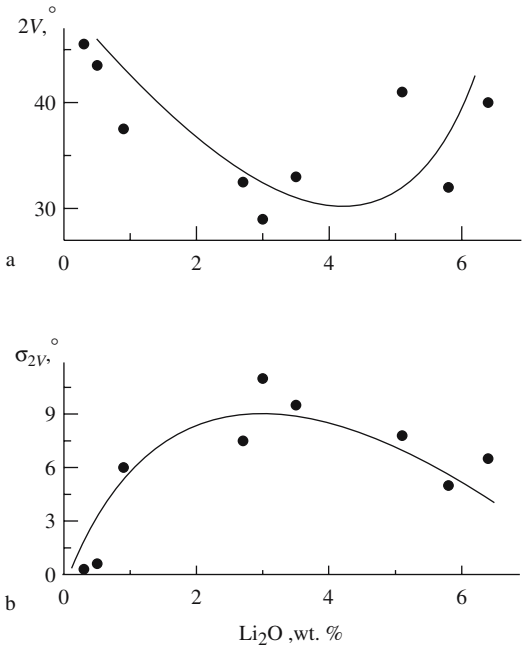

Figure 4.8. (*a*) The average value of axial angle $2V$ (*b*) and its dispersion σ_{2V} as a function of the Li_2O concentration in crystals of lithium-aluminum mica

optical properties of $2M_1$ muscovites are well-known. Therefore, it is possible using Equations (4.12) and (4.13) to obtain $2V$ values of 50°–70° for the pure $1M$ modification of which the $2M_1$ is composed. The value of the axial angle is strongly correlated to the lithium content.

This trend is complicated by the change of $2V$ due to stacking faults of two-dimensional structural units. Figure 4.8 shows the average values of $2V$ and their dispersion for the micas with different Li_2O concentrations. The muscovites with less Li_2O have stable $2V$s of about 45° with almost no dispersion. For the intermediate Li_2O concentrations, $2V$s decreases more than would be suggested by the chemical composition alone. Using maximal $2V$, of 56° and 48° for polylithionite and muscovite, respectively, gives $2V$ for the intermediate lepidolite of $2M_1$ or $2M_2$ modifications equal to 43°. The measured values vary, however, in the range of 29–33°. The micas of these compositions are characterized by the greatest layer disorder (micro-heterogeneity).

Micas with the largest concentration of Li_2O (polylithionate) should have the stable $1M$ modification with $2V$ angles of about 55–60°. In reality, we see average values varying from 30° to 42° among samples from different ore deposits. Although dispersion of the axial angle $2V$ is smaller than the intermediate lepidolites, it remains high due to high concentrations of stacking faults in the polylithionites.

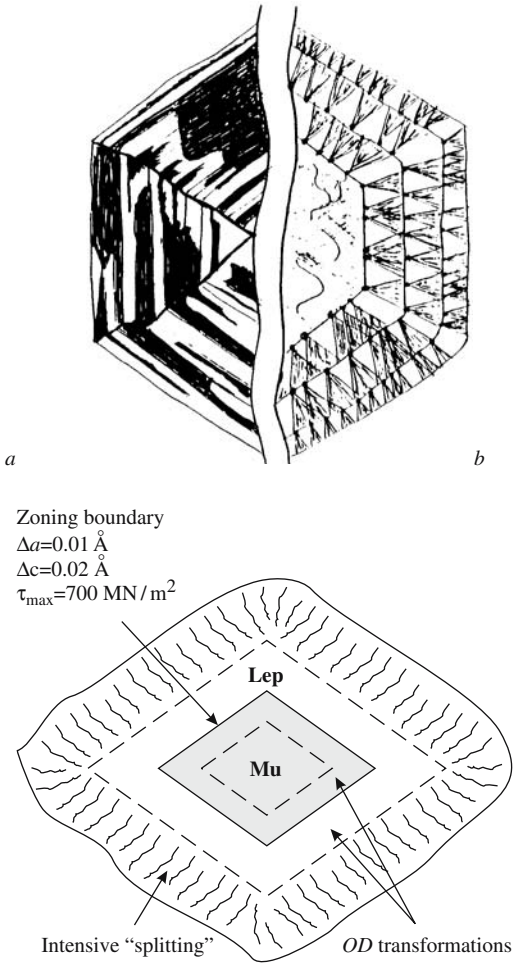

Figure 4.9. The *OD*-anatomy of lepidolite from rare-metal pegmatites. (*a*) concentric zoning and growth sector zoning distribution of *OD*-substructures (hatched areas), (*b*) nucleation of stacking faults at the inclusions and broadening of them in the crystal growth direction, (*c*) muscovite crystal (**Mu**) with lepidolite rim (**Lep**). At the zoning boundary between muscovite and lepidolite the lattice constants *a* and *b* change significantly resulting in large internal stress (τ_{max}) and stress induced deformations

Optical anomalies in individual lepidolite crystals are characterized by concentric zoning and growth sector zoning (Figure 4.9). However, as for potassium ferrocyanide trihydrate, the deformation-growth (Punin, 1987, 1994, 2002) etiology of the layering disorder results in optical structures that follow the zoning boundaries only in part and often intersects them.

The examples considered above show that the simplest optical methods are informative if we do not need to know the concrete polytype composition but are interested in the overall balance of order/disorder. Moreover, small concentrations of stacking faults are much more easily detected optically than by x-ray diffraction. For this reason the "pure" (according to x-ray diffraction data) polytype modifications reveal significant dispersion of the axial values. Samples with similar compositions and diffraction patterns can be optically quite distinct.

4.2.5. Polysynthetic Twinning

Multiple parallel, lamellar twinning is called polysynthetic. Polysynthetic twinning builds *OD*-crystals with different polytypes and arrangements of stacking faults. Since such twinning manifests itself in different orientations of two-dimensional structure units around the normal to the stacking plane it is not necessary to consider it as distinct from polytypism. However, in the general case of non-polytype structure, optical indicatrices are misoriented with respect to the twinning axis or normal to the twinning plane. As a rule, there are no coincident indicatrix axes. The following examples illustrate such structures.

4.2.5.1. Calcite

Calcite ($CaCO_3$) crystals are characterized by polysynthetic twinning on the $(01\bar{1}2)$ plane. Correspondingly, the optical indicatrices of the twin lamellae are rotated around the normal to this plane. In the crystal physical coordinate frame, the axes X and Z coincide with the trigonal a and c axes, Y is perpendicular to the plane XOZ (Figure 4.10) and the optic axis rotates by the angle $\psi = 52.2°$ in the plane

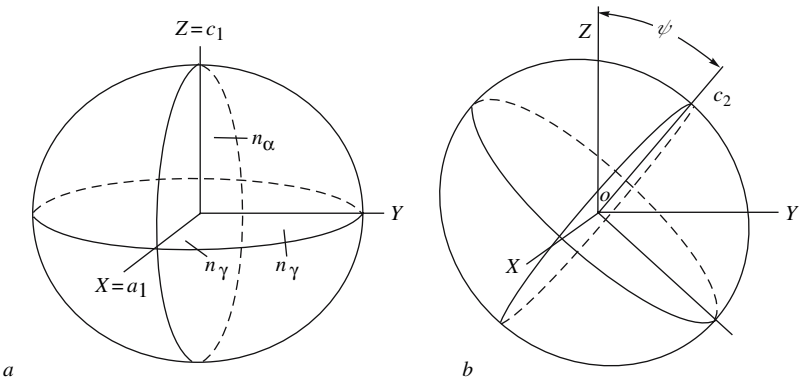

Figure 4.10. Orientation of the optical indicarix of calcite in the crystal physical coordinate frame X, Y, Z). (*a*) initial orientation (host), (*b*) twin orientation. The hexagonal crystal axes of these two orientations $a_1 = a_2 = X$ (indicatrix axis n_ω), c_1 and c_2 (indicatrix axis n_ε) (after Hauser and Wenk, 1976)

YOZ. This rotation of the optical indicatrix can be characterized by the following rotation matrix

$$\widehat{\mathbf{R}} = \begin{pmatrix} 1 & 0 & 0 \\ 0 & \cos\psi & \sin\psi \\ 0 & -\sin\psi & \cos\psi \end{pmatrix}. \tag{4.22}$$

Two other twin systems can be obtained by additional rotations around Z by angles of 120° and 240° (Figure 4.10). Therefore, in a general case the rotation matrix for all three twinning orientations $i = 2, 3, 4$ is expressed as follows

$$\widehat{\mathbf{R}}_i = \begin{pmatrix} \cos\phi_i & -\sin\phi_i\cos\psi & -\sin\phi_i\sin\psi \\ \sin\phi_i & \cos\phi_i\cos\psi & \cos\phi_i\sin\psi \\ 0 & -\sin\psi & \cos\psi \end{pmatrix} \tag{4.23}$$

where $\phi_2 = 0$, $\phi_3 = 120°$ and $\phi_4 = 240°$. For $i = 2$, expression (4.23) reduces to (4.22). Hauser and Wenk (1976) calculated properties of such heterogeneous but optically homogeneous crystals (thickness of lamellae smaller than the light wavelength) by averaging the dielectric permittivity tensors. For the simple twin with only two orientations, the dielectric permittivity tensor has the form

$$\hat{\kappa} = f_1\widehat{\kappa_1} + f_2\widehat{\kappa_2} = f_1\widehat{\kappa_1} + f_2\widehat{\mathbf{R}_2}\widehat{\kappa_1}\widehat{\mathbf{R}_2}^{-1}, \tag{4.24}$$

where the dielectric permittivity tensor of calcite in the crystal physical coordinate frame $\widehat{\boldsymbol{\kappa}}_1$ is

$$\widehat{\kappa_1} = \begin{pmatrix} \kappa_o & 0 & 0 \\ 0 & \kappa_o & 0 \\ 0 & 0 & \kappa_e \end{pmatrix} = \begin{pmatrix} \omega^2 & 0 & 0 \\ 0 & \omega^2 & 0 \\ 0 & 0 & \varepsilon^2 \end{pmatrix}. \tag{4.25}$$

Substitution of Equations (4.22) and (4.25) into (4.24) and solution of the eigenvalues $\widehat{\boldsymbol{\kappa}}$ gives the resulting optical indicatrix. The indicatrix will be biaxial with the axis n_γ parallel to X and n_α in the plane YOZ between outcrops of the c axes of different twin lamellae. It makes the angle θ with Z from c_2 (Figure 4.10). Thus, the principal refractive indices, the orientation of the optical indicatrix θ, and the axial angle $2V_\gamma$ are as follows

$$\begin{aligned} n_\gamma &= n_\omega \\ n_\beta &= \left[n_\omega^2 + n_\varepsilon^2 + Q\left(n_\omega^2 - n_\varepsilon^2\right)\right]^{1/2} \Big/ \sqrt{2} \\ n_\alpha &= \left[n_\omega^2 + n_\varepsilon^2 - Q\left(n_\omega^2 - n_\varepsilon^2\right)\right]^{1/2} \Big/ \sqrt{2} \\ \tan\theta &= \tan\psi - (1-Q)\big/(f_2\sin 2\psi) \\ \tan^2 V_\gamma &= \frac{n_\alpha^{-2} - n_\beta^{-2}}{n_\beta^{-2} - n_\gamma^{-2}} \approx \frac{2Q}{1-Q} \end{aligned} \tag{4.26}$$

where $Q = \left(1 - 4f_1 f_2 \sin^2 \psi\right)^{1/2}$. Q here, and in Equation (4.12), has the same meaning and θ is equivalent to φ in (4.10). Thus the measurement of the axial angle gives the fraction of the second type of twin lamellae. The measurement of the axial angle does not permit the differentiation of lamellae of the first or second kind. If the crystal simultaneously contains all four types of lamellae (original and three twinning orientations) the expression (4.24) transforms to

$$\widehat{\kappa} = \sum_{i=1}^{4} f_i \widehat{\kappa_i} = f_1 \widehat{\kappa_1} + \sum_{i=2}^{4} f_i \widehat{\mathbf{R}}_i \widehat{\kappa_1} \widehat{\mathbf{R}}_i^{-1} \tag{4.27}$$

with $\widehat{\mathbf{R}}_i$ found from Equation (4.23). In this case, the solution is cumbersome and the reverse problem, finding the volume fractions of lamellae in different twinning orientations f_i, can be solved numerically using three different optical parameters. Figure 4.11 shows the orientation of the optical indicatrix in a twinned crystal of calcite. In order to verify the model, two crystals of calcite were deformed. Hauser and Wenk's (1976) measured optical indicatrix orientations agreed well with the volume fractions of different twin lamellae found by x-ray diffraction.

4.2.5.2. Feldspar

Marfunin (1959a,b) used a simple construction for modeling the optical indicatrix of polysynthetic feldspar twins that is based on symmetry arguments, Mallard's indicatrix summation, and the Wulff net. Submicroscopic twins of the crystals of any symmetry can belong either to the point group $2/mmm$ (one common indicatrix axis) or to the point group $2/m$ (general case). The first case considered in section 4.1.3 is simple, but infrequently applicable. Generally, if the fractions of different lamellae are equal $f_1 = f_2$ and one axis of the resulting indicatrix coincides with the twinning axis (or with the normal to the twinning plane) the other two axes lie within the lamellae.

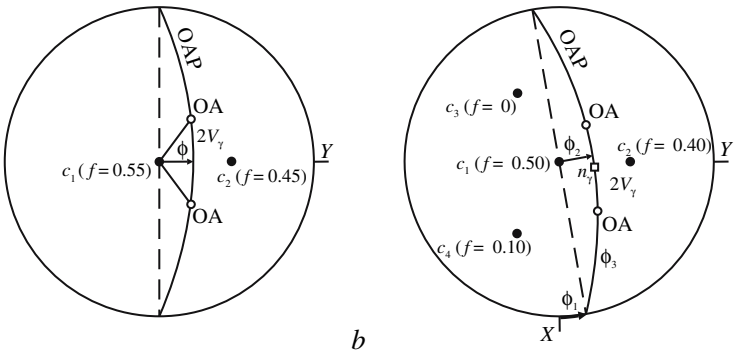

Figure 4.11. Stereographic projection of the upper hemisphere of the calcite crystals. (*a*) single twin, (*b*) multiple twinning (general case) (after Hauser and Wenk, 1976)

4.2.6. Ex-Solution Structures

Ex-solution refers to those processes whereby homogeneous solid solutions separate into distinct crystalline phases. Generally components associated with ex-solution have not only the different orientations but also the different indicatrix shapes. The approach introduced in section 4.2.5.1 was successfully applied by Hauser and Wenk (1976) for calculations of feldspar solid solutions. Alkali feldspar is characterized by polysynthetic twinning in accordance with several twin laws as well as ex-solution structures.

Most plagioclases are apt to show the ex-solution structures (Deer *et al*., 1992). Hauser and Wenk (1976) calculated the optical characteristics of various albite-anorthite ($NaAlSi_3O_8 - CaAl_2Si_2O_8$) solid solutions for both the high- and low-modifications: (1) a solid solution of An2.5 (2.5% anorthite) and An92.5, and (2) ex-solution with An2.5, An35, An65 and An92.5. In the second case, much better agreement between experiment and theory has been achieved (Figure 4.12). Some unexplained discrepancies were observed for the axial angle in peristerites, an iridescent form of albite.

4.2.7. Syntaxy

Description of organized intergrowths of more than one phase is called syntaxy. Syntaxy requires application of the most general expressions (4.6) - (4.8), since the components in most cases have different optical indicatrices. The final expressions for the indicatrices can be cumbersome and often do not permit the determination of component volume fractions from the optical data.

This case is illustrated by formation of heterogeneous crystals in the system ammonium chloride/urea/water (Franke *et al*., 1987; Punin *et al*., 1993). Depending on the aqueous solution composition $x = \frac{[CO(NH_2)_2]}{[CO(NH_2)_2]+[NH_4Cl]}$ three different phases can be the major precipitate: ammonium chloride (cubic) if $0 \leq x \leq 0.6$, the double salt $NH_4Cl \cdot CO(NH_2)_2$ (orthorhombic) if $0.6 \leq x \leq 0.75$, and urea (tetragonal) if $0.75 \leq x \leq 1$ (Figure 4.13). However, all the crystals formed with $x \neq 0$ or 1 were heterogeneous. The crystals of ammonium chloride and urea contain intergrowths of the double salt while crystals of the double salt contain intergrowths of urea. Ammonium chloride is anomalously birefringent due to the double salt, urea is anomalously biaxial, and the axial angle of the double salt varies widely. Sometimes if the lamellae are thicker than the light wavelength the system becomes optically heterogeneous with distorted conoscopic figures (section 4.3). The fraction of the second phase f was calculated with the Mallard's method as a function of the solution composition x (Punin, 1989a; Punin *et al*., 1993) for all three limiting phases (Figure 4.13). Compositions were confirmed by x-ray diffraction. Low concentrations (< 0.5–1%) of the double salt in ammonium chloride crystals cannot be detected by the comparatively insensitive x-ray analysis; optical methods are better for this purpose.

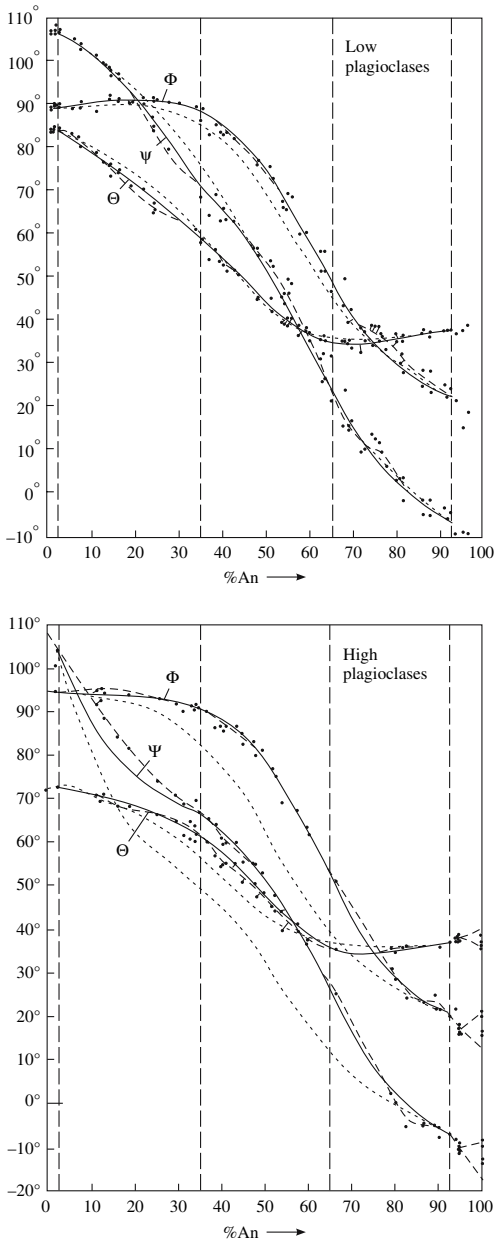

Figure 4.12. Euler angles Φ, Θ and Ψ describing the orientation of the optical indicatrix in relation to the crystal coordinates in plagioclase. Measured points interpolated (dashed line) are compared with the calculated curves assuming a solid solutions of An2.5 and An92.5 (dotted line) and ex-solutions with An2.5, An35, An65 and An92.5 (solid line). (*a*) low-plagioclase series, (*b*) high-plagioclase series (after Hauser and Wenk, 1976)

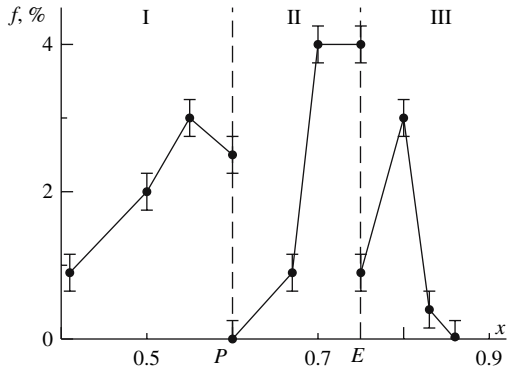

Figure 4.13. Concentration of the second phase (double salt in the fields I and III, and urea in the field II, respectively, f, %) in crystals as a function of the aqueous solution composition x for crystallization in the system ammonuim chloride-urea-water. I, II, III – fields of crystallization of ammonium chloride, double salt, and urea, respectively, P – peritonic, E – eutonic

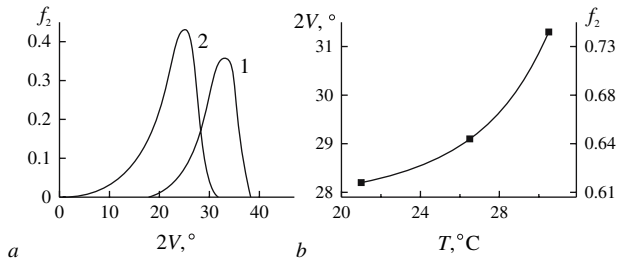

Figure 4.14. The fraction of urea intergrowths in crystals of the double salt (f, %) as a function of (a) the mother solution composition x and (b) growth temperature T (b). $x = 0.5$ and 0.7 for the curves 1 and 2, respectively

Syntactic intergrowth is a complex process strongly controlled by growth conditions. Figures 4.13 and 4.14 show compositional dependencies plotted against different solution supersaturations and temperatures. The optical anomalies provide a means of the quick characterization of such heterogeneous substances.

4.2.8. Chaotic Misorientation of Components

Many layered compounds, especially sheet silicates, can form fine aggregates within sub-parallel and even entirely chaotic misorientations of individuals. Drits *et al.* (1966) distinguished two cases for clay minerals.

1. Misorientation in only one plane (basal plane). The biaxial minerals become pseudo-uniaxial. Since most clay minerals direct X normal to the basal plane, the chaotic misorientation of individuals within this basal plane leads to a uniaxial

optical indicatrix with $n_{\alpha'} = n_\alpha$ and $n_{\gamma'} = \sqrt{n_\beta n_\gamma}$. The layering of N different phases with volume fractions f_i results in the following refractive indices

$$n_{\alpha'} = \sum_{i=1}^{N} f_i (n_\alpha)_i$$

$$n_{\gamma'} = \sum_{i=1}^{N} f_i \sqrt{(n_\beta)_i (n_\gamma)_i} \tag{4.28}$$

2. Misorientation in all directions results a completely disordered system that is optically isotropic and characterized by an average refractive index

$$\overline{n} = \sum_{i=1}^{N} f_i \sqrt[3]{(n_\gamma)_i (n_\beta)_i (n_\alpha)_i}. \tag{4.29}$$

Drits *et al*. (1966) verified expressions (4.28) and (4.29) experimentally for synthetic mixtures of montmorillonite $(Na, Ca)(Al, Mg)_6(Si_4O_{10})_3(OH)_6 \cdot nH_2O$), kaolinite ($Al_2Si_2O_5(OH)_4$) glauconite ($(K, Na)(Fe^{3+}, Al, Mg)_2(Si, Al)_4O_{10}(OH)_2$), and inter-layer deficient mica, as well as for the natural mixtures of kaolinite, montmorillonite, and muscovite. For natural samples, the fractions of phases were found independently by x-ray diffraction. The differences between calculated and measured refractive indices were found to be equal to 0.001 (sometimes up to 0.002), corresponding to the differences in volume fractions of about 5–6%. This permits the use of optical methods for the rapid, accurate determination of the mixture compositions.

4.3. OPTICALLY HETEROGENEOUS SYSTEMS

4.3.1. Introduction

If lamellae have a thickness greater than the wavelength of light, they each interact with polarized light as independent crystals. Thus, a common indicatrix cannot be constructed for such an *optically heterogeneous* crystal. For an arbitrary orientation no extinction is observed under orthoscopic examination. In heterogeneous systems, orthoscopic illumination is often not sufficient for the characterization of optical anomalies. Conoscopy is required. It enables us to calculate the mutual orientation of components. Conoscopy samples many wave vectors. For some directions the eigenmodes in different components may be the same leading to observable extinction. Light passing through an optical system is defined not only by the orientation of components but by their thicknesses. Therefore, the volume fractions of components can be calculated as well. Here, we consider this problem only for the simplest two-component system with a special misorientation of the component indicatrices.

Consider a crystal consisting of two components that have differently shaped indicatrices misoriented by the angle ψ around the axis n_c that is coincident with

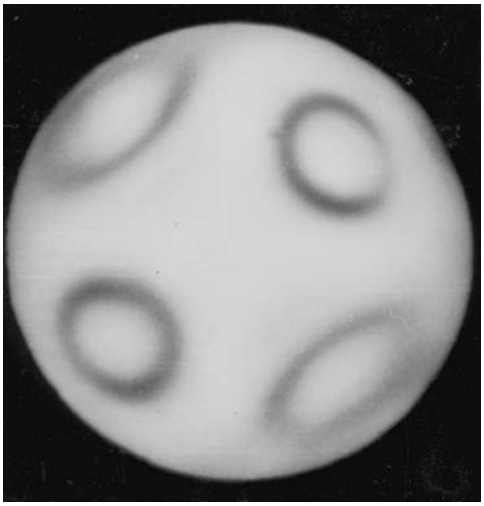

Figure 4.15. Example of an interference figure for heterogeneous potassium ferrocyanide trihydrate crystal (see Color Section following page 254)

either X or Z (misorientation around Y is not considered here). The optical heterogeneity manifests itself in distortions of interference (conoscopic) figures. Deviations from the standard conoscopic figures manifest themselves in deformation of isochromes and the unusual behavior of isogyres. Examples of distorted interference figures of potassium ferrocyanide trihydrate are shown in Figure 4.15.

Distorted interference figures were repeatedly observed in natural mica (Groth, 1895; Sokolov, 1953, first published in 1911), synthetic fluorphlogopite (Bloss *et al*., 1963; Shmelev and Bobr-Sergeev, 1970), and potassium ferrocyanide trihydrate (Toyoda *et al*., 1960). They were correctly ascribed to the superposition of lamellae with different orientations and/or shapes of the optical indicatrix. However, no quantitative description of the anomalous conoscopy has been given. Below we consider some important features of distorted interference figures without claiming a rigorous description of these complicated phenomena.

4.3.2. Isogyres

4.3.2.1. General remarks

An isogyre is a locus in a conoscope characterized by the same vibration directions (Bloss, 1961; Tatarsky, 1965). A dark isogyre has vibration directions coincident with the microscope polarizer and analyzer. Consider the behavior of an isogyre in a standard conoscopic figure (Kamb, 1958). The conoscope in Figure 4.16 shows the directions X and Y corresponding to vibration directions. Consider the acute bisectrix (AB) figure, where direction W lies in the optic axial plane, U is normal to the optic axial plane, and $2V$ is the axial angle. The position of any point can be

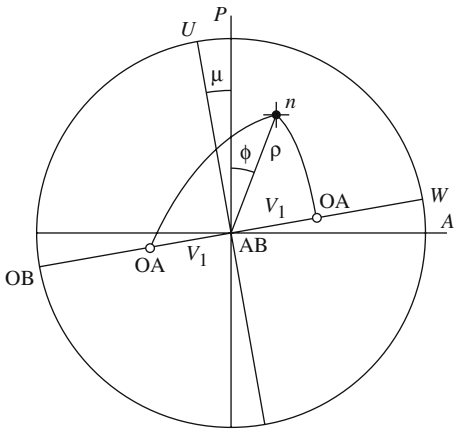

Figure 4.16. The view field of conoscope. *P*, *A* - orientations of vibration directions in polarizers, OA - outcrops of the optic axes, AB and OB denote acute and obtuse bisectrices, respectively. Direction *W* lies in the optical axial plane, *U* is normal to the optic axial plane

described by the azimuthal angle ϕ and the polar distance $\rho = \sin\Theta$, where Θ is the angle between the normal to the section plane and the light direction. Vibration directions at point n are found from the Biot-Fresnel rule (Zavariyskii, 1953; Shuvalov, 2005). Let μ be the angle between extinction positions in orthoscopy and the microscope stage rotation measured counterclockwise. At n, the extinction takes place when vibration directions coincide with polarizers X and Y. From this conditions the distance of the isogyre apex from the center of field of view can be found as follows (Kamb, 1958):

$$\frac{\rho_1^2}{1-0.5\rho_1^2}\sin 2\mu = \frac{\rho^2}{1-0.5\rho^2} \tag{4.30}$$

where $\rho_1 = \sin V$ and ρ in Equation (4.30) is a polar coordinate for the unit circle. The visible field of view differs from the true field corresponding to the polar coordinate ρ because of refraction at the crystal air interface. Recalculation of the real field of view requires application of Mallard's formula (Bloss, 1961; Tatarsky, 1965) and knowledge of the size of the field of view. For a heterogeneous crystal, vibration directions for light traveling through a crystal in various directions are usually different for different components. Thus, isogyres are not visible. However, during the complete stage rotation the isogyres become visible four times. Since positions of isogyres for the each component are known from Equation (4.30) we can follow isogyres for the heterogeneous crystal as well.

4.3.2.2. Layering of two components with arbitrary axial angles mutually rotated around the bisectrix

For any arbitrary rotation of a system with respect to the cross hairs, the orientations of component isogyres are different and consequently none are visible. When the microscope stage is rotated, the isogyres of the components start moving in the field of view with different velocities and/or along different directions. At a certain position, both isogyres will be located at the same points (Figure 4.17A). In other words, the vibration directions at the merging points coincide with the vibration directions of the polarizer and analyzer. The coincident points become dark. This will occur four times during a rotation of 2π. Writing Equation (4.30) for each component and equating their left sides gives

$$\sin^2 2\mu^* = \frac{\sin^2 2\psi}{1+\left(\frac{B_2}{B_1}\right)^2 - 2\frac{B_2}{B_1}\cos 2\psi} \tag{4.31}$$

where $B_i = 1/\rho_i^2 - 0.5$ and subscript $i = 1, 2$ denotes corresponding components. Here, μ^* is the angle between the extinction position of one component and the

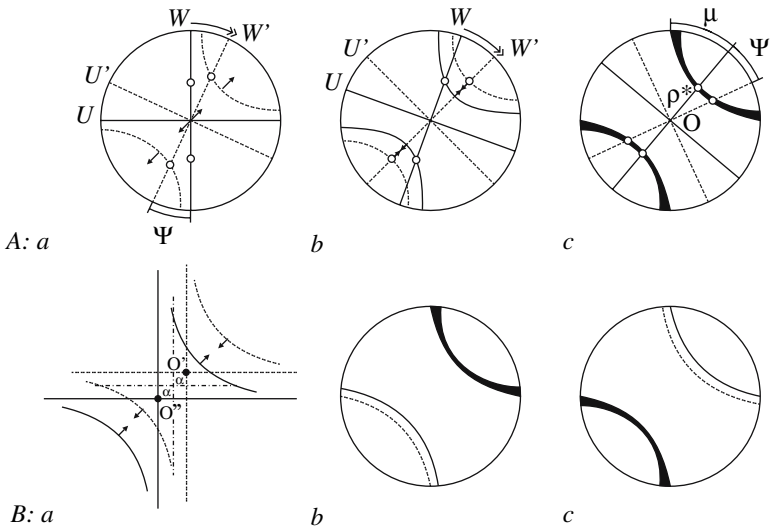

Figure 4.17. Appearance of isogyres during stage rotation. (*A*) Simultaneous appearance of the branches of the isogyre: (*b*, *c*) Successive positions of the stage rotating in the direction of the double unidirectional arrow from the extinction position of first component (*a*). Solid and dashed lines are the optical elements of the components misoriented by the angle ψ. Bold arrows denote directions of isogyres motion. *B* – alternate appearance of two isogyre branches. (*a*) direction of the isogyre branch motion (solid and dashed crosses – asymptotes of corresponding to isogyres, dot-dashed lines - cross hair position) (*b*, *c*) conoscopic figures for different orientations of the stage

appearance of the visible isogyre. Substitution of μ^* into Equation (4.31) gives

$$(4.32) \qquad (\rho^*)^2 = \frac{2\sin 2\psi}{\sin 2\psi + 2B_1\left[1 + \left(\frac{B_2}{B_1}\right)^2 - 2\frac{B_2}{B_1}\cos 2\psi\right]^{1/2}}$$

where ρ^* is the distance between the apex of the isogyre and center of the field of view. The value 2arcsin ρ^* can be called the effective axial angle of the heterogeneous structure. Note that Equations (4.31) and (4.32) contain only the axial angles of components and the mutual misorientation of their indicatrices. They do not contain the volume fractions of components since the position of the isogyres does not depend on the crystal thickness.

Isogyres can become coincident at the extinction position, $\rho^* = 0$ if $\psi = 0$ or $90°$ (the optic axial planes of the components are either parallel or perpendicular to each other) or if one of the components is uniaxial ($2V_1 = 0,\ \rho_1 = 0$, hence, $B_1 = \infty$). During stage rotation of 2π a dark cross appears four times in the absence of visible isogyres in any other positions. In orthoscopy, this system shows complete extinction and is indistinguishable from a single crystal. This situation is characteristic of heterogeneous potassium ferrocyanide trihydrate.

4.3.2.3. Layering of two components having arbitrary axial angles and mutually misorientated by rotation around an oblique direction forming a small angle with the bisectrix

The situation described in the sub-heading is realized for fluorphlogopite and some lepidolites. We can neglect small deviations of the rotation vector from the indicatrix axis in calculating the indicatrix of the optically homogeneous crystals. For example, for $1M$ fluorphlogopite the angle α is equal to $1.25°$. But, even small angles can strongly affect the conoscopic figure. In this case, the rotation of the microscope stage results in the appearance of two visible branches of the isogyre, at different rotations, in opposite quadrants. This may be seen by separating the acute bisector's points of emergence (point O in Figure 4.17Ac) by the angle 2α (O' and O'' in Figure 4.17Ba. For simplicity, the bisectors are rotated along the diagonal of the cross hairs). After this transformation, the isogyre branches become invisible and it is necessary to rotate the stage to achieve superposition. Correspondingly, this will be accompanied by the appearance of an isogyre in quadrant I or III depending on the direction of rotation.

The angle of rotation between the appearance of two branches of the visible isogyre $\Delta\mu^*$ can be found from (4.30) by differentiation $\partial\mu/\partial\rho$ and considering $\Delta\mu^* \approx \dfrac{\partial\mu}{\partial\rho}\alpha$. This expression is cumbersome and we do not show it. The calculations performed show that for a given α, the value of $\Delta\mu^*$ increases as the axial angles of components $2V_i = 2\arcsin\rho_i$ decrease and the effective axial angle of the heterostructure $2\arcsin\rho^*$ increases. Measurements for fluorphlogopite give the value of $\Delta\mu^*$ in the range of 0–20° (Punin *et al.*, 1985b). Certainly, the value of

$\Delta\mu^*$ depends on the optical characteristics of the components and is independent of their volume fractions. The wide range of $\Delta\mu^*$ values in fluorphlogopite is explained by the complex heterogeneity, for which the components are not the polytype modifications but optically homogeneous domains composed of layers of sub-wavelength thickness.

4.3.3. Isochromes

Anomalous conoscopic figures are varied (see figures in Sokolov, 1953). Principally, the shape of isochromes in optically heterogeneous systems cannot be described by Cassinian ovals, that family of quartic curves in which the product of distances from two fixed points is constant. Nevertheless, it is possible to indicate some common characteristics of distorted isochromes including the following:

1. Deformation of Cassinian ovals, including their extension and contraction, skews and local curvature.
2. Disruption and relative displacement of isochromes along a common isogyre. Segments of isochromes form distorted rings or spirals.
3. Appearance of two symmetric dark (isotropic) spots or *compensation points*. Distinct from the two first characteristics that continuously vary during the stage rotation, the compensation points do not change their positions. These positions depend on the optical properties of the components, their misorientation, and volume fractions. Formation of these points is discussed below.

As indicated, the vibration directions of two components are different for all the points in the conoscope except those lying along the coinciding isogyres. The points of emergence of the optic axes for both components lie at the common

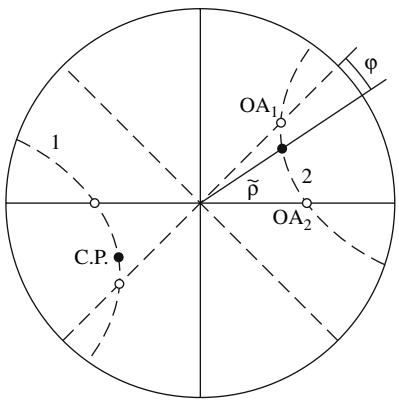

Figure 4.18. Location of the compensation points (C.P., denoted by small filled circles) in the interference figure. Straight dashed lines mark directions that lie in the optic axial plane of the component 1 and normal to this direction. Straight solid lines denote the corresponding directions for component 2. Small open circles denote outcrops of the optic axes (OA) of components 1 and 2. Curved dashed lines correspond to the common isogyres

isogyre (Figure 4.18). At the points of isogyre branches lying between the points of emergence of the optic axes, the vibration directions of corresponding (either fast or slow) waves are mutually perpendicular. At the external segments of the isogyre branches these directions are parallel. Two conclusions may be drawn. First, the points of the common isogyre (and only these points in the field of view of the conoscope) preserve their color (retardation) during rotation of the microscope stage. Secondly, the path differences between two optic axes of the components that are attained by light traveling through each of the components, are subtracted. Therefore, there should exist an isotropic compensation point at which the intensity of the transmitted light is zero. The positions of the compensation points may be determined from the well-known expressions for the birefringence of arbitrary indicatrix sections (Pockels, 1906; Shuvalov, 2005) and under the condition of zero retardation. Then the polar distance between the compensation point and the emergence points of the common axes of the component indicatrices $\widetilde{\rho}$ can be related to the thickness ratio of components h_2/h_1 (or the ratio of their volume fractions f_2/f_1) by the following Equation:

$$\frac{(n_c-n_a)_2^2\,h_2^2}{(n_c-n_a)_1^2\,h_1^2}=\frac{\rho_1^2\left[\rho_1^2\widetilde{\rho}^2\left(\frac{1}{\widetilde{\rho}^2}+\frac{1}{\rho_1^2}-\cos^2\varphi\right)^2-4\sin^2\varphi\right]}{\rho_2^2\left[\rho_2^2\widetilde{\rho}^2\left(\frac{1}{\widetilde{\rho}^2}+\frac{1}{\rho_2^2}-\cos^2(\varphi+\psi)\right)^2-4\sin^2(\varphi+\psi)\right]} \tag{4.33}$$

where $\rho_i=\sin V_i$ and $\varphi=\phi+\mu$ is the angle for the stage rotation between the extinction position of the first component and the position when the compensation point lies at one of the cross hairs.

An Equation like (4.33) can be obtained for any other point of the isogyre if the retardation at this point is measured with the quartz wedge or compensator. Such an expression is necessary if nothing is known about the heterogeneous crystal and the optical properties of components ($2V_i$, $(n_c-n_a)_i$, their misorientation ψ and ratio of volume fractions f_2/f_1) must be found from the conoscopic figure. Usually some information is known *a priori* and the number of parameters to be measured can be reduced.

4.3.4. Modeling Distorted Conoscopic Figures

Distorted conoscopic figures can be calculated using the data on the optical properties and mutual misorientation of components. In principle, such a calculation can be performed for any number of components, however, we restrict ourselves only to two-component systems. The relative intensity of the light I/I_0 travelling from the crystal plate can be calculated from the expression (Pockels, 1906; Shubnikov, 1960):

$$I/I_0=\sin^2 2\eta\sin^2\left(\delta/2\right) \tag{4.34}$$

where the angle η corresponds to the angle between the vibration directions of one polarizer and an eigendirection of the crystal. Here, $\delta = \dfrac{\pi h_l \left(n_{\gamma'} - n_{\alpha'}\right)}{\lambda}$ is the retardation defined by the difference of refractive indices in a section $(n_{\gamma'} - n_{\alpha'})$ as well as by the light path in a crystal h_l and the wavelength λ. For a plane parallel plate, the light path is equal to $h_l = h/\cos\rho$, where h is the thickness. Using this formula the intensity of the light can be calculated for any point in the crystal with the polar coordinates ϕ and ρ enabling a simulation of the conoscope. For the calculation of η and δ at the point (ϕ, ρ) we can use the Equations following from the Biot-Fresnel rule (Zavariyskii, 1953; Shuvalov, 2005) or directly transform the dielectric impermittivity tensor. The behavior of isogyres is described by η in Equation (4.34). The shape of isochromes reflects the change of retardation (δ). Bethke and Birnie (1980) wrote the first program designed for the calculation of conoscopic pictures. At the present, the modeling of conoscopic figures is routine as shown by the simulations of conoscopic figures for optically active crystals (Konstantinova *et al*., 2002; Rudoi *et al*., 2003).

For two-component, optically heterogeneous systems with the volume fractions $f_i = h_i/(h_1 + h_2)$ $i = 1, 2$ one can calculate the values of η_i and δ_i for each component at a given point (ϕ, ρ) and then apply the well known expression for the light intensity traveling through two superimposed plates placed between the crossed polarizers (Pockels, 1906; Hartshorne and Stuart, 1970):

$$
\begin{aligned}
I/I_0 = &- \sin 2\eta_1 \cos 2\eta_2 \sin 2(\eta_2 - \eta_1) \sin^2\left(\frac{\delta_1}{2}\right) + \\
&+ \cos 2\eta_1 \sin 2\eta_2 \sin 2(\eta_2 - \eta_1) \sin^2\left(\frac{\delta_2}{2}\right) + \\
&+ \sin 2\eta_1 \sin 2\eta_2 \cos^2(\eta_2 - \eta_1) \sin^2\left(\frac{\delta_1 + \delta_2}{2}\right) - \\
&- \sin 2\eta_1 \sin 2\eta_2 \sin^2(\eta_2 - \eta_1) \sin^2\left(\frac{\delta_2 - \delta_1}{2}\right)
\end{aligned}
\tag{4.35}
$$

If the components are not misoriented, and $\eta_1 = \eta_2$, Equation (4.35) becomes (4.34).

4.3.5. Calculation of the Distorted Conoscopic Figures: Some Examples

4.3.5.1. Layering of uniaxial and biaxial lamellae

Layering of uniaxial and biaxial lamellae is the simplest case. Consider a heterostructure consisting of a uniaxial component ($n_\beta = n_\gamma = 1.588$, $n_\alpha = 1.552$, optical axis normal to lamellae, volume fraction equal to f_1) and a biaxial component ($n_\gamma = 1.588$, $n_\beta = 1.582$, $n_\alpha = 1.552$, $2V = 48°$, acute bisectrix (α) normal to the lamellae, volume fraction equal to f_2). The conoscopic figures will depend on the volume fractions of components. If one component is dominant, the distortions

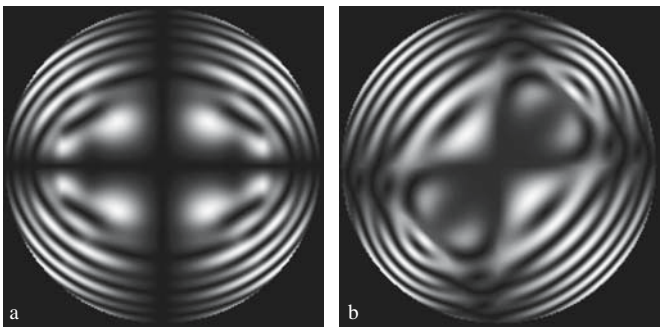

Figure 4.19. Calculated conoscopic figures for heterostructure consisting of uniaxial and biaxial components. The wavelength of monochromatic light is 565 nm. The field of view $\rho_{\max.} = 40°$, $h = 0.4$ mm, the volume fractions of components $f_1/f_2 = 1$. The stage rotation from the extinction position of the biaxial component, the angle η, is equal to (*a*) 0° and (*b*) 45°

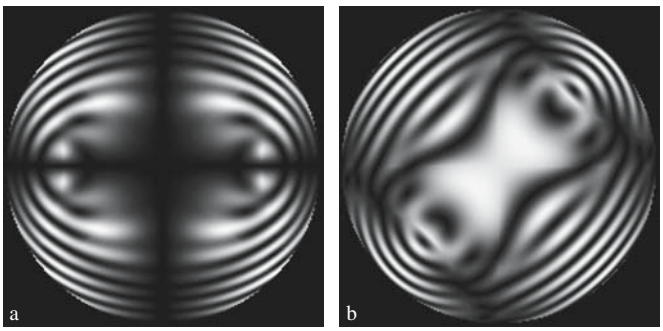

Figure 4.20. Calculated conoscopic figures for heterostructure consisting of uniaxial and biaxial components with volume fractions of $f_1/f_2 = 1/3$. For other data see Figure 4.19

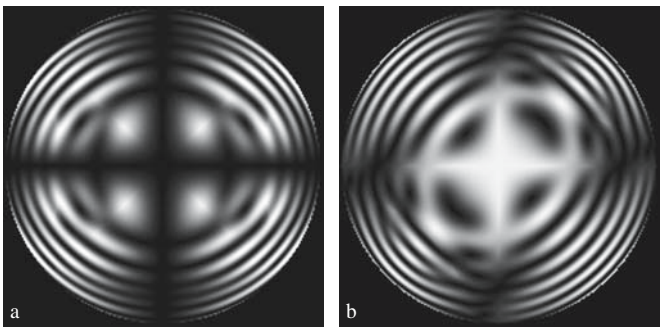

Figure 4.21. Calculated conoscopic figures for heterostructure consisting of uniaxial and biaxial components with volume fractions of components $f_1/f_2 = 3/1$. For other data see Figure 4.19

of the conoscopic figure will be modest. The strongest distortions take place for equal volume fractions. Figures 4.19–4.21 show distorted conoscopic figures of such a heterostructure for the different orientations of the biaxial component φ with respect to the polarizers and for the different volume fractions of components f_i. Symmetry arguments necessitate only the consideration of $\pi/4$ stage rotation. The overall thickness of the crystal is taken as $h = h_1 + h_2 = 0.4\,\text{mm}$.

Analysis of the conoscopic figure shows that the dark cross appears in the field of view four times during the complete stage rotation. Its appearance corresponds to the extinction position of the biaxial component. During rotation of the stage the extinction of the crossed branches redistributes itself so that one part of the branch fades and gives the illusion of cross twisting. At the same time, the center becomes bright obviating the typical Maltese extinction cross. Rotation by 45° imposes two diagonal symmetry planes with respect to the crossed polarizers. In two quadrants, hyperbolic curves are observed. The compensation points are located in the same quadrants. In two other quadrants, interference rings are visible and have diagonal positions. Comparisons of model calculations with experimental patterns show that the modeling carried out for one wavelength reproduces quite well the main features of the distorted conoscopic figures obtained with white light.

4.3.5.2. Layering of misoriented biaxial lamellae

Layered biaxial lamellae provides greater conoscopic variation since the angle of mutual misorientation ψ changes as does the orientation of the system with respect to the crossed polarizers and variation of volume fractions of components. Consider the same heterogeneous system as previously, substituting a second biaxial component for the uniaxial one. For comparison, we show the standard conoscopic figure ($\psi = 0$, Figure 4.22) and model calculations for $\psi = 30°$, $60°$ and $90°$ (Figure 4.23–4.28).

The optical distortions are most pronounced for the equal volume fractions. The pattern acquires two symmetry planes in following cases: (1) The position of the crossed polarizers coincides with the bisectors of the angles formed by the optic axial planes of the components (Figure 4.23b). In this case, the compensation points lie on one of the cross hairs (vertical in Figure 4.23b) and are symmetrically surrounded with the pieces of the lemniscates—Cassinian ovals resembling a figure of eight—of the first and the second components. Along the second crosshair is a broad extinction not quite reaching the center. (2) Bisectors of angles formed by the optic axial planes of the components coincide with the diagonals (Figure 4.23a). In this case, the figure is similar to the conoscopic figure of the biaxial crystal rotated by 45° from the extinction position. The hyperbolic branches of a visible isogyre appear at the vertices where the compensation points are located. The isochromes closest to these points are disrupted, displaced along the isogyre branches, and closed at the isochromes of the next higher order.

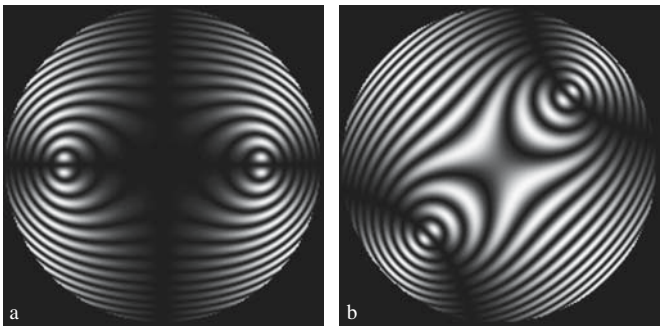

Figure 4.22. Calculated conoscopic figures of a typical biaxial crystal. $\lambda = 565\,\text{nm}$, $\rho_{\max.} = 40°$, $h = 0.4\,\text{mm}$. The counterclockwise stage rotation from the extinction position (η) (a) $= 0°$ and (b) $= 45°$

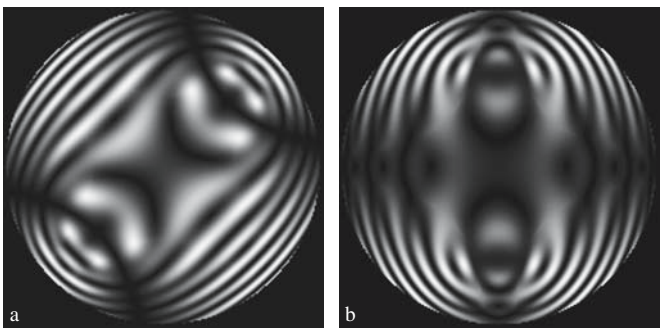

Figure 4.23. Calculated conoscopic figures of heterostructure consisting of two identical biaxial components. $f_1/f_2 = 1$, $\psi = 30°$, $\eta = (a)$ 30 and (b) 75°. For other data see Figure. 4.22

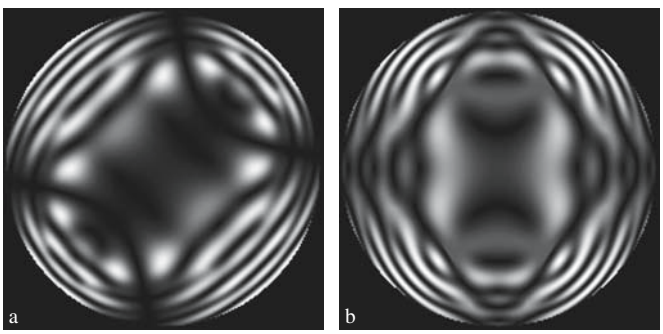

Figure 4.24. Calculated conoscopic figures of heterostructure consisting of two identical biaxial components. $f_1/f_2 = 1$, $\psi = 60°$, $\eta = (a)$ 15° and (b) 60°. For other data see Figure. 4.22

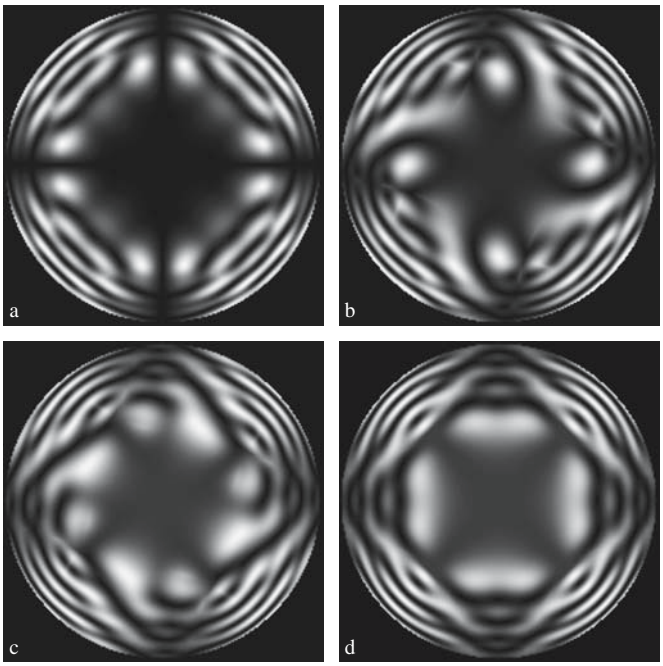

Figure 4.25. Calculated conoscopic figures of the heterostructure consisting of two identical biaxial components. $f_1/f_2 = 1$, $\psi = 90°$, $\eta = (a)\ 0°$, $(b)\ 15°$, $(c)\ 30°$, and $(d)\ 45°$. For other data see Figure. 4.22

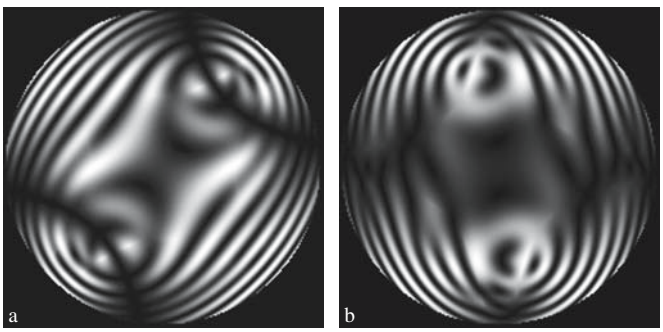

Figure 4.26. Calculated conoscopic figures of the heterostructure consisting of two identical biaxial components. $f_1/f_2 = 1$, $\psi = 30°$, $\eta = (a)\ 30°$ and $(b)\ 75°$. For other data see Figure. 4.22

If the components are misoriented by $\psi = 90°$ as in potassium ferrocyanide trihydrate, for example, the conoscopic figure with equally thick components acquires a four-fold symmetry axis irrespective of the position of the microscope stage (Figure 4.25). Under orthoscopic examination the system shows normal extinction

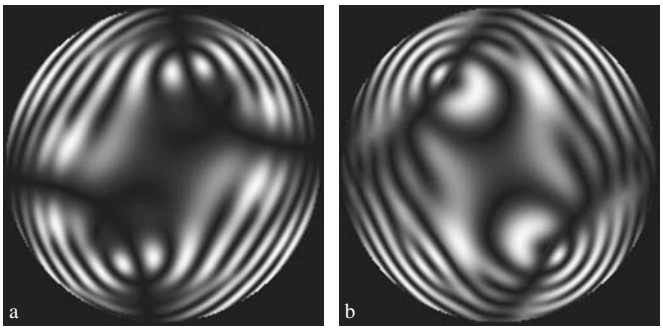

Figure 4.27. Calculated conoscopic figures of the heterostructure consisting of two identical biaxial components. $f_1/f_2 = 1,\ \psi = 60°,\ \eta = (a)\ 15°$ and $(b)\ 60°$. For other data see Figure. 4.22

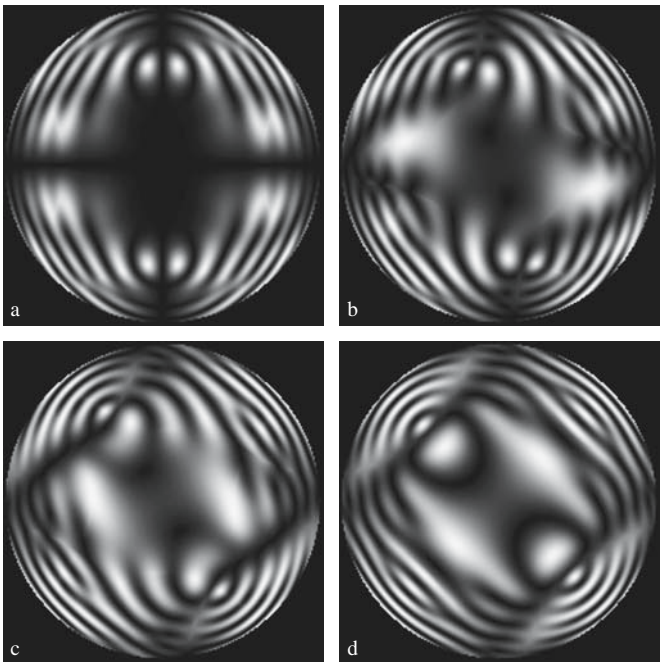

Figure 4.28. Calculated conoscopic figures of the heterostructure consisting of two identical biaxial components. $f_1/f_2 = 1/3,\ \psi = 90°,\ \eta = (a)\ 0°,\ (b)\ 15°,\ (c)\ 30°$, and $(d)\ 45°$. For other data see Figure. 4.22

(see above), but the shape of the conoscopic figure is diagnostic of the optical heterogeneity. The isochromes have a characteristic square shape in the parallel, perpendicular and diagonal positions of the optic axial plane of the crystal relative to the crosshairs. They are helical in all other positions.

As in the case of layering of uniaxial and biaxial components, the dominating lamellae give the main contribution to the resulting conoscopic figure that can be seen against the more complex background. The conoscopic figure is close to the standard as the misorientation angle ψ decreases and approaches zero. Comparison of model calculations with experimental patterns shows that the modeling carried out for one wavelength reproduces quite well the main features of distorted conoscopic figures obtained with white light.

4.3.5.3. Polysynthetic twinning in calcite

Polysynthetic twins occur in calcite when two sets of lamellae are interleaved. The optic axis of one set typically coincides with the illumination direction. The orientation of the second system of layers can be found from Equation (4.22). Such a heterostructure consisting of two uniaxial components results in complicated conoscopic figures even for the case of equal component volume fractions (Figure 4.29). The situation is complicated by the fact that (0001) is not a cleavage plane and the preparation of appropriate sections is difficult.

4.3.6. Distorted Conoscopic Figures as a Characteristic of Crystal Inhomogeneity

Equations (4.31)–(4.33) enable the calculation of the main characteristics of heterostructures using parameters from distorted conoscopic figures. However, such calculations are time consuming. The modeling of conoscopic figures has been carried out only for the two-component systems and only for special component misorientations.

Anomalous conoscopic figures can always be used as a qualitative indication of crystal heterogeneity. As the thickness of either one or both components decreases, the intensity of light traveling through the crystal approaches the value given by

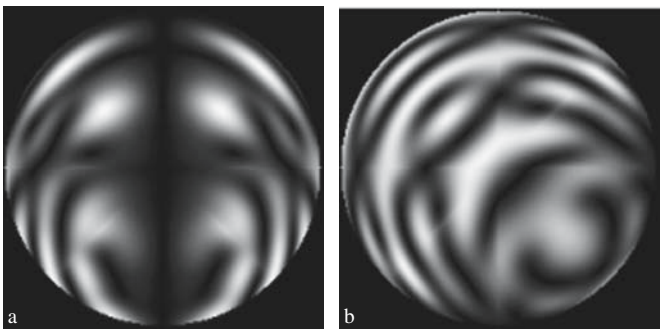

Figure 4.29. Calculated conoscopic figures of the polysynthetic calcite ($n_\omega = 1.658$, $n_\varepsilon = 1.456$) twin consisting of two types of lamellae. $\lambda = 565\,\text{nm}$, $\rho_{\max.} = 40°$, $f_1/f_2 = 1$, $\psi = 90°$, $\eta = (a)\ 0°$ and $(b)\ 45°$

expression (4.34), where η and δ define the thicker component in the first case or the limiting optically homogeneous system in the second case. Distortions of the isochromes fade and the compensation points move to the emergent points of the optic axes in the first case and transform into the emergent points of the optic axes in the second case.

Although it is not easy to formulate a quantitative measure of distortion of conoscopic figures, simple qualitative estimates are nevertheless worthwhile. Kotelnikova *et al.* (1989) and Punin (1989a) characterized the degree of distortion of

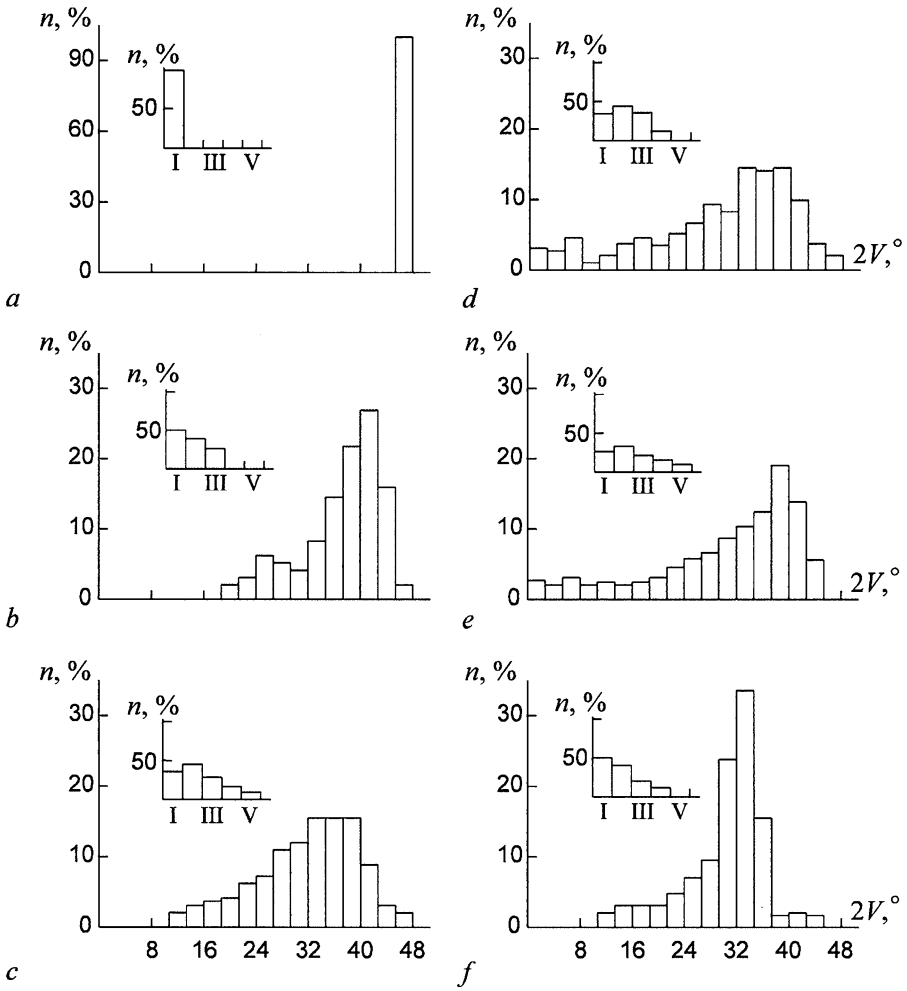

Figure 4.30. Effect of the chemical composition on the axial angle $2V$ and on the distortions of the conoscopic figures (I–V) for the lithium-aluminum micas. Content of Li_2O (%): (*a*) less 0.7, (*b*) 0.7–1.2, (*c–e*) 1.2–4.0, (*f*) 4.0–5.8

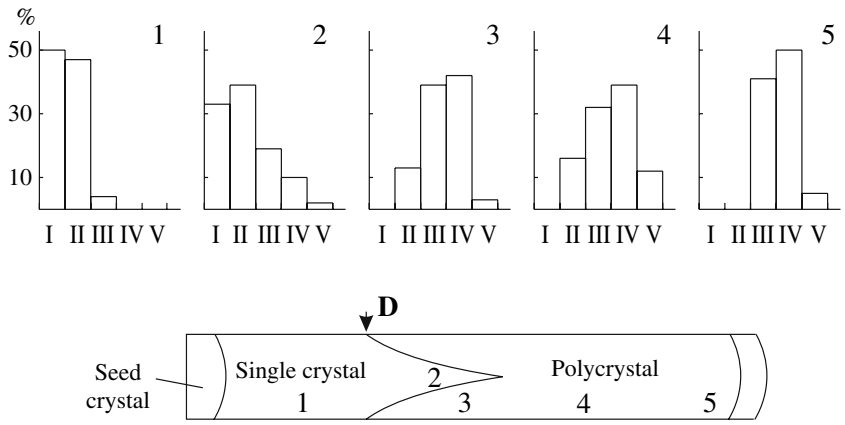

Figure 4.31. Distribution of fluorphlogopite ($Mg_3K(AlF_2O(SiO_3)_3)$) crystals as function of conoscopic distortions in different zones (I–V) of the ingot. **D** – the furnace position at the moment of the abrupt change of the growth temperature

conoscopic figures with a five-point scale. Histograms obtained for samples from different regions or deposits can then be compared. Researchers (Sokolov *et al*., 1987; Punin *et al*., 1989; Punin, 2005) plotted the histograms for the lithium-aluminum micas from the rare-metal pegmatites as a function of crystal composition (Figure 4.30). The sequence *a–f* corresponds to the change of chemical-morphological types of micas from the perimeter to the core of pegmatite veins from 5 ore-deposits. Another example is shown in Figure 4.31 in which furnace damage was followed by the change of the crystallization rate and enrichment of a flourphlogopite ingot by impurities in the course of the directional crystallization (Punin, 1989a; Punin and Shtukenberg, 2005). Such a drastic change of the growth conditions and crystal composition resulted in conoscopic figure distortions. Both examples show the value of the qualitative description of the distorted conoscopic figures for the study of heterogeneous crystals.

4.4. HETEROGENEITY AT DIFFERENT LENGTH SCALES

In most cases, phase or chemical heterogeneity coexists on the sub-microscopic and macroscopic levels. Such a situation occurs with polytype and syntactic intergrowths, polysynthetic twinning *etc*. Optical phenomena proper to both homogeneous and heterogeneous crystals should be observed. For lithium-aluminum micas with varied Li_2O content (Figure 4.30), the axial angle is correlated with the distortion of the conoscopic figures. Moreover, varying degrees of conoscopic figure distortion are often present within one and the same crystal. Depending on the origin of the heterogeneity, these variations may or may not conform to growth sector zoning (Figure 4.4).

CHAPTER 5

SUPERIMPOSITION OF OPTICAL ANOMALIES

5.1. GENERAL REMARKS

Optical anomalies of different etiologies often coexist but rarely have investigators tried to distinguish them. One exception is the attempt to parse anomalous birefringence in epitaxial films of synthetic garnet $(Y_{0.53}Nd_{0.47})_3Ga_5O_{12}$ on $Gd_3Ga_5O_{12}$ between stress-induced anisotropy caused by lattice mismatch with the substrate and growth-induced anisotropy (Kitamura *et al*., 1986a). In this chapter we analyze the superposition of optical anomalies in the grossular-andradite garnets and alums (Shtukenberg *et al*., 2001a,b).

The three main sources of optical anomalies discussed in Chapters 2–4 respectively, are internal stress, kinetic ordering, and phase heterogeneity. However, in real, imperfect, impure crystals, these sources of optical anomalies spill out of their respective chapters and mix in confounding ways. For example, consider a crystal in which isomorphous structural units are distributed inhomogeneously over the crystal volume due to growth under imperfect conditions. This results directly in inhomogeneity-induced *internal strain and stress*, themselves a source of piezo-optic distortion. Greater optical complexity will likely arise during plastic relaxation of this stress. Various *dislocation ensembles* can work as independent sources of optical anomalies while relaxation of internal stress may occur via formation of heteropolytypes and mixed-layer structures, complex twinning, and other *heterogeneous structures* (Punin, 1987; 1994; 2000). Finally, *kinetic ordering of structural units* is likely in the formation of mixed crystals. Thus, isomorphous replacement may induce a cascade of optical consequences illustrated schematically in Figure 5.1.

For example, optical distortions in lepidolite $(KLi_2Al(Al, Si)_3O_{10}(F, OH)_2)$ (Sokolov *et al*., 1987), are due to complicated polytype intergrowths that induce strong internal stress. In quartz, optical anomalies originate from the kinetic ordering of atoms (Tsinober and Samoilovich, 1975), internal stress (Frood and Mills, 1978) and polysynthetic Brazil twinning (Melankholin and Grum-Grzhimailo, 1954).

Below we consider briefly the most pronounced features of optical anomalies of different etiologies.

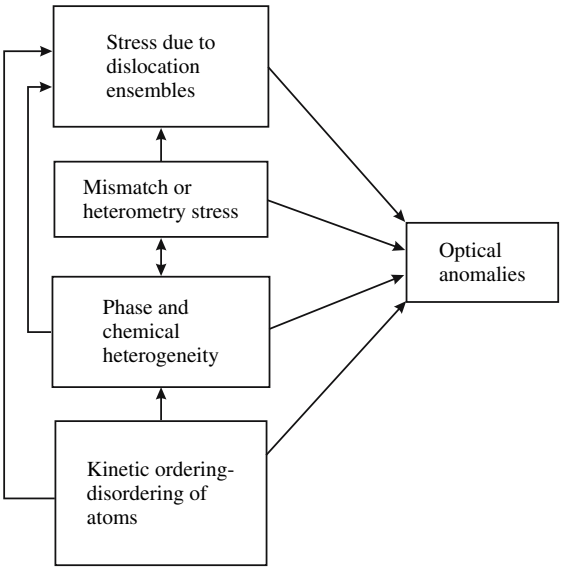

Figure 5.1. Interrelations between different phenomena that induce the optical anomalies

5.2. INTERNAL STRESS

Internal stress is the most widespread source of optical anomalies occurring in essentially all the crystals. The specific features of these optical anomalies are different for stress induced by heterometry and by dislocation ensembles.

5.2.1. Compositional Heterometry

The following observations are characteristic of optical anomalies from compositional heterometry.

1. Complicated distributions of composition and unit cell dimensions are manifest in concentric zoning and growth sector zoning.
2. Optical anomalies are concentrated at the compositional boundaries where vibration directions often reorient by 90°.
3. Birefringence and axial angle ($2V$) are proportional to the gradients of component concentrations but not to the concentrations themselves.
4. Optical anomalies are not diminished by annealing.
5. There are some symmetry restrictions on the distribution of optical anomalies that result from the section shape and the distribution of components. If the crystal has a *morphological* symmetry plane oriented normal to the growth zoning and to the section plane, on this symmetry plane the vibration direction Z' will always be parallel or perpendicular to this plane (Figure 2.22).

6. Evidences of relaxation processes often accompany optical anomalies. These include: formation of growth cracks, dislocation ensembles, blockage structures, growth bending or twisting, and mechanical twinning.
7. Simple models of stress evaluation (section 2.8) usually overestimate optical anomalies. This can be explained in large measure by brittle and plastic relaxation of the heterometry-induced stress.
8. Growth conditions do not affect heterometry-induced anomalies directly, but they can indirectly influence the distribution of components, temperature, and the stress relaxation.

5.2.2. Dislocations and Dislocation Ensembles

The following observations are characteristic of optical anomalies from dislocations:
1. Stress induced by dislocations, as opposed to that induced by compositional heterometry, is localized in relatively small area or stripes where the optical anomalies are likewise accumulated.
2. Single dislocations display birefringent rosettes or stripes depending on their orientation.
3. Slip planes and dislocation bundles are evidenced by stripes where the stress sign and indicatrix orientation changes.
4. Thermoplastic stress with dislocation-induced anomalies can resemble heterometry-induced stress.

5.3. KINETIC ORDERING

Optical anomalies due to kinetic ordering are less frequent but still common to a wide variety of natural and synthetic crystals. Their characteristic features are listed below.
1. Distributions of optical anomalies resulting from kinetic ordering are characterized by sector and sub-sector zoning more pronounced than for compositional heterometry. The symmetry and orientation of the optical indicatrix is controlled by the local symmetry of the growing face or growth steps on the face.
2. The degree of ordering is usually slight requiring accurate data to characterize the desymmetrization. An intensity difference for symmetry related reflections is among the most sensitive indicator of symmetry reduction.
3. Optical deviations resulting from kinetic ordering depend on composition and anomalies are usually most strongly manifest in equi-molar solid solutions made of fully miscible components.
4. Optical anomalies related to kinetic ordering decrease as the growth temperatures decrease and growth rates increase.
5. High-temperature annealing can obviate optical anomalies by restoring a statistical distribution of guests.
6. Fracture does not relieve the optical anomalies.

5.4. CRYSTAL HETEROGENEITY

Optical anomalies due to crystal heterogeneity are as rule quite distinct from two other types considered above.

1. Optically heterogeneous crystals are usually characterized by imperfect extinction under orthoscopic examination and by distorted conoscopic figures. Cleavage of lamellae changes optical properties leading to homogeneity in thin sections.
2. The scale of layering, whether smaller or larger than the light wavelength, can be inferred from differences in homogeneous and heterogeneous systems.
3. The distribution of the optical anomalies may be determined by concentric zoning, growth sector zoning, or specific crystallographic directions. For example, if a crystal contains several growth sectors but does not display optical sector zoning, the phase heterogeneity is likely a consequence of exsolution of the solid solution or of shear and autodeformation polymorph (polytype) phase transformations.
4. The characteristics of optically homogeneous crystals strongly vary for different crystals in an ensemble or even within the same crystal. Cutting such crystals or splitting them along cleavage planes can strongly affect the axial angle and indicatrix orientation.

Optical anomalies can be affected by the growth conditions that change the state and quantity of impurities, or the preferred polytype modification *etc*. These are virtually impossible to enumerate given the wide spectrum of optical effects influenced by growth conditions. However, it is possible elaborate general features due to autodeformation processes such as complex polytype intergrowths or polysynthetic twinning. In these cases, effects of growth conditions are similar to those observed for the compositional heterometry-induced stress (section 2.8.5).

5.5. OPTICAL ANOMALIES IN UGRANDITE GARNETS

Optical anomalies in solid solutions of uvarovite, grossular, and andradite garnets are readily seen in thin sections. They have been carefully analyzed in some 60 papers published in the past century. No optically anomalous mineral has been so thoroughly studied. Today, most of the important sources of optical anomalies in ugrandite garnets are well understood.

Optical indicatrix. Anomalous birefringence in garnets can reach 0.015. The birefringence may be distributed homogeneously or display "microcline grid" patterns (Kir'yanov, 1941; Hirai and Nakazawa, 1986b), however, growth sector zoning and concentric zoning are most typical.

Growth sector zoning. Each growth sector displays its distinct optical properties. The orientation of the indicatrix is strongly controlled by the growth front orientation (Table 3.2). However, there are some exceptions: the crystals described by

Kir'yanov (1941), Starkov (1950), and Shtukenberg *et al*. (2001a) show changes in the orientation of the optical indicatrix by 90° from one growth zone to another. The sector zoning is often complicated by sub-sector zoning and slight variations in orientation of the optical indicatrix resulting from vicinal face orientations (Akizuki, 1984).

Concentric zoning. The orientation of the optical indicatrix is usually more or less the same in concentric zones but the magnitude of birefringence can vary. Most frequently isotropic and anisotropic zones alternate (Stose and Glass, 1938; Lessing and Standish, 1973; Murad, 1976; Hirai and Nakazawa, 1982; Hirai *et al*., 1982; Akizuki *et al*., 1984). Sometimes distinct anisotropic zones alternate (Rossman and Aines, 1986; Hirai and Nakazawa, 1986b). Concentric zones have been observed that not only differ in birefringence but also differ by 90° in the orientation of the optical indicatrix (Kir'yanov, 1941; Starkov, 1950; Shtukenberg *et al*., 2001a). The optical zoning is correlated to various levels of compositional zoning: the macrolevel, the mesolevel, and the microlevel.

At the *macroscale*, rough, non-periodic compositional zones varying in thickness from tens of microns to millimeters are probably related to changes of composition of the growth medium (Nakano *et al*., 1989).

At the *mesoscale*, periodic zones are superimposed onto others from tens to hundreds of microns thick. Such zoning is induced by changes of growth conditions or by self-organization. Mesoscale zones, sometimes of constant thickness, sometime variable, are parallel to the growth front plane (Murad, 1976; Hirai *et al*., 1982; Akizuki *et al*., 1984; Hirai and Nakazawa, 1982, 1986a,b; Pollok *et al*., 2001). Sometimes the zones are not parallel to the growth front. This is assumed to be a consequence of exsolution structure of the solid solution $Ca_3(Al, Fe)_2(SiO_4)_3$ (Hirai and Nakazawa, 1982, 1986a,b; Jamtveit, 1991).

At the *microscale* are fine zones about 1000 Å thick (Hirai and Nakazawa, 1982) within anisotropic lamellae. The zones have identical composition by analytical electron diffraction microscopy but different refractive indices by optical diffraction that can ascribed to micro-twins (Hirai and Nakazawa, 1982). On the other hand, simulation of diffraction patterns showed that the fine compositional zoning can present at the microscale forming zones with a thickness of tens to hundreds of unit cells (Ivanova *et al*., 1998).

Various Effectors

Crystal composition is the predominant determinant of anomalous birefringence in garnets. As previously stated (Figure 3.41), for isotropic end members the maximum birefringence is usually attained in the middle of the series (Kalinin, 1967; Hariya and Kimura, 1978; Hirai and Nakazawa, 1982; Akizuki *et al*., 1984; Allen and Buseck, 1988; Nakano *et al*., 1989).

Temperature and pressure increases reduce anomalous birefringence (Figure 3.45) (Kalinin, 1967; Hariya and Kimura, 1978; Milke, 2004). High-temperature annealing usually, but not always, decreases the anomalous

birefringence in garnets. Data from various authors can significantly differ from each other (Hariya and Kimura, 1978)—see section 3.4.5.3.

Composition of the growth medium. Optical anomalies in garnets are affected by various components of the growth medium including H_2O, CO_2, NaCl, Na_2CO_3, among others (Kalinin, 1967; Hariya and Kimura, 1978)—see section 3.5.2.

Sources of Optical Anomalies in Ugrandite Garnets

To account for the optical anomalies in garnets nearly all known sources have been proposed (McAloon and Hofmeister, 1993; Hofmeister *et al*., 1998; Andrut and Wildner, 2001; Shtukenberg *et al*., 2001a). These can be briefly summarized as follows:

1. Stress (strain, deformation)
   a. Plastic deformation (Allen and Buseck, 1988).
   b. Stress from single dislocations and dislocation ensembles (Figure 2.7), as well as from twin and grain boundaries (Hofmeister *et al*., 1998).
   c. Internal stress induced by compositional inhomogeneity (Lessing and Standish, 1973; Shtukenberg *et al*., 2001a).
2. Ordering of structural units
   a. Ordering of trivalent cations (Al, Fe, Cr, and occasionally V) over the octahedral sites (Takéuchi *et al*., 1982; Shtukenberg *et al*., 2002, 2005). The ordering may be either kinetic (Akizuki, 1984; Shtukenberg *et al*., 2001a, 2002, 2005) or thermodynamic (Hatch and Griffen, 1989) in origin.
   b. Ordering of divalent cations (Ca, Fe, Mg, Mn) on dodecahedral sites supplemented by ordering over octahedral sites (Allen and Buseck, 1988; Griffen *et al*., 1992).
   c. Orientational ordering of OH^- groups (Rossman and Aines, 1986; Akizuki, 1989).
   d. Ordering of transition elements over dodecahedral sites (Ca) resulting in the magneto-optic effect (Blanc and Maisonneuve, 1973).
3. Phase and chemical inhomogeneity of crystals
   a. Complex polysynthetic twinning (Ingerson and Barksdale, 1943; Brown and Mason, 1994).
   b. Fine oscillatory zoning (Ivanova *et al*., 1998; Pollok *et al*., 2001).

One can find circumstances under which each of these sources is operative. However, they are not equally likely. Growth ordering of aluminum, iron and chromium among the octahedral sites, the source considered in detail in Chapter 3, most commonly explains the strong anomalous birefringence and its complicated distribution over the crystal. One need not invoke compositional inhomogeneity, formation of dislocation ensembles, or exotic impurities. This kind of optical anomaly can be detected in most ugrandite crystals of middling composition formed at relatively low temperatures and growth rates.

Optical anomalies due to ordering of cations on octahedral sites are often superimposed on anomalies related to heterometry-induced stress as strong variations of crystal composition are common among the ugrandites (section 2.8.2.4). Heterometry is less important in the garnets than kinetic ordering. Stress on dislocation ensembles (section 2.6.2.1) is detected infrequently. Nevertheless, all three sources were found to simultaneously contribute to the anomalous birefringence in grandite garnets from western Mali (Shtukenberg *et al*., 2001a).

5.6. OPTICAL ANOMALIES IN SOLID SOLUTIONS OF ALUMS

Mixed crystals of alums $A^{+}M^{3+}(SO_4)_2 \cdot 12H_2O$, have long been known to show growth sector zoning (Brauns, 1885) considered in detail in Chapter 3 as a consequence of the kinetic ordering of cations. Other sources of anomalous birefringence in alums have been also detected, particularly the optical anomalies related to compositional heterometry-induced stress and to stress on dislocations. To detect these additional sources of optical anomalies it is necessary to anneal the kinetic order and its associated anomalous birefringence. The annealing of alum $(K, NH_4)Al(SO_4)_2 \cdot 12H_2O$ between 70 and 80 °C for a few days removes the birefringence related to growth desymmetrization but does not homogenize the chemical composition throughout. Lesser anomalies now become manifest. Figures 2.6 and 3.6c show the birefringence induced by dislocation bundles and section 2.8.3.2 (Figures 2.41, 3.6c) discusses the optical anomalies related to sector specific heterometry-induced stress. Growth desymmetrization induces relatively high birefringence only in the octahedron growth sectors. In the smaller cube and rhombic dodecahedron growth sectors desymmetrization is not as pronounced and the stress contribution becomes comparable.

5.7. DETECTING SUPERIMPOSED SOURCES OF OPTICAL ANOMALIES

As optical anomalies from various sources often coexist, it would be valuable to establish criteria for parsing them among various etiologies. For this purpose, we can use the features of optical anomalies described in sections 5.2–5.4 and listed in Table 5.1. Distortions of the optical patterns typically increase in the following order: stress on dislocations < compositional heterometry-induced stress < kinetic ordering of atoms < phase and chemical heterogeneity.

The anomalous birefringence in crystals of ammonium chloride with impurities of copper and some other heavy metals (Platonova *et al*., 1994) is illustrative of a superposition of optical anomalies; optical complexity increases with copper concentration. It was shown that copper incorporates into the crystal lattice either via two-dimensional isomorphism or syntactic intergrowths of ammonium chloride with copper chloride and the double salt of copper-ammonium chloride. Copper atoms can also occupy interstitial sites in the ammonium chloride crystal structure. Optical

Table 5.1. Features of optical anomalies (OA) related to different sources

Source of optical anomalies (OA)	1	2	3	4
Optical sector zoning	++	+−	++	+−
Optical sub-sector zoning	+	+−	++	—
Concentric zoning	+	+−	++	+−
Significant optical variation within one growth sector or within one growth zone	++	++	+−	+−
Relationship between OA and cracks	++	+−	—	—
Absence of extinction under orthoscopic examination and distorted conoscopic figures	+−	+−	+−	+
Significant variations of OA over the crystal ensemble	+	+	+−	++
Redistribution of OA due to crystal cleavage	++	—	—	+
Relationship between OA and crystal composition	—	—	+	+
Relationship between OA and composition gradients	++	+	—	+
Decreasing OA during annealing	+−	+−	+	—

Remarks: 1 – compositional heterometry-induced stress, 2 – stress on dislocations and inclusions, 3 – kinetic ordering of atoms, 4 – phase and chemical heterogeneity. ++: nearly always present, +: detected often, +: occasional and usually weak, —: this feature is not associated with this source.

anomalies can be induced by compositional heterometry-induced stress, stress on the boundaries between different phases, superimposition of optical indicatrices in heterogenous crystals, and even by ordering of copper atoms and complex ions in the crystal structure. The etiologies of the optical anomalies in this case are not known. This compelling system requires further study. It is likely, however, that the optical methods will require complementary analyses by diffraction, spectroscopy, and high-resolution microscopy.

5.8. *FAUX* OPTICAL ANOMALIES

Finally, we conclude with a case of a crystal whose circular extinction masquerades as anomalous birefringence.

A birefringent crystal will induce an ellipticity in linearly polarized light incident in a general direction. The differential transmission of left and right circularly polarized light has the effect of increasing the ellipticity of linearly polarized light as well (Figure 5.2). Therefore, a crystal showing strong circular extinction will appear to be birefringent.

Such a crystal is that of the dye 1,8-dihydroxyanthraquinone. The anomalous birefringence of these bright orange square plates was reported by Neuhaus (1943).

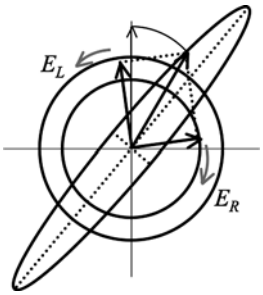

Figure 5.2. The differential attenuation of two counterpropagating circular polarized rays will produce elliptically polarized light
Source: Figure courtesy of Dr. Kacey Claborn, Ph.D. Dissertation, University of Washington, 2006, Figure 3-8.

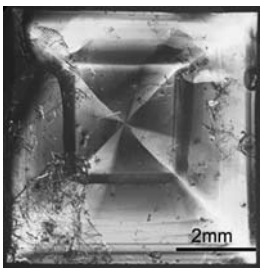

Figure 5.3. Anomalous birefringence of 1,8-dihydroxyanthraquinone between crossed polarizers
Source: Reprinted with permission from Claborn, K., Puklin-Faucher, E., Kurimoto, M., Kaminsky, W. and Kahr, B. "Circular Dichroism Imaging Microscopy: Application to Enantiomorphous Twinning in Biaxial Crystals of 1,8-Dihydroxyanthraquinone" J.Am.Chem. Soc. 2003, 125, p.14825-14831. Copyright 2003 American Chemical Society (see Color Section following page 254)

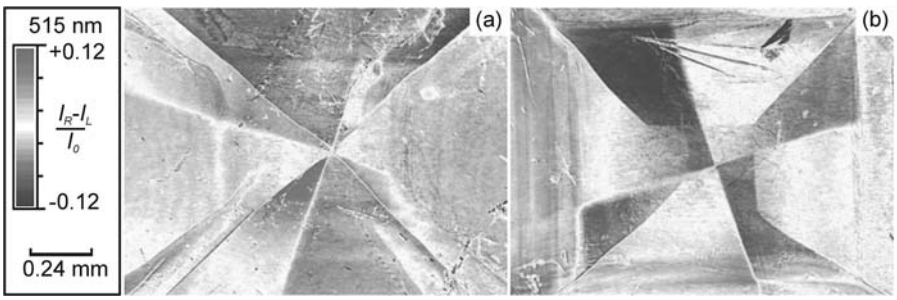

Figure 5.4. False color micrographs of crystals of 1,8-dihydroxyanthraquinone in which red indicates the preferential transmission of left circularly polarized light and blue indicates the preferential transmission of right circularly polarized light
Source: Reprinted with permission from the Royal Society of Chemistry, Kaminsky, W., Claborn, K., Kahr, B. "Polarimetric Imaging of Crystals" *Chem. Soc. Rev.* 2004, 8, p.514-525. Copyright 2004 Royal Society of Chemistry (see Color Section following page 254)

Despite the clearly tetragonal morphology and x-ray crystal structure (Kahr and McBride, 1992), the crystals seemed to show pronounced linearly birefringence when viewed along [001] and complex extinction patterns (Figure 5.3). The contribution of circular dichroism to the ellipticity was confirmed by measuring the difference in transmitted left and right circularly polarized light (Figure 5.4). The contrast revealed that the crystals in the space groups $P4_1$ an $P4_3$ were enantiomorphously twinned so as to give "pinwheel" patterns revealing crystals of one enantiomorph embedded in a heterochiral host (Claborn *et al*., 2003). The origin of the pinwheels patterns is as yet unknown.

This example illustrates that there are etiologies of optical anomalies yet to be found and explained.

CONCLUSION

Reinhard Brauns, in summing up his own treatise on optically anomalous crystals (1891), the only such treatise until the present volume, he whittled his six causal categories of optical anomalies in crystals down to an essential three: Anomalies due to differently oriented lamellae, anomalies due to the intergrowth of more than one phase, and anomalies as a result of inner tension or stress. Brauns' investigations differ from ours in several respects. In each of the three major categories, we see strikingly, the changes that have been wrought by an extra century of crystal chemistry and crystal physics. Brauns often only inferred polytypism by analogy to the optical properties of artificially layered materials. He could not always identify distinct phases and the determination of their relationships to one another was not always possible. And, he treated photoelasticity qualitatively, predating as he did, the great systematizers of crystal physics, Voigt and Pockels. Nevertheless, we can only admire the good judgments of the earlier investigators whose work Brauns collected. We might be inclined to say, that in the absence of what we today would demand as hard evidence, they were endowed with excellent instincts and intuition. However, this would be a pejorative conclusion. Their intuition was based on painstaking observation of a kind that scientists are less inclined towards today in the age of instrument analysis. We might concede that intuition based on experience is just another way of saying intelligence.

The one piece of the puzzle that was missed by Brauns and his contemporaries was kinetic desymmetrization. In the absence of crystal structures, this would be too much to expect. The foresight of Tammann and Shubnikov is remarkable in presupposing that crystals could have 'isomers' of greater or lesser symmetry – order-disorder and that transitions would naturally, according to the Neumann-Curie principle, lead to new physical observables. These judgments were confirmed in a succession of studies. However, the message about solid solutions was brought home slowly. Kitaigorodsky, in his *Mixed Crystals* (1984), failed to see the importance of rate controlled phenomena and emphasized isomorphism to the exclusion of all else in the formation of mixed crystals.

It would be an exaggeration to say that all problems of anomalous crystal optics have been solved, however, the most common deviations have surely lost much of their mystery. Therefore, it is reasonable to return to a question formulated at the outset: is the term 'optical anomaly' useful and necessary? As stated by Kahr and McBride (1992) "a phenomenon that seems anomalous to one generation can seem

commonplace to a succeeding generation with more sophisticated expectations." For example, imperfect forms – symmetry equivalent faces of unequal size - were in the Nineteenth Century considered crystallographic anomalies. Haüy referred to such distortions as "pathologies", while Karnojitzky used "teratologies". In this language, we see the long-standing predisposition of crystallographers to higher symmetries. Distortions are born of monsters (Gk. *Teras*) and disease (Gk. *Pathologicos*). Thus, x-ray crystallographers will often struggle to squeeze a model into the highest possible symmetry, even when alternative physical evidence exists that a lower symmetry is more appropriate. Naturally, high symmetry says less, but the meaning of optically anomalous crystals is in the narratives that they tell, and quite often, these can be long stories.

In this sense, anomalous crystal optics is merely the study of the optical properties of real crystals. Deviations from expected or idealized symmetry motivates the investigator to seek out reasons for such deviations. This leads us to a new depth of understanding of growth and structure. We aspired to demonstrate this idea throughout.

We leave the reader with a reminder of the practical applications of optical anomalies for detection and quality control of imperfections of technically important crystals and their role in determining the growth histories of minerals.

Among the blank spots to which we can point future researchers is the study of the effects of growth conditions on optical anomalies, and the convolution of superimposed anomalies. It is also likely that new linear optical anomalies will arise, especially those related to optically active point groups, as methods of optical analysis become more sophisticated and more sensitive.

A number of rather new methods of analysis have yet to touch the problem of optically anomalous crystals and promise greater insights. In particular, we cite scanning probe microscopies for the direct observation of crystal growth mechanisms, and force field calculations for modelling the adsorption of crystal growth units. Finally, we would like to emphasize that despite the profusion of increasingly sophisticated methods of crystallographic analysis, the simple optical microscope remains an extraordinarily discerning and comparatively inexpensive device for the study of crystalline matter and its imperfections.

REFERENCES

Abbott RN Jr (1993) Calculation of the orientation of the optical indicatrix in monoclinic and triclinic crystals: The point-dipole model. *Am. Mineral*. **78**:952–956

Abbott RN Jr (1994) Electronic polarizability of oxygen and various cations in selected triclinic minerals: point-dipole theory. *Can. Mineral*. **32**:909–918

Abbott RN Jr (1996) Optical properties of $C2/c$ pyroxenes: a point-dipole explanation. *Can. Mineral*. **34**:595–603

Adams HG, Cohen LH, Rosenfeld JL (1975a) Solid inclusion piezothermometry I: Comparison Dilatometry. *Am. Mineral*. **60**:574–583

Adams HG, Cohen LH, Rosenfeld JL (1975b) Solid inclusion piezothermometry II: Geometric basis, calibration for the association quartz-garnet and application to some pelitic schists. *Am. Mineral*. **60**:584–598

Agranovich VM, Ginzburg VL (1984) Crystal optics with spatial dispersion and excitons. Springer-Verlag, Berlin

Akizuki M (1981a) Crystal growth and phase transition of intermediate microcline. *Neues Jahr. Mineralogie Mh*. **4**:181–189

Akizuki M (1981b) Origin of optical variation in analcime. *Am. Mineral*. **66**:403–409

Akizuki M (1981c) Origin of optical variation in chabazite. *Lithos* **14**:17–21

Akizuki M (1984) Origin of optical variation in grossular-andradite garnet. *Am. Mineral*. **69**:328–338

Akizuki M (1985) The origin of sector twinning in harmotome. *Am. Mineral*. **70**:822–828

Akizuki M (1986) Al-Si ordering and twinning in edingtonite. *Am. Mineral*. **71**:1510–1514

Akizuki M (1987a) Al, Si order and the internal texture of prehnite. *Can. Mineral*. **25**:707–716

Akizuki M (1987b) An explanation of optical variation in yugawaralite. *Mineral. Mag*. **51**:615–620

Akizuki M (1987c) Crystal symmetry and order-disorder structure of brewsterite. *Am. Mineral*. **72**:645–648

Akizuki M (1989) Growth structure and crystal symmetry of grossular garnets from Jeffrey mine. *Am. Mineral*. **74**:859–864

Akizuki M, Harada K (1988) Symmetry, twinning, and parallel growth of scolecite, mesolite, and natrolite. *Am. Mineral*. **73**:613–618

Akizuki M, Konno H (1985a) Internal texture and abnormal optical properties of apophyllite. *Neues Jahr. Mineralogie Abh*. **151**:99–115

Akizuki M, Konno H (1985b) Order-disorder structure and the internal texture of stilbite. *Am. Mineral*. **70**:814–821

Akizuki M, Konno H (1987) Growth twinning in phacolite. *Mineral. Mag*. **51**:427–430

Akizuki M, Nishido H (1988) Epistilbite: symmetry and twinning. *Am. Mineral*. **73**:1434–1439

Akizuki M, Sunugawa I (1978) Study of the sector structure in adularia by means of optical microscopy, infra-red absorption, and electron microscopy. *Mineral. Mag*. **42**:453–462

Akizuki M, Terada T (1998) Origin of abnormal optical property of apophyllite. *Neues Jahr. Mineralogie Mh*. N **5**:234–240

Akizuki M, Hampar MC, Zussman J (1979) An explanation of anomalous optical properties of topaz. *Mineral. Mag*. **43**:237–241

Akizuki M, Nakai H, Suzuki T (1984) Origin of iridescence in grandite garnet. *Am. Mineral*. **69**:896–901

Akizuki M, Nishido H, Fujimoto M (1989) Herschelite: morphology and growth sectors. *Am. Mineral*. **74**:1337–1342

Akizuki M, Kudoh Ya, Kuribayashi T (1996) Crystal structures of the {011}, {610}, and {010} growth sectors in brewsterite. *Am. Mineral*. **81**:1507–1512

Akizuki M, Kudoh Ya, Satoh Y (1993) Crystal structure of orthorhombic {001} growth sector of stilbite. *Eur. J. Mineral*. **5**:839–843

Akizuki M, Kuribayashi T, Nagase T, Kitakaze A (2001) Triclinic liddicotite and elbaite in growth sectors of tourmaline from Madagascar. *Am. Mineral*. **86**:364–369

Akizuki M, Nisidon H, Kudon Y, Watanabe T, Kurata K (1994) Sector growth and symmetry of (F,OH) apatite from the Asio mine, Japan. *Mineral. Mag*. **58**:307–14

Allen FM, Burnham CA (1992) Comprehensive structure model for vesuvianite: symmetry variation and crystal growth. *Can. Mineral*. **30**:1–18

Allen FM, Buseck PR (1988) XRD, FTIR and TEM studies of optically anisotropic grossular garnets. *Am. Mineral*. **73**:568–584

Anan'ev SA, Konovalenko SI (1984) Effect of internal stress on the optical properties of eremeyevite. *Geology and Geophysics, Sib. Otd. Akad. Nauk SSSR* **N 9**:97–103 (in Russian)

Andrut M, Wildner M (2001) The crystal chemistry of birefringent natural uvarovites: Part I. Optical investigations and UV-VIS-IR absorption spectroscopy. *Am. Mineral*. **86**:1219–1230

Anonymous comments about Brewster's work. (1821) *Edinburgh Philosophical Journal* **5**:216

Anufriev AM, Bulka GR, Vinokurov VM, Krinari GA, Nizamutdinov NM, Urasin MA, Khasanova NM (1980) Dissymmetrization and microinhomogeneity of crystals of minerals. In: Mineral inhomogeneity and crystal growth. Materials of 11 IMA Congress Nauka, Moscow, pp 10–18 (in Russian)

Armbruster T, Oberhansli R (1988) Crystal-chemistry of double ring silicates—structural, chemical and optical variation in osumilites. *Am. Mineral*. **73**:585–594

Artini E (1907) Della forma cristallina alcuni derivati del benzolo. Dendiconti, Instituto Lombard di Scienze e Lettere, Rebeschini di Turati, Milano

Azimov PYa (2000) Formation of growth zoning in metamorphic garnets (effect of *P-T* conditions and fluid regime). Dissertation, St. Petersburg (in Russian)

Azimov PYa, Shtukenberg AG (2000) Simulation of phase diagrams for water-salt systems with solid solutions. *Russian J. Inorg. Chem*. **45**:1302–1309

Azimov PYa, Shtukenberg AG (2003) Numerical modelling of growth zoning at nonstationary crystallization of solid solutions—Metamorphic garnets. *Math. Geol.* **35**:405–430

Babkin PV (1960) On the optical anomalies of cassiterite. In: Materials on geology and row materials of North-East of USSR. (N14):51–60 (in Russian)

Balarew C (1987) Mixed crystals and double salts between metal (II) salt hydrates. *Z. Kristallogr*. **181** (N 1–4):35–82

Balestrino G, Paroli P, Geller S (1986) Growth anisotropy in the Nd-Y and Pr-Y iron garnets. *Phys. Rev. B* **34**:8104–8106

Barabanov VF (1975) Mineralogy of tungsten bearing Transbaikalia mines, vol 2. LGU Press, Leningrad (in Russian)

Barry TI, Moore WJ (1964) Amethyst: Optical properties and paramagnetic resonance. *Science* **144**: 289–290

Barry TM, McNamara P, Moore WJ (1965) Paramagnetic resonance and optical properties of amethyst. *J. Chem. Phys.* **42**:2599–2606

Bass JD (1995) Elasticity of minerals, glasses and melts. In: Ahrens ThJ (ed) Mineral physics and crystallography. A Handbook of Physical Constants, *Am. Geophys. Union, AGU Reference Shelf Ser*. **2**:45–63

Batsanov SS (1966) Refractometry and chemical structure. D Van Nostrand Company Inc, NJ, Toronto, NY, London

Batsanov SS (2000) Structural chemistry (facts and dependencies). Dialog-MGU, Moscow (in Russian)

Baur WH, Fischer RX (2003) On the significance of small deviations from higher symmetry. *Mineral. Mag*. **67**:793–797

Becke F (1894) Der Aufbau der Kristalle aus Anwachskegln. *Lotos,* 14.

Belikov BP (1970) Elastic properties of rock-forming minerals and rocks. Nauka, Moscow (in Russian)
Belouet C (1980) Growth and characterization of single-crystals of KDP family. Progress in crystal growth and the characterization of materials. **3**:121–156
Belouet C, Monnier M, Crouzier R (1975) Strong isotopic effects on lattice-parameters and stability of highly deuterated D-KDP single crystals and related growth problems. *J. Cryst. Growth* **30**:151–157
Belyustin AV, Stepanova NS (1981) Relationships between anomalous biaxiality in KDP crystals and growth conditions. In: Smirnov YuM (ed) Physics of crystallization. KGU Press, Kalinin, pp 65–70 (in Russian)
Belyustin AV, Portnov VN, Stepanova NS (1970) Anomalous double refraction in crystals of potassium dihydrogen phosphate. *Sov. Phys. Crystallogr*. **14**:617–619
Benedict JB, Cohen D, Lovell S, Rohl A, Kahr B (2006) What is syncrystallization? The state of a pH indicator in single crystals of phthalic acid. *J. Am. Chem. Soc.* **128**:5548–5559
Bernauer F (1929) Gedrillte Krystalle. *Gebrüder Borntraeger*, Berlin
Beskrovanov VV (1992) Ontogeny of diamond. Nauka, Moscow (in Russian)
Bethke CM, Birnie RW (1980) Computer synthesis of optical interference figures. *Am. Mineral*. **65**: 1294–1301
Biot J-B (1818) Mémoire sur les lois générales de la double refraction et de la polarisation dans les corps regulièrement cristallisés. *Mémoires de la Académie Royale des Sciences* **III**:177–384
Biot J-B (1842) Mémoire sur la polarisation lamellaire. *Mémoires de l'Académie royale des Sciences de l'Institut de France* **18**:539–725
Blanc Y, Maisonneuve J (1973) Sur la biréfringence des grenats calciques. *Bulletin de la société française de minéralogie et de cristallographie* **96**(N 4/5): 320–321
Bliznakov G, Kirkova E, Nikolayeva K A (1971) Study of the rate-controlling stage of the process of crystal growth in solutions. *Kristall und Technik* **6**(N 1):33–38
Bloss FD (1961) An introduction to the methods of optical crystallography. Holt, Rinehart and Winston, New York
Bloss FD, Gibbs GV, Cummings D (1963) Polymorphism and twinning in synthetic fluorphlogopite. *J. Geol.* **71**:537–547
Boettcher AL, Wyllie PJ (1967) Biaxial calcite inverted from aragonite. *Am. Mineral*. **52**:1527–1529
Boiko VS, Garber RI, Kosevich AM (1991) Reversible plasticity of crystals. Nauka, Moscow (in Russian)
Boley BA, Weiner JH (1960) Theory of thermal stresses. Wiley, New York
Born M, Wolf E (1980) Principles of optics. Pergamon, Oxford
Bragg WL (1924) The refractive indices of calcite and aragonite. *Proc. Roy. Soc. London Series* A **105**:370–386
Bragg WL, Pippard AB (1953) The form birefringence of macromolecules. *Acta Cryst*. **6**:865–867
Brauns R (1885) Einige Beobachtungen und Bemerkungen zur Beurtheilung optisch anomaler Krystalle. *Neues Jahr. Minerol. Geol. Palaentol.* **I**:96–118
Brauns R (1891) Die optischen Anomalien der Kristalle. Preisschr Jablonowski - Ges, Leipzig
Brauns R (1898) Über Polymorphie und die optischen Anomalien von chlor - und bromsaurem Natron, *Neues Jahr. Mineral. Geol. Palaentol.* **I**:40–59
Brewster D (1815) On the effects of simple pressure in producing that species of crystallisation which forms two oppositely polarised images, and exhibits the complementary colours by polarised light. *Phil. Trans. Roy. Soc. London* **105**:60
Brewster D (1816) On the communications of the structure of doubly-refracting crystals to glass, muriate of soda, fluor spar, and other substances by mechanical compression or dilitation. *Phil. Trans. Roy. Soc. London* **106**:15
Brewster D (1818a) On the laws of polarization and double refraction in regularly crystallized bodies. *Phil Trans Roy Soc London* **I**:199–272
Brewster D (1818b) On the optical properties of muriate of soda, fluate of lime, and the diamond, as exhibited in their action upon polarized light. *Trans. Roy. Soc. Edinburgh* **8**: 157–164
Brewster D (1821) Account of a remarkable structure in apophyllite, with observations on the optical peculiarities of that mineral. *Trans. Roy. Soc. Edinburgh* **9**:317–336.

Brewster D (1822) Observations on the relation between the optical structure and the chemical composition of the apoplhyllite and other minerals of the zeolite family in reference to the preceding analysis of M Berzelius. *Edinburgh Phil. J.* **7**:12–18

Brewster D (1835) Observations relative to the structure and origin of the diamond. *Phil. Mag.* **7**:245–250

Brown D, Mason RA (1994) An occurrence of sectoral birefringence in almandine from the Gagnon Terrane, Labrador. *Can. Mineral*. **32**:105–110

Buckley H (1930) The influence of RO_4" and related ions on the crystallization of sodium chlorate, *Z. Kristallogr.* **75**:15–31

Buckley H (1951) Crystal growth. Wiley, NY

Bulka GR, Vinokurov VM, Nizamutdinov NM, Hasanova NM (1980) Dissymmetrization of crystals: theory and experiment. *Phys. Chem. Minerals.* **6**:283–293

Bullard T, Kurimoto M, Avagyan S, Jang S-H, Kahr B (2004) Luminescent labeling of growth hillocks in dye-doped potassium hydrogen phthalate. *Am. Crystallogr. Ass. Trans.* **39**:62–72

Burke JG (1966) Origins of the science of crystals. University of California Press, Berkeley

Carpenter MA, Putnis A (1985) Cation order and disorder during crystal growth: some implications for natural mineral assemblages. In: Thompsom AB, Rubie DC (eds) Methamorphic reactions: Kinetics, textures, and deformation. Springer, Berlin, pp 1–26

Carrington A, McLachlan AD (1967) Introduction to magnetic resonance with applications to chemistry and chemical physics. Harper and Row, New York

Carter R (1991) Solid state chemistry. Part I. Mechanistic studies on the decomposition of didecanolyl peroxide. Part II. Possible insights into mechanisms of crystal growth through the cryslatline packing of 2-(hydroxymethyl)-2-methyl-1,3-propanediol. PhD Dissertation, Yale University

Chakraborty S, Ganguly J (1992) Cation diffusion in alumosilicate garnets: experimental determination in spessartine-almandine diffusion couples, evaluation of effective binary diffusion coefficients, and applications. *Contrib. Mineral. Petrol*. **111**:74–86

Chase AB, Lefever RA (1960) Birefringence of synthetic garnets $R_3Ga_5O_{12}$, $R_3Al_5O_{12}$ (R=Y, Yb, Tr). *Am. Mineral*. **45**:1126–1129

Cheredov VN (1993) Imperfections of synthetic fluorite crystals. Nauka, St.Petersburg (in Russian)

Chernov AA (1970) Growth of co-polymer chains and mixed crystals – trial-and-errors statistics. *Physics Uspekhi* 100, N 2, 277–328 (in Russian)

Chernov AA (1984) Modern crystallography, vol 3. Formation of crystals. Springer, Berlin

Chernov AA, Lewis J (1967) Computer model of crystallization of binary systems: kinetic phase transitions. *J. Phys. Chem. Solids*. **28**:2185–2198

Chistiakova MB, Osolodkina GA, Razmanova ZP (1964) Milarite from the Cenrtal Kazakhstan. *Dokl. Akad. Nauk SSSR* **159**(N 6):1305–1308 (in Russian)

Claborn K, Puklin-Faucher E, Kurimoto M, Kaminsky W, Kahr B. (2003) Circular dichroism imaging microscopy: Application to enantiomorphous twinning in 1,8-dihydroxyanthrquinone. *J. Am. Chem. Soc.* **125**:14825–14831

Claborn K, Chu A-S, Jang S-H, Su F, Kaminsky W, Kahr B (2005) Circular extinction imaging: determination of the absolute orientation of embedded chromophores in enantiomorphously twinned $LiKSO_4$ crystals. *Crystal Growth and Design* **5**:2117–2123

Correns CW (1949) Growth and dissolution of crystals under linear pressure. *Discussions of the Faraday Society* **5**:267–271

Correns CW, Nagelschmidt G (1933) Über Faserbau und optische Eigentschften von Chalzedon. *Z. Kristallogr*. **85**:199–213

Crank J (1975) The mathematics of diffusion. Oxford University Press, Oxford

Crundwell G (1997) Optical anomalies in solid solutions of simple isomorphous salts. Dissertation, Purdue University

Crundwell G, Gopalan P, Bakulin A, Peterson ML, Kahr B (1997) Effect of habit modification on optical and X-ray structures of sodium halate mixed crystals: the etiology of anomalous double refraction. *Acta Cryst*. B**53**:189–202

Cummins PG, Dunmur DA, Munn RW, Newham RJ (1976) Applications of the Ewald method I. Calcucation of multipole lattice sums. *Acta Cryst*. A**32**:847–853

Curie P (1894) Sur la symétrie des phénomènes physiques: symétrie d'un champ électrique et d'un champ magnétique. *Journal de Physique, 3e série* pp 393–415

Darwin C (1859) On the Origin of Species. http://wwwliteratureorg/authors/darwin-charles/the-origin-of-species-6th-edition/chapter-05html

De Wette FW, Schacher GE (1965) Internal field in general dipole lattice. *Phys. Reviews* A **137**:78–91

Deer WA, Howie RA, Zussman J (1992) Rock-forming minerals. Longman, London

Demina TV (1980a) Crystal chemical features and physical properties of synthetic cordierite. *Zapiski Vsesouznogo Mineralogicheskogo Obschestva* **109**(N 1):37–49 (in Russian)

Demina TV (1980b) Composition, structure and physical properties of synthetic cordierite crystals. Dissertation, Novosibirsk (in Russian)

Demina TV (1990) Effect of growth medium on the composition, properties and morphology of synthetic cordierite crystals. *Zapiski Vsesouznogo Mineralogicheskogo Obschestva* **119**(N 4): 74–83 (in Russian)

Demina TV, Afonina GG (1994) On the variations of axial angle values in cordierites. *Zapiski Vserossiiskogo Mineralogicheskogo Obschestva* **123**(N 6):59–76 (in Russian)

Demina TV, Mikhailov MA (2000) Hexagonal compounds with beryl structure: relations between optical anomalies and the crystal anatomy. *Zapiski Vserossiiskogo Mineralogicheskogo Obschestva* **129**(N 5):81–89 (in Russian)

Demina TV, Mikhailov MA (2001) Optical anomalies and anatomy of crystal aggregates with the beryl structure. *Zapiski Vserossiiskogo Mineralogicheskogo Obschestva* **130**(N2):112–121 (in Russian)

Demina TV, Mikhailov MA, Beloserova OYu (2003) Synthetic minerals of beryl group: symmetry and srtucture ordering vs. chemical composition and anatomy of the crystals. *Zapiski Vserossiiskogo Mineralogicheskogo Obschestva* **132**(N 5):1–21 (in Russian)

Denisov AV, Punin YuO, Gabrielyan VT, Grunsky OS, Shtukenberg AG (2006a) Physical and physical-chemical processes accompanying powder synthesis, crystal growth and annealing in different $PbMoO_4$ media. Part 4 Anomalous biaxiality and thermoplastic strains in $PbMoO_4$ crystals in connection with the conditions of their crystal growth. *Crystallography Reports* **51**:128–134

Denisov AV, Punin YuO, Shtukenberg AG, Grunsky OS (2006b) Study of optical anomalies and calculation of the internal stress in the lead molybdate crystals grown by Czochralski method. *Vestnik SPbGU Ser* **7**(N 1):106–110 (in Russian)

De Yoreo JJ, Woods BW (1993) A study of residual stress and the stress-optic effect in mixed crystals of $K(D_xH_{1-x})_2PO_4$. *J. Appl. Phys*. **73**:7780–7789

De Yoreo JJ, Rek ZU, Zaitseva NP, Woods BW (1996) Sources of optical distortion in rapidly grown crystals of KH_2PO_4. *J. Cryst. Growth* **166**:291–297

Dornberger-Schiff K, Grell G (1982) The concepts of "crystal", "OD crystal", and "MDO crystal". *Sov. Phys. Crystallogr*. **27**:73–77

Dowty E (1976) Crystal structure and crystal growth II. Sector zoning in minerals. *Am. Mineral*. **61**:460–469

Dressler L (1986a) Crystallographic nature of optical microinhomogeneities in fluorite (CaF_2). *Cryst. Res. Technol*. **21**(N 4): K53–K57

Dressler L (1986b) Residual stress fields in cylindric Bridgman-Stockbarger crystals of fluorite. *Cryst. Res. Technol*. **21**(N 8):1085–1089

Drits VA (1997) Mixed-layer minerals. In: Merlino S (ed) EMU notes in mineralogy. Vol. 1. *Modular aspects of minerals*. Eötvos University Press, Budapest, pp 153–190

Drits VA, Murav'ev VI, Shutov VD (1966) New aspects of the optical study of sheet minerals. Voprosi mineralogii osadochnikh obrasovanii, vol 7. LGU Press, L'vov, pp 15–31 (in Russian)

Dunmur DA (1972) The local electric field in anisotropic molecular crystals. *Molecular Physics* **23**: 109–115

Elsen GH, Ettenberg M (1978) Synthesis of $A^{III}B^{V}$ heteroepitaxial structures. In: Goodman CHL (ed) Crystal growth. Theory and techniques. vol 2, Plenum Press, New York, London, pp 9–76

Ermilova LP, Moleva VA, Klevtsova RF (1960) Chukhrovite—new mineral from the Central Kazakhstan. *Zapiski Vsesouznogo Mineralogicheskogo Obschestva* **89**(N 1):15–25 (in Russian)

Erofeev MV (1871) Crystallographic and crystal optic study of tourmalines. *Zapiski Imperatorskogo Saint Petersburg Mineralogicheskogo Obschestva* **11(**N 6):81–126 (in Russian)

Euler H, Kirfel A, Klapper H, Stukenberg A (1999) Strukturuntersuchungen an zwei Alaun-Einkristallen: $(K_{0.5}(NH_4)_{0.5})Al(SO_4)_2 \cdot 12H_2O$ und $K(Al_{0.6}Cr_{0.4})(SO_4)_2 \cdot 12H_2O$. 7 Jahrestagung der Deutschen Gesellschaft für Kristallographie (DGK) vom 8 bis 10 März 1999 in Leipzig, Referate Supplement Issue No 16, *Z. Kristallogr*. p 30

Fedorov ES (1953a) Universal method and study of feldspars (reissue). In: ES Fedorov universal stage. *Akad. Nauk* SSSR Press, Moscow, pp 145–190 (in Russian)

Fedorov ES (1953b) Optical anomalies in plagioclases (reissue). In: ES Fedorov universal stage. *Akad. Nauk* SSSR Press, Moscow, pp 191–194 (in Russian)

Feng ZF, Zhang XD, Wang YQ, Li ZY, Cheng BY, Zhang DZ (2005) Negative refraction and imaging using 12-fold symmetry quasicrystals. *Phys. Rev. Let.* 94, Art No. 247402

Fishman YuM (1970) X-ray topographic investigation of defects and diffraction contrast in crystals of group KH_2PO_4. Dissertation, Moscow

Foord SE, Mills BA (1978) Biaxiality in "isometric" and "dimetric" crystals. *Am. Mineral*. **63**:316–325

Fraga H, Gali S, Font-Altaba M (1982) Sector zoning as a growth phenomenon and its influence in the optical properties of crystals. The case of grossular-andradite garnets. *Estudios geologicas* **38**(N 3–4):173–178

France WG, Davis PP (1936) Adsorption at crystal-solution interfaces. IX. The concentration of foreign substances in solution relative to the quantity adsorbed by the host crystal. *J. Phys. Chem*. **40**:177–185

Frank-Kamenetsky VA (1964) The nature of structural impurities and inclusions in minerals. LGU Press, Leningrad (in Russian)

Frank FC, Lang AR, Evans DJE, Rooney M-LT, Spear PM, Welbourn (1990) Orientation-dependent nitrogen incorporation on vicinals on synthetic diamond cube growth surfaces. *J. Cryst. Growth* **100**:354–376

Franke VD, Punin YuO, Kotelnikova EN, Voloshina OA, Ivanova TI (1987) Formation of adsorption-mixed crystals in the system ammonium chloride–carbamide–water. In: Synthesis and analysis of pure substances. GGU Press, Gorkii, pp 41–48 (in Russian)

Frank-Kamenetskaya OV, Rozhdestvenskaya IV (2004) Atomic defects and crystal structure of minerals. Advances in Science and Technics, vol 33. YANUS, Saint Petersburg

Frank-Kamenetskaya OV, Rozhdestvenskaya IV, Bannova II, Kostitsyna AV, Kaminskaya TN, Gordienko VV (1995) Dissymmetrization of crystal structures of sodium pollucites. *Crystallography Reports* **40**:645–654

Franko NYu, Ped'ko BB, Sorokina II (2004) Relation between the real structure and optical inhomogeneity of lithium niobate single crystals. *Crystallography Reports* **49**:94–99

Freer R, Edwards A (1999) An experimental study of Ca-(Mg, Fe) interdiffusion in silicate garnets. *Contrib. Mineral. Petrol*. **134**:370–379

Fridman SS (1972) The study of optical inhomogeneities of KDP crystals in relation to growth conditions. PhD Thesis, Gorkii (in Russian)

Frondel C (1940) Effect of dyes on the crystal habit and optical characteristics of NaF, LiF, NaCl, KCl, KBr, and KI. *Am. Mineral*. **25**:91–110

Frondel C (1978) Characters of quartz fibers. *Am. Mineral*. **63**:17–27

Frondel C (1985) Systematic compositional zoning in the quartz fibers of agates. *Am. Mineral*. **70**: 975–979

Gali S (1983) Grandite garnet structures in connection with the growth mechanism. *Z. Kristallogr*. **163**:43–52

Gaubert P (1894) Utilisation du polychroïsme produit artificiellement, pour l'observation des anomalies optiques dans les substances pseudo-cubiques. *Bulletin Société Française de Minéralogie* **17**:121–124

Gaubert P (1900) Sur la coloration artificielle des cristaux. *Bulletin Société Française de Minéralogie* **23**:211–221

Gaubert P (1905) Sur la syncrystallisation de deux substance différentes. *Bulletin Société Française de Minéralogie* **28**:180–184

Gaubert P (1912) Sur le polychroïsme de cristaux de sulfate de potassium colorés artificiellement. *Comptes Rendus* **155**:649–651

Gaubert P (1915) Recherches sur les cristaux de salmiac et de sel imbibés de matières étrangères pendant leur accroissement. *Bulletin Société Française de Minéralogie* **38**:149–182

Gaubert P (1930) Sur la cristallisation du nitrate de plomb. Influence des matières étranères tenues en suspension dans l'eau-mère. *Bulletin Société Française de Minéralogie* **53**:157–171

Gavrieli J, Matthews A, Bar-Matthews M, Szafranek D (1992) Hydrothermal breakdown reactions of grossular and pyrope garnets in $MgCl_2$ and $CaCl_2$ solutions at 2 kbar and 550 and 750 °C. *Eur. J. Mineral*. **4**:793–811

Ge C-Z, Wang H-W, Ming N-B (1993) Birefringence images of screw dislocations viewed end on in cubic crystals containing a long-range stress field. *J. Appl. Phys*. **74**:139–145

Geday M, Kreisel J, Glazer AM, Roleder K (2000) Birefringence imaging of phase transitions: application to $Na_{0.5}Bi_{0.5}TiO_3$. *J. Appl. Cryst*. **33**:909–914

Geschwind S, Remeika JP (1961) Paramagnetic resonance of Gd^{3+} in Al_2O_3. *Phys. Rev.* **122**:757–761

Glazer AM (2002) WINOPTACT: A computer program to calculate optical rotatory power and refractive indices from crystal structure data. *J. Appl. Cryst*. **35**:652

Glazer AM, Lewis JG, Kaminsky W (1996) An automatic optical imaging system for birefringent media. *Proc. Math., Phys. Eng. Sci.,* **452**: 2751–2765

Goldman DS, Rossman GR (1978) The site distribution of iron and anomalous biaxiality in osumilite. *Am. Mineral*. **63**:490–498

Gopalan P, Kahr B (1993) Reevaluation structures for mixed crystals of simple isomorphous salts, $Ba_xPb_{1-x}(NO_3)_2$. *J. Solid State Chem*. **107**:563–567

Gopalan P, Peterson ML, Crundwell G, Kahr B (1993) Reevaluation structures for mixed crystals of simple isomorphous salts: $NaCl_xBr_{1-x}O_3$. *J. Am. Chem. Soc*. **115**:3366–3367

Gorskaya MG, Punin YuO, Sokolov PB, Krezer YuA (1992) Compositional inhomogeneity and heterometry in the crystals of polychromic tourmalines. *Mineral. J*. **14**(N 3):8–20 (in Russian)

Gotman YaD (1939) Some anomalies of cassiterite properties. *Dokl. Akad. Nauk* SSSR **23**(N 5): 469–471 (in Russian)

Graham EB, Raab RE (1983) On the Jones birefringence. *Proc. Roy. Soc. London* A **390**:73–90

Graziani G, Lucchesi S, Scandale E (1990) General and specific growth marks in pegmatite beryls. *Phys. Chem. Minerals* **17**:379–384

Griffen DT (1992) Silicate crystal chemistry. Oxford University Press, NY

Griffen DT, Hatch DM, Phillips WR, Kulaksiz S (1992) Crystal chemistry and symmetry of a birefrigent tetragonal pyralspite$_{57}$-grandite$_{25}$ garnet. *Am. Mineral*. **77**:399–406

Groth PH (1895) Physikalische Kristallographie und Einleitung in die kristallographische Kenntniss der wichtigsten Substanzen. Engelmann, Leipzig

Hall MH Jr (1959) The theory of groups. The Macmillian Company, New York

Hariya Y, Kimura M (1978) Optical anomaly in garnet and its stability field at high pressure and temperatures. *J. Facuty Sci*., Hokkaido University series IV **18**:611–624

Hartshorne NH, Stuart A (1970) Crystals and the polarising microscope. Edward Arnold Ltd, London

Härtwig J (1981) Surface relaxation of a crystal plate with a step-like distribution of impurity atoms. *Cryst. Res. Technol*. **16**:1297–1307

Hatch DM, Griffen DT (1989) Phase transition in the grandite garnets. *Am. Mineral*. **74**:151–159

Hauser J, Wenk HR (1976) Optical properties of composite crystals. *Z. Kristallogr*. **143**:188–219

Hirai H, Nakazawa H (1982) Origin of iridescence in garnet: An optical interference study. *Phys. Chem. Minerals* **8**:25–28

Hirai H, Nakazawa H (1986a) Grandite garnet from Nevada: Confirmation of origin of iridescence by electron microscopy and interpretation of a moiré-like texture. *Am. Mineral*. **71**:123–126

Hirai H, Nakazawa H (1986b) Visualising low symmetry of a grandite garnet on precession photographs. *Am. Mineral*. **71**:1210–1213

Hirai H, Sueno S, Nakazawa H (1982) Lamellar texture with chemical contrast in grandite garnet from Nevada. *Am. Mineral*. **67**:1242–1247

Hirth JP, Lothe J (1968) Theory of dislocations. McGraw-Hill, NY

Hofmeister AM, Schaal RB, Campbell KR, Berry SL, Fagan TJ (1998) Prevalence and origin of birefringence in 48 garnets from the pyrope-almandine-grossularite-spessartine quaternary. *Am. Mineral.* **83**:1293-1301

Hollister LS, Gancarz AJ (1971) Compositional sector-zoning in clinopyroxene from the Norce Area, Italy. *Am. Mineral*. **56**:959–979

Hughes JM, Cameron M, Crowley KD (1991a) Ordering of divalent cations in the apatite structure: Crystal structure refinement of natural Mn- and Sr-bearing apatite. *Am. Mineral*. **76**:1857–1862

Hughes JM, Cameron M, Mariano AN (1991b) Rare-earth-element ordering and structural variations in natural rare-earth-bearing apatites. *Am. Mineral*. **76**:1165–1173

Hurle DTJ (1993) Crystal pulling from the melt. Springer-Verlag, Berlin, New York

Ikornikova NYu (1939) Crystallographic study of beryl crystals from the Schoerl mountain. *Zapiski Vsesouznogo Mineralogicheskogo Obschestva* **68**:536–555 (in Russian)

Ikornikova-Lemmlein NYu (1946) On the optical anomalies in brookite. *Dokl. Akad. Nauk* SSSR **53**(N 3):255–258 (in Russian)

Ikornikova NYu, Tomilovskii GE (1953) Inhomogeneity of corundum resulting in optical anomalies. *Trudi Instituta Kristallographii Akad. Nauk SSSR* **8**:203–214 (in Russian)

Indenbom VL (1960) Dislocation description of the simplest plastic deformation phenomena. In: Klassen-Nekludova MV (ed) Itogi Nauki. Phisiko-Matematicheskie Nauki N 3, Acad. Nauk SSSR, Moscow, pp 117–158 (in Russian)

Indenbom VL (1964) Theory of stress and dislocation formation in the growth of crystals. *Sov. Phys. Crystallogr*. **9**:57–64

Indenbom VL, Kroupa F (1979) Surface deformation due to non-homogeneous distribution of solute atoms in crystals. *Czech. J. Phys*. B**29**:338–347

Indenbom VL, Nikitenko VI (1962) Study of stress in semiconductors by means of cathode-ray transformer. In: Klassen-Necludova MV (ed) Stress and dislocations in crystals. VINITI Press, Moscow, pp 8–33 (in Russian)

Indenbom VL, Tomilovskii GE (1957a) Inner stresses around single dislocations. *Dokl. Akad. Nauk SSSR* **115**(N 4):723–726 (in Russian)

Indenbom VL, Tomilovskii GE (1957b) Macroscopic edge dislocations in a corundum crystal. *Sov. Phys. Crystallogr*. **2**:183–187

Indenbom VL, Tomilovskii GE (1958) The measurement of internal stress in crystals of synthetic corundum. *Sov. Phys. Crystallogr*. **3**:599–605

Indenbom VL, Urusovskaya AA (1959) What are irrational twins? *Sov. Phys. Crystallogr*. **4**:84–91

Indenbom VL, Nikitenko VI, Milvidsky LS (1962) On the dislocation structure of silicon. In: Klassen-Necludova MV (ed) Stress and dislocations in crystals. VINITI Press, Moscow, pp 55–60 (in Russian)

Ingerson E, Barksdale JD (1943) Iridescent garnet from the Adelaide mining district, Nevada. *Am. Mineral*. **28**:303–312

Ivanova TI, Shtukenberg AG, Punin YuO, Frank-Kamenetskaya OV, Sokolov PB (1998) On the complex zonality in grandite garnets and implications. *Mineral. Mag*. **62**:857–868

Jaeger FM (1917) Lectures on the principle of symmetry and its applications in all natural science. Elsevier, Amsterdam

Jaffe HW (1988) Crystal chemistry and refractivity. Cambridge Univ. Press, Cambridge

Jamtveit B (1991) Oscillatory zonation in hydrothermal grossular-andradite garnet: Nonlinear dinamics in region of immiscibility. *Am. Mineral*. **76**:1319–1327

Johanssen A (1918) Manual of petrographic methods. McGraw-Hill Book Company, New York

Jones RC (1948) A new calculus for the treatment of optical systems VII. properties of N-Matrices. *J. Optical Soc. Am.* **38**:671–685

Kahr B, Gurney RW (2001) Dyeing crystals. *Chem. Rev*. **101**:893–951

Kahr B, McBride JM (1992) Optical anomalous crystals. *Angew. Chem. Int. Ed. in English.* **31**:1–26

Kahr B, Lovell S, Subramony JA (1998) The progress of logwood extract. *Chirality*. **10**:66–77

Kalinin DV (1967) On the relation between anisotropic garnets, chemical composition and chemical conditions of their synthesis. *Dokl. Akad. Nauk SSSR* **172**(N 5):1167–1170 (in Russian)

Kamb WB (1958) Isogyres in interference figures. *Am. Mineral*. **43**:1029–1067

Kaminsky W (2000) Experimental and phenomenological aspects of circular birefringence and related properties in transparent crystals. *Reports on Progress in Physics* **63**:1575–1640

Kaminsky W (2005) WinXMorph: A computer program to draw crystal morphology, growth sectors and cross-sections with export files in VRML V20 utf8-virtual reality format. *J. Appl. Crystallogr.* **38**:566–567

Kaminsky W, Claborn K, Kahr B (2004) Polarimetric imaging of crystals. *Chem. Soc. Rev*. **33**:514–525

Karnojitzky AN (1891a) Crystal optical studies of tourmalines. *Zapiski Imperatorskogo SPb Mineralogicheskogo Obschestva* **27**:209–288 (in Russian)

Karnojitzky AN (1891b) On the optical anomalies of beryl. *Zapiski Imperatorskogo SPb Mineralogicheskogo Obschestva* **27**:1–14 (in Russian)

Karnojitzky AN (1891c) On the optical structure of dioptase. *Vesti Estestvoznaniya* pp 163–165 (in Russian)

Katz A, Rikukawa H (2005) First principles studies of large birefringence in alkaline-earth orthoborate crystals. *Phys. Rev*. B **72**: 041101(R)

Kennunen DS, Punin YuO, Franke VD, Smetannikova OG (2002) Effect of adsorption of dye diamine sky blue on the habit and imperfections of potassium alum crystals. *Vestnik SPbGU* Ser **7**(N 4):25–33 (in Russian)

Khlopin BG, Tolstaya MA (1940) Structure of pseudo-mixed crystals of the methylene blue barium nitrate type. *Zhur. Fiz. Khim*. **14**:941–952 (in Russian)

Kifrel A (1996) Cation distribution in olivines and orthopyroxenes. An interlaboratory study. *Phys. Chem. Minerals* **23**:503–519

Kingma KJ, Downs JW (1989) Crystal-structure of a birefringent andradite. *Am. Mineral*. **74**:1307–1316

Kir'yanov RN (1941) On the garnets from Palkino mineral mines near to Sverdlovsk. *Zapiski Vsesouznogo Mineralogicheskogo Obschestva* N **1**:23–45 (in Russian)

Kitamura K, Komatsu H (1978) Optical anisotropy associated with growth striation of yttrium garnet $Y_3(Al, Fe)_5O_{12}$. *Kristall und Technik* **13**:811–816

Kitamura V, Kouchi A, Hosoya S, Sunagawa I (1982) Growth and dissolution of $NaClO_3$ crystal in aqueous solution. *Mineral J*. **11** (3):9–137

Kitamura K, Iyi N, Kimura S, Cherrier F, Davignes JM, Le Gall H (1986a) Growth-induced optical anisotropy of epitaxial garnet films grown on (110)-oriented substrates. *J. Appl. Phys*. **60**:1486–1489

Kitamura K, Kimura S, Desvignes JM, Le Gall H (1986b) Optical properties of growth induced anisotropy in LPE garnet and its growth conditions dependence. *J. Cryst. Growth* **74**:453–461

Kittel C (1996) Introduction to solid state physics. Wiley, New York

Klapper H (1971) Röntgentopographische Untersuchungen vor Gitterstörungen in Benzil-Einkristallen. *J. Cryst. Growth* **10**:13–25

Klapper H (1998) Structural defects in crystals and techniques for their detection. *Material Science Forum* **276–277**:291–306

Klassen-Nekludova MV (1953) Mechanical properties of synthetic corundum as studied by means of optical control. In: Physical properties of synthetic corundum. *Trudi Instituta Kristallographii Akad. Nauk SSSR* **8**:151–164 (in Russian)

Klassen-Nekludova MV (1960) Mechanical twinning of crystals. Academy of Science USSR, Moscow (in Russian)

Kolesnikov AI (1983) Sector zoning in paratellurite single crystals. In: Smirnov YuM (ed) Physics of crystallization. KGU press, Kalinin, pp 98–103 (in Russian)

Kolesnikov AI (1996) Effect of growth conditions on the defect distribution in pure and doped paratellurite crystals. Dissertation, Tver (in Russian)

Konstantinova AF, Konstantinov KK, Nabatov BV, Evdischenko EA (2002) Modern application packages for rigorous solution of problems of light propagation in anisotropic layered media. I. General solution of boundary problems in crystal optics. *Crystallography Reports* **47**:645–652

Konstantinova AF, Stepanov AN, Korostel' LA, Kornilov AV, Kulagin NA, Otobaev GR (1993) Anomalous dichroism and birefringence in $SrTiO_3$ crystals. *Crystallography Reports* **38**:813–817

Korago AA, Kozlov AV (1988) Textures and structures of the vein quartz from the rock crystal bearing areas. Nedra, Leningrad (in Russian)

Kotelnikova EN, Punin YuO, Frank-Kamenetsky VA (1989) Combined method for study of disordered polytypes In: Frank-Kamenetsky VA, Shmakin BM (eds) Methods of diffraction studies of crystalline materials. Nauka, Novosibirsk, pp 107–118 (in Russian)

Kroll H, Lueder T, Schlenz H, Kirfel A, Vad T (1997) The Fe^{2+}, Mg distribution in orthopyroxene: A critical assessment of its potential as a geospeedometer. *Eur. J. Mineral*. **9**:705–733

Kuznetsov VA (1968) Crystallization kinetics of corundum, quartz and zinkite. In: Lobachev AN (ed) Hydrothermal synthesis of crystals. Nauka, Moscow, pp 77–89 (in Russian)

Kuznetsov EA, Chzhao-Lin Li (1960) Dispersion of birefringence, chemical composition and structure of beryls. *Vestnik Moskovskogo Universiteta* (N 6):46–58 (in Russian)

Lager GA, Armbruster Th, Pohl D (1987) Prediction of refractive indices in minerals from crystallographic data: Applications and limitations of the point-dipole model. *Phys. Chem. Minerals* **14**:177–80

Landau LD, Lifshitz EM (1986) Course of theoretical physics. 7. Theory of elasticity. Butterworth-Heinemann, Oxford

Landolt H, Börnstein R (1979) Numerical data and functional relationships in science and technology elastic, piezoelectric, pyroelectric, piezooptic, electrooptic constants and nonlinear dielectric susceptibilities of crystals new series, Group III, vol 11. Springer-Verlag, Berlin, Heidelberg, New York

Lang AR (1967) Causes of birefringence in diamond. *Nature* **213**:248–251

Lapides IL, Kovalenok VI, Koval PV (1977) Micas of rare-metal granitoids. Nauka, Novosibirsk (in Russian)

Larsen ES, Berman H (1934) The microscopic identification of the nonopaque minerals. US Geological Survey Bulletin

Lasaga A (1981a) Rate laws of chemical reactions. In: Lasaga AC, Kirkpatrick RJ (eds) Reviews in mineralogy, vol 8. Washington DC, pp 1–68

Lasaga A (1981b) The atomistic basis of kinetics: defects in minerals. In: Lasaga AC, Kirkpatrick RJ (eds) Reviews in mineralogy, vol 8. Washington DC, pp 261–320

Lasaga AC, Cygan RT (1982) Electronic polarizabilities of silicate minerals. *Am. Mineral*. **67**:328–334

Lebedev NN (1937) Temperature stress in the theory of elasticity. ONTI, Gl. Red. Techno-Theor. Lit., Leningrad, Moscow (in Russian)

Lemmlein GG (1948) Sector structures in crystals. Akademizdat, Moscow, Leningrad (in Russian)

Lemmlein GG (1973) Morphology and genesis of crystals. Nauka, Moscow (in Russian)

Leonova EM, Beskolova LI (1977) Deformations of interference figures of KDP crystals. In: Single crystals and scintillators. Khar'kov 57–60 (in Russian)

Lessing P, Standish RP (1973) Zoned garnet from Crested Butte, Colorado. *Am. Mineral*. **58**:840–842

Lodochnikov VN (1930) Principles of microscopic methods for the study of crystalline solids. Nauchnoe Khim.-Technol. Izd., Moscow (in Russian)

Lorentz HA (1936) In: Zeeman P, Fokker AD (eds) Collected Papers. vol 2. Nijhoff, Amsterdam, pp 1–119.

Maiwa K, Tsukamoto K, Sunagawa I (1990) Activities of spiral growth hillocks on the (111) faces of barium nitrate crystals growing in an aqueous solution. *J. Cryst. Growth* **102**:43–53

Malinin AYu, Pankov VS, Chumak VD, Vindansh AP (1973) Internal stress in crystals of Al-Mg spinel. *Izvestiya Akad. Nauk SSSR Ser. Phys*. **37**(N 11):2367–2370 (in Russian)

Mallard E (1876) Explication des phénomènes optiques anomaux que présentent un grand nombre de substances cristallisés. *Ann. Mines Mem. Ser. 7eme* **10**:60–196

Mallard E (1886) Sur les hypthothèses diverses proposes pour expliquer les anomalies optiques des cristaux. *Bulletin de la société francaise de mineralogy* **IX**:54–74

Mao SY, Schmid H, Triscone G, Mueller J (1999) Spontaneous magnetization and magnetic susceptibility of a ferroelectric/ferromagnetic/ferroelastic single domain crystal of nickel bromine boracite $Ni_3B_7O_{13}Br$. *Journal of Magnetism and Magnetic Materials* **95**:65–75

Marfunin AS (1959a) Optics of sub-microscopically twinned crystals. *Dokl. Akad. Nauk SSSR* **127** (N 5):869–872 (in Russian)

Marfunin AS (1959b) The feldspars: Phase relations, optical parameters, and geological distribution. Trudi Instituta Rudnikh Mestorozhdenii, petrographii, mineralogii i geochimii. *Akad. Nauk SSSR Press*, Moscow, vol 78 1962 (in Russian)

Marshall SA, Reinberg AR (1963) Paramagnetic resonance absorption spectrum of trivalent iron in single crystal calcite. *Phys. Rev.* **132**:134–142

Martin J (1891) Beitrige zur Kenntniss der optischen Anomalien einaxiger Krystalle. *Neues Jahr. Mineral. Geol. Paleontol.* **7**:1–54

Mazzi F, Galli E (1978) Is each analcime different? *Am. Mineral*. **63**:448–460

McAloon BP, Hofmeister AM (1993) Single-crystal absorption and reflection infrared spectroscopy of birefrigent grossular-andradite garnets. *Am. Mineral*. **78**:957–967

McAloon BP, Hofmeister AM (1995) Single-crystal IR spectroscopy of grossular-andradite garnets. *Am. Mineral*. **80**:1145–1156

McBride JM (1989) Symmetry reduction in solid solutions: A new method for materials design. *Angew. Chem. Int. Ed. in English* **28**:377–379

McBride JM, Bertman SB (1989) Using crystal birefringence to study molecular recognition. *Angew. Chem. Int. Ed. in English* **28**:330–333

Melankholin NM, Grum-Grzhimailo SV (1954) Methods of the optical study of crystals. *Akad. Nauk SSSR Press*, Moscow (in Russian)

Melankholin, NM, Slavnova EN (1959) Uptake of Capri blue by growing lead nitrate crystals. *Sov. Phys. Crystallogr*. **4**:529–534

Mendelson S (1961) Birefringence due to dislocations in glide bands of rocksalt single crystals. *J. Appl. Phys*. **32**:1999–2004

Merli M, Ungaretti L, Oberti R (2000) Leverage analysis and structure refinement of minerals. *Am. Mineral*. **85**:532–542

Merlino S (1997) (ed) EMU notes in mineralogy. Vol. 1. Modular aspects of minerals. Eötvos University Press, Budapest

Milke R (2004) Spiral growth of grossular under hydrothermal conditions. *Am. Mineral*. **89**:211–218

Mill BV, Butashin AV (1986) Formation of real structure of melt grown single crystals of calcium-gallium-germanium garnet and its solid solutions. In: Smirnov YuM (ed) Physics of crystallization. KGU Press, Kalinin, pp 11–19 (in Russian)

Minerals (handbook) (1972) Moscow vol 3, N 1 (in Russian)

Ming NB, Ge CZ (1990) Direct observation of defects in transparent crystals by optical microscopy. *J. Cryst. Growth* **99**:1309–1314

Mookherjee M, Redfern SAT, Zhang M, Harlov DE (2002) Orientational order-disorder of $N(D, H)_4^+$ in tobelite. *Am. Mineral*. **87**:1686–1691

Munn RW (2000) Calculation of the refractive indices in the optically anomalous crystal of 1,5-dichloro-2,3-dinitrobenzene. *J. Chem. Phys.* **113**:8774–8782

Murad E (1976) Zoned, birefringent garnets from Thera Island, Santorini Group (Aegean Sea). *Mineral. Mag*. **40**:715–719

Murav'ev VI, Drits VA (1970) Phenomenon of optical miscibility and its application for the study of optical silicates. In: Clays, mineralogy and practical importance. Nauka, Moscow, pp 22–27 (in Russian)

Nakano T, Lakahara H, Nishida N (1989) Intracrystalline distribution of major elements in zoned garnet from scarn in the chichibu mine, central Japan: illustration by color-coded maps. *Can. Mineral*. **27**:499–507

Narasimhamurty TS (1981) Photoelastic and electro-optic properties of crystals. Plenum, NY

Náray-Szabó (1938) Note on the structure of analcime. *Z. Kristallogr*. **99**:291

Nelmes RJ, Tun Z, Kuhs WF (1987) A compilation of accurate structural parameters for KDP and DKDP, and a users guide to their crystal-structures. *Ferroelectrics* **71**:125–141

Neuhaus A (1941a) Über die anomale Mischbarkeit organischer Substanzen (Anomale Mischkristalle IV). *Z. Kristllogr*. **103**:297–327

Neuhaus A (1941b) Anomale Mischkristalle und orientierte Abscheidung, *Angew. Chemie.* **54**: 527–536

Neuhaus A (1942) Das anomale Mischsystem K_2SO_4-Ponceaurot (Anomale Mischkristalle V). *Z. Kristallogr*. **104**:197–224

Neuhaus A (1943) Partiell-isomorphe Systeme *Z. Kristallogr.* **105**:161–219

Neumann FE (1841) Die Gesetze der Doppelbrechung des Lichts in comprimirten oder ungleichförmig erwärmten unkrystallinischen Körpern. *Poggendorff's Annalen der Physiko.* **54**:448–491

Newton Isaac (1952) Optics. Dover, New York

Nikitenko VI (1966) Polarization-optical study of stress induced by atomic-size dislocation. In: Polarization-optical method of stress examination. Nauka, Leningrad, pp 145–147 (in Russian)

Nikitenko VI, Indenbom VL (1962) Relationships between stress and dislocations in a germanium crystal. In: Klassen-Necludova MV (ed) Stress and dislocations in crystals. VINITI Press, Moscow, pp 34–42 (in Russian)

Nikitenko VI, Osip'yan YuA (1975) Influence of dislocations on optical, electric and magnetic properties of crystals. In: Vainshtein BK, Chernov AA (eds) Problems of modern crystallography. Nauka, Moscow, pp 239–261 (in Russian)

Nikitenko VI, Indenbom VL, Richkova SV, Verkhovsky EI (1962) Mechanical stress in junction diodes. In: Klassen-Necludova MV (ed) Stress and dislocations in crystals. VINITI Press, Moscow, pp 43–47 (in Russian)

Nizamutdinov NM, Bulka GR, Gainullina NM, Vinokurov VM (1976a) Subsets of cosets in Wittke-Garrido color symmetry groups. In: Vinokurov VM (ed) Physical properties of minerals and rocks. KGU Press, Kazan, pp 49–60 (in Russian)

Nizamutdinov NM, Bulka GR, Gainullina NM, Vinokurov VM (1976b) Symmetry of defects distribution in regular systems of points and properties of directions of ESR spectra. In: Vinokurov VM (ed) Physical properties of minerals and rocks. KGU Press, Kazan, pp 3–48 (in Russian)

Nizamutdinov NM, Bulka GR, Khasanova NM, Shchepkin VD, Vinokurov VM (1977) Scheme of removing the orientational degeneracy of the positions in crystal structures, asymmetrization of the crystals, and its appearance in the ESR spectra of the Cu^{2+} ions in $ZnSeO_4 \cdot 6H_2O$ crystals. *Sov. Phys. Crystallogr.* **22**:445–450

Novak GA, Gibbs GV (1971) The crystal chemistry of the silicate garnets. *Am. Mineral.* **56**:791–825

Nowick A, Burton J (ed). (1975) Diffusion in solids. Recent developments. Academic Press, New York

Nye JF (1949a) Plastic deformation of silver chloride. I. Internal stresses and the glide mechanism. *Proc. Roy. Soc. A* **198**:190–204

Nye JF (1949b) Plastic deformation of silver chloride. II. Photoelastic study of the internal stress in glide packets. *Proc. Roy. Soc. A* **200**:47–66

Nye JF (1985) Physical properties of crystals: Their representation by tensors and matrices. Oxford University Press, Oxford

Oberimov IV, Shubnikov AV (1926) The study of plastic deformations in rock salt by means of optical methods *Zh. Ross. Phys. Khim. Obsch.* **58**:817 (in Russian)

Ohkawa M, Yoshiase A, Takeno S (1994) Structural investigation of high- and low-symmetry vesuvianite. *Mineral. J.* **17**(N 1):1–20

O'Loane K (1980) Optical activity in small molecules, nonenantiomorphous crystals, and nematic liquid crystals. *Chem. Rev.* **80**:41–61

Orlov YuL, Tatjanina NA (1973) Birefringence patterns and their origin in diamond crystals. In: New data on the USSR minerals proceedings of fersman mineralogical museum. Nauka, Moscow, pp 108–118 (in Russian)

Overhauser AW, Butler NR (1976) Questions about the Mayer-El Naby optical anomaly in potassium. *Phys. Rev. B* **14**:3371–3376

Pakhomova VI, Silnitskaya GB, Kozurov BK, Rez IS (1978) Effect of impurities on some features of KH_2PO_4 crystals real sutructure. *Inorganic Materials* **14**:1320–1323 (in Russian)

Parise JB, Cuff C, Moore FH (1980) A neutron diffraction study of topaz: evidence for a lower symmetry. *Mineral. Mag.* **43**:943–944

Partlow DP, Cohen AJ (1986) Optical studies of biaxial Al-related color centers in smoky quartz. *Am. Mineral.* **71**:589–598

Passchier CW, Trouw RAJ (1995) Microtectonics. Springer, Berlin

Pecherskaya SG, Mikhailov MA, Demina TV, Bogdanova LA, Belozerova OYu (2003) Symmetry and ordering of compounds with a beryl-type structure in the Mg-enriched part of the beryllium indialite-cordierite-beryl system. *Crystallography Reports* **48**:363–369

Petroff JF, Dunia E, Belouet C, Monnier M (1975) Growth defects in KDP and D-KDP single-crystals, *Acta Cryst*. A**31**:S211

Petrophysics. (1992) Handbook, vol 1. Nedra, Moscow (in Russian)

Platonova NV, Punin YuO, Franke VD, Ktelnikova EN (1994) Cocrystallization of Cu^{2+} with NH_4Cl by means of anomalous isomorphism. *J. Struct. Chem.* **35**(N 5):70–78 (in Russian)

Pockels F (1906) Lehrbuch der Kristalloptik. Druck und Verlag von Teubner BG, Leipzig und Berlin

Pohl D (1978) Electronic polarizabilities of ions in doubly refracting crystals. *Acta Cryst*. A**34**:574–578

Poirier JP (1985) Creep of crystals: High temperature deformation processes in metals, ceramics and minerals. Cambridge University Press, Cambridge, New York

Pollok K, Jamtveit B, Putnis A (2001) Analytical transmission electron microscopy of oscillatory zoned grandite garnet. *Contrib. Mineral. Petrol*. **141**:358–366

Predvoditelev AA (1975) The modern state of investigations in the field of dislocation ensembles. In: Vainshtein BK, Chernov AA (eds) Problems of modern crystallography. Nauka, Moscow, pp 262–275 (in Russian)

Predvoditelev AA, Tyapunova NA, Zininkova GM, Bushueva GV (1986) Physics of crystals with defects. MGU Press, Moscow (in Russian)

Punin YuO (1987) Formation of autodeforamtion defects in crystal growth from solution. In: Growth of crystals, vol 14. Consultants Bureau, New York, London, pp 121–131

Punin YuO (1989a) Anomalous optics of the layered heterogeneous crystals. *Zapiski Vsesouznogo Mineralogicheskogo Obschestva* 118, N 1, 76–90 (in Russian)

Punin YuO (1989b) Pathology of mineral individuals. *Mineralogical Journal* **11**(N 1):92–98 (in Russian)

Punin YuO (1992) Heterometry stress for the inhomogeneous impurity distribution in crystals. In: Smirnov YuM (ed) Physics of crystallization. TGU Press, Tver, pp 86–98 (in Russian)

Punin YuO (1994) Structure-orientation instability of a growing crystal. *J. Struct. Chem.* **35**(N 5):50–59 (in Russian)

Punin YuO (2000) Effect of the crystal habit on formation of autodeformation defects. *Zapiski Vserossiiskogo Mineralogicheskogo Obschestva* **129**(N 6):1–11 (in Russian)

Punin YuO (2002) Instability of single crystal growth and principle of maximum entropy production. *Zapiski Vserossiiskogo Mineralogicheskogo Obschestva* **131**(N 3):51–61 (in Russian)

Punin YuO, Kotelnikova EN (1983) Polytypism and genetic information. In: New ideas in genetic mineralogy. Nauka, Leningrad pp 54–60 (in Russian)

Punin YuO, Shtukenberg AG (2005) Anomalous crystal optics of heterogeneous crystals. *Crystallography Reports* **50**:297–307

Punin YuO, Zhogoleva VYu (1980) On the growth conditions of potassium ferrocyanide crystallization. *Inorganic Materials* **16**:1785–1788 (in Russian)

Punin YuO, Kotelnikova EN, Frank-Kamenetsky VA (1985a) Layer distortions in crystals of synthetic fluorphlogopite. In: Crystallography and crystal chemistry. vol 5. LGU Press, Leningrad, pp 40–58 (in Russian)

Punin YuO, Kotelnikova EN, Frank-Kamenetsky VA (1985b) X-ray and optical study of layer regularity laws in synthetic fluorphlogopite. In: Crystallography and crystal chemistry. vol 5. LGU Press, Leningrad, pp 78–89 (in Russian)

Punin YuO, Kuzmina MA, Il'inskaya TG (1986) Anomalous biaxiality and dislocations in pentaerythritol crystals. In: Smirnov YuM (ed) Physics of crystallization. KGU Press, Kalinin, pp 53–59 (in Russian)

Punin YuO, Kotelnikova EN, Zhogoleva VYu, Isaeva GP (1982) Disordering, syntaxy and twinning of polytypes for the example of potassium ferrocyanide. In: Crystallography and crystal chemistry. vol 4. LGU Press, Leningrad, pp 6–24 (in Russian)

Punin YuO, Ivanova TI, Kotelnikova EN, Franke VD (1993) On the types of two-dimensional isomorphism co-crystallysation. *Zapiski Vserossiiskogo Mineralogicheskogo Obschestva* **122**(N 1):26–36 (in Russian)

Punin YuO, Kotelnikova EN, Makagonova YuE, Sokolov PB (1997) Heterometry and autodeformation in lithium-aluminum micas. *Zapiski Vserossiiskogo Mineralogicheskogo Obschestva* **126**(N 2):23–36 (in Russian)

Punin YuO, Kotelnikova EN, Sokolov PB, Krezer YuL, Semina EYu (1989) The nature of polytype intergrowths of lithium-aluminum micas. *Zapiski Vsesouznogo Mineralogicheskogo Obschestva* **118**(N 5):1–12 (in Russian)

Putnis A, Angel RJ (1985) Al, Si ordering in cordierite using "magic angle spinning" NMR. *Phys. Chem. Minerals* **12**:217–222

Putnis A, Bish DL (1983) The mechanism and kinetics of Al, Si ordering in Mg-cordierite. *Am. Mineral*. **68**:60–65

Putnis A, McConnell JDC (1980) Principles of mineral behaviour. Blackwell Scientific Publications, Oxford

Rakovan J (2002) Growth and surface properties of apatite. In: Kohn ML, Rakovan J, Hughes JM (eds) Reviews in Mineralogy, vol 48. Washington DC, pp 51–87

Rakovan J, Reeder RJ (1994) Differential incorporation of trace elements and dissymmetrization in apatite: the role of surface structure during growth. *Am. Mineral*. **79**:892–904

Reeder RJ (1992) Carbonates: growth and alteration microstructures. In: Buseck PR (ed) Reviews in Mineralogy, vol 27. Washington DC, pp 381–424

Reis H, Papadopoulos MG, Munn RW (1998) Calculation of macroscopic first-, second-, and third-order optical susceptibilities for the urea crystal. *J. Chem. Phys*. **109**:6828–6838

Reis H, Papadopoulos MG, Hättig C, Angyán J, Munn RW (2000) Distributed first and second order hyperpolarizabilities: An improved calculation of nonlinear optical susceptibilities of molecular crystals. *J. Chem. Phys*. **112**:6161–6172

Report of the Ad interim commission on aperiodic crystals (1992) *Acta Cryst* A**48**:928

Ribbe PH (1980a) Staurolite. In: Ribbe PH (ed) Reviews in mineralogy, vol 5. Washington DC, pp 171–187

Ribbe PH (1980b) Topaz. In: Ribbe PH (ed) Reviews in mineralogy, vol 5. Washington DC, pp 215–230

Ristic RI, Sherwood, Shripathi T (1991) The role of dislocations and mechanical deformation in growth rate dispersion in potash alum crystals. In: Garside J, Davey RJ, Jones AG (eds) Advances in industrial crystallization. Butterworth Heinenmann, Oxford, pp 77–91

Rosenfeld JL (1969) Stress effects around quartz inclusions in almandine and the piezothermometry of coexisting aluminum silicates. *Am. J. Sci*. **267**:317–351

Rossman GR, Aines RD (1986) Birefrigent garnet from Asbestos, Quebec, Canada. *Am. Mineral*. **71**:779–780

Rossmanith E, Armbruster Th (1995) The intensity of forbidden reflections of pyrope: Umweganregung or symmetry reduction? *Z. Kristallogr*. **210**:645–649

Rozhdestvenskaya IV, Frank-Kamenetskaya OV, Shtukenberg AG, Bannova II (2001) Triclinic structure of birefringent crystal of $K(Al_{0.95}Cr_{0.05})(SO_4)_2 \cdot 12H_2O$. *Journal of Structural Chemistry* **42**:628–638

Rudoi KA, Nabatov BV, Stroganov VI, Konstantinova AF, Alekseeva LV, Evdischenko EA, Kidyarov BI (2003) Conoscopic figures of optically active uniaxial crystals. *Crystallography Reports* **48**:300–304

Rumyantsev VN, Novozhilov AI (1980) Dependence of aluminum center concentration and anomalous pleochroism in synthetic quartz on some crystallization parameters. *Sov. Phys. Crystallogr*. **25**:75–78

Saha (1959) Geochemical and x-ray investigation of natural and synthetic analcites. *Am. Mineral*. **44**:303–313

Sakamoto M, Yamada T (1980) Plastic deformation in highly-concentred KCl–KBr solid solution single crystal from 16K to 923 K. Jpn. *J. Appl. Phys*. **19**:1617–1625

Salje E (1991) Strain-related transformation twinning in minerals. *Neues Jahr. Mineralogie Abh*. **163 (**N 1):43–86

Samoilovich MI, Tsinober LI, Khadzhi VE, Lelekova ME (1968) Determining the activation energy of formation of smoky centers in synthetic quartz containing aluminum. *Sov. Phys. Crystallogr*. **13**:734–736

Sapozhnikov AN, Ivanov VG, Levitskii VI, Piskunova LF (1993) Structural-mineralogical features of lazurite from the South-West Pamir. *Zapiski Vserossiiskogo Mineralogicheskogo Obschestva* **122 (**N 1):108–115 (in Russian)

Scandale E, Lucchesi S, Graziani G (1984) Optical anomalies of beryl crystal. *Phys. Chem. Minerals* **11**(N 2):60–66

Scandale E, Lucchesi S, Graziani G (1990) Growth defects and growth marks in pegmatite beryls. *Eur. J. Mineral*. **2**:305–311

Schwandt CS, Cygan RT, Westrich HR (1995) Mg self-diffusion in pyrope garnet. *Am. Mineral*. **80**: 438–490

Schwandt CS, Cygan RT, Westrich HR (1996) Ca self-diffusion in grossular garnet. *Am. Mineral*. **81**:448–451

Seiler P (1992) Measurement of accurate Bragg intensities. In: Domenicano A, Hargittai I (eds) Accurate molecular structures. Their determination and importance. Oxford University Press, Oxford

Sénarmont, H (1854) Experiénces sur la production artificielle du polychroïsme dans less substances crystallisees. *Ann. Chem. Phys.* **3**:319-336

Shafranovskii II (1974) Sketches on mineralogical crystallography. Nedra, Leningrad (in Russian)

Shafranovskii II, Mikheev VI, Mokievsky VA (1952) On the problem of eichenwaldite existing inside eremeyevite. *Zapiski Vsesouznogo Mineralogicheskogo Obschestva* (N 1):28–40 (in Russian)

Shamburov VA, Kucherova IV (1966) Variation in anomalous birefringence in crystals of KH_2PO_4. *Sov. Phys. Crystallogr*. **10**:558–560

Shannon RD (1976) Revised effective ionic radii and systematic studies of interatomic distances in halides and chalcogenides. *Acta Cryst*. A**32**:751–767

Sherwood JN, Ristic R, Wojciechowski K (1993) Morphology and growth kinetics of large sodium chlorate crystals grown in the presence and absence of sodium dithionate impurity. *J. Phys. Chem*. **97**:10774–10782

Sherwood JN, Ristic R, Shevunov BYu (1994) Growth of the tetrahedral faces of sodium chlorate crystals in the presence of dithionate impurity. *J. Cryst. Growth* **139**:336–343

Shimon LJW, Vaida M, Frolow F, Lahav M, Leiserowitz L, Weissinger-Lewin Y, McMullan RK (1993) Symmetry lowering in crystalline solid solutions: A study of cinnamanide-thienylacrylamide by X-ray and neutron diffraction and solid state photochemistry. *Faraday Discussions* **95**:307–327

Shinoda K, Aikawa N (1994a) Polarized IR spectra of optically anomalous topaz under FITR spectroscopy. Abstracts 16th general meeting international mineralogical association, 4–9 September, 1994, Pisa, Italy, pp 373–374

Shinoda K, Aikawa N (1994b) The orientation of the OH-dipole in an optically anisotropic crystal: An application to the OH-dipole in topaz. *Phys. Chem. Minerals* **21**:21–24

Shmelev GG, Bobr-Sergeev AA (1970) On the conoscopic figures and 2*Vs* in micas. Ezhegodnik-69 Sibirskogo Instituta Geochimii, Irkutsk, pp 251–254 (in Russian)

Shternberg AA (1962) Heterometry: the relation of morphology to cracking in crystals containing impurities. *Sov. Phys. Crystallogr*. **7**:92–96

Shtukenberg AG (1997) Optical anomalies in crystals of inorganic solid solutions. Dissertation, St. Petersburg (in Russian)

Shtukenberg AG (2005) Metastability of atomic ordering in lead–strontium nitrate solid solutions. *J. Sol. State Chem*. **178**:2608–2612

Shtukenberg AG, Punin YuO (1996) Optical anomalies in crystals *Zapiski Vserossiiskogo Mineralogicheskogo Obschestva* **125**(N 4):104–120 (in Russian)

Shtukenberg AG, Punin YuO (2003) Trend of anomalous birefringence in alum crystals: a new effect of the growth ordering phenomenon. *Neues Jahr. Mineralogie Mh.* (N 6):241–253

Shtukenberg AG, Punin YuO (2004) Optical anomalies in crystals. Nauka, St.Petersburg (in Russian)

Shtukenberg AG, Punin YuO, Kotelnikova EN, Sukharzhevsky SM (1994a) Anomalous crystal optics of isomorphous-mixed crystals. Bulletin of SPbGU. Ser 4, Part 2, N 11, pp 109–110 (in Russian)

Shtukenberg AG, Punin YuO, Kotelnikova EN, Sukharzhevsky SM (1994b) Optical dissymmetrization of crystals and inhomogeneity in distribution of isomorphous components. *J. Struct. Chem.* **35**(N 5): 60–69 (in Russian)

Shtukenberg AG, Soloviev VN, Punin YuO (1994c) Anomalous birefringence in crystals of isomorphous series of alums. In: Smirnov YuM (ed) Physics of Crystallization. TGU Press, Tver, pp 76–81 (in Russian)

Shtukenberg AG, Punin YuO, Kovalev OG (1998) Temperature behavior of optical anomalies in alum crystals. *Crystallography Reports* **43**:465–468

Shtukenberg AG, Punin YuO, Soloviev VN (2000a) Effect of growth conditions on the birefringence of mixed crystals revealed in alum solid solutions. *Mineral. Mag*. **64**:837–845

Shtukenberg AG, Rozhdestvenskaya IV, Frank-Kamenetskaya OV, Bannova II, Kulakova SV, Ivanova TI, Punin YuO (2000b) Dissymmetrization of crystal structures of alum with anomalous birefringence. *Crystallography Reports* **45**:919–925

Shtukenberg AG, Punin YuO, Frank-Kamenetskaya OV, Kovalev OG and Sokolov PB (2001a) On the origin of anomalous birefringence in grandite garnets. *Mineral. Mag*. **65**:445–459

Shtukenberg AG, Punin YuO, Haegele E, Klapper H (2001b) On the origin of inhomogeneity of anomalous birefringence in mixed crystals: an example of alums. *Phys. Chem. Minerals* **28**:665–674

Shtukenberg AG, Popov DYu, Punin YuO (2002) An application of the point-dipole model to the problem of optical anomalies in grandite garnets. *Mineral. Mag*. **66**:275–286

Shtukenberg AG, Rozhdestvenskaya IV, Popov DYu, Punin YuO (2004) Kinetic ordering of atoms in sodium chlorate-bromate solid solutions. *J. Sol. State Chem*. **177**:4732–4742

Shtukenberg AG, Popov DYu, Punin YuO (2005) Growth ordering and anomalous birefringence in ugrandite garnets. *Mineral. Mag*. **69**:537–550

Shtukenberg AG, Euler H, Kirfel A, Popov DYu (2006a) Symmetry reduction and cation ordering in solid solutions of strontium-lead and barium-lead nitrates. *Z. Kristallogr*. **221**:681–688

Shtukenberg AG, Punin YuO, Frank-Kamenetskaya OV (2006b) Kinetic ordering of atoms and growth dissymmetrization in crystalline solid solutions. *Russian Chem. Rev*. (in press)

Shubnikov AV (1960) Principals of optical crystallography. Consultants Bureau, New York

Shubnikov AV (1961) Symmetry and physical properties of growth pyramids. *Sov. Phys. Crystallogr*. **6**:319–322

Shubnikov AV (1988) On the woks of Pierre Curie on symmetry. *Computational Mathematics and Applications* **16**:357–364

Shubnikov AV, Kopstik VA (1974) Symmetry in science and art (Archard GD trans, and Harker D ed). Plenum Press, New York

Shuvalov L (2005) Modern crystallography, vol 4. physical properties of crystals. Springer

Sirotin YuI (1956) Temperature stress resulting from the heating and cooling of crystals. *Sov. Phys. Crystallogr.* **1**:555–562

Sirotin I, Shaskolskaya MP (1982) Fundamentals of crystal physics. Mir Publishers, Moscow

Slavnova EN (1956) Characteristics of interaction of organic dyes with the faces of isomorphous nitrate crystals. *Dokl. Akad. Nauk SSSR (English Translation)* **107**:693–696

Slavnova EN (1958) New data on the interactions of organic impurities with inorganic crystals. Growth of crystals, Reports of the first conference on crystal growth. Consultants Bureau, New York, pp 117–125

Slavnova EN (1959a) The main trends in the study of inorganic crystals containing organic impurities. Growth of crystals, vol 2. Consultants Bureau, New York, pp 32–35

Slavnova EN (1959b) The adsorption of thionin blue by growing lead nitrate crystals, and the effects on the morphology of the crystals. Growth of crystals, vol 2. Consultants Bureau, New York, pp 121–131

Slavnova EN (1960) Effect of concentration of thionine blue on its adsorption from aqueous solutions by growing crystals of lead nitrate. *Sov. Phys. Crystallogr*. **5**:81–87

Smirnov YuM, Alyavdin VF, Onischina NM, Abakumova NB (1982) Sector zoning of CMN single crystals. In: Smirnov YuM (ed) Physics of crystallization. KGU Press, Kalinin, pp 73–77 (in Russian)

Smith JV (1974) Feldspar minerals. I. Crystal structure and physical properties. Springer, Heidelberg, New York

Sokolov PB, Punin YuO, Kotelnikova EN, Krezer YuL, Predtechenskii NN (1987) Lithium-aluminum micas from rare-metal pegmatites. *Mineral. J*. **9**(N 1):55–63 (in Russian)

Sokolov VI (1953) Optical characteristics of minerals: Interference figures of micas (reissue). In: ES Fedorov universal stage. Akad. Nauk SSSR, Moscow, pp 394–408 (in Russian)

Speer JA (1980) Zircon. In: Ribbe PH (ed) Reviews in mineralogy, vol 5. Washington DC, pp 67–112

Starkov NP (1950) Optically anomalous garnets from the Saroba mountain, south Ural. *Zapiski Vsesouznogo Mineralogicheskogo Obschestva* (N 4):283–290 (in Russian)

Stepanova NS (1970) Method of concentration convection and its application to growth of KDP crystals. Dissertation, Gorkii (in Russian)

Stepanova NS, Belyustin AV (1975) Cracking of potassium dihydrophosphate crystals containing colloid inclusions. *Inorganic Materials* **11**:1457–1460 (in Russian)

Stepanov VI, Moleva VA (1962) On ralstonite from Ilmen mountains, Kazakhstan and Kamchtka. *Zapiski Vsesouznogo Mineralogicheskogo Obschestva* **2**(N 5):556–572 (in Russian)

Stoiber RE, Morse SA (1974) Crystal indentification with the polarizing microscope. Chapman and Hall, New York, London

Stose GW, Glass JJ (1938) Garnet crystals in cavities in metamorphosed Triassic conglomerate in York Country, Pennsylvania. *Am. Mineral*. **23**:430–435

Steuer W (2004) Twenty years of structure research on quasicrystals. Part 1. Pentagonal, octagonal, decagonal, and dodecagonal quasicrystals. *Z. Kristallogr*. **219**:391–446

Strunz H, Wilk H (1974) Jeremejewit als Edelstein aus SW-Afrika. *Z. Dutsch. Gemmol. Ges.* **23** (N 2):142–150

Sunagawa I (2005) Growth, morphology and perfection. Cambridge University Press, Cambridge

Sunagawa I, Urano A (1999) Beryl crystals from pegmatites: morphology and mechanism of crystal growth. *J. Gemmol*. **26**:521–533

Suvorova EI, Chernov AA (1994) Anomalous biaxiality and orthorhombic inclusions in KDP crystals. *Crystallography Reports* **39**:827–833

Takano J, Takano K (1959) The relation between optical anomaly and crystal structure. *J. Geol. Soc*. Japan **65**:236–247

Takéuchi Y, Haga N (1976) Optical anomaly and structure of silicate garnets. *Proc. Japan Acad*. **52**:228–231

Takéuchi Y, Haga N, Umizu S, Sato G (1982) The derivative structure of silicate garnets in grandite. *Z. Kristallogr*. **158**:53–99

Tammann G (1917) Die anomalie Molekülverteilung in Mischkristallen als Ursache ihrer anomalen Doppelbrechung. *Nachrichten der Gesellschaft Wissschaften in Göttingen Mathematisch. Physikalische Klasse* **2**:226–235

Tanaka T, Akizuki M, Kudoh Y (2002a) Optical properties and crystal structure of triclinic growth sectors in vesuvianite. *Mineral. Mag*. **66**:261–274

Tanaka T, Kimura R, Akizuki M, Kudoh Y (2002b) Origin of low-symmetry growth sectors in edingtonite and yugawaralite, and crystal structure of the k{110} and v{120} sectors of yugawaralite. *Mineral. Mag*. **66**:409–420

Tatarsky VB (1965) Crystal optics and the immersion method. Nedra, Moscow (in Russian)

The Encyclopedia of mineralogy. (1981) Frye K (ed) Hutchinson Ross Publishing Company, Stroudsburg, Pennsylvania

Timoshenko S, Goodier JN (1982) Theory of elasticity. McGraw Hill, Singapore

Toyoda M, Niizeki N, Waku S (1960) Optical and structural anomalies in potassium ferrocyanide trihydrate crystals. *J. Phys. Soc. Jap*. **15**:1831–1841

Treivus EB (1979) Kinetics of crystal growth and dissolution. LGU Press, Leningrad (in Russian)

Treivus EB (1987) Effect of the temperature and supersaturation on the growth of the main faces of sodium bromate and potassium nitrate. *Vestnik LGU,* Ser 7, **1**(N 7):17–23 (in Russian)

Tröger WE, Bambauer HU, Taborszky F, Trochim HD (1979) Optical determination of rock-forming minerals. E Schweizerbart'sche Verlagbuchhandlung, Stuttgart

Tschermak G (1884) Handbook of mineralogy. Imperator. Akad. Nauk, St. Petersburg (in Russian)

Tsinober LI (1962) A feature of the pleochroism of colored synthetic quartz. *Sov. Phys. Crystallogr*. **7**:113–114

Tsinober LI, Samoilovich MI (1975) Distribution of structural defects and anomalous optical symmetry in quartz crystals. In: Vainshtein BK, Chernov AA (eds) Problems of modern crystallography. Nauka, Moscow, pp 207–218 (in Russian)

Tsinober LI, Samoilovich MI, Demina TV, Bobr-Sergeev AA (1977) Effect of the symmetry of the faces on the structural ordering of aluminum in cordierite crystals. *Sov. Phys. Crystallogr*. **22**:200–202

Tsinober LI, Samoilovich MI, Gordienko LA, Chentsova LG (1967a) Anomalous pleochroism in synthetic smoky quartz crystals. *Sov. Phys. Crystallogr*. **12**:53–56

Tsinober LI, Samoilovich MI, Khadzhy VE, Lelekova MV (1967b) Effect of anomalous pleochroism on the quartz crystallization temperature. *Dokl. Akad. Nauk SSSR* **176**(N 3):676–678 (in Russian)

Turner FJ (1975a) Biaxial calcite: occurrence, optics and associated minor strain phenomena. *Contrib. Mineral. Petrol*. **50**:247–255

Turner FJ (1975b) Biaxiality in relation to visible twinning in experimentally deformed calcite. *Contrib. Mineral. Petrol*. **53**:241–252

Urusovskaya AA (1962) Formation of fields with lattice re-orientation during deformation of single and polycrystals. In: Klassen-Necludova MV (ed) Stress and dislocations in crystals. VINITI publisher, Moscow, pp 75–116 (in Russian)

US Bureau of Mines. Dictionary of mining, mineral, and related terms (1997) American Geological Institute, Alexandria, Virginia

Vaida M, Shimon LJW, Weisinger-Lewin Y, Frolow F, Lahav M, Leiserowitz L, McMullan RK (1988) The structure and symmetry of crystalline solid solutions. *Science* **241**:1475–1479

Vainshtein BK, Fridkin VM, Indenbom VL (1982) Modern crystallography II: Structure of crystals. Springer Verlag, Berlin

Van Enckvort WJP (1982) Verification of crystal growth models by detailed surface microtopography and X-ray diffraction topography. Dissertation, Nijmegen

Van Enckevort WJP, Van Der Linden WH (1979) On the relation between etch pits or growth hillocks and dislocations on the (111) faces of potassium aluminium alum. *J. Cryst. Growth* **47**:196–202

Vardanyants LA (1941) The problem of optical biaxiality of uniaxial minerals. *Zapiski Vsesouznogo Mineralogicheskogo Obschestva* N **1**:16–22 (in Russian)

Varshavsky AV (1968) Anomalous birefringence and inner morphology of diamond. Nauka, Moscow (in Russian)

Vasbutskii GL (1941) The natural change of color and some other cassiterite properties. *Zapiski Vsesouznogo Mineralogicheskogo Obschestva Ser 2*, **70**(N 2):185–224 (in Russian)

Vedeneeva NE, Slavnova EN (1952) Spectrophotometric investigation of stained nitrates and of crystals of pure dyes. *Trans. Inst. Cryst. Acad. Sci*. USSR **7**:135–158

Vergasova LP, Semenova TF, Epifanova VB, Filatov SK, Chubarov VM (2004) Meniaylovite $Ca_4AlSi(SO_4)F_{13} \cdot 12H_2O$ – a new mineral in volcanic exhalations. *Vulcanology and Seismology* (N 2):3–8 (in Russian)

Vinokurov VM, Bulka GR, Nizamutdinov NM, Khasanova NM (1977) Autonomic tangential selectivity during the crystal growth. *Dokl. Akad. Nauk SSSR* **237**:1388–1391 (in Russain)

Vladimirov VI, Romanov AE (1986) Disclinations in crystals. Nauka, Leningrad (in Russian)

Voigt W (1910) Lehrbuch der Kristallphysik. Teubner, Leipzig

Walther JV, Wood BJ (1986) Mineral-fluid reaction rates. In: Walther JV and Wood BJ (eds) Fluid-rock interactions during metamorphism. *Advances in Physical Geochemistry*, vol 5. Springer, Berlin, pp 194–211

Weissbuch I, Addadi L, Lahav M, Leiserowitz L (1991) Molecular recognition at crystal interfaces. *Science* **253**:637–645

Weissbuch I, Lahav M, Leiserowitz L, Meredith GR, Vanherzeele H (1989) Centrosymmetric crystals as host matrices for second-order nonlinear effects. *Chemistry of Materials* **1**:114–118

Wildner M, Andrut M (2001) The crystal chemistry of birefringent natural uvarovites: Part II. Single-crystal X-ray structures. *Am. Mineral*. **86**:1231–1251

Winchell AN, Winchell H (1951) Elements of optical mineralogy. John Wiley and Sons, New York

Winchell AN, Winchell H (1964) The microscopical characters of artificial inorganic solid substances: optical properties of artificial minerals. Academic Press, New York, London

Wood BJ, Walther JV (1983) Rates of hydrothermal reactions. *Science* **222**:413–415

Yasuhiro O, Tomoyuki H, Takuro I (1987) Phase transitions in mixed crystal system $K_{1-x}(NH_4)_xH_2PO_4$. *J. Phys. Soc*. Japan **56**:577–602

Yoder HSJr (1950) Stability relations of grossularite. *J. Geol.* **58**:221–253

Yushkin NP, Shafranovskii II, Yanulov KP (1987) Principals of symmetry in mineralogy. Nauka, Leningrad (in Russian)

Zakharchenko TA (1976) Calculation of refractive indices and polarizabilities for the crystal of $K_2Cu(SO_4)_2 \cdot 6H_2O$. In: Vinokurov VM (ed) Physical properties of minerals and rock. KGU Press, Kazan, pp 97–103 (in Russian)

Zavariyskii AN (1953) On the optical study of minerals in convergent polarized light. In: Fedorov ES, Universal Stage Akad. Nauk SSSR Press, Moscow, pp 456–505 (in Russian)

Zemyatchensky PA (1900) Emerald and beryl of Ural emerald mines. *Trudi Imperatorskogo SPb Obschestva Estestvoispitatelei* **29**(N 5):1–20 (in Russian)

Zilbershtein AKh (1990) Optical properties of deformed minerals and thermobarometry. Nedra, Moscow (in Russian)

Zilbershtein AKh, Yanan Bao, Shafranovsky GI (1995) New polarization-optical method for the estimation of growth temperature and pressure of inhomogeneous crystals (demonstrated on the example of diamond with olivine inclusion). *Optics and Spectroscopy* **78**:802–807 (in Russian)

Zilbershtein AKh, Shebanov AD, Larin AM (1996) Polarization-optical method for the estimation of the formation temperature of polycrystalline aggregates (on the example of natural rapakivi granite). *Solid State Spectroscopy* **80**:238–241 (in Russian)

Zolotarev AA, Dyhuraev ZT, Pekov IV, Mikhailova KV (2000) Eremeevite from pegmatite veins of east Pamir. *Zapiski Vserossiiskogo Mineralogicheskogo Obschestva* **129**(N 2):64–70

APPENDICES

APPENDIX 1: NOMENCLATURE OF SOME MINERALS FREQUENTLY CITED IN THIS WORK.

Garnet Nomenclature

The garnet minerals with the general formula $A_3Y_2(SiO_4)_3$ are neosilicates, that is they have isolated SiO_4 tetrahedra connected by interstitial cations including calcium, magnesium, aluminium, iron(II), iron (III), chromium, manganese, titanium and some others. The most abundant garnets are classified according their chemical composition as pyrope ($Mg_3Al_2(SiO_4)_3$), almandine ($Fe_3Al_2(SiO_4)_3$), spessartite ($Mn_3Al_2(SiO_4)_3$), grossular ($Ca_3Al_2(SiO_4)_3$), andradite ($Ca_3Fe_2(SiO_4)_3$), and uvarovite ($Ca_3Cr_2(SiO_4)_3$). The garnets make up two main solid solution series, the pyralspites (pyrope-almandine-spessarite) and the ugrandites (uvarovite-grossularite-andradite). Pyralspites have Al in the Y site. Ugrandites have calcium in the A site. Partial substitution of SiO_4^{4-} anion by $4OH^-$ groups results in formation of hydrogarnets.

Mica Nomenclature

Micas are phyllosilicates (layered silicates). Typically, they are composed of one octahedral silicate sheet between two tetrahedral silicate sheets. These sandwiches are separated by cations, most commonly K, Na, Ca. The tetrahedral sheet contains most commonly Si, Al, and Fe^{3+} coordinated to four oxygens in which three out of the four are shared between neighboring cations. The octahedral sheets most commonly contain Li, Fe^{2+}, Fe^{3+}, Mg, Al, Ti that are coordinated to six oxygens, although some of the sites are typically occupied by anions such as OH or F. Octahedra share edges.

Mica polytypes are typically referred to by a code of the general form NS_a, where:

N = number of layers in the unit cell;

S = symmetry of the polytpe (T = trigonal, M = monoclinic, Tr = tetragonal *etc.*);

a = number of different possible sub-arrangements.

In Chapter 4, we most often consider monoclinic micas referred to by the following symbols:

$1M$: single layer with an $a/3$ shift (e.g. synthetic fluorphlogopite $Mg_3K(AlF_2O(SiO_3)_3)$.

$2M_1$: $+120°$ rotation followed by a $-120°$ rotation making a two-layer monoclinic unit cell (e.g. muscovite $KAl_2(AlSi_3O_{10})(F, OH)_2$).

$2M_2$: $+60°$ rotation followed by a $-60°$ rotation making a two-layer monoclinic unit cell. (e.g. lepidolite $KLi_2Al(Al, Si)_3O_{10}(F, OH)_2$).

APPENDIX 2. OPTICAL ANOMALIES (OA) IN NATURAL AND SYNTHETIC CRYSTALS.

Table P2.1. Optical anomalies in cubic crystals

N	Compound, crystal class, system		Δn_{max}	Sources of OA				Reference
a	*b*	*c*	*d*	1	2	3	4	*e*
1	Alkali halogenides, KCl, KBr, NaCl, KI, LiF *etc.*, $m\bar{3}m$	SN	>0		III			(Brauns, 1891; Mendelson, 1961; Vainshtein *et al.*, 1982; Sakamoto and Yamada, 1980; Shuvalov, 2005)
2	Alum $(K(Al, Cr)(SO_4)_2 \cdot 12H_2O$, $(K, NH_4)Al(SO_4)_2 \cdot 12H_2O$ among others), $m\bar{3}$	S	0.0001	III	III	III		(Brauns, 1891; Van Enckevort, 1982; Shtukenberg *et al.*, 1994b; 1998; 2000; 2001b*)
3	Ammounim chloride (pure and impure), NH_4Cl, 432	S	>0	I	III		III	(Punin *et al.*, 1993; Platonova *et al.*, 1994)
4	Analcime, $NaAlSi_2O_6 \cdot H_2O$, $m\bar{3}m$	N	>0			II		(Náray-Szabó, 1938; Saha, 1959; Takano and Takano, 1959; Mazzi and Galli, 1978; Akizuki, 1981b)
5	Chukhrovite, $Ca_3(Y, Ce)Al_2(SO_4)F_{13}) \cdot 10H_2O$, $m\bar{3}$	N	>0			I		(Ermilova *et al.*, 1960)
6	Diamond, C, $m\bar{3}m$	N	0.0001		III			(Varshavsky, 1968; Orlov and Tatjanina, 1973*; Frank *et al.*, 1990; Beskrovanov, 1992; Zilbershtein *et al.*, 1995)
7	Eulitite, $Bi_4Si_3O_{12}$, cub.	N	>0					(Brauns, 1891)
8	Faujasite, $Na_2Ca(Al_2Si_5O_{14}) \cdot 6.6H_2O$, $m\bar{3}m$	N	>0					(Brauns, 1891)
9	Fluorite, CaF_2, $m\bar{3}m$	NS	$4.5 \cdot 10^{-6}$		III			(Lodochnikov, 1930; Dressler, 1986a,b; Cheredov, 1993)

(Continued)

Table P2.1. (Continued)

N	Compound, crystal class, system		Δn_{max}	Sources of OA				Reference
a	*b*	*c*	*d*	1	2	3	4	*e*
10	Garnets, $m\bar{3}m$:							
	Grossular-hydrogrossular, $Ca_3Al_2(SiO_4, (OH)_4)_3$	N	0.0001			II		(Akizuki, 1989)
	Pyralspites, $(Ca, Fe, Mg, Mn)_3Al_2(SiO_4)_3$	N	0.001	I	II			(Griffen *et al.*, 1992; Hofmeister *et al.*, 1998*)
	Synthetic garnets, $Y_3Al_5O_{12}$, $(Y, Nd)_3Ga_5O_{12}$, $Ca_{3-x}Nd_xGa_{2+x}Ge_{3-x}O_{12}$ *etc.*	S	>0	I	III	II		(Chase and Lefever, 1960; Nikitenko and Osip'yan, 1975; Kitamura and Komatsu, 1978; Balestrino *et al.*, 1986; Kitamura *et al.*, 1986a,b; Mill and Butashin, 1986; Ge *et al.*, 1993)
	Ugrandites, $Ca_3(Al, Fe, Cr, V)_2(SiO_4)_3$	NS	0.02	III	III	III		(Brauns, 1891; Akizuki, 1984; McAloon and Hofmeister, 1993*; Andrut and Wildner, 2001*; Wildner and Andrut, 2001*; Shtukenberg *et al.*, 2001a*; 2002; 2005, this work) #
11	Germanium, Ge, $m\bar{3}m$	S	>0	III	III			(Nikitenko and Indenbom, 1962)
12	Haüyne, $(Na, Ca)_{4-8}Al_6Si_6O_{24}(SO_4, S)_{1-2}$, $m\bar{3}m$	N	>0					(Brauns, 1891)
13	Meniaylovite, $Ca_4AlSi(SO_4)F_{13} \cdot 12H_2O$, $m\bar{3}$	N	>0			I		(Vergasova *et al.*, 2004)
14	Nitrates $(Pb, Ba, Sr)(NO_3)_2$, 23	S	0.002		III	III		(Brauns, 1891; Maiwa *et al.*, 1990; Ge *et al.*, 1993; Gopalan and Kahr, 1993; Shtukenberg, 2005; Shtukenberg *et al.*, 2006a)

15	Pharmacosiderite, $KFe_4(AsO_4)_3(OH)_4 \cdot (6–7)H_2O$, $m\bar{3}m$	N	>0				(Brauns, 1891)
16	Pollucite, $Cs_xNa_{1-x}AlSi_2O_6 \cdot (1-x)H_2O$, $m\bar{3}m$	N	>0			I	(Frank-Kamenetskaya *et al.*, 1995)
17	Ralstonite, $Na_xMg_xAl_{2-x}(OH, F)_6 \cdot H_2O$, $m\bar{3}m$	N	0.0002			I	(Brauns, 1891; Stepanov and Moleva, 1962; Minerals, 1972)
18	Rhodizite, $CsAl_4Be_4B_{11}O_{25}(OH)_4$, $\bar{4}3m$	N	>0				(Brauns, 1891)
19	Senarmontite, Sb_2O_3, $m\bar{3}m$	N	>0				(Brauns, 1891)
20	Silver chloride, AgCl, $m\bar{3}m$	S	>0		III		(Nye, 1949)
21	Silicon, Si, $m\bar{3}m$	S	0.00001	III	III		(Nikitenko, 1966; Vainshtein *et al.*, 1982; Indenbom *et al.*, 1962; Indenbom and Nikitenko, 1962)
22	Sodalite (nosean, lazurite), $Na_4Al_3Si_3O_{12}Cl$, $m\bar{3}m$	N	>0				(Brauns, 1891; Lodochnikov, 1930; Sapozhnikov *et al.*, 1993)
23	Sodium chlorate-bromate, $Na(ClO_3, BrO_3)$, 23	S	0.02		II	III	(Brauns, 1891; Gopalan *et al*, 1993; Crundwell *et al.*, 1997; Shtukenberg *et al.*, 2004, this work)
24	Sphalerite, ZnS, $m\bar{3}m$	N	>0		III		(Brauns, 1891)
25	Spinel, $MgAl_2O_4$, $m\bar{3}m$	SN	>0	III	I		(Malinin *et al.*, 1973)
26	Strontium titanate, $SrTiO_3$, $m\bar{3}m$	S	0.0001		I	II	(Konstantinova *et al.*, 1993)
27	Zunyite, $Al_{13}Si_5O_{20}(OH, F)_{18}Cl$, $m\bar{3}m$	N	0.005				(Minerals, 1972)

Table P2.2. Optical anomalies in trigonal, tetragonal and hexagonal crystals

N	Compound, crystal class, crystal system		$2V_{max}$, deg.	Sources of OA				Reference
a	*b*	*c*	*d*	1	2	3	4	*e*
1	Anatase, TiO_2, $4/mmm$	N	>0					(Deer *et al.*, 1992)
2	Apatite, $Ca_5(PO_4)_3(OH, F)$, $6/m$	N	44	I		II		(Brauns, 1891; Vardanyants, 1941; Takano and Takano, 1959; Foord and Mills, 1978; Hughes *et al.*, 1991a,b; Rakovan and Reeder, 1994; Akizuki *et al.*, 1994; Rakovan, 2002)
3	Apophyllite, $KCa_4(Si_4O_{10})_2(F, OH) \cdot 8H_2O$, $4/mmm$	N	88			II		(Brauns, 1891; Akizuki and Konno, 1985; Akizuki and Terada, 1998; Kahr and McBride, 1992)
4	Autunite, $Ca(UO_2)_2(PO_4)_2 \cdot (10–12)H_2O$, $4/mmm$	N	>0					(Brauns, 1891; Takano and Takano, 1959)
5	Benzil, $(C_6H_5C(O)-)_2$	S	>0					(Klapper, 1971; Kahr and McBride, 1992)
6	Beryl, $Be_3Al_2Si_6O_{18}$, $6/mmm$	N	26	II				(Karnojitzky, 1891b; Brauns, 1891; Ikornikova, 1939; Foord and Mills, 1978; Scandale *et al.*, 1984, 1990; Graziani *et al.*, 1990; Kuznetsov and Chzhao-Lin Li, 1960; Sunagawa and Urano, 1999, this work)
7	Brucite, $Mg(OH)_2$, $\bar{3}m$	N	4.5					(Brauns, 1891)
8	Calcite, $CaCO_3$, $\bar{\bar{3}}m$	NS	50		I	I	III	(Brauns, 1891; Boettcher and Wyllie, 1967; Turner, 1975a,b; Hauser and Wenk, 1976; Foord and Mills, 1978)
9	Carbamide (urea, $CO(NH_2)_2$), $\bar{4}$	S	40				III	(Franke *et al.*, 1987; Punin, 1989a; Punin *et al.*, 1993)

10	Cassiterite, SnO_2, $\bar{4}/mmm$	N	38	II			(Gotman, 1939; Vasbutskii, 1941; Vardanyants, 1941; Babkin, 1960)
11	Cerite, $(Ce, Ca)_9(Mg, Fe)Si_7(O, OH, F)_{28}$, $\bar{3}m$ or $3m$	N	25				(Minerals, 1972)
12	Cesium tartrate, 32	S	>0				(Kahr and McBride, 1992)
13	Chabazite (including herschelite, phacolite), $Ca_2Al_4Si_8O_{24} \cdot 13H_2O$, $\bar{3}m$	N	85			II	(Brauns, 1891; Akizuki, 1981c; Akizuki and Konno, 1987; Akizuki *et al.*, 1989)
14	Cinchonamine, trig.	S	>0				(Kahr and McBride, 1992)
15	Cordierite, $Mg_2Al_3(AlSi_5O_{18})$, $6/mmm$	SN	90	II		III	(Tsinober *et al.*, 1977; Demina, 1980a,b, 1990; Carpenter and Putnis, 1985; Demina and Afonina, 1994; Demina and Mikhailov, 2000, 2001; Demina *et al.*, 2003; Pecherskaya *et al.*, 2003)
16	Corundum, Al_2O_3, $\bar{3}m$	SN	30	III	III		(Brauns, 1891; Ikornikova and Tomilovskii, 1953; Klassen-Nekludova, 1953; Indenbom and Tomilovskii, 1957a,b, 1958)
17	Deoxypentaerythritol, $\bar{4}$	S	>0			II	(Kahr and McBride, 1992; Carter, 1991)
18	Di(11-bromoundecanoyl) peroxide, 422	S	>0			II	(McBride and Bertman, 1989; Kahr and McBride, 1992)
19	Dioptase, $Cu_6(Si_6O_{18}) \cdot 6H_2O$, $\bar{3}$	N	>0				(Karnojitzky, 1891c)
20	Edingtonite, $BaAl_2Si_3O_{10} \cdot 4H_2O$, $\bar{4}2m$	N	54			II	(Akizuki, 1986; Tanaka *et al.*, 2002b)
21	Eremeyevite, $Al_6(BO_3)_5(OH)_3$, $6mm$	N	35	I			(Shafranovskii *et al.*, 1952; Strunz and Wilk, 1974; Foord and Mills, 1978; Anan'ev and Konovalenko, 1984; Zolotarev *et al.*, 2000)

(Continued)

Table P2.2. (Continued)

N	Compound, crystal class, crystal system		$2V_{max}$, deg.	Sources of OA				Reference
a	*b*	*c*	*d*	1	2	3	4	*e*
22	Eudialite, $Na_4(Ca, Ce, Fe, Mn)_2ZrSi_6O_{17}(OH, Cl)_2$, $3m$	N	>0					(Brauns, 1891)
23	Guanidinium carbonate, 422	S	>0					(Kahr and McBride, 1992)
24	Hematolite, $(Mn, Mg, Al)_{15}(OH)_{23}(AsO_4)_2(AsO_3)$, 3	N	>0					(Brauns, 1891)
25	Ice, H_2O, $6/mmm$	NS	>0					(Brauns, 1891)
26	Kleinite, $Hg_2N(Cl, SO_4)\cdot nH_2O$, $6/mmm$	N	85	I				(Minerals, 1972; Foord and Mills, 1978)
27	Lithium niobate, $LiNbO_3$, $3m$	S	>0		II			(Franko *et al*., 2004)
28	Lycopodine-hydrochloride $\cdot 6H_2O$, trig.	S	>0					(Kahr and McBride, 1992)
29	Magnesite $MgCO_3$, $\bar{3}m$	N	>0				III	(Brauns, 1891)
30	Milarite, $K_2Ca_4Be_4Al_2Si_{24}O_{60}\cdot H_2O$, $6/mmm$	N	>0					(Brauns, 1891; Takano and Takano, 1959; Chistiakova *et al*., 1964)
31	Nepheline, $Na_3K(AlSiO_4)_4$, 6	N	>0					(Vardanyants, 1941)
32	Osumilite, $(K, Na)_2(Fe, Mg)_4(Al, Fe)_3Si_{24}O_{60}\cdot 2H_2O$, $6/mmm$	N	40			I		(Goldman and Rossman, 1978; Armbruster and Oberhansli, 1988)
33	Paratellurite, TeO_2, 422	S	1.3	I				(Kolesnikov, 1983, 1996)
34	Pentaerythritol, $C(CH_2OH)_4$, $4mm$	S	8	III		II		(Punin *et al*., 1986; Punin, 1992; Kahr and McBride, 1992)

35	Potassium and ammonium dihydrophospate (including solid solutions), $(K, NH_4)H_2PO_4$, $\bar{4}2m$	S	1.5 up to 4	III	III			(Shamburov and Kucherova, 1966; Belyustin *et al.*, 1970; Stepanova, 1970; Fridman, 1972; Leonova and Beskolova, 1977; Pakhomova *et al.*, 1978; Belyustin and Stepanova, 1981; Suvorova and Chernov, 1994; Shtukenberg *et al.*, 1994a,b)
36	Potassium ferrocyanide (yellow prussiate), $K_4Fe(CN)_6 \cdot 3H_2O$, $4/m$	S	102				III	(Toyoda *et al.*, 1960; Punin and Zhogoleva, 1980; Punin, 1987; Punin and Kotelnikova, 1983; Punin, 1989a; Kotelnikova *et al.*, 1989)
37	Quartz, SiO_2, 32	NS	25	II	II	III		(Brauns, 1891; Lodochnikov, 1930; Barry and Moore, 1964; Barry *et al.*, 1965; Tsinober *et al.*, 1967; Samoilovich *et al.*, 1968; Tsinober and Samoilovich, 1975; Tsinober *et al.*, 1977)
38	Rutile, TiO_2, $4/mmm$	N	20				I	(Brauns, 1891; Foord and Mills, 1978)
39	Scheelite, $CaWO_4$, $4/m$	N	>0					(Brauns, 1891)
40	Siderite, $FeCO_3$, $\bar{3}m$	N	>0					(Brauns, 1891)
41	Smithsonite, $ZnCO_3$, $\bar{3}m$	N	>0				III	(Brauns, 1891)
42	Strychnine sulfate $\cdot 6H_2O$, tetr.	S	>0					(Kahr and McBride, 1992)
43	Thorite, $ThSiO_4$, $4/mmm$	N	6	I				(Minerals, 1972)
44	Tourmaline, $(Na, Ca)(Al, Li, Mg, Fe)_3$ $Al_6(Si_6O_{18})(BO_3)_3$ $(OH, O)_3(OH, F)$, $3m$	N	30	III		III		(Karnojitzky, 1891a; Brauns, 1891; Foord and Mills, 1978; Gorskaya *et al.*, 1992; Akizuki *et al.*, 2001)
45	*Trans, trans*-cyclopentane-1,2,3-tricarboxylic acid, hex.	S	>0					(Kahr and McBride, 1992)

(Continued)

Table P2.2. (Continued)

N	Compound, crystal class, crystal system		$2V_{max}$, deg.	Sources of OA				Reference
a	*b*	*c*	*d*	1	2	3	4	*e*
46	Vesuvianite, $Ca_{19}(Mg, Fe, Al)_{13}Si_{18}O_{68}(O, OH, F)_{10}$, $4/mmm$	N	45	I		1		(Brauns, 1891; Lodochnikov, 1930; Allen and Burnham, 1992; Ohkawa *et al*., 1994; Tanaka *et al*., 2002a)
47	Wulfenite, $PbMoO_4$, $4/m$	S	3	II	II			(Denisov *et al*., 2006a,b)
48	Zinc (or magnesium) dimalate dihydrate, tetr.	S	> 5					(Kahr and McBride, 1992)
49	Zircon, $ZrSiO_4$, $4/mmm$	N	10	I				(Brauns, 1891; Winchell and Winchell, 1951; Takano and Takano, 1959; Speer, 1980)
50	β-methyl-D-glucoside, tetr.	S	>0					(Kahr and McBride, 1992)
51	1,5-dichloro-2,3-dinitrobenzene (DCDNB), 422	S	30			II		(Kahr and McBride, 1992)
52	1,8-dihydroxyanthraquinone, 4	S	>0					(Kahr and McBride, 1992; Claborn *et al*., 2003)
53	3,4-dihydroxy-3,4-diphenylbutane, tetr.	S	>0					(Kahr and McBride, 1992)
54	5-chloro-1,2,3-trinitrobenzene (DTNB), 422	S	>0			II		(Kahr and McBride, 1992)
55	$Ce_2Mg_3(NO_3)_{12} \cdot 24H_2O$, $\bar{3}$	S	10					(Smirnov *et al*., 1982)
56	HgI_2, $4/mmm$	S	>0					(Brauns, 1891)
57	$NaIO_4 \cdot 3H_2O$, 3	S	>0					(Brauns, 1891)
58	$(Pb, Sr, Ca)(S_2O_6) \cdot 4H_2O$, 622	S	25			I		(Brauns, 1891; Crundwell, 1997)
59	$ZnSeO_4 \cdot 6H_2O$, 422	S	>0			III		(Vinokurov *et al*., 1977; Nizamutdinov *et al*., 1977; Anufriev *et al*., 1980; Bulka *et al*., 1980)

Table P2.3. Optical anomalies in orthorhombic, monoclinic and triclinic crystals

N	Compound, crystal class, crystal system		Sources of OA				Reference
a	*b*	*c*	1	2	3	4	*d*
1	Boracite, $Mg_6B_{14}O_{26}Cl_2$, $Pca2_1$	N					(Tschermak, 1884)
2	Brewsteirte, $(Sr, Ba)_2Al_2Si_{12}O_{32} \cdot 10H_2O$, $2/m$	N			II		(Akizuki, 1987c; Akizuki *et al.*, 1986)
3	Brookite, TiO_2, mmm	N	I				(Ikornikova-Lemmlein, 1946)
4	Clinochlore (pennine), $(Mg, Fe)_5Al(Si, Al)_4O_{10}(OH)_8$, $2/m$	N				I	(Brauns, 1891)
5	Epidote, $Ca_2(Al, Fe)_3O(SiO_4)(Si_2O_7)OH$.	N	I		I		(Dowty, 1976)
6	Epistilbite, $Ca_3Al_6Si_{18}O_{48} \cdot 16H_2O$, $2/m$	N			II		(Akizuki and Nishido, 1988)
7	Fluorphlogopite, $Mg_3K(AlF_2O(SiO_3)_3$, $2/m$	S				III	(Bloss *et al.*, 1966; Shmelev and Bobr-Sergeev, 1970; Punin *et al.*, 1985a,b; Punin, 1989a)
8	Harmotome, $Ba_2Al_4Si_{12}O_{32} \cdot 12H_2O$, $2/m$	N			II		(Akizuki, 1985)
9	Heliophyllite, $Pb_6As_2O_7Cl_4$, orth.	N					(Brauns, 1891)
10	Heulandite, $Ca_4(Al_8Si_{28}O_{72}) \cdot 24H_2O$, $2/m$	N					(Brauns, 1891)
11	Leucophanite, $(Na, Ca)_2BeSi_2(O, OH, F)_7$, mon.	N					(Brauns, 1891)
12	Mesolite, $Na_{16}Ca_{16}Al_{48}Si_{72}O_{240} \cdot 64H_2O$, 2	N			II		(Akizuki and Harada, 1988)

(Continued)

Table P2.3. (Continued)

N	Compound, crystal class, crystal system		Sources of OA				Reference
a	*b*	*c*	1	2	3	4	*d*
13	Micas (lepidolite $KLi_2Al(Al, Si)_3O_{10}(F, OH)_2$, muscovite $KAl_2(AlSi_3O_{10})(F, OH)_2$), $2/m$	N				III	(Sokolov, 1953; Kotelnikova *et al.*, 1989; Punin, 1989a; Punin *et al.*, 1989)
14	Natrolite, $Na_{16}Al_{16}Si_{24}O_{80} \cdot 16H_2O$, $mm2$	N			II		(Akizuki and Harada, 1988)
15	Perovskite, $CaTiO_3$, mmm	N				I	(Brauns, 1891)
16	Plagioclase, $(Na, Ca)Al_{1-2}Si_{3-2}O_8$, 1	N	II			III	(Lodochnikov, 1930; Fedorov, 1953b; Hauser and Wenk, 1976)
17	Potassium feldspar (including adularia), $K(AlSi_3O_8)$, $2/m$	NS	II		II	III	(Tschermak, 1884; Lodochnikov, 1930; Marphunin, 1959b; Hauser and Wenk, 1976; Tsinober *et al.*, 1977; Akizuki and Sunagawa, 1978; Akizuki, 1981a; Carpenter and Putnis, 1985)
18	Prehnite, $Ca_2Al_2Si_3O_{10}(OH)_2$, $2mm$	N					(Brauns, 1891; Akizuki, 1987a)
19	Pyroxene, $Ca(Fe, Mg, Mn)Si_2O_6$, $2/m$	N	I		II		(Lodochnikov, 1930; Carpenter and Putnis, 1985)
20	Rochelle salt, $KNaC_4H_4O_6 \cdot 4H_2O$, $2mm$	S					(Brauns, 1891)
21	Scolecite, $Ca_8Al_{16}Si_{24}O_{80} \cdot 24H_2O$, m	N			II		(Akizuki and Harada, 1988)
22	Staurolite, $Fe_2Al_9O_7(OH)(SiO_4)_4$, $2/m$	N	I		I		(Ribbe, 1980)
23	Stilbite, $Na_2Ca_4Al_{10}Si_{26}O_{72} \cdot 34H_2O$, $2/m$	N			II		(Akizuki and Konno, 1985b; Akizuki *et al.*, 1993)

24	Topaz, $Al_2SiO_4(OH, F)_2$, *mmm*	N	III		(Akizuki *et al*., 1979; Ribbe, 1980; Parise *et al*., 1980; Shinoda and Aikawa, 1994a,b)
25	Xanthophyllite, $Ca(Mg, Al)_3(Al_3Si)O_{10}(OH)_2$, $2/m$	N			(Takano and Takano, 1959)
26	Yugawaralite, $CaAl_2Si_6O_{16} \cdot 4H_2O$, *m*	N	II		(Akizuki, 1987b; Tanaka *et al*., 2002b)
27	$CO(NH_2)_2 \cdot NH_4Cl$, orth.	S		III	(Franke *et al*., 1987; Punin *et al*., 1993)
28	$NaNH_4(SO_4, CrO_4) \cdot 2H_2O$, 222	S		I	(Brauns, 1891)

Remarks: This table list emphasizes crystals with anomalous linear birefringence. Crystals with anomalous linear dichroism, especially those cases associated with dye additives, are tabulated in Kahr and Gurney (2001). N – natural crystals, S – synthetic crystals. Cubic crystals are characterized by their maximal value of birefringence (Δn_{max}), while trigonal, tetragonal and hexagonal crystals are characterized by their maximal axial angle ($2V_{max}$). Orthorhombic, monoclinic, and triclinic optically anomalous crystals are distinguished by the following features: sector zoning; unusual optical indicatrix; and composition independent variation of optical properties. Arabic numbers denote the sources of optical anomalies: 1 – compositional heterometry-induced stress, and thermoplastic stress; 2 – stress on inclusions, dislocations and dislocation ensembles; 3 – kinetic ordering-disordering of structural units; 4 – phase and/or chemical heterogeneity. In the case of 1,8-dihydroxyanthraquinone, circular dichroism is masquerading as birefringence. None of the stated categories are appropriate. Roman numbers indicate our estimates of the reliability of the data. III – origin of optical anomalies is incontrovertible and quantitative; II – origin of optical anomalies is likely and qualitative; I – speculative origin, unconfirmed. References: the items marked by symbol * contain many references on the subject. We did not intend to review all the literature published before 1940, since it contains a little information on the etiology of optical anomalies. One exception is our frequent citation of Brauns (1891). He gives comprehensive review of the 19th C. literature. His book is unusual because it surveys the literature for some substances and presents new data on others. We made no effort to distinguish those instances where Brauns is a primary source from those in which it is a secondary source. A number of optically anomalous organic crystals are cited secondarily in the review by Kahr and McBride (1992). For the ugrandite garnets (marked by symbol #) a significant number of references are omitted because of space constraints. The reference “this work” indicates that this book contains significant amount of unpublished data.

APPENDIX 3. PIEZOOPTIC $\pi_{\lambda\mu}$ AND ELASTOOPTIC $p_{\lambda\mu}$ TENSORS FOR DIFFERENT CRYSTAL SYSTEMS AND CRYSTAL CLASSES (NYE, 1985; SHUVALOV, 2005).

If these tensors have different forms both the variants are given, otherwise only piezooptic tensor is provided. The relationship between complete and abbreviated indices is as follows:

$$\pi_{\lambda\mu} = \begin{cases} \pi_{ijkl} \;\; ij \leftrightarrow \lambda = 1, 2, ..6 \quad kl \leftrightarrow \mu = 1, 2, 3 \\ 2\pi_{ijkl} \; ij \leftrightarrow \lambda = 1, 2, ..6 \quad kl \leftrightarrow \mu = 4, 5, 6 \end{cases}$$

$$p_{\lambda\mu} = p_{ijkl} \quad ij \leftrightarrow \lambda = 1, 2, ..6 \quad kl \leftrightarrow \mu = 1, 2, 3..6$$

Cubic system

(crystal classes 23, $m\bar{3}$)

$$\begin{bmatrix} \pi_{11} & \pi_{12} & \pi_{21} & 0 & 0 & 0 \\ \pi_{21} & \pi_{11} & \pi_{12} & 0 & 0 & 0 \\ \pi_{12} & \pi_{21} & \pi_{11} & 0 & 0 & 0 \\ 0 & 0 & 0 & \pi_{44} & 0 & 0 \\ 0 & 0 & 0 & 0 & \pi_{44} & 0 \\ 0 & 0 & 0 & 0 & 0 & \pi_{44} \end{bmatrix}$$

(crystal classes 432, $\bar{4}3m$, $m\bar{3}m$)

$$\begin{bmatrix} \pi_{11} & \pi_{12} & \pi_{12} & 0 & 0 & 0 \\ \pi_{12} & \pi_{11} & \pi_{12} & 0 & 0 & 0 \\ \pi_{12} & \pi_{12} & \pi_{11} & 0 & 0 & 0 \\ 0 & 0 & 0 & \pi_{44} & 0 & 0 \\ 0 & 0 & 0 & 0 & \pi_{44} & 0 \\ 0 & 0 & 0 & 0 & 0 & \pi_{44} \end{bmatrix}$$

Hexagonal system

(crystal classes 6, $\bar{6}$, 6/*m*)

$$\begin{bmatrix} \pi_{11} & \pi_{12} & \pi_{13} & 0 & 0 & 2\pi_{16} \\ \pi_{12} & \pi_{11} & \pi_{13} & 0 & 0 & -2\pi_{16} \\ \pi_{31} & \pi_{31} & \pi_{33} & 0 & 0 & 0 \\ 0 & 0 & 0 & \pi_{44} & \pi_{45} & 0 \\ 0 & 0 & 0 & -\pi_{45} & \pi_{44} & 0 \\ -\pi_{16} & \pi_{16} & 0 & 0 & 0 & \pi_{11} - \pi_{12} \end{bmatrix}$$

(crystal classes 622, 6*mm*, $\bar{6}m2$, 6/*mmm*)

$$\begin{bmatrix} \pi_{11} & \pi_{12} & \pi_{13} & 0 & 0 & 0 \\ \pi_{12} & \pi_{11} & \pi_{13} & 0 & 0 & 0 \\ \pi_{31} & \pi_{31} & \pi_{33} & 0 & 0 & 0 \\ 0 & 0 & 0 & \pi_{44} & 0 & 0 \\ 0 & 0 & 0 & 0 & \pi_{44} & 0 \\ 0 & 0 & 0 & 0 & 0 & \pi_{11} - \pi_{12} \end{bmatrix}$$

$$\begin{bmatrix} p_{11} & p_{12} & p_{13} & 0 & 0 & p_{16} \\ p_{12} & p_{11} & p_{13} & 0 & 0 & -p_{16} \\ p_{31} & p_{31} & p_{33} & 0 & 0 & 0 \\ 0 & 0 & 0 & p_{44} & p_{45} & 0 \\ 0 & 0 & 0 & -p_{45} & p_{44} & 0 \\ -p_{16} & p_{16} & 0 & 0 & 0 & (p_{11} - p_{12})/2 \end{bmatrix}$$

$$\begin{bmatrix} p_{11} & p_{12} & p_{13} & 0 & 0 & 0 \\ p_{12} & p_{11} & p_{13} & 0 & 0 & 0 \\ p_{31} & p_{31} & p_{33} & 0 & 0 & 0 \\ 0 & 0 & 0 & p_{44} & 0 & 0 \\ 0 & 0 & 0 & 0 & p_{44} & 0 \\ 0 & 0 & 0 & 0 & 0 & (p_{11} - p_{12})/2 \end{bmatrix}$$

Tetragonal system

(crystal classes 4, $\bar{4}$, 4/*m*)

$$\begin{bmatrix} \pi_{11} & \pi_{12} & \pi_{13} & 0 & 0 & \pi_{16} \\ \pi_{12} & \pi_{11} & \pi_{13} & 0 & 0 & -\pi_{16} \\ \pi_{31} & \pi_{31} & \pi_{33} & 0 & 0 & 0 \\ 0 & 0 & 0 & \pi_{44} & \pi_{45} & 0 \\ 0 & 0 & 0 & -\pi_{45} & \pi_{44} & 0 \\ -\pi_{61} & \pi_{61} & 0 & 0 & 0 & \pi_{66} \end{bmatrix}$$

(crystal classes 422, 4*mm*, $\bar{4}2m$, 4/*mmm*)

$$\begin{bmatrix} \pi_{11} & \pi_{12} & \pi_{13} & 0 & 0 & 0 \\ \pi_{12} & \pi_{11} & \pi_{13} & 0 & 0 & 0 \\ \pi_{31} & \pi_{31} & \pi_{33} & 0 & 0 & 0 \\ 0 & 0 & 0 & \pi_{44} & 0 & 0 \\ 0 & 0 & 0 & 0 & \pi_{44} & 0 \\ 0 & 0 & 0 & 0 & 0 & \pi_{66} \end{bmatrix}$$

Trgonal system

(crystal classes 3, $\bar{3}$)

$$\begin{bmatrix} \pi_{11} & \pi_{12} & \pi_{13} & \pi_{14} & \pi_{25} & 2\pi_{16} \\ \pi_{12} & \pi_{11} & \pi_{13} & -\pi_{14} & \pi_{25} & 2\pi_{16} \\ \pi_{31} & \pi_{31} & \pi_{33} & 0 & 0 & 0 \\ \pi_{41} & \pi_{41} & 0 & \pi_{44} & \pi_{45} & 2\pi_{52} \\ -\pi_{52} & \pi_{52} & 0 & -\pi_{45} & \pi_{44} & 2\pi_{41} \\ -\pi_{16} & \pi_{16} & 0 & \pi_{25} & \pi_{14} & \pi_{11}-\pi_{12} \end{bmatrix}$$

$$\begin{bmatrix} p_{11} & p_{12} & p_{13} & p_{14} & -p_{25} & \pi_{16} \\ p_{12} & p_{11} & p_{13} & -p_{14} & p_{25} & -\pi_{16} \\ p_{31} & p_{31} & p_{33} & 0 & 0 & 0 \\ p_{41} & -p_{41} & 0 & p_{44} & p_{45} & \pi_{52} \\ -p_{52} & p_{52} & 0 & -p_{45} & p_{44} & \pi_{41} \\ -p_{16} & p_{16} & 0 & p_{25} & p_{14} & (p_{11}-p_{12})/2 \end{bmatrix}$$

(crystal classes 32, $3m$, $\bar{3}$)

$$\begin{bmatrix} \pi_{11} & \pi_{12} & \pi_{13} & \pi_{14} & 0 & 0 \\ \pi_{12} & \pi_{11} & \pi_{13} & -\pi_{14} & 0 & 0 \\ \pi_{31} & \pi_{31} & \pi_{33} & 0 & 0 & 0 \\ \pi_{41} & -\pi_{41} & 0 & \pi_{44} & 0 & 0 \\ 0 & 0 & 0 & 0 & \pi_{44} & \pi_{41} \\ 0 & 0 & 0 & 0 & \pi_{14} & \pi_{11}-\pi_{12} \end{bmatrix}$$

$$\begin{bmatrix} \pi_{11} & p_{12} & p_{13} & p_{14} & 0 & 0 \\ \pi_{12} & p_{11} & p_{13} & -p_{14} & 0 & 0 \\ \pi_{31} & p_{31} & p_{33} & 0 & 0 & 0 \\ \pi_{41} & -p_{41} & 0 & p_{44} & 0 & 0 \\ 0 & 0 & 0 & 0 & p_{44} & p_{41} \\ 0 & 0 & 0 & 0 & p_{14} & (p_{11}-p_{12})/2 \end{bmatrix}$$

Monoclinic system

x_2 parallel to 2-fold axis or $\perp$ to m

$$\begin{bmatrix} \pi_{11} & \pi_{12} & \pi_{13} & 0 & \pi_{15} & 0 \\ \pi_{21} & \pi_{22} & \pi_{23} & 0 & \pi_{25} & 0 \\ \pi_{31} & \pi_{32} & \pi_{33} & 0 & \pi_{35} & 0 \\ 0 & 0 & 0 & \pi_{44} & 0 & \pi_{46} \\ \pi_{51} & \pi_{52} & \pi_{53} & 0 & \pi_{55} & 0 \\ 0 & 0 & 0 & \pi_{64} & 0 & \pi_{66} \end{bmatrix}$$

x_2 parallel to 2-fold axis or $\perp$ to m

$$\begin{bmatrix} \pi_{11} & \pi_{12} & \pi_{13} & 0 & 0 & \pi_{16} \\ \pi_{21} & \pi_{22} & \pi_{23} & 0 & 0 & \pi_{26} \\ \pi_{31} & \pi_{32} & \pi_{33} & 0 & 0 & \pi_{36} \\ 0 & 0 & 0 & \pi_{44} & \pi_{45} & 0 \\ 0 & 0 & 0 & \pi_{54} & \pi_{55} & 0 \\ \pi_{61} & \pi_{62} & \pi_{63} & 0 & 0 & \pi_{66} \end{bmatrix}$$

Orthorhombic system

$$\begin{bmatrix} \pi_{11} & \pi_{12} & \pi_{13} & 0 & 0 & 0 \\ \pi_{21} & \pi_{22} & \pi_{23} & 0 & 0 & 0 \\ \pi_{31} & \pi_{32} & \pi_{33} & 0 & 0 & 0 \\ 0 & 0 & 0 & \pi_{44} & 0 & 0 \\ 0 & 0 & 0 & 0 & \pi_{55} & 0 \\ 0 & 0 & 0 & 0 & 0 & \pi_{66} \end{bmatrix}$$

Triclinic system

$$\begin{bmatrix} \pi_{11} & \pi_{12} & \pi_{13} & \pi_{14} & \pi_{15} & \pi_{16} \\ \pi_{21} & \pi_{22} & \pi_{23} & \pi_{24} & \pi_{25} & \pi_{26} \\ \pi_{31} & \pi_{32} & \pi_{33} & \pi_{34} & \pi_{35} & \pi_{36} \\ \pi_{41} & \pi_{42} & \pi_{43} & \pi_{44} & \pi_{45} & \pi_{46} \\ \pi_{51} & \pi_{52} & \pi_{53} & \pi_{54} & \pi_{55} & \pi_{56} \\ \pi_{61} & \pi_{62} & \pi_{63} & \pi_{64} & \pi_{65} & \pi_{66} \end{bmatrix}$$

APPENDIX 4. ORIENTATION OF THE CRYSTAL PHYSICAL BASIS (X_1, X_2, X_3) (SHUVALOV, 2005).

System	Orientation with respect to crystallographic basis (a, b, c)	Orientation with respect to symmetry operations
Triclinic	$x_3 \| \| c$ or $x_2 \| \| b$ or $x_1 \| \| a$	—
Monoclinic	$x_2 \| \| b$ and $x_1 \| \| a$ (or $x_3 \| \| c$). Sometimes $x_3 \| \| b$ and $x_1 \| \| a$ (or $x_2 \| \| c$)	$x_2 \|\|$ to 2-fold axis or $\perp$ to the mirror plane m. Sometimes $x_3 \|\|$ to 2-fold axes or $\perp$ to mirror plane m
Orthorhombic	$x_3 \| \| c$, $x_2 \| \| b$, $x_1 \| \| a$	x_3 is parallel to 2-fold axes x_1, $x_2 \|\|$ to two other 2-fold axes or $\perp$ to the mirror planes m
Tetragonal	$x_3 \| \| c$, $x_2 \| \| b$, $x_1 \| \| a$	x_3 is parallel to axis 4 (or $\bar{4}$); x_1, $x_2 \|\|$ to two other 2-fold axes or $\perp$ to the mirror planes m (if they are present); for the crystal class $\bar{4}2m$ usually x_1, $x_2 \|\|$ to 2-fold axes
Trigonal and hexagonal	$x_3 \| \| c$, $x_1 \| \| a$. For the symmetry classes $3m$ and $\bar{6}m2$ sometimes $x_2 \| \| b$	$x_3 \|\|$ to axis 3, $\bar{3}$, 6 or $\bar{6}$; $x_1 \|\|$ to 2-fold axes (if present, except for symmetry class $\bar{6}m2$); for classes $3m$ and $\bar{6}m2$ usually $x_1 \perp$ to the mirror plane m, sometimes $x_2 \perp$ to the mirror plane m
Cubic	$x_3 \| \| c$, $x_2 \| \| b$, $x_1 \| \| a$	x_1, x_2, and $x_3 \|\|$ to three mutually $\perp$ to 4-fold axes (or $\bar{4}$), or if they are absent to 2-fold axes

INDEX

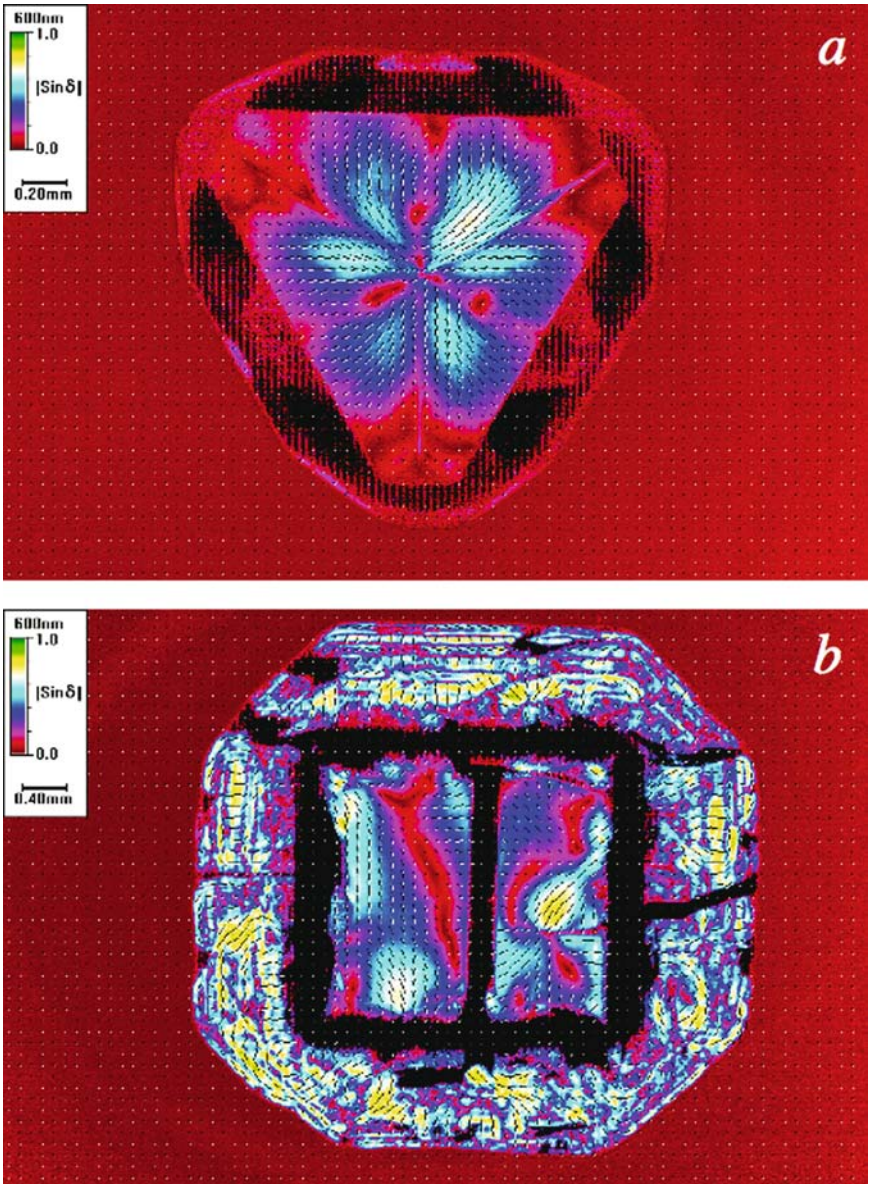

Figure F.1. Anomalous birefringence images of sections of diamond cut (*a*) perpendicular to the threefold axis, and (*b*) perpendicular to the fourfold axis. The false color scale plotted as $|\sin\delta|$ where $\delta = 2\pi\Delta nL/\lambda$, $\Delta n = n_{\perp} - n_{\parallel}$, L is the sample thickness, and λ is the wavelength of light. Hash marks indicate the extinction directions, the orientation of the most refracting directions
Source: Figure courtesy of Dr. M. Geday.

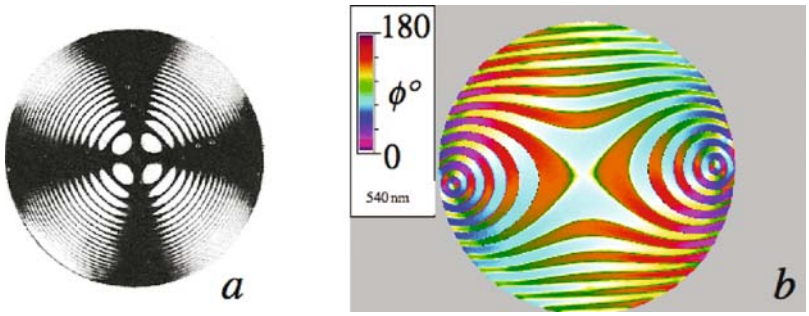

Figure 1.4. (*a*) Typical uniaxial interference figure in monochromatic light from Shubnikov (1960). (*b*) Conoscopic interference of a biaxial crystal along the acute bisectrix made with rotating polarizer method (Glazer *et al*., 1996). Image plotted as the direction of the most refractive vibration measured in degrees counterclockwise from the horizontal axis
Source (a): Taken from Shubnikov, A.V. *Principals of Optical Crystallography* 1960, reproduced with permission from 'Consultants Bureau, New York'.
Source (b): Figure courtesy of Professor Werner Kaminsky, Department of Chemistry, University of Washington

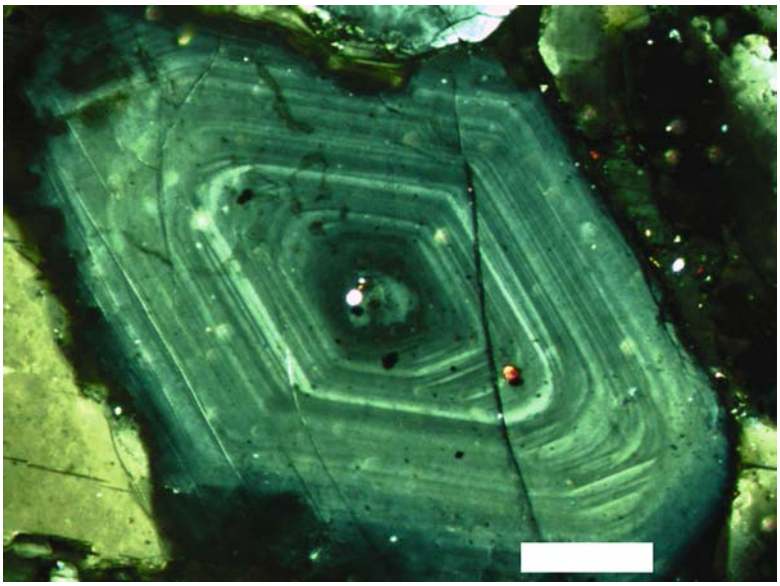

Figure 1.5. Concentric, compositional zoning of plagioclase ($(Na, Ca)(Al, Si)_4O_8$) from crystal-lapilli (volcano B. Tolbacheck, Kamchatka, Russia). Variation in albite ($NaAlSi_3O_8$) to anorthite ($CaAl_2Si_2O_8$) ratio manifests itself in variations of birefringence and extinction position. Scale bar = 0.22 mm

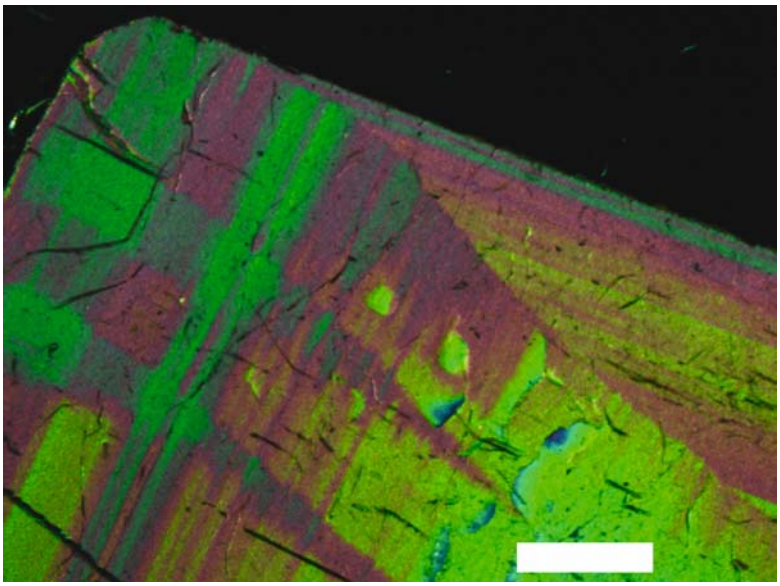

Figure 1.6. Concentric zoning and growth sector zoning of birefringence in epidote [$Ca_2(Al, Fe)_3O(SiO_4)(Si_2O_7)OH$] related to variations of chemical composition. The sample was kindly provided by P.B. Sokolov. Scale bar = 0.88 mm

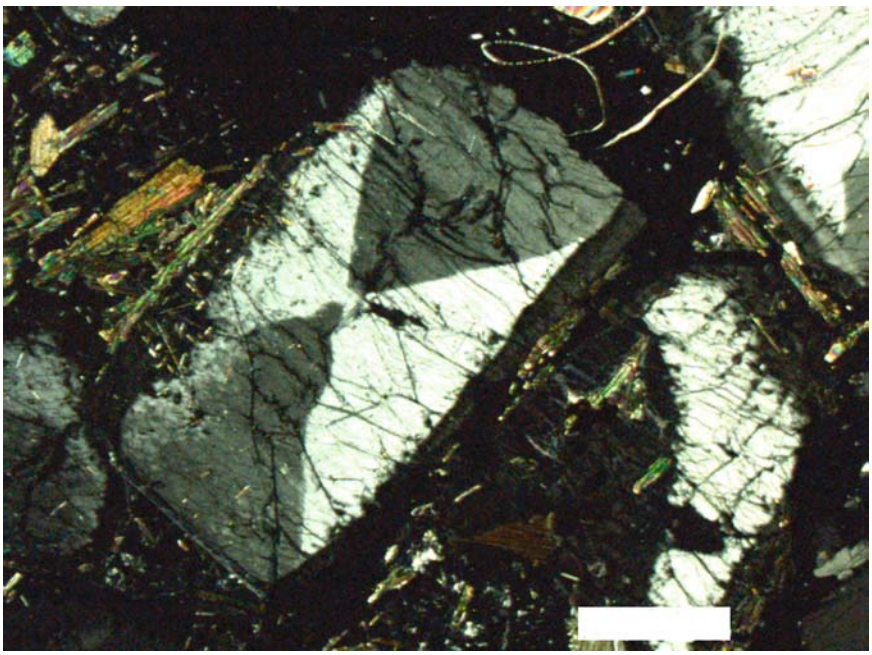

Figure 1.7. Growth sector zoning in birefringence in eudialyte $(Na_4(Ca, Ce, Fe, Mn)_2ZrSi_6O_{17}(OH, Cl)_2)$ related to variations of chemical composition. Scale bar = 0.88 mm

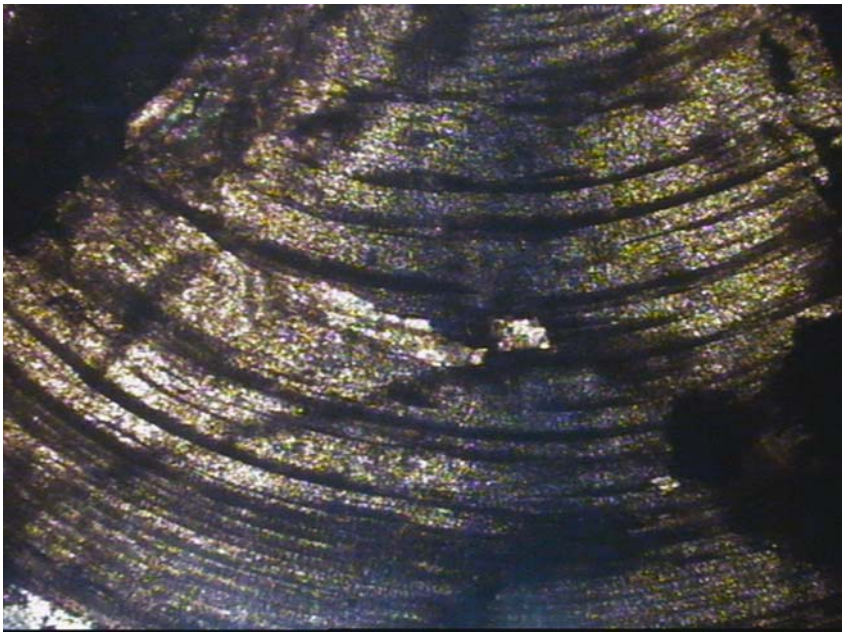

Figure 1.9. Wavy extinction in mica crystal curved due to relaxation of internal stress. Extinction is observed only in stripes, in which vibration directions in the crystal are parallel to vibration directions in the crossed polarizers oriented vertically and horizontally

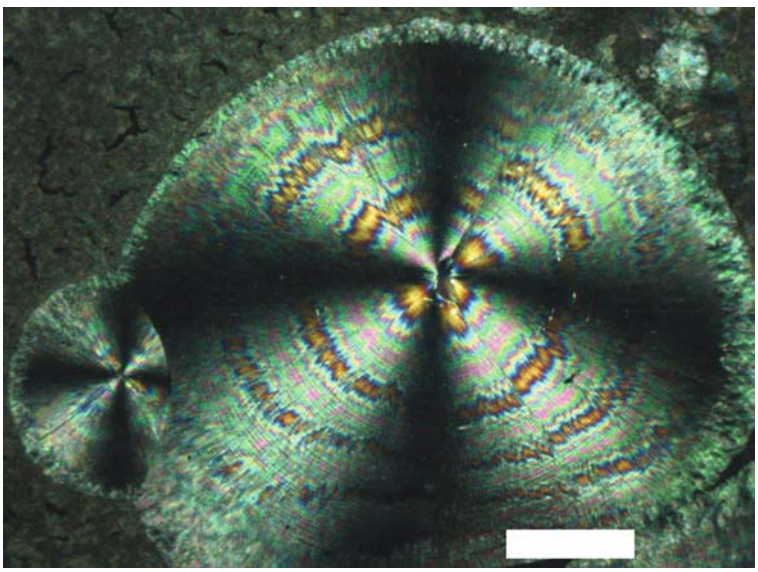

Figure 1.10. Hippuric acid ($C_6H_5CONHCH_2COOH$) spherulites between crossed polarizers. An extinction cross, typical for spherulites, arises when the refracting components are parallel with either the crossed polarizer or analyzer. The concentric banding is best accounted for by assuming fibrous crystallites twisting about the radius. Scale bar = 0.44 mm

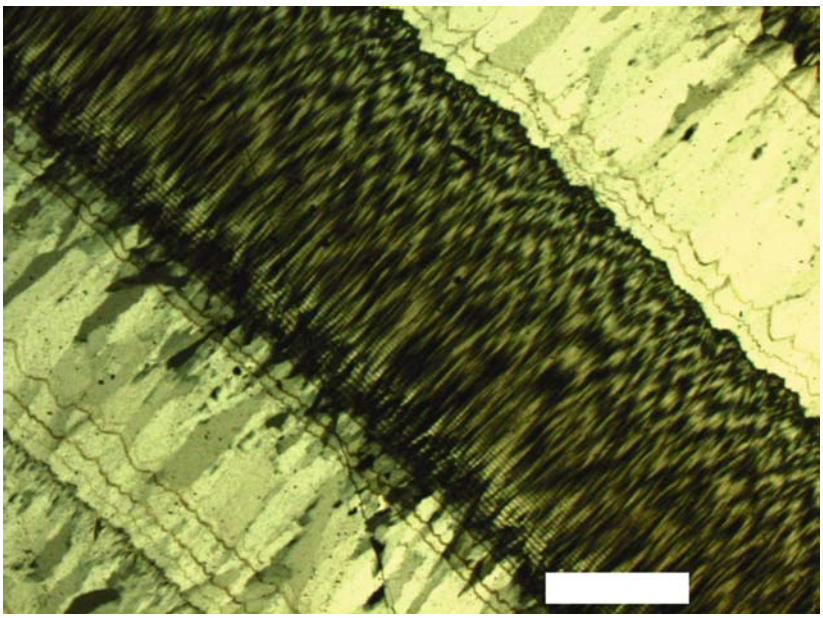

Figure 1.11. Chalcedony (fibrous SiO_2) spherulites between crossed polars. Twisting of crystalline fibers gives rise to rhythmic bands of extinction. Since the distance between bands is variable the twisting period is not constant. Scale bar = 0.88 mm

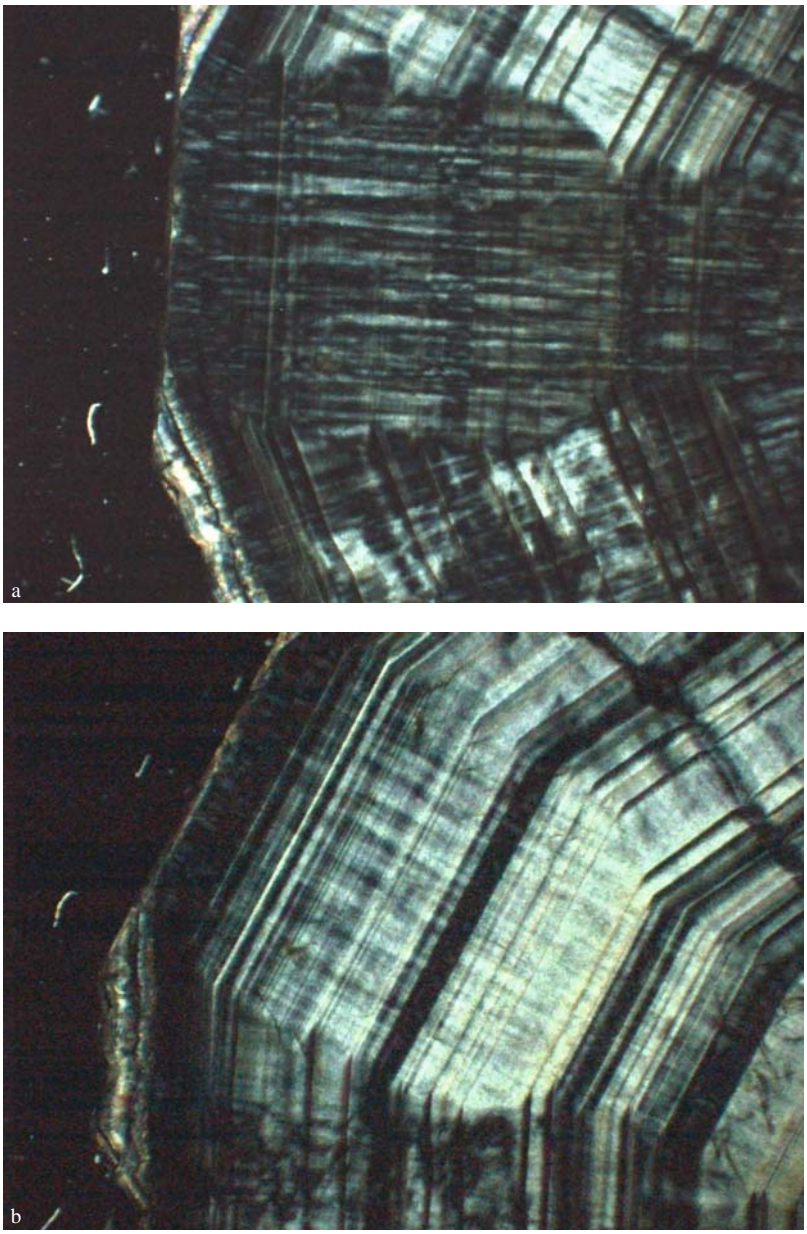

Figure 2.7. Birefringence bands in garnet $Ca_3(Al, Fe)_2(SiO_4)_3$ from the Dalnegorsk mine, Far East, Russia. These bands originate from elastic stress on dislocation bundles and are directed normal to the growth front. (*a*) and (*b*) correspond to different crystal orientations relative to the crossed polarizers directed vertically and horizontally, respectively. The growth front positions are marked by numerous concentric zoning boundaries. Birefringence more or less homogeneously distributed over concentric zones is caused by growth desymmetrization (see Chapter 3). The sample was kindly provided by P.B. Sokolov

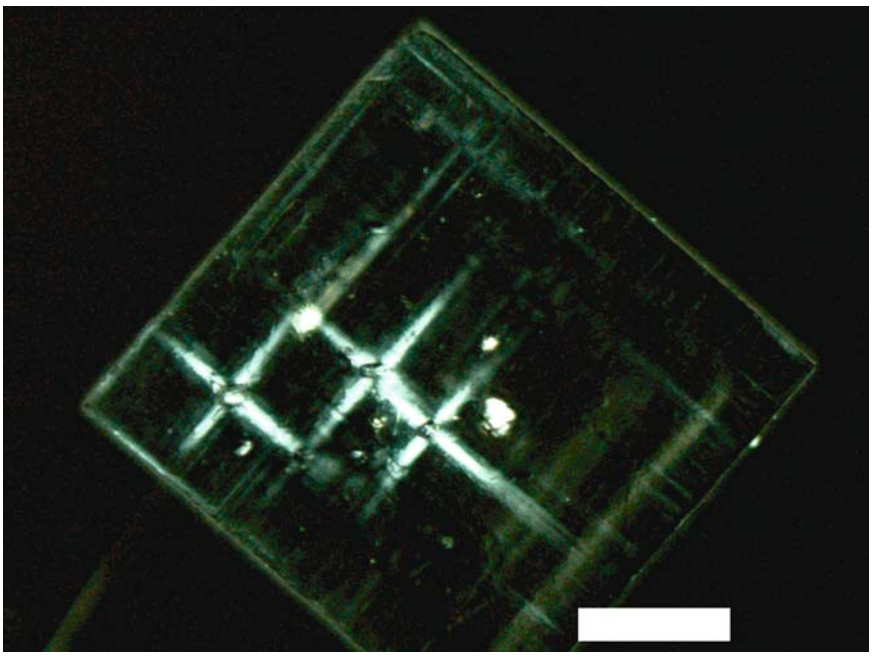

Figure 2.12. Slip bands in ammonium chloride induced by pricking the crystal surface with a needle. Scale bar= 0.88 mm

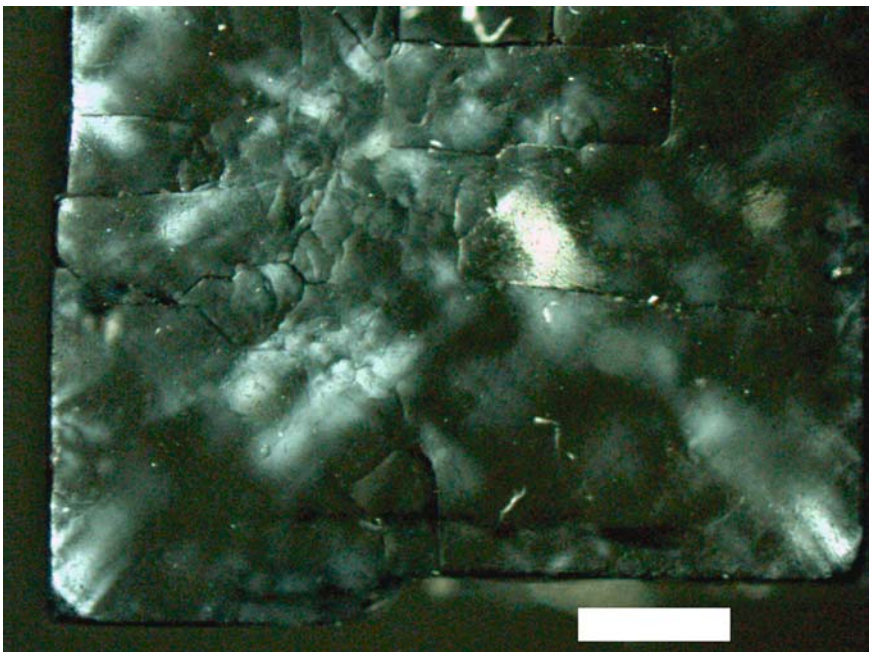

Figure 2.13. Anomalous birefringence in potassium chloride originating from stress on the block boundaries. Scale bar= 0.88 mm

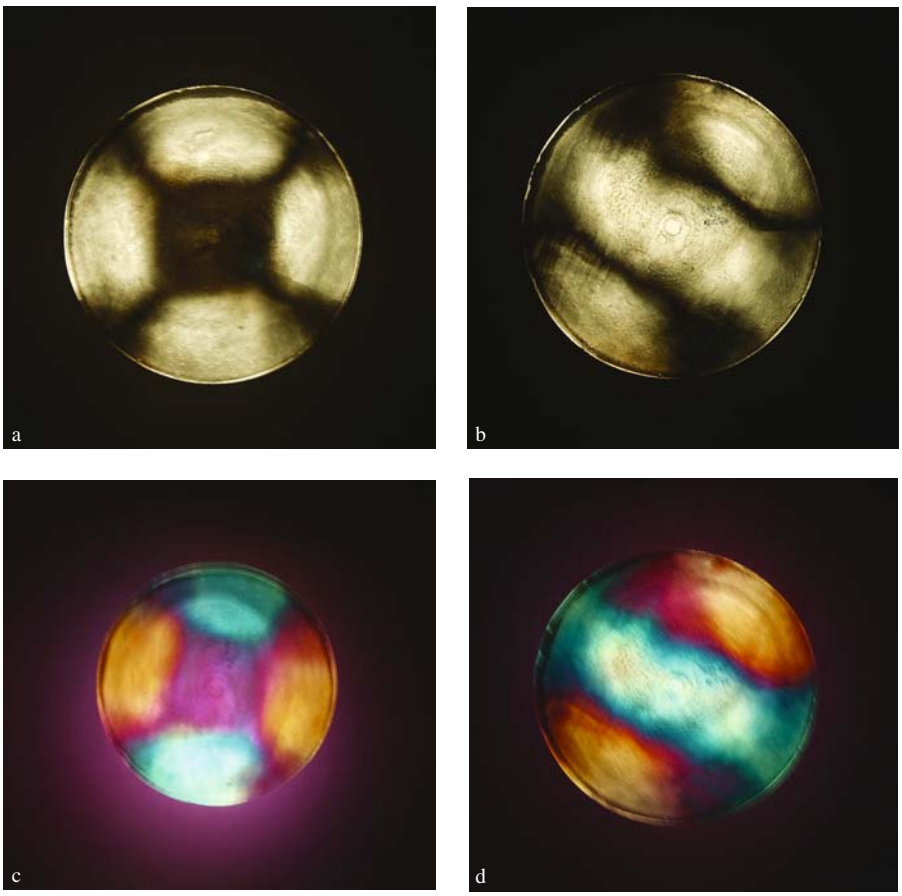

Figure 2.17. Orthoscopic optical pattern of anomalous birefringence in fluorite grown by Stockbarger method. The axis of illumination coincides with the ingot axis (two-fold axis). Rotation of the microscope stage by 45° transforms the dark cross in (*a*) into two hyperbolas in (*b*). (*c*, *d*) The same images taken with first order red retarder. Polarizer and analyzer have diagonal orientations. Pictures kindly provided by L.A. Pyankova

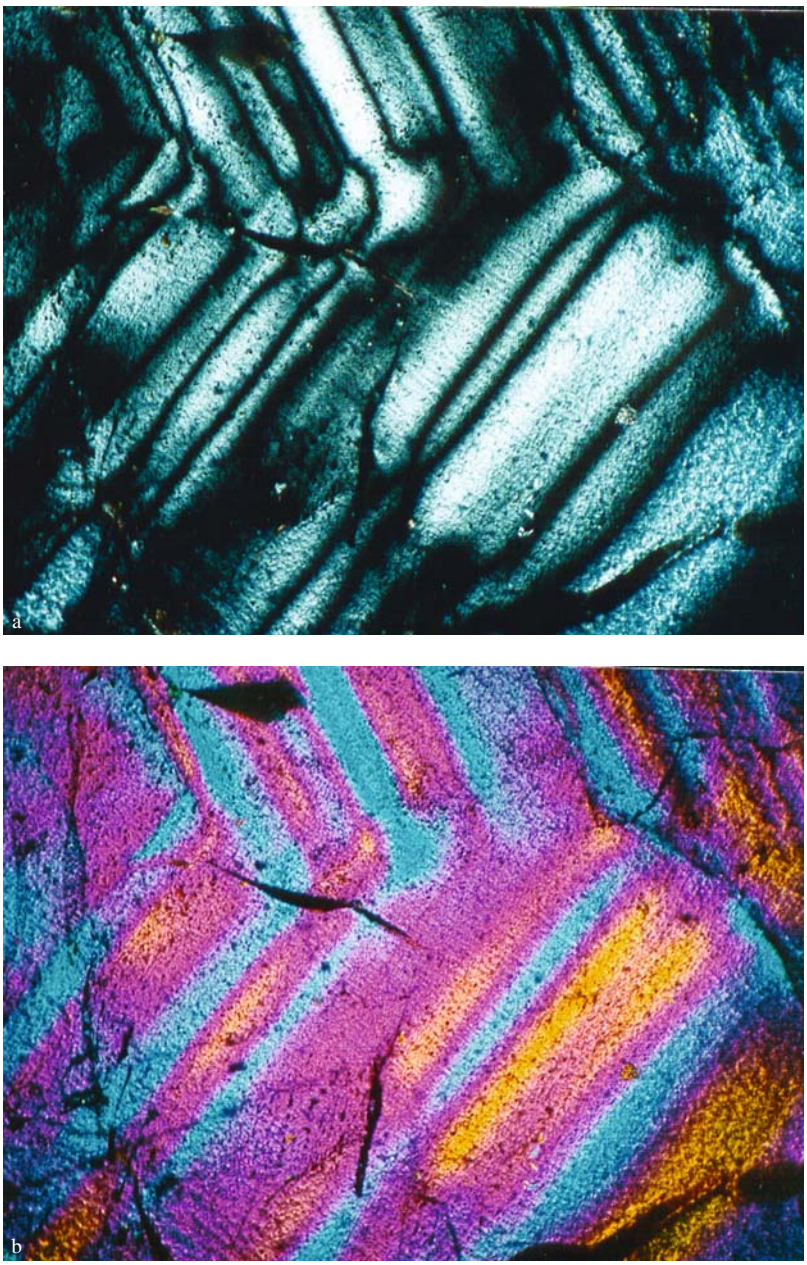

Figure 2.27. (*a*) Photomicrograph of grossular-andradite garnet between crossed polarizers with alternation of Z' and X' orientations between the neighboring zones. Boundaries between zones in two adjacent {211} growth sectors seen as narrow black lines. (*b*) The same picture taken with a first order red retarder. Picture size = 0.44 mm. Sample kindly provided by P.B. Sokolov

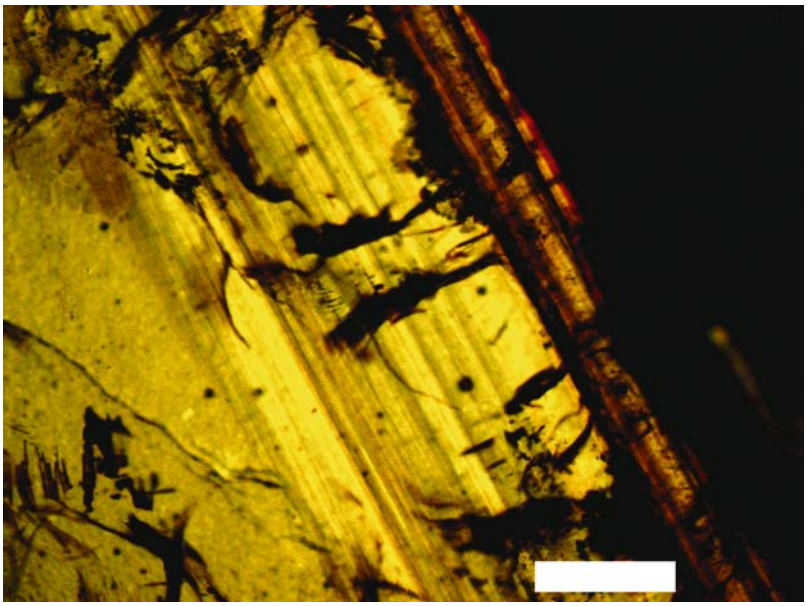

Figure 2.28. Photomicrograph of grossular-andradite garnet in polarized light (no analyzer inserted) with zones visible by color. At the boundaries of outer darker zones, regular systems of cracks appear. These cracks caused by compositional heterometry-induced stress are directed either normal or diagonal to the growth front and run well into the crystal. Scale bar = 0.88 mm. Sample kindly provided by P.B. Sokolov

Figure 2.33. Anomalous birefringence in (0001) section of beryl, schematically shown in Figure 2.34. Birefringence changes at zone boundaries and cracks are visible

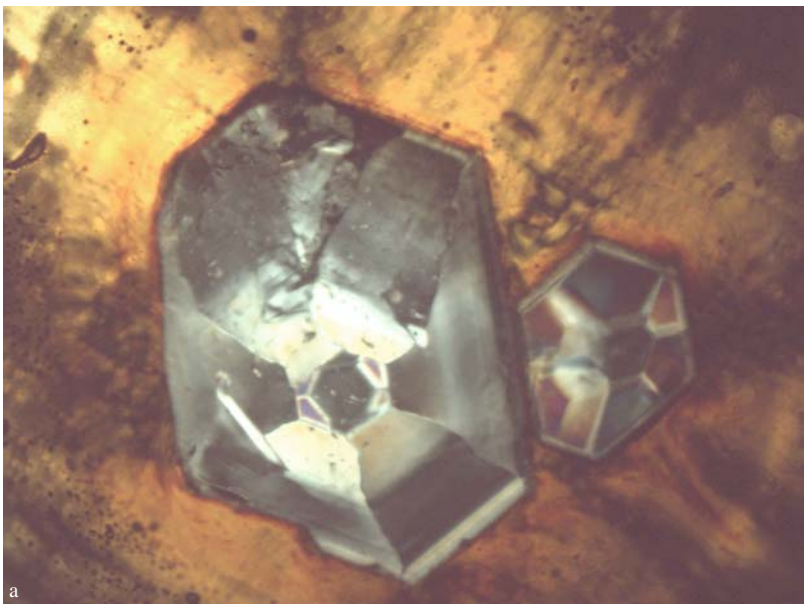

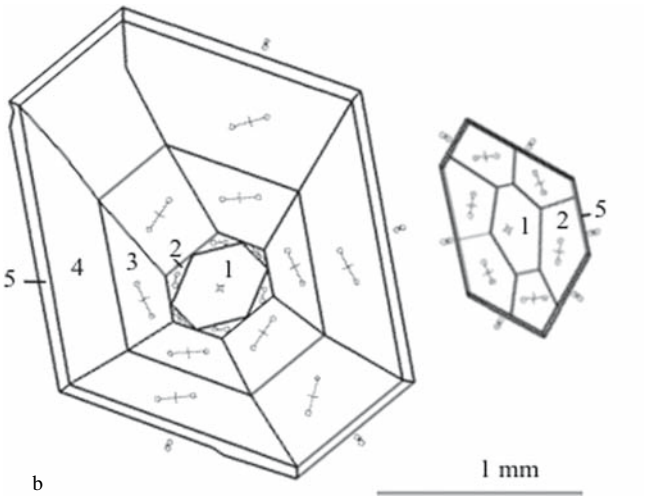

Figure 3.4. Optical sector zoning in jeremejevite $Al_6B_5O_{15}(F, OH)_3$ (0001) section (two crystals). (*a*) Photomicrograph; (*b*) Idealization after (Zolotarev *et al*., 2000). Growth sectors: (1) pinacoid {0001} $2V = 0°$, (2–4) hexagonal dipyramid, $2V = 3°$, (5) hexagonal prism, $2V = 10–18°$. The samples were kindly provided by V.A. Mikhailov

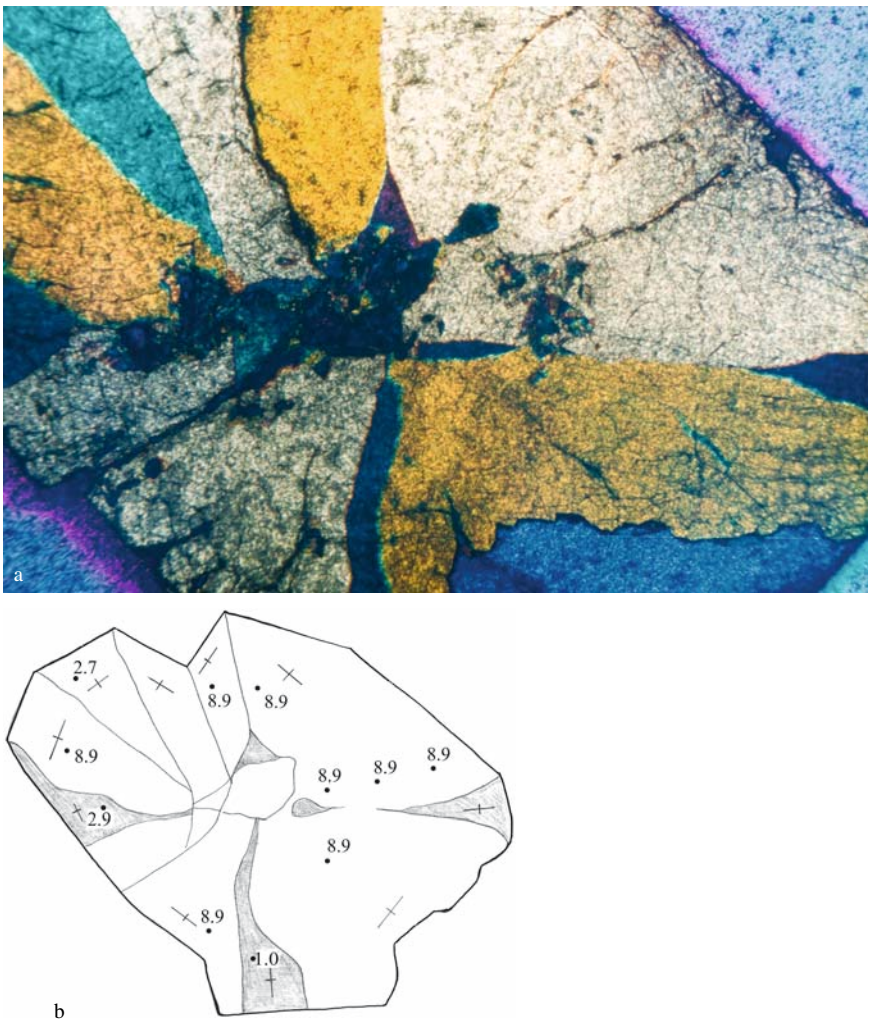

Figure 3.7. Grossular-andradite garnet from the Bazhenovo mine (Ural mountains, Russia) between the crossed polarizers with a first order red retarder. (*a*) Photomicrograph and (*b*) Cartoon based on (*a*). The {110} growth sectors of different orientations are visible. Crosses denote orientations of vibration directions X' and Z'. Numbers indicate birefringence $\times 10^{-3}$. Crystal size ~ 1 cm. The growth direction [110] in hatched and unhatched growth sectors form distinct angles with respect to the section plane

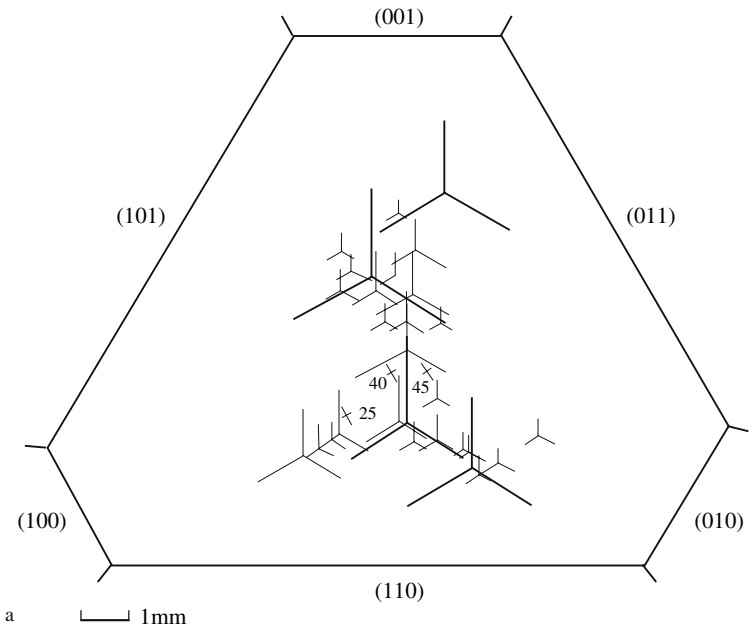

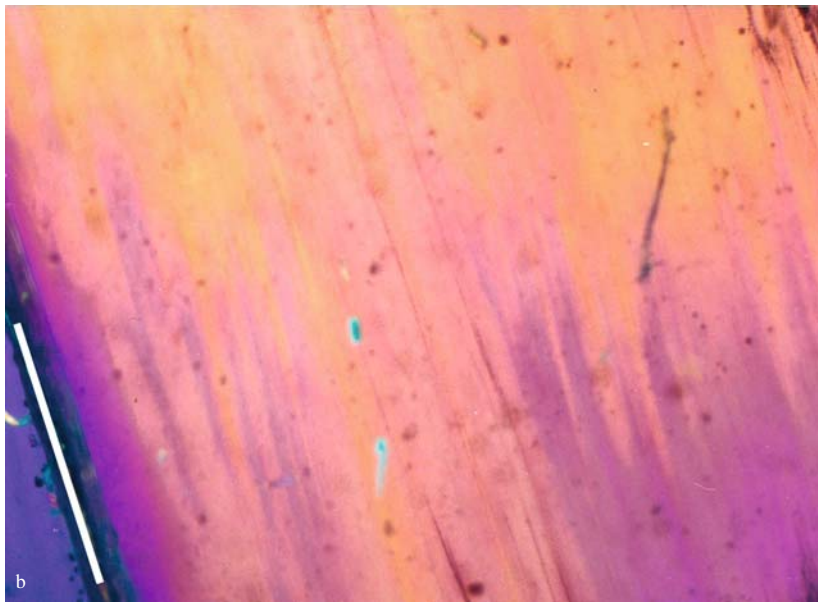

Figure 3.8. (*a*) Subsector zoning in alum $(K_{0.77}Rb_{0.23})Al(SO_4)_2 \cdot 12H_2O$ {111}, section parallel to (111) growth face. Sub-sector boundaries shown by bold lines are the boundaries between different vicinal faces on the crystal surface. Sub-sector boundaries shown by thin lines are observed between crossed polarizers. Numbers denote birefringence $\times 10^{-7}$. (*b*) The same crystal with section through the center of (111) face parallel to the growth direction [111] between crossed polarizers and with a first order red retarder. White line marks position of (111) face

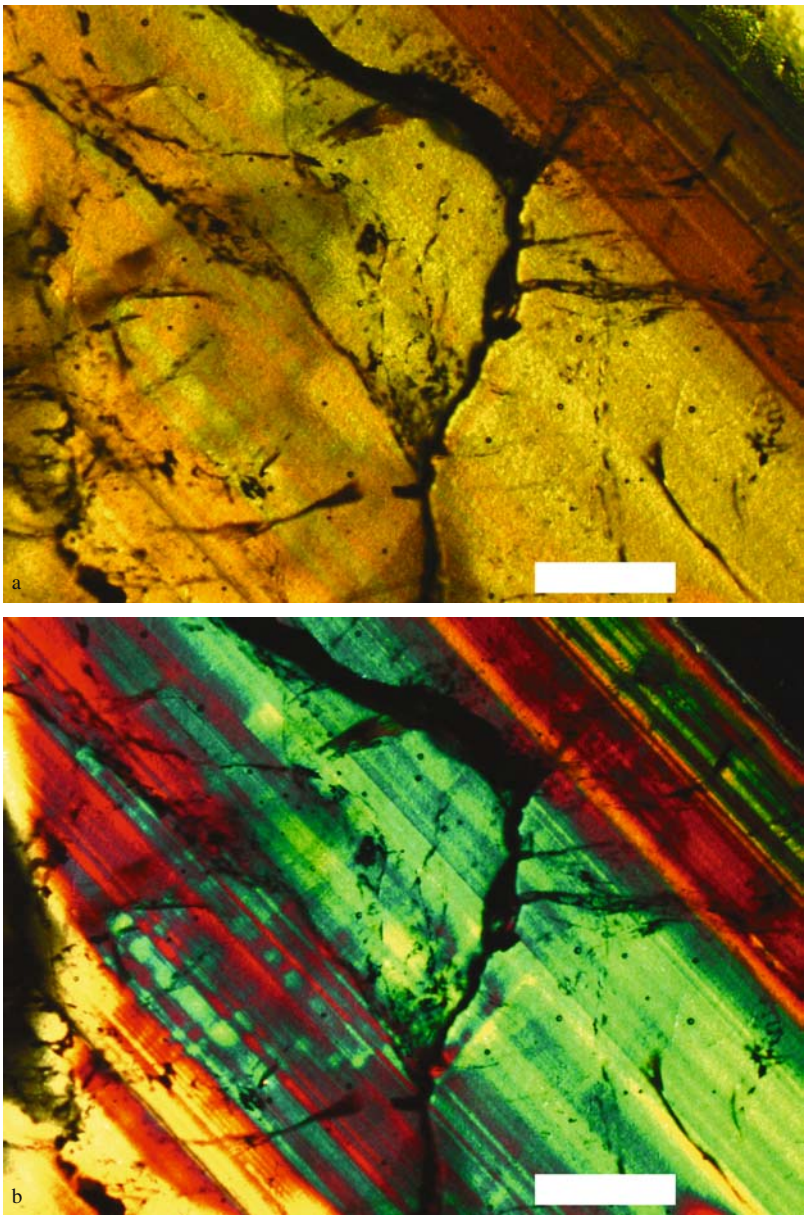

Figure 3.14. Optical zoning in {110} growth sector of grossular-andradite garnet. (*a*) In polarized light without analyzer. (*b*) Between crossed polarizers with a first order red retarder. Scale bar = 0.88 mm

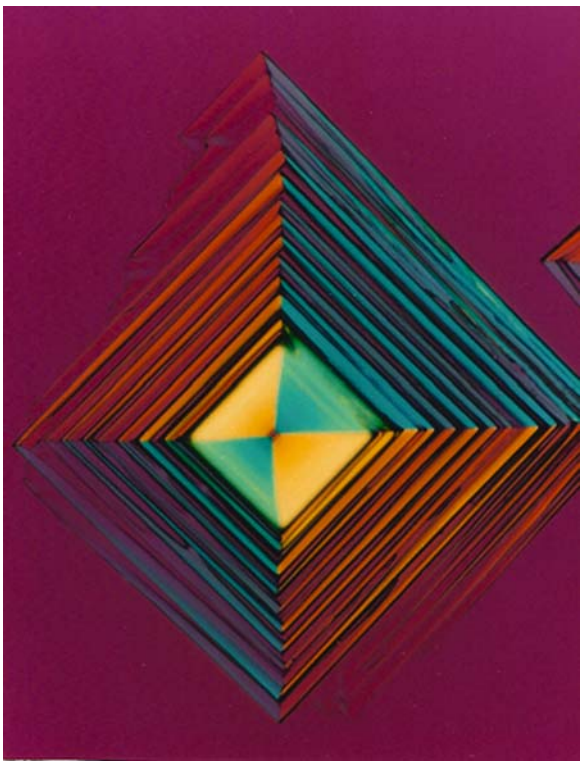

Figure 3.18. Photomicrograph of 1,5-dichloro-2,3-dinitrobenzene grown from chloroform. Crystal between crossed polarizers with a first order red retarder in the diagonal position. Diagonal width = 0.24 mm. Thickness = 0.024 mm at perimeter of central bright square
Source: Reprinted with permission from Kahr, B., McBride, J.M. "Optically Anomolous Crystals" *Angewandle Chemie, International Edition in English*, 1992, *31* p.1–26. Copyright 1992 Wiley-VCH, STM

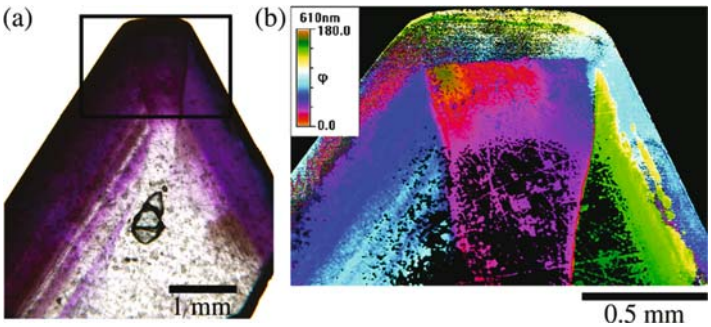

Figure 3.23. (*a*) Barium nitrate with {111} habit grown in the presence of methylene blue. (*b*) Map of the absorption of the most absorbing direction measured counterclockwise from the horizontal
Source: Originally published in Liu, X. Y. and De Yoreo, J.J. *Nanoscale Structure and Assembly at Solid-Fluid Interfaces*, 2004, 700 p., Copyright 2004 Springer (formerly Kluwer Academic Publishers, Boston)

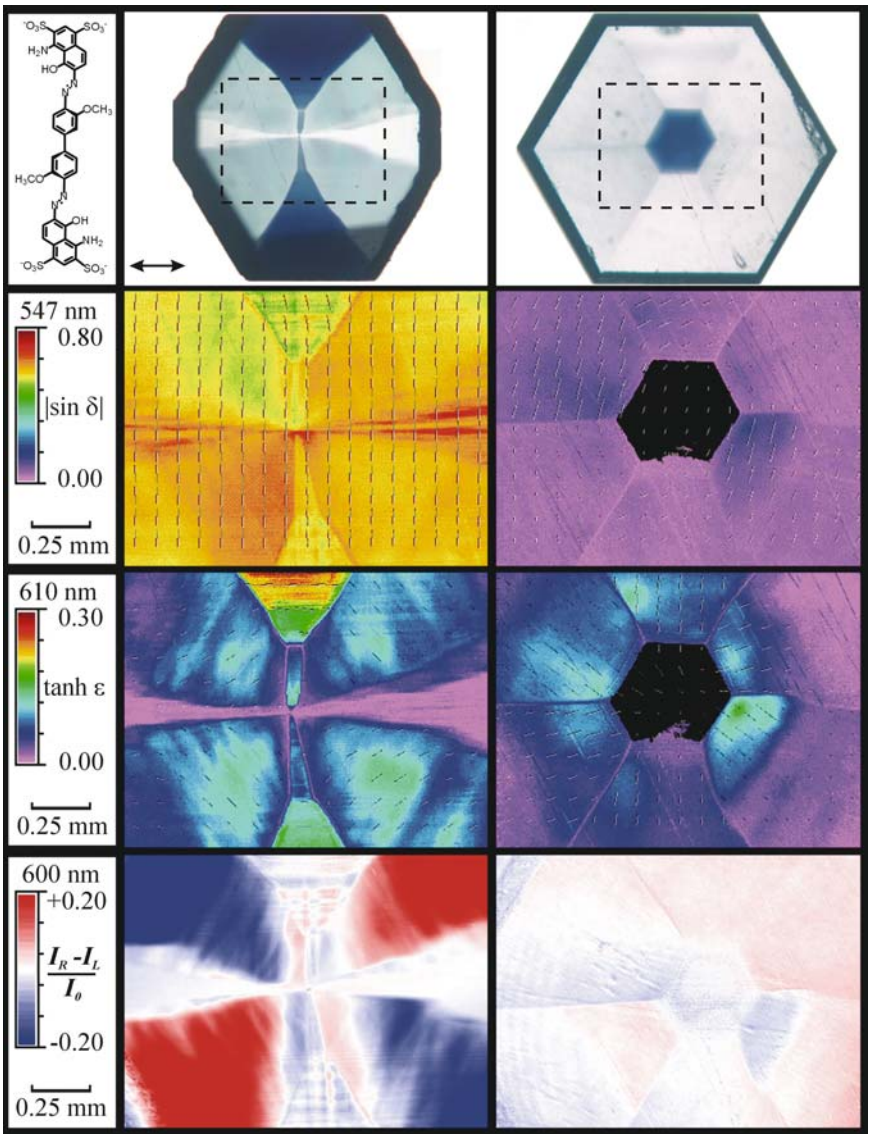

Figure 3.24. Chicago sky blue dyed $LiKSO_4$ crystals. Images in the left column are made along the [100] direction of 0.68 mm thick section, [001] is vertical. Images in the right column are made along the [001] of 0.38 mm thick section. (a, b) Photographs in light polarized along the arrow. Dotted, rectangular enclosures are imaged below. (c, d) Linear birefringence micrographs, $\delta = 2\pi L\Delta n/\lambda$. (e, f) Linear dichroism micrographs, $\tanh \varepsilon = 2(T' - T'')/(T' + T'')$. (g, h) circular extinction micrographs, $(I_R - I_L)/I_o$

Source: Reprinted with permission from Claborn, K., Chu, A.S., Jang, S.H., Su, F., Kaminsky, W. and Kahr, B. "Circular Extinction Imaging: Determination of the Absolute Orientation of Embedded Chromophores in Enantiomorphously Twinned $LiKSO_4$ crystals" *Cryst. Growth Des*. **2005,** *5*, p.2117–2123. Copyright 2005 American Chemical Society

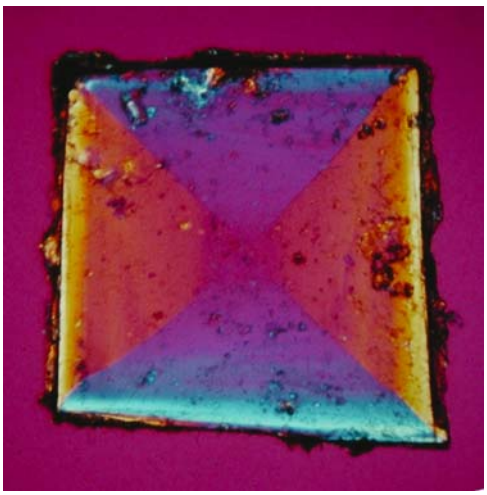

Figure 3.35. Growth sector zoning in crystal of di-11-bromoundecanoyl peroxide containing 15% of the corresponding compound in which one bromine atom was replaced with hydrogen. View along [001] between crossed polarizers with a first order red retarder
Source: Reprinted with permission from McBride, J.M. and Bertman, S.B. "Using Crystal Birefringence to Study Molecular Recognition" *Angewandle Chemie, International*, Edition in English, 1989, *28* p. 330–333. Copyright 1989 Wiley-VCH, STM

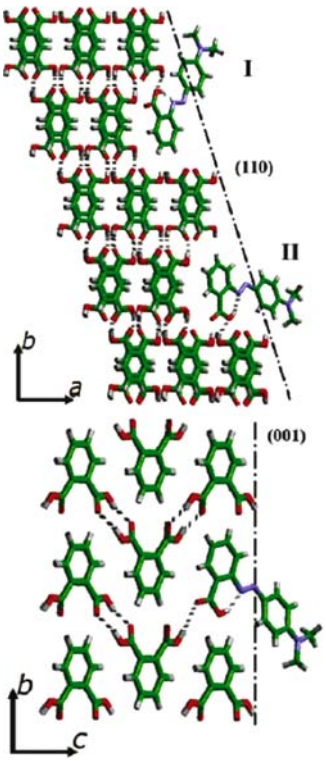

Figure 3.36. Simulations of methyl red ($((CH_3)_2N-C_6H_4-N=N-C_6H_5CO_2H)$) docking to two distinct sites (I) and (II) on the asymmetric (110) surface above and the one unique site on the (001) with local symmetry *m*. Black dashed lines denote lowest energy stable surfaces for the indicated facets *Source*: Reprinted with permission from Benedict, J.B., Cohen, D.E., Lovell, S., Rohl, A.L. and Kahr, B. "What is syncrystallization? States of pH indicator methyl red in single phthalic acid crystals" *J. Am. Chem. Soc,* 2006, *128*, p.5548–5559 Copyright 2003 American Chemical Society

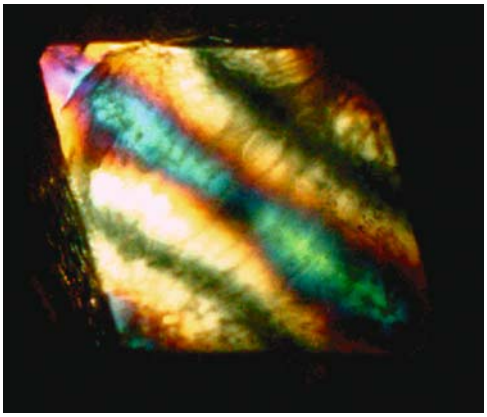

Figure 4.2. Anomalous birefringence in NH_4Cl related to syntactic intergrowth with $MnCl_2 \cdot (NH_4Cl)_2 \cdot 2H_2O$. Crystal size ~ 0.8 mm

Figure 4.15. Example of an interference figure for heterogeneous potassium ferrocyanide trihydrate crystal

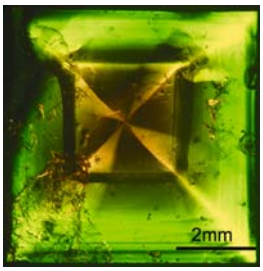

Figure 5.3. Anomalous birefringence of 1,8-dihydroxyanthraquinone between crossed polarizers
Source: Reprinted with permission from Claborn, K., Puklin-Faucher, E., Kurimoto, M., Kaminsky, W. and Kahr, B. "Circular Dichroism Imaging Microscopy: Application to Enantiomorphous Twinning in Biaxial Crystals of 1,8-Dihydroxyanthraquinone" *J.Am.Chem. Soc.* 2003, 125, p.14825-14831. Copyright 2003 American Chemical Society

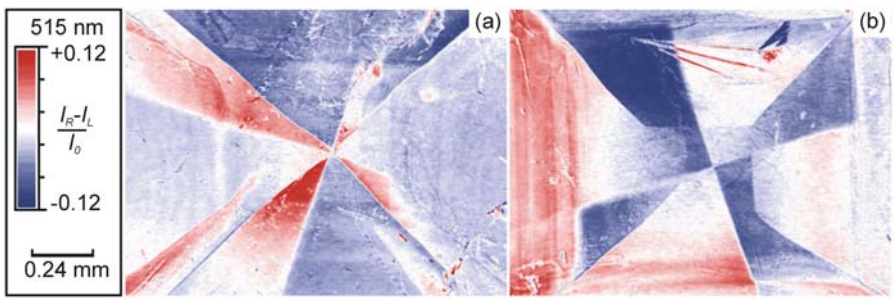

Figure 5.4. False color micrographs of crystals of 1,8-dihydroxyanthraquinone in which red indicates the preferential transmission of left circularly polarized light and blue indicates the preferential transmission of right circularly polarized light
Source: Reprinted with permission from the Royal Society of Chemistry, Kaminsky, W., Claborn, K., Kahr, B. "Polarimetric Imaging of Crystals" *Chem. Soc. Rev.* 2004, 8, p.514-525. Copyright 2004 Royal Society of Chemistry